5-2018

# Adsorption of Light Alkanes on the Surface of Substrates with Varying Symmetry and Composition

Nicholas Allan Strange
*University of Tennessee*

To the Graduate Council:

I am submitting herewith a dissertation written by Nicholas Allan Strange entitled "Adsorption of Light Alkanes on the Surface of Substrates with Varying Symmetry and Composition." I have examined the final electronic copy of this dissertation for form and content and recommend that it be accepted in partial fulfillment of the requirements for the degree of Doctor of Philosophy, with a major in Chemistry.

John Z. Larese, Major Professor

We have read this dissertation and recommend its acceptance:

Takeshi Egami, Jeffrey D. Kovac, Brian K. Long

Accepted for the Council:

Dixie L. Thompson

Vice Provost and Dean of the Graduate School

(Original signatures are on file with official student records.)

# Adsorption of Light Alkanes on the Surface of Substrates with Varying Symmetry and Composition

A Dissertation Presented for the
Doctor of Philosophy
Degree
The University of Tennessee, Knoxville

Nicholas Allan Strange
May 2018

# ACKNOWLEDGEMENTS

I would like to express my sincerest gratitude to Prof. J.Z. Larese who has served as my graduate research advisor, scientific mentor, and most importantly a close friend over the past several years. You have taught me that being a scientific Shepard is way more interesting/fun than being a sheep. The knowledge you have provided me with far exceeds the realm of science and will never be forgotten. I can't thank you enough for the opportunities you have provided me with. My hope is that we continue to share similar interests in science and can continue to work together for years to come. I would also like to especially thank Maryann Larese who kept JZL sane during my time in the group and made sure I always felt included when travelling as the lone student for experiments/conferences.

My wife Brittany has made the biggest sacrifice of all in allowing me to pursue my dreams of performing scientific research at a high level. We moved to Knoxville only a week after we got married so I could begin this journey and for that, I am forever indebted. Thank you for your never-ending encouragement, support, and love. I wouldn't have survived the late nights without you by my side (or at least sleeping on the couch). You are second to none as a wife and mother. I love you, forever.

Thank you to my beautiful daughter, Addison, who's contagious smile and personality instantly changes the tone of any rough day. She fortunately inherited all the good traits from her mother, and constantly is a reminder to be better. Thank you for the motivation to finish my thesis so I can spend time watching you grow up.

To my parents: Thank you for providing me with the opportunity to pursue my dreams. Your constant support and encouragement never goes unnoticed. I am forever in your debt. Hopefully this in part makes up for all the early years when it was a constant struggle to get me to pay attention in school.

To Mr. Kitty: There has always been a second world in my life that exists in the early hours of the morning. Thank you for the years of staying by my side while I burned midnight oil; even when it was learning just for the hell of it, you were there with me. I miss you buddy.

To the Larese group members I have had the pleasure working with (Nathaniel Bass, Andy Hicks, George Rouvelas, Chris Crain, Daniele Paradiso, Fatema Wahida, Zach Stroupe, Andrew Pedersen, Luther Langston): Thank you for the useful conversations and assistance during my time at UT.

# ABSTRACT

Adsorption plays an integral role in a variety of fundamentally and technologically important processes such as lubrication, gas separation and purification, wetting behavior, energy storage, heterogenous catalysis, biologically inspired materials, and the theory of phase transitions. As a result, adsorption phenomena are extensively studied in chemistry, physics, and biology each for uniquely different reasons. The homologous series of normal alkanes represent a class of organic molecules that are important in the fuel industry. From a fundamental perspective, the series of normal alkanes provide a route whereby physical and chemical properties relevant to adsorption can be examined with only subtle changes in molecular size and length. The alkanes also exhibit a well-known odd-even effect in some condensed phase physical properties. In the current study, the physical adsorption properties of the normal alkanes (methane-decane) on MgO, graphite, and boron nitride were investigated using volumetric adsorption isotherms and molecular dynamics simulations. This portion of the study focuses on determining the thermodynamics of adsorption as well as predicting the adsorption structures and dynamics. As a secondary study, the chemical adsorption of ethanol was examined on the surface of transition-phase aluminas using volumetric adsorption, temperature-programmed desorption, and inelastic neutron scattering. The purpose of this work was to observe the surface-catalyzed reaction of chemically bound ethanol with Lewis and Brø[oe]nsted acid sites present on the aluminas in-situ. The results of the projects described have

significant implications in the design of new materials for gas separation and purification as well as heterogenous catalysis.

# PREFACE

Surface chemistry represents one of the most fundamentally and technologically important areas in science; though it is often overlooked or even forgotten. However, modern technology relies heavily on a sound understanding of the underlying phenomena that dictate surface interactions. A variety of processes in chemistry, physics, and biology occur at the boundary between two phases. Additionally, some of the most profound areas in current scientific research involve surfaces including lubrication, gas separations and purification, adhesion, energy storage, renewable energy, and catalysis. Even recently, Kosterlitz and Thouless were awarded the Nobel Prize in physics for developing a microscopic theory of melting for two-dimensional (2D) materials (Kosterlitz 1972).

Behind the curtains, surface chemistry plays a significant role in basic everyday human life. The diffusion of ions in and out of cells relies on membrane transport mechanisms dictated by surface functional groups. Surfactants in the lungs, made up of a combination of lipids and proteins, are designed to reduce the surface tension of the air/liquid interface by forming a reactive monolayer surface (Veldhuizen 2000). The beading of water on a car windshield results from the wetting behavior of water on glass. It is the responsibility of the surface scientist to further the development of science that addresses key societal challenges.

Chemistry is often considered a practical and applied science. However, surface science does not exclusively fall into the realm of chemistry. Physical interactions such as van der Waals forces are the dominating factor in

physisorption. Thus, physics must also play a considerable role in the interfacial regime. In terms of Pasteur's quadrant, surface science resides at the top right where there is both a quest for fundamental understanding as well as a consideration for use (Stokes 1997); Hence the applicability of surface science in industrial catalysis as well as the fundamental understanding of 2D melting in Kosterliz, Thouless, Halperin, Nelson, and Young's (KTHNY) theory.

The aim of the research contained within this dissertation is to provide necessary information for enhancing fundamental understanding of surface interactions and to also improve methods for surface-catalyzed reactions important in the industrial realm; thus, the work performed has both fundamental and practical implications. This has been accomplished using a multi-faceted approach, including adsorption methods, spectroscopy, and computation, providing a detailed description of the systems of interest. The physical adsorption of the first ten normal alkanes (methane through decane) has been investigated on magnesium oxide (MgO), graphite, and hexagonal boron nitride (hBN) using volumetric adsorption isotherms and molecular dynamics (MD) simulations. Adsorption experiments on these three different substrates reveal how a change in chemical composition and surface symmetry influences the adsorption thermodynamics, monolayer solid structures, layer growth, and dynamics within the thin films. The homologous series of normal alkanes are ideal for providing a direct route for examining adsorption properties with subtle increases in molecular size. A secondary focus involves the adsorption of ethanol on the surface of

transition-phase aluminas. This interaction involves chemical adsorption where the ethanol is catalytically dehydrated to form ethylene by activated sites on the alumina surface. Volumetric adsorption isotherms, temperature-programmed desorption (TPD), and inelastic neutron scattering (INS) were employed to examine the surface-catalyzed dehydration reaction at each step in the process.

In the first chapter, a brief history of adsorption will be presented in order to provide the reader with a chronological timeline of discoveries and technological advancements that have led to modern surface science and adsorption as they are known today. The bulk and surface structures of the substrates used in this study will be then be described followed by an examination of the behavior of bulk $n$-alkanes. MD theory will be covered along with some of the useful functions that can be calculated from trajectories. The materials and methods used in this work are detailed in chapter 2. The next four chapters correspond to each of the publications that have resulted from these studies: chapter 3 – adsorption of octane, nonane, and decane on MgO(100), chapter 4 – adsorption of methane through decane on hBN, chapter 5 – adsorption of pentane and hexane on graphite, and chapter 6 – catalytic dehydration of ethanol on the surface of transition-phase aluminas. Chapter 7 will summarize the results from the above experiments and present directions for future work.

# TABLE OF CONTENTS

# LIST OF TABLES

# LIST OF FIGURES

# CHAPTER ONE – INTRODUCTION AND BACKGROUND INFORMATION

## Introduction to Molecular Adsorption

Adsorption isotherm measurements (constant temperature) can provide information about specific surface area, pore structure and size distribution, particle size distributions, thermodynamics, and phase transitions. The isothermal volumetric approach is frequently used because it is experimentally the easiest measurement to perform. Conveniently, the constant temperature model is also the least complex to describe mathematically. While there are several approaches to performing adsorption isotherm measurements, this study will focus on the gas-solid adsorption experiment. In these types of experiments a well dispersed solid (generally a powder), called the adsor*bent* is contained within a small volume at a constant temperature. Gas molecules, termed the adsor*bate*, are introduced to the solid within a closed volume at a particular pressure. The interaction between the adsorbate and adsorbent can be probed using a variety of techniques including vapor pressure measurements, low energy electron diffraction (LEED), NMR, calorimetry, Auger electron spectroscopy, and ellipsometry each with their own respective advantages and disadvantages. Table 1 below highlights the capabilities of a selected group of experimental techniques used to study molecular adsorption. This investigation utilizes pressure transducers to measure adsorption volumetrically. As the

Table 1 – Experimental methods for examining adsorption phenomena.

Reproduced from M. Bienfait. (Bienfait 1980)

| | | Thermo-dynamics | Long range order | Vibrations | Electron surface states | Fluid mobility | Short range order | Interaction energy |
|---|---|---|---|---|---|---|---|---|
| **Electrons** | Elastic | | Structure | Debye temperature | Surface transitions | | | |
| | Inelastic AES ELS | Adsorption isotherms | | | | | Configuration | |
| **Neutrons** | Elastic coherent | Phase diagram | Structure | Debye temperature | | | Correlation range | |
| | Elastic incoherent | | | Debye temperature | | | | |
| | Inelastic coherent | | | Phonons | | | | |
| | Inelastic incoherent | Phase diagram | | Localized modes | | Diffusion coefficient | | |
| **R X** | Elastic | | Structure | Debye temperature | | | Correlation range | |
| | EXAFS | | | | | | Configuration | |
| **Adsorption Isotherms** | | Phase diagram | | | | | | Enthalpy/ Entropy |
| **Calorimetry** | | Phase diagram | | | | | | Enthalpy Specific heat |
| **IR** | | | | Localized modes | | | | |
| **NMR** | | | | | | Mobility | | |
| **Mössbauer** | | | X | Debye temperature | | Mobility | X | |
| **Neutral beams (He)** | | | | X | | | | Interaction states |
| **Photo-emission** | | | | | Surface states | | Configuration | |

adsorbate molecules interact with the adsorbent, the pressure decreases until it reaches an equilibrium value. For the sake of simplicity, the discussion in the following sections will be limited to adsorbate molecules that interact with a surface through physical forces (i.e. physisorption).

There are a variety of theoretical approaches which have been used to describe fundamental molecular adsorption, however there has yet to be revealed a single equation or method that exactly explains the behavior of all types of adsorption.  For example, many of the models that accurately represent monolayer physical adsorption tend to fail in describing multilayer behavior that exists when a film partially or fully wets a substrate due to molecule-molecule and molecule substrate attractive forces. Furthermore, perturbation of the substrate by the atoms/molecules in the adsorbed phase has impeded the ability to macroscopically describe adsorption using standard thermodynamics. Two recent developments have made it possible to further the current understanding of microscopic and molecular-level adsorption phenomena. First, improvement of experimental techniques and instrumentation has made it possible to extend the boundaries of experimentally accessible phase space. In particular, the ability to achieve low temperatures (<100 K) and pressures where small molecules (e.g. hydrogen, helium, methane) exhibit unique behavior in the adsorbed phase. Further, the ability to generate substrate materials with homogenous surfaces, particularly in carbonaceous archetypes, has greatly improved the reproducibility of such measurements. It is not surprising that significant advancements have

recently been made in understanding the interaction of noble gases and small organic molecules on the surface of graphite. Secondly, the application of computer simulation methods to model adsorption systems has enhanced the ability to understand natural interfacial phenomena observed in experimentation. The bridge between these computational and experimental approaches lies in the approximation of intermolecular forces represented by simple functions which have been empirically parameterized. Nevertheless, the interpretation of experiments ultimately drives the effort for improving theoretical models and the current understanding of interfacial phenomena.

### A Brief History

The study of adsorption has been around for centuries, yet not formally coined "adsorption" until 1881 (Kayser 1881). One of the first accounts of adsorption was recorded in Talmud's Book of Judges. In these writings Gideon observed the absorption of water into wool, though it was not understood to be a natural phenomenon. It wasn't until the 18th century that quantitative measurements were carried out. Most of these studies involved the uptake of vapors by clays and charcoal. During the early part of the 20th century, McBain formally established the difference between adsorption and absorption (McBain 1909). This divided the field into porous and non-porous materials as it is considered today. The field of adsorption branched into chromatography in 1903 when Tswett discovered that particular substances exhibited selective uptake (Tswett 1990). The first quarter of the 20th century signaled to beginning of

attempts aimed at deriving a theory for adsorption phenomena. In 1930, Herbert Freundlich popularized an empirical relationship for solution-based adsorption (Freundlich 1930). This simple relationship, having no theoretical foundations is defined as,

$$\frac{x}{m} = Kp^{1/n} \qquad (1)$$

where $x$ is the mass of the adsorbate, $m$ is the mass of the adsorbent, and $p$ is the equilibrium pressure of the adsorbate. The Freundlich equation fails to accurately describe isotherms at high pressures where the adsorbate saturates and forms bulk. One of the early theoretical descriptions of adsorption theory stemmed from Michael Polanyi, who defined an adsorption potential (Polanyi theory) as the differential molar work of adsorption (Polanyi 1914). The behavior of adsorbed atoms/molecules are dependent upon the distance from the adsorption potential. This theory forms the basis for volumetric adsorption methods where thermodynamic equilibrium is defined by a chemical potential change of zero as defined by the difference between adsorbed and bulk vapor pressures. Dubinin later refined this adsorption potential as the negative work performed by the system (Dubinin 1952). This development led to the formulation of adsorption thermodynamics.

An early classification scheme for five types of van der Waals adsorption isotherms was proposed by Brunauer *et al.* (Brunauer 1940) and later updated by the International Union of Pure and Applied Chemistry – IUPAC (see Figure 1). This arrangement should not be interpreted as an exhaustive list of what is
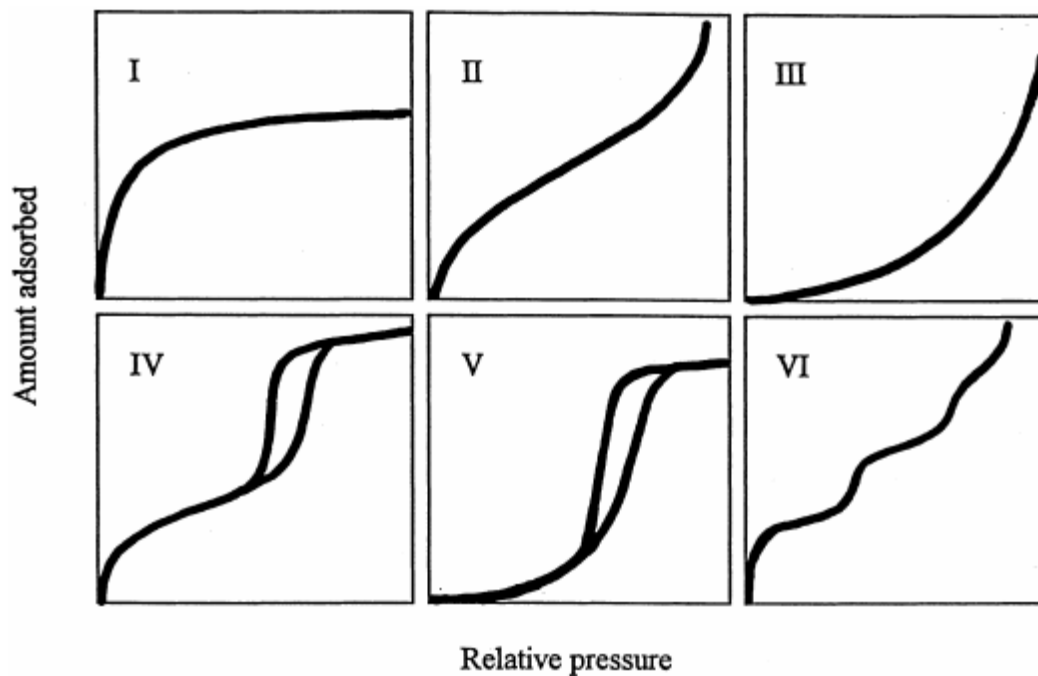
Figure 1 – IUPAC classification for adsorption isotherms (IUPAC 1985)

possible in nature. It is important to recognize that some isotherms are not able to be categorized by these five classes. It is also possible that a particular adsorption system can exhibit behavior representative of multiple classes of isotherms. The following sections will highlight representative behavior of these five "classes" and further expand upon two of the more commonly observed types.

Type I shown in Figure 1 is widely known as the Langmuir adsorption isotherm and will be discussed in the following section. Isotherms with behavior similar to type II were labeled "BET isotherms" by Brunauer, Emmett, and Teller who first described an approximated mathematical model to account for multiple-layer (multilayer) condensation. The BET isotherm is an extension of the Langmuir adsorption isotherm and will also be discussed in more detail later. The isotherm measurements performed in this study are loosely categorized as type II, but as will be shown later, the behavior observed is not exact. Type III isotherms occur when the intermolecular forces between adsorbate molecules are sufficiently great to overcome the interaction with the substrate. In this situation, there is no layer condensation and the vapor pressure asymptotically approaches the saturated vapor pressure. Isotherms comparable in shape to types IV and V experience low pressure behavior similar to that of types II and III but exhibit a considerable increase in vapor pressure until the saturated vapor pressure is reached where the shape abruptly diverges convex to the abscissa. This behavior is common in measurements made on/in porous materials. Types

8

IV and V also exhibit a hysteresis loop upon molecular desorption which can be related to the pore size distribution through the Kelvin equation.

### *Langmuir Model of Monomolecular Adsorption*

The Langmuir equation for monolayer adsorption is well known as one of the earliest attempts at deriving a theoretical model for adsorption phenomena. This kinetic-based approach derived by Irving Langmuir in 1918, assumes there is a discrete number of binding sites on the surface of an adsorbent. The atoms adsorbed on these discrete sites are immobile (i.e. localized model). At equilibrium, the rate of evaporation must proportional to the rate of condensation as,

$$k_1 S_1 = k_2 P S_0 = k_2 P (S - S_1) \quad (2)$$

where $S_1$ sites are occupied and $S_0$ sites are unoccupied, k is the rate constant for the adsorption process, and P is the pressure. Alternatively, this expression can be expressed as,

$$v = \frac{v_m b P}{(1 + bP)} \quad (3)$$

where the site occupancies have been converted to volume adsorbed in one monolayer and *b* represents the reduced rate constant. In the low-pressure region of the Langmuir isotherm, the amount adsorbed is nearly linear with the increase in pressure. At higher pressures, the amount adsorbed converges to the volume in one monolayer. One of the significant deficiencies of this model is that molecule-molecule (MM) interactions are neglected, when in fact intermolecular

forces can play a substantial role in adsorption behavior particularly near and above monolayer coverages. Thus, the thermodynamics of adsorption calculated using a statistical mechanical approach from this model only account for $N$ numbers of non-interacting molecules with sites of energy, $Q$ which clearly finds discrepancies with experiments. Since the Langmuir isotherm is incapable of accounting for multiple condensed layers, later formulations described in the following sections aimed to improve upon this elementary description by accounting for both MM interactions and multilayer formation.

### *Multilayer Models*

Following the results of Langmuir, in 1938, Brunauer, Emmett, and Teller (BET) developed an isotherm equation based on a generalization of Langmuir's isotherm equation which accounts for multilayer adsorption (Brunauer 1938). Using the assumption that the rate constants for condensation and evaporation are independent of surface coverage, BET added kinetic terms for exchange between two adjacent layers resulting in a new isotherm equation of the type,

$$v = \frac{v_m c p}{(p_0 - p)\{1 + (c-1)(p/p_0)\}} \quad (4)$$

Where $v_m$ is the volume of gas adsorbed in a monolayer, p is the equilibrium vapor pressure, $p_o$ is the saturated vapor pressure, and $c$ is a constant. This assumes that each multilayer can be treated individually as a Langmuir monolayer. For the purpose of comparing to experimental adsorption isotherm measurements, the BET isotherm equation is conveniently written,

$$\frac{p}{v(p_0-p)} = \frac{1}{v_m c} + \frac{c-1}{v_m c}\frac{p}{p_0} \qquad (5)$$

where a linear fit to *p/p*$_o$ versus *p/v(p*$_o$*-p)* can be applied to determine the

monolayer volume and heat of adsorption. The BET equation still fails to account

for lateral MM interactions and assumes that the *n>1* layers formed above the

monolayer are equivalent. Furthermore, the energy distribution from surface

binding sites is assumed to be perfectly homogenous which has been shown not

to be the case for many substrates.  Brunauer *et al.* later introduced four

additional terms to the original BET equation to account for capillary

condensation and accuracy at higher relative pressures which became known as

the BDDT equation. While the BET equation cannot always reliably predict the

thermodynamics of adsorption, it is often used to determine specific surface

areas for the adsorption of nitrogen on the surface of relatively simple non-

porous substrates.

### *Statistical Mechanics*

Following the development of the Langmuir and BET equations from

principles of kinetics, a statistical thermodynamic derivation was carried out by

Cassie where it was proposed that an entropy of mixing allowed a liquid

multilayer phase to condense below the saturation pressure (Cassie 1944).

Terrell Hill refined Cassie's result stating the correct result was obtained with an

incorrect argument. He later provided the statistical mechanical derivation for

mobile adsorption and adsorption with a limited number of multilayers. In a ten-

part series in the Journal of Chemical Physics, Hill provided derivations for greater complexities addressing intermolecular forces, surface heterogeneities, capillary condensation, and solution thermodynamics. The use of statistical mechanics applied to adsorption phenomena has led to the development of Monte Carlo (MC) and molecular dynamics (MD) techniques, which are exactly solvable using statistical methods, though they are limited by the accuracy of the intermolecular potentials used in the simulation. These "computer experiments" have been used to validate approximations made in statistical mechanical theory. The MC and MD techniques can also be directly compared to results from experiments.

### *Integral Equations*

The Langmuir and BET models for adsorption assume there is single site occupancy, each of which have the same probability of adsorption. On real surfaces there are multiple adsorption sites with different binding energies (e.g. MgO). Heterogeneities on the substrate result in a variation of surface energies which are not accounted for in previous models. Thus, Langmuir proposed that distinguishable adsorption sites could be approximated by a sum of Langmuir equations each normalized by the abundance of a particular site. This provided the foundation for what are now known as integral equations. Zeldovich later showed how the sum can be replaced by an integral if the number of dissimilar sites is large (Zeldovich 1934).

### Surface Wetting

Of particular importance to the adsorption of liquids on solid surfaces is a consideration of wetting phenomena. Surface wetting is somewhat coupled with the absorbed surface structure as will be discussed later. Wetting is a phenomenon typically associated with the interface between a liquid and a solid where the extent of wetting is determined through a contact angle between the liquid and the solid. There are three notable types of wetting: complete wetting, incomplete wetting, and non-wetting (see Figure 2). In the complete wetting scenario, the liquid spreads across the solid surface homogenously where the resulting contact angle between the liquid and the solid is 0°. At the other extremum, non-wetting is observed whenever the liquid forms a perfect spherical droplet with a contact angle of 180° on the solid surface. The intermediate phenomenon, incomplete wetting, is any variation in between the two extrema. Incomplete wetting is most frequently encountered for the types of interactions involved in this particular study.

### Overlayer Structures

The epitaxial structure of an adsorbed solid phase also dictates the mechanism of film growth with increasing coverage. There are two possibilities that can arise important to the molecules in this study. First, a commensurate structure exists when the lattice of the adsorbed phase is in registry with the lattice of the substrate surface. This phase can exist as long as the symmetries of the two phases align with an integer multiple. One way to label a
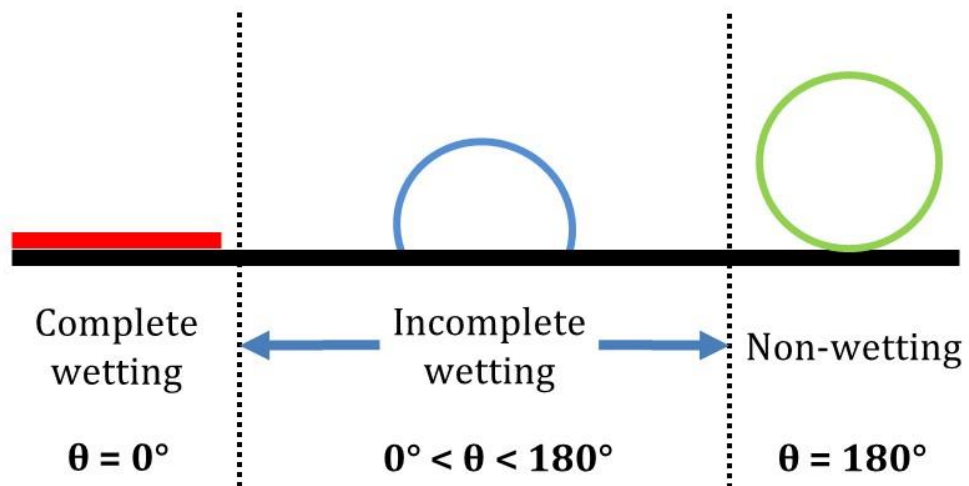
Figure 2 – Illustration of the contact angle in wetting phenomena

commensurate lattice is through Woods' notation. This method offers a route whereby the overlayer structure can be specified in terms of the substrate surface structure. An example of this is shown in Figure 3. The multiplicity of the basis vectors is defined in parentheses with any rotation angles following. If the overlayer structure is a primitive lattice, the parentheses are sometimes preceded by a "*p.*"  For a centered overlayer structure, a "*c*" is used as a prefix.

An incommensurate structure is one where the lattice of the adsorbed phase is out of registry with the substrate's lattice. Both situations can exist for a variety of reasons. It is clear that for adsorption to occur, the interaction between the adsorbate molecules and substrate atoms (MS interaction), must exceed the intermolecular forces between two adsorbate molecules (MM) at a given chemical potential at constant temperature. In the commensurate phase, the MS interaction is sufficiently large to direct the binding of adsorbate molecules. If the substrate-induced structure of adsorbate molecules is similar to the bulk molecular structure, the films tend to grow in discrete steps. In the incommensurate case, the MS force is not sufficient to direct the adsorbed phase. For this situation, mechanism of film growth depends on both the epitaxial structure at the interface, the similarity to the bulk condensed phase structure, as well as the coverage.

### *The Volumetric Adsorption Isotherm Experiment*

For the adsorption isotherm measurements performed in the current studies, each dosing step involved the introduction of an amount of gas
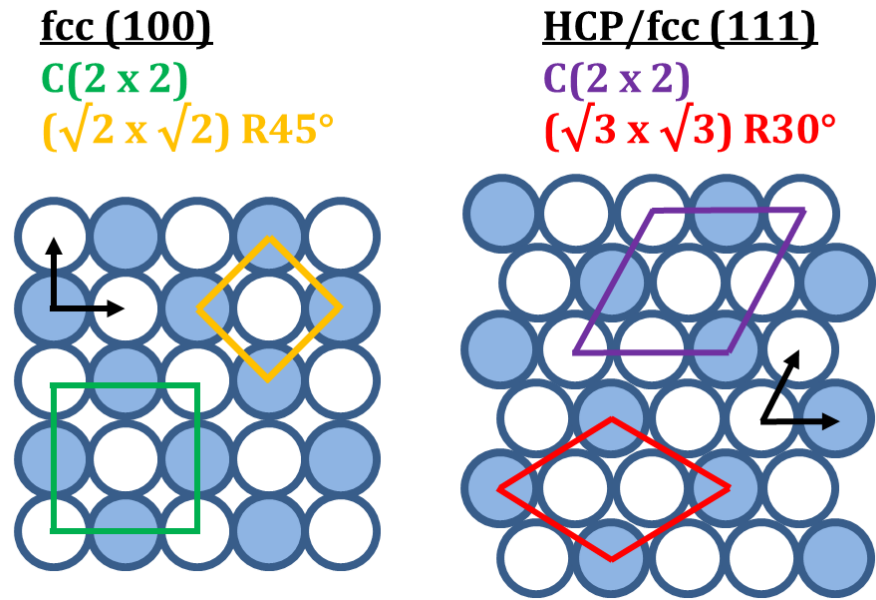
Figure 3 – Example overlayer structures on cubic and hexagonal surface lattices

(determined by the pressure and volume) into a known volume. This amount of gas was subsequently allowed to expand into a sample cell held at a constant temperature and volume. The equation for a single dosing sequence is expressed as,

$$n_{ads_i} = \Delta n_{enter\ cell_i} - \Delta n_{headspace} \quad (6)$$

$$n_{ads_i} = \frac{\Delta p_i V_{dose}}{RT_{room\ temp}} - \frac{(p_{f_i} - p_{f_{i-1}})V_{headspace}}{RT_{ISO}} \quad (7)$$

The term on the left side of this equation is straightforward and is equal to the total number of moles entering the sample volume. The term on the right-hand side is applied in order to subtract the number of moles in the vapor from the total moles entering the cell. These measurements are performed in thermodynamic equilibrium, meaning that at the endpoint of each dosing sequence, the molecules in the vapor phase are in equilibrium with the molecules in the adsorbed phase as determined by the pressure at a constant volume. Thus if the chemical potential is defined as,

$$\mu = RT \ln P \quad (8)$$

then it must hold true that at the completion of a dosing sequence,

$$\Delta \mu = \mu_{ads} - \mu_{vapor} = RT \ln \left( \frac{P_{ads}}{P_{vapor}} \right) = 0 \quad (9)$$

The dosing sequence is continued until the saturated vapor pressure of the adsorbate at the sample temperature is reached. At this point the adsorbate molecules no longer condense in layers on the surface of the substrate, but

17

rather are in a phase that is nearly identical to a bulk three-dimensional vapor. The results of these measurements are plotted as the total number of moles adsorbed versus the equilibrium vapor pressure. The total number of moles can be determined from a summation over consecutive doses expressed as,

$$\sum_{i=1}^{N} n_{ads_i} = \frac{(\sum_{i=1}^{N} \Delta p_i)V_{dose}}{RT_{room\ temp}} - \frac{p_{f_i}V_{headspace}}{RT_{ISO}} \quad (10)$$

In equation 10, the pressure term on the right-hand side has been summed over sequences, but simply reduces to the equilibrium vapor pressure at the "*n*th" dose. A more convenient way to express the abscissa is in terms of reduced pressure ($P/P_o$) where the equilibrium vapor pressure is normalized by the saturated vapor pressure at the sample temperature. Alternatively, from a thermodynamic standpoint, it is useful to express the reduced pressure in terms of difference in chemical potential as shown above. An example of an adsorption isotherm measurement for methane on graphite is illustrated in Figure 4.

While the temperature fluctuations were monitored using resistance or diode thermometers mounted above and below the sample cell, the experimental sample temperature was determined from the saturated vapor pressure, where Antoine's equation in the form,

$$\log_{10} P = A - \frac{B}{T+C} \quad (11)$$

was used to convert the experimental vapor pressure to temperature. Antoine's equation is a specialized semi-empirical form of the Clausius-Clapeyron equation where parameters are obtained from fits to experimental data. Antoine's equation

18
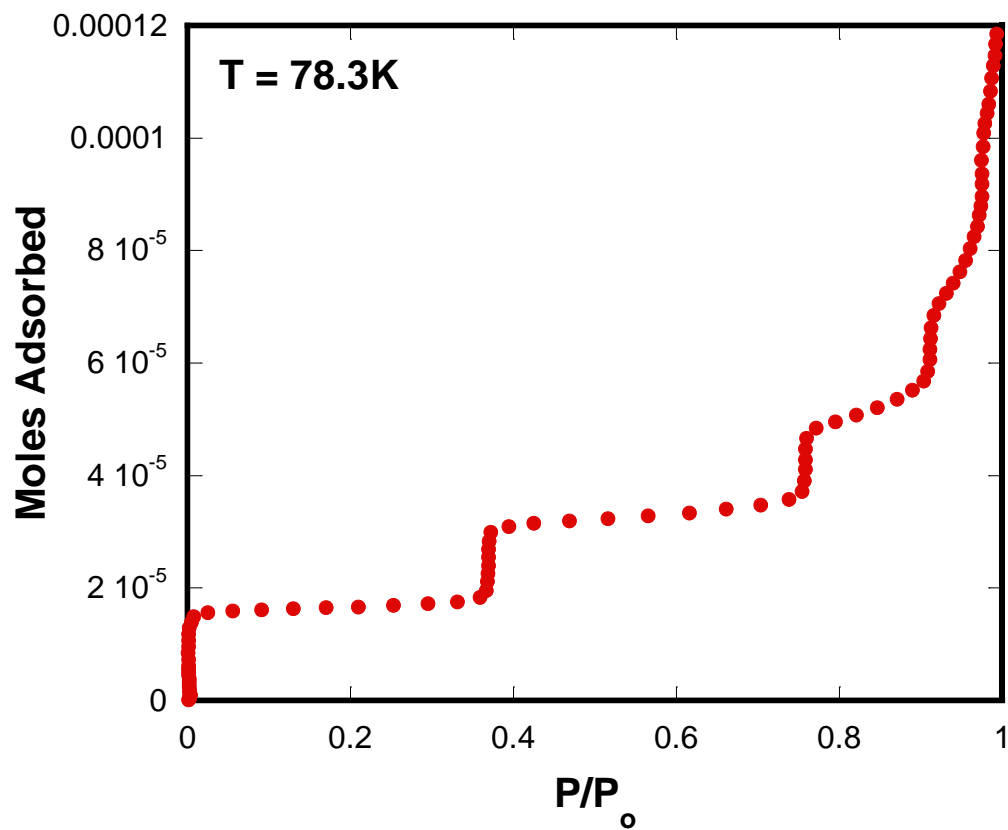
Figure 4 – Adsorption isotherm of methane on graphite at T = 78.3 K

does not typically span the entire temperature range between the triple point and critical temperatures but sets of data are available for narrow temperature ranges with considerable accuracy. The parameters used in the described experiments are presented in the materials and methods section.

### *Determination of Surface Coverage – The Point B Method*

There have been numerous suggestions about the actual location of monolayer completion, but none have withstood the test of time more than the Point B method, developed by Emmett and Brunauer (Emmett 1937). This approach utilizes the fact that the profiles of physical adsorption isotherm measurements generally yield an approximate S-shape. At low temperatures, the pressure of the system remains nearly zero as the molecules begin to form the monolayer. Near monolayer completion, the isotherm diverges and becomes concave with respect to the abscissa and remains nearly linear until bilayer completion. An initial proposition for the location of monolayer completion involved extrapolation of the linear portion between the first and section layering features to the y-axis (point A method). This was later modified by using intersection the linear region above the monolayer feature with a line fit through low pressure data below monolayer completion. Comparison of this location on the adsorption isotherm curve illustrated that the error was minimal when using the point B method in comparison with the value determined from the BET equation. While there multiple occurrences of deviations in surface area between the point B method and BET method, the point B method has been used with

success for previous measurements of rare gases and small organic molecules on the surface of graphite and MgO(100). An example of applying this method to the adsorption isotherm measurements is shown in

Figure 5. The information from the point B method can be used in order to determine the surface area of the substrate as long as the solid structure is known *a priori*. For methane on graphite, the adsorbed structure at 78.3 K is a commensurate √3 x √3 lattice with an areal density of 0.0636 molecules/Å². Thus, the graphite used in this study was determined to have a surface area of 34.02 m²/g. Most of the adsorption isotherm measurements in this study were performed at temperatures well above the monolayer melting point. The number of molecules in the monolayer can only reveal an average area occupied by a molecule in the monolayer. The actual area projected on the surface by a molecule can only be determined if the monolayer solid structure is known.

### Determination of the Thermodynamics of Adsorption

Figure 4 is essentially a constant temperature phase diagram for the chemical potential as a function of surface coverage. The thermodynamic values associated with these layer condensations can be calculated using a method developed by Larher where,

$$\ln\left(\frac{p_{(n)}}{p_{(\infty)}}\right) = \frac{u_{(n)} - u_{(\infty)}}{RT} - \frac{1}{R}\left(s_{(n)} - s_{(\infty)}\right) \quad (12)$$

Here, the logarithm of the ratio between the pressures of saturated vapor pressure and the "*n*th" transition can be related to the molar enthalpy and

21
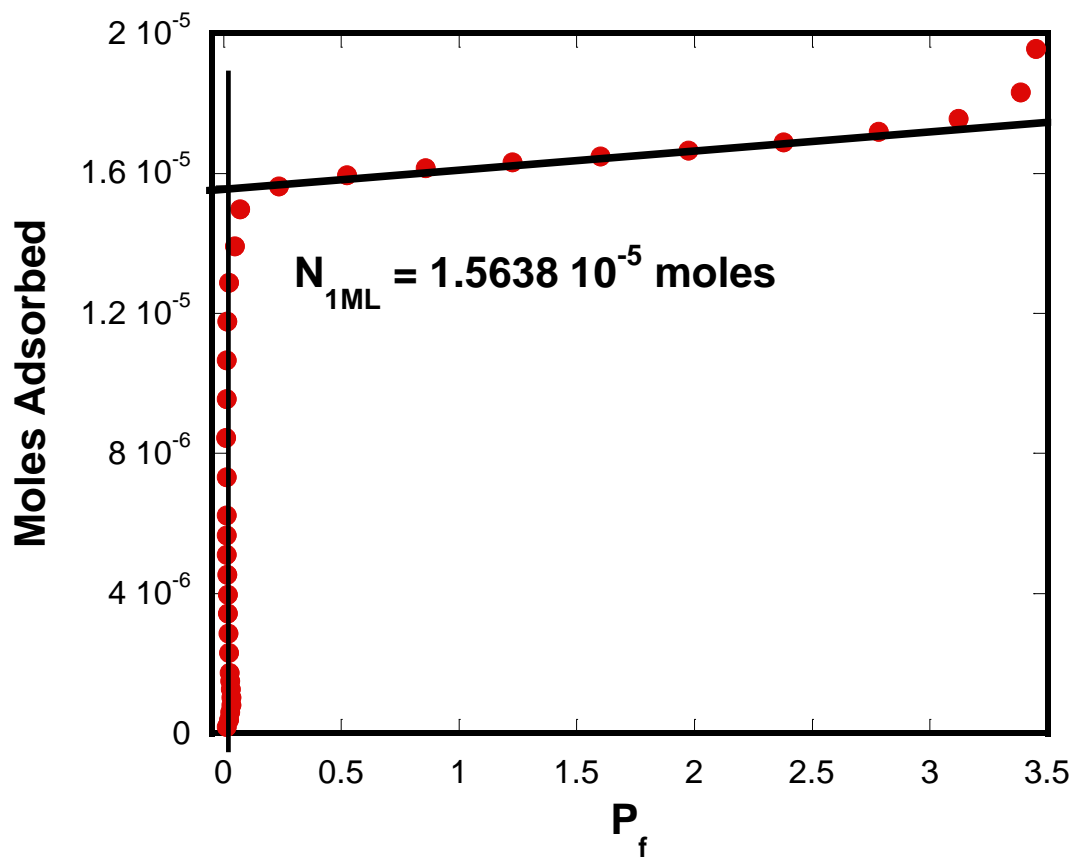
Figure 5 – Example of the Point B method for methane adsorbed on graphite at T

= 78.3 K

entropy. In this approach, the locations of these, layering features are identified by taking the numerical derivative of the raw data and fitting an appropriate peak function. For most of these features, Gaussian and Lorentzian peak functions are sufficiently accurate (see Figure 6). The numerical derivative is related to the two-dimensional compressibility by,

$$K_{2D} = \frac{Ap}{N_A k_B T N^2}\left(\frac{dN}{dp}\right) \quad (13)$$

where $A$ is the surface area of the substrate, $p$ is the equilibrium vapor pressure, $N_A$ is Avagadro's number, $k_B$ is Boltzmann's constant, $T$ is temperature, and $N$ is the number of moles adsorbed. The compressibility is one way to scale behavior between films and bulk solids. In three dimensions, the compressibility represents the change in volume with respect to a change in pressure, where the inverse quantity is defined as the bulk modulus. In two dimensions, it is defined as the change in molecular area with a change in spreading pressure. The inverse $K_{2D}$ (proportional to numerical derivative peak width) has also been shown to reveal information about locations of layering critical temperatures and other phase transitions. Thus, the heats of adsorption and differential enthalpies and entropies can be calculated for each layer using the equations,

$$Q_{ads} = R A_{(n)} \quad (14)$$

$$\Delta H_{(n)} = -R\left(A_{(n)} - A_{(\infty)}\right) \quad (15)$$

$$\Delta S_{(n)} = -R\left(B_{(n)} - B_{(\infty)}\right) \quad (16)$$

| y = m1+m2*exp(-(x-m3)^ 2/m4^... | | |
|---|---|---|
| | Value | Error |
| m1 | 3.8152 | 0.043521 |
| m2 | 9.3792 | 0.062511 |
| m3 | 0.62202 | 0.00028489 |
| m4 | 0.060799 | 0.0005575 |
| Chisq | 6.8252 | NA |
| R | 0.99743 | NA |
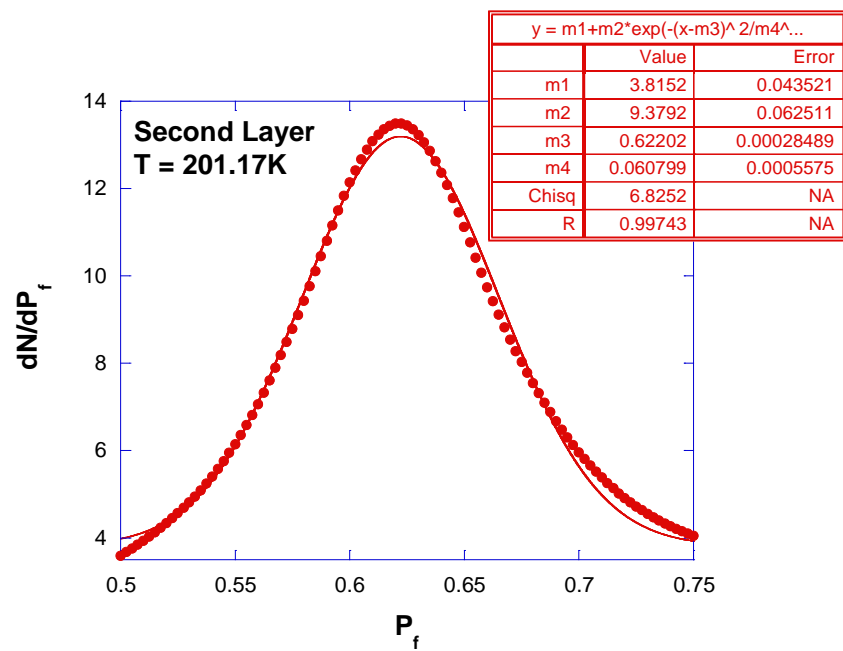
Figure 6 – Gaussian function fit to numerical derivative of isotherm

where the *A* terms refer to the slope of a linear fit to the plot of *ln(p)* versus *1/T* and the *B* parameter is the y-intercept. A general example of these types of plots is shown in Figure 7.

## Molecular Dynamics Theory

### *Introduction to Molecular Dynamics*

Simulations of large atomic and molecular systems using *ab initio* approaches are generally not feasible due to the mathematical complexity and time required in performing calculations on many-body systems. Methods that account for quantum mechanical behavior are typically limited to approximately 100 atoms. One approach that bypasses the need to consider quantum mechanical properties involves using molecular dynamics (MD) methods, which employs intermolecular force fields to describe interactions between large numbers of atoms and molecules. Alder and Wainwright developed this method in 1959 for hard-sphere systems (Alder 1959). In the MD approach, electronic motions are somewhat ignored and the motions between nuclei determine the overall energy of the system.  Furthermore, in models containing large numbers of atoms and/or molecules, thermodynamics, structure, and transport coefficients can be evaluated using statistical averages and distribution functions. MD simulations also approximate behavior of materials in the condensed phase more accurately than *ab initio* approaches because the intermolecular potentials within
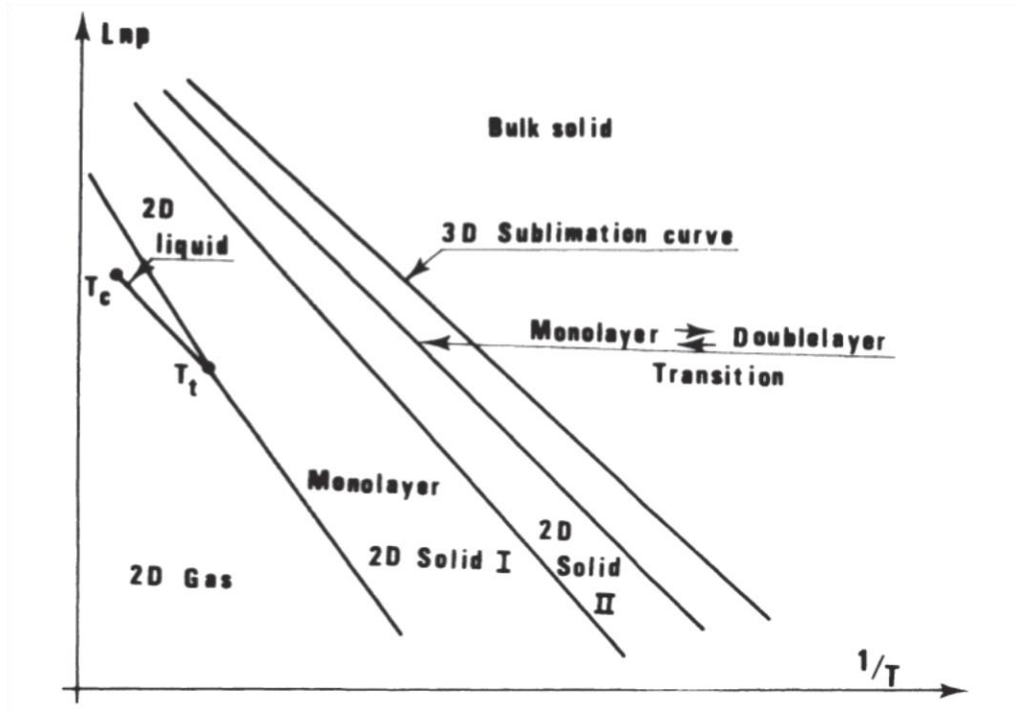
Figure 7 – Clausius-Clapeyron phase diagram for vdW adsorption on

graphite(0001)  (Bienfait 1980)

the force field are well described and can be parameterized to fit experimental data. However, since these force fields are approximations to the true intermolecular potentials, there is generally a tradeoff between computational efficiency and accuracy. Hence, it is imperative in MD simulations to choose a force field with sufficient detail to accurately model the desired properties. The simulations performed in this work utilized both the COMPASS (Sun 1998) and Universal (Rappé 1992) force fields which are described later in more detail.

### *Equations of Motion*

The molecular transport in classical MD simulations is calculated using Newtonian mechanics where the equation,

$$\boldsymbol{F_i}(t) = m_i \boldsymbol{a}_i(t) \quad \rightarrow \quad -\frac{\partial V}{\partial \boldsymbol{r_i}} = m_i \frac{\partial^2 \boldsymbol{r_i}}{\partial t^2} \quad (17)$$

is continuously evaluated at each time step (user-defined), provided a set of initial coordinates and velocities combined with the molecular force field for describing the inter- and intra-molecular components of the total energy. The method used to solve the equations of motion is called the finite-difference method. In this approach the energy of the system is calculated at time *t* which a set of coordinates and momenta. The equation is re-evaluated at time *t+Δt* where the time step is small compared with the motion of interest. The method of integration used to solve these equations is important in providing realistic and accurate results. In the Materials Studio Forcite module, the Velocity Verlet algorithm is implemented.

While this approach allows one to explore the constant energy depiction, many *real* experimental systems tend to be influenced by the environment (i.e. heat transfer, external pressure, etc.). Therefore, these methods employ statistical ensembles where the energy is no longer necessarily conserved where structural and dynamical properties can be calculated using statistical averages/fluctuations and distribution functions. The calculations in this study were performed using the canonical ensemble where the number of molecules, sample volume, and temperature are kept constant. When using the canonical ensemble, thermodynamic temperature (isothermal) is maintained by applying a thermostat. This is typically achieved by employing a series of "Nose-Hoover" thermostats functionally described as,

$$H = \langle \Psi | \hat{H}_e | \Psi \rangle + \frac{1}{2} \sum_{i=1}^{N} \sum_{j=1}^{N} \frac{Z_i Z_j}{|R_i - R_j|} + \sum_{i=1}^{N} \frac{p_i^2}{2M_i} + \sum_{i=1}^{M} \frac{p_{\xi i}^2}{2Q_i} + N_f k_B T \xi_1 + k_B T \sum_{i=2}^{M} \xi_i \quad (18)$$

where $Q_i$ is a fictitious mass (Nose parameter) and $\xi_i$ is the thermostat degrees of freedom. A modification to the Nose-Hoover thermostat has recently been made and applied to the current study where an additional Langevin friction and noise term (NHL thermostat) allows for quicker equilibration without the need to decrease $Q_i$. Thus the equation of motion for $\zeta$ appears as,

$$\frac{d\zeta}{dt} = \frac{\sum_{i=1}^{N} \frac{p_i^2}{2m_i} - N_f k_B T_0}{Q} - \gamma \zeta + \sqrt{\frac{2\gamma k_B T_0}{Q}} \dot{W} \quad (19)$$

where *W* is a Wiener process and $\gamma$ influences the strength of the stochastic process (i.e. decay time). The first term scales $\zeta$ to zero while the final term

increases $\zeta$ where the average of $Q\zeta^2$ is approximately the product of Boltzmann's constant and the defined temperature. It is clear that as $\gamma$ approaches zero, the function reduces to that of the Nose-Hoover thermostat.

### *Central Force Fields*

The COMPASS (Sun 1998) force field was used in this study to calculate energies for alkanes on the surface of graphite and MgO(100). COMPASS is a semi-empirical class II force field where the interactions between atoms are described by simple empirically-parameterized functions. Class II force fields are advantageous over class I force fields because they contain cross-terms which account for the coupling of internal coordinates (e.g. angle bend causing simultaneous change in bond length). The coefficients in this force field were determined first using *ab initio* methods, then parameterized for different atom types by making fits to experimental data. The total functional form of the COMPASS force field is defined as,

$$E_{total} = E_b + E_a + E_{tor} + E_{inv} + + E_{cc} + E_{elecrostatic} + E_{non-bond} \quad (20)$$

The types of functions that represents these terms are provided in Table 2.

The most important functional contribution to the total energy for the adsorption of alkanes on graphite and MgO is from non-bonding intermolecular forces. The intermolecular forces in the above summation are represented by a 9-6 Lennard-Jones potential. It is important to note that the Universal force field utilizes the 12-6 Lennard-Jones potential. Comparatively, the 12-6 potential tends

Table 2 – Functional forms for terms in the COMPASS Forcefield total energy

| Energy Term | Functional Type | Functional Representation |
|---|---|---|
| Bond Stretching | Harmonic | $\dfrac{K_0}{2}(R - R_0)^2$ |
| Angle Bending | Harmonic | $\dfrac{K_0}{2}(\theta - \theta_0)^2$ |
| Torsional Angle | Dihedral | $\dfrac{1}{2}\sum_j \{B_j(1 - d_j cos[n_j\phi])\}$ |
| Inversion (out-of-plane) | Wilson Angle | $\dfrac{K_0}{2}\chi_{av}^2$ |
| Electrostatic | Coulombic | $C\dfrac{q_i q_j}{\varepsilon R}$ |
| Non-bonding | 9-6 Lennard-Jones | $D_0\left[2\left(\dfrac{\sigma}{R}\right)^9 - 3\left(\dfrac{\sigma}{R}\right)^6\right]$ |

to be extreme in the repulsive component, while the 9-6 potential is known to be too attractive at longer intermolecular distances. The Lennard-Jones potential is discussed in greater detail below. While it is useful to compare the dynamics among molecules with varying carbon backbone size, the differences in functional descriptions make it difficult to draw conclusions about adsorption on different substrates. However, the COMPASS force field is ideal for the molecules in these studies because the original parameterization focused on linear and cyclic alkanes in a condensed state.

Molecular dynamics calculations for the linear alkanes on hBN were performed using the Universal force field (Rappe *et al.*). Unfortunately, very few advanced force fields exist which have been parameterized for atomic interactions with boron. Universal force field is a general force field designed to describe interactions among all elements in the periodic table based on a set of rules. Though the parameters used in the force field have not been corrected by experimentation, Perim *et al.* have shown the usefulness of this force field when modeling boron nitride nanotubes. The terms that contribute to the summation in total energy are the same as for COMPASS with the exception that there is no contribution from cross-coupling terms. However, the functional forms used to describe these interactions differ from COMPASS as can be seen in Table 3. Further MD simulations will be performed in the future as class II force fields containing boron become more prevalent with increasing studies on two-dimensional materials.

Table 3 – Functional forms for terms in the Universal Forcefield total energy

| Energy Term | Functional Type | Functional Representation |
|---|---|---|
| Bond Stretching | Harmonic | $\dfrac{K_0}{2}(R - R_0)^2$ |
| Angle Bending | Cosine Harmonic | $\dfrac{K_0}{2}(cos\theta - cos\theta_0)^2$ |
| Torsional Angle | Dihedral | $\dfrac{1}{2}\sum_{j}\{B_j(1 - d_j cos[n_j\phi])\}$ |
| Inversion (out-of-plane) | Umbrella | $\chi_0 \neq 0;\ \dfrac{K_0}{2\,sin^2(\chi_0)}(cos\chi - cos\chi_0)^2$ $\chi_0 \neq 0;\ K_0(1 - cos\chi)$ |
| Electrostatic | Coulombic | $C\dfrac{q_i q_j}{\varepsilon R}$ |
| Non-bonding | 12-6 Lennard-Jones | $4D_0\left[\left(\dfrac{\sigma}{R}\right)^{12} - \left(\dfrac{\sigma}{R}\right)^{6}\right]$ |

### *Lennard-Jones Potential*

The *n*-alkanes interact with the surfaces of MgO, graphite, and hBN primarily through weak intermolecular forces called van der Waals (vdW) forces. These types of interactions are dictated by relative orientations of molecules. However, the isotropic form of this intermolecular force is commonly modeled using the Lennard-Jones (LJ) potential (Jones 1924). This model depends on the distance between two neutral atoms and contains both a repulsive and attractive term. The repulsive force arises from the overlap of electron orbitals at small distances. The attractive term accounts for the attraction due to vdW forces. For the 12-6 LJ potential, the repulsive term is represented by a $r^{-12}$ term (where r is the distance between two objects) and the attractive term is represented by an $r^{-6}$ term. The one-dimensional 12-6 LJ potential is written as,

$$V_{LJ}(r) = 4\varepsilon \left[ \left(\frac{\sigma}{r}\right)^{12} - \left(\frac{\sigma}{r}\right)^{6} \right] \quad (21)$$

and can be viewed for two xenon atoms in Figure Figure 8. The force of the LJ potential can be found from its negative differential with respect to position. The radius at which the force equals zero defines the equilibrium distance separating the two atoms. There are other numerical functions that have been shown to accurately describe vdW forces including the Morse potential, Buckingham potential, and even variations on the LJ potential (i.e. 12-10, 9-6, 10-4-3, etc.). However, the 12-6 variation of the LJ potential is the most common and used to describe non-bonding interactions in the Universal forcefield.

33
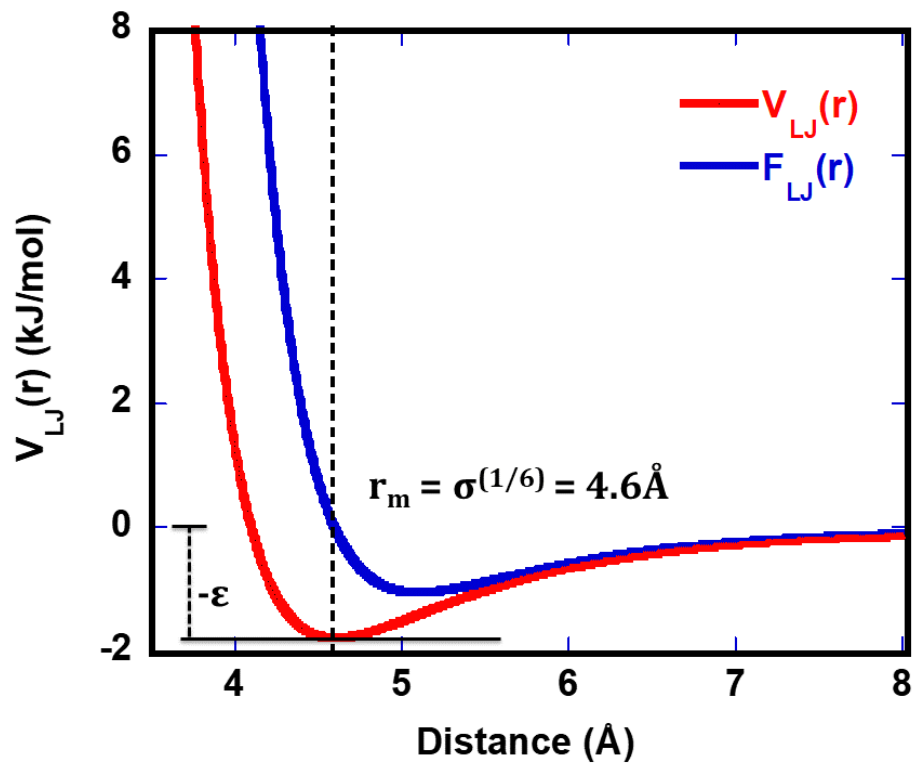
Figure 8 – Illustration of 12-6 Lennard-Jones potential for two xenon atoms

having σ = 4.10 Å and ε = 1.77 kJ/mol

### *Analysis of Trajectories*

*Radial Distribution Function, (RDF)*

Radial distribution functions (RDF) were calculated for the monolayer structures of butane through octane adsorbed on hBN as a function of temperature. The information contained within the RDF is useful for interpreting experimental diffraction measurements. While the RDF decays as $1/r^2$, the most valuable information for the monolayer alkane structure is contained in the small r region. Specifically, this region provides information about the parallel versus perpendicular order for nearest neighbors in the molecular film. The RDF provides the probability of finding an atom at radial distance, r, in a sphere with infinitesimal thickness from a reference atom taken as the origin. The RDF can be further expanded to account for different atom types as,

$$R(\boldsymbol{r}) = \chi_a \chi_b \rho g_{ab}(\boldsymbol{r}) = \frac{1}{N} \langle \sum_{i=1}^{N_a} \sum_{i=1}^{N_b} \delta(\boldsymbol{r} - \boldsymbol{r}_i + \boldsymbol{r}_j) \rangle \quad (22)$$

where $\chi_a$ and $\chi_b$ are the mole fractions of atom *a* and *b* respectively. In this equation, sums are taken over all atoms in the system and the delta functions are the positions of atoms relative to a reference point, **r**. The RDF is a specialized radial form of the atomic pair distribution function (Egami 2003) and can be related to its counterpart by

$$R(\boldsymbol{r}) = 4\pi r^2 \rho_o g(\boldsymbol{r}) \quad (23)$$

It is well understood that the pair distribution function is related to the total scattering function via a Fourier transform. Mathematically, this is expressed as,

$$S(\boldsymbol{Q}) = 1 + \frac{1}{Q}\int_0^\infty G(\boldsymbol{r})\sin(\boldsymbol{Q}\boldsymbol{r})\,d\boldsymbol{r} \quad (24)$$

where G(r) is the reduced pair distribution function. The total scattering function, S($\boldsymbol{Q}$) is accessible from x-ray or neutron diffraction experiments which is weighted by the atomic form factor or scattering lengths respectively.

*Concentration Profile, C(z)*

A concentration profile (i.e. density profile) is a measure of the number of atoms along a vector direction per unit volume. In Materials Studio, the concentration profile is defined as:

$$C(z) = relative[set]_{slab} = [set]_{slab}/[set]_{bulk} \quad (25)$$

where the $[set]_{slab}$ is equal to the number of atoms in a slab normalized by the volume of the slab and the $[set]_{bulk}$ is equal to the total number of atoms in the system divided by the total volume. This reduces a less complicated form,

$$C(z) = \frac{number\ of\ atoms\ in\ slab}{total\ number\ of\ atoms}\cdot number\ of\ slabs \quad (26)$$

The concentration profile is a structural quantity which can provide useful information about the ordering of layers with respect to the distance from the surface. Additionally, since this quantity can be averaged over a time sequence, information about re-orientational dynamics is revealed.

*Mean-Square Displacement (MSD)*

The mean-squared displacement was calculated in order to study the onset of translational dynamics as a function of temperature. Since the alkanes

36

have several conformational degrees of freedom, the centers of mass were used as the reference for the MSD calculations. The MSD was calculated as,

$$\langle(\Delta r)^2\rangle = \frac{1}{N}\sum_{i=1}^{N}|r_i(t) - r_i(0)|^2 \quad (27)$$

Using the Einstein relation, the self-diffusion coefficients were calculated from the derivative of the long-time scale MSD,

$$D = \frac{1}{6}\lim_{t\to\infty}\frac{d}{dt}\sum_{i=1}^{N}\langle|r_i(t) - r_i(0)|^2\rangle \quad (28)$$

Using this approach, care was taken to avoid inclusion of the initial non-linear ballistic regime as well as ending frames (i.e. 500ps) where the statistics are poor. The self-diffusion coefficient also has an Arrhenius-like relationship with temperature. Thus, the natural logarithm of the diffusion coefficients was plotted against 1/T, where the activation barrier was calculated from the slope.

*Velocity Autocorrelation Function (VACF)*

Green-Kubo relations offer a secondary approach for calculating the self-diffusion coefficient. The velocity autocorrelation function is defined as,

$$\psi(t) = \frac{1}{N}\sum_{i=1}^{N}(v_i(t_o) \cdot v_i(t_o + n\Delta t)) \quad (29)$$

The integral of this correlation function at sufficiently long times provides the self-diffusion coefficient expressed as,

$$D = \frac{1}{3}\int_0^\infty \langle v_i(0) \cdot v_i(t)\rangle dt \quad (30)$$

Additionally, since the VACF is a time dependent correlation function for self-motions, the Fourier transform of this function provides a power spectrum, which can be related to the vibrational spectrum obtained from experiment.

*Rotational Autocorrelation Function (RAF)*

The rotational autocorrelation function can provide information about molecular configurational changes and their time dependence. Longer normal alkanes are a class of molecules that exhibit configurational changes about their torsional angles. These dynamical motions can be quantified using the rotational autocorrelation function.

*Dynamic Incoherent Structure Factor (DISF)*

Using the program, MDANSE (Molecular Dynamics Analysis for Neutron Scattering Experiments) (Goret 2016), a variety of space-time correlation functions can be calculated which are related to quantities measurable in thermal neutron scattering experiments. The dynamic incoherent structure factor ($S_{inc}(\mathbf{Q},\omega)$) can be used to generate a neutron vibrational density of states from a molecular dynamics trajectory. This quantity is related to the double differential cross section (i.e. the measured quantity in inelastic neutron scattering) by,

$$\frac{d^2\sigma}{d\Omega dE} = N \cdot \frac{k}{k_o} S(\mathbf{Q},\omega) \quad (31)$$

In MDANSE, the DISF is obtained from the Fourier transform of the incoherent intermediate scattering function which can be directly calculated from a molecular dynamics trajectory. The incoherent intermediate scattering function is defined as,

38

$$F(\boldsymbol{Q},t) = \frac{1}{N}\sum_\alpha b_{\alpha,inc}^2 \langle \exp[-i\boldsymbol{Q}\cdot\widehat{\boldsymbol{R}}_\alpha(0)] \exp[i\boldsymbol{Q}\cdot\widehat{\boldsymbol{R}}_\alpha(t)]\rangle \quad (32)$$

where b is the incoherent part of the total scattering length and **R** is the position operator of nuclei species *α.* The intermediate scattering function is calculated on a rectangular grid of equidistantly spaced points on time and Q axes.

## Crystalline Substrates

### *Magnesium Oxide*

Magnesium oxide (MgO) has a variety of industrial uses such as fuel additives, fire retardants, ceramics/cements, among others. The electronics industry has also taken an interest in a variety of MgO nanostructures which exhibit semiconducting behavior when stimulated by photons. More importantly, metal oxides are often used in heterogenous catalysis as a catalyst support for metals (Xinghua 2010). For example, nickel-decorated aluminum oxide has been used to convert furfural to pentane. Thus, MgO, a prototypical metal oxide, is a potentially interesting substrate for investigating the adsorption of normal alkanes.

MgO has a cubic (rock salt) crystalline structure (see Figure 9) with a lattice constant of 4.212 Å and is typically characterized as an electronic insulator. The crystal is held together by a purely ionic bonding network between $Mg^{2+}$ and $O^{2-}$ ions (Zhang 2012). The (100) plane of MgO is the predominantly exposed facet since cleavage can only be attained along this direction. The (110)
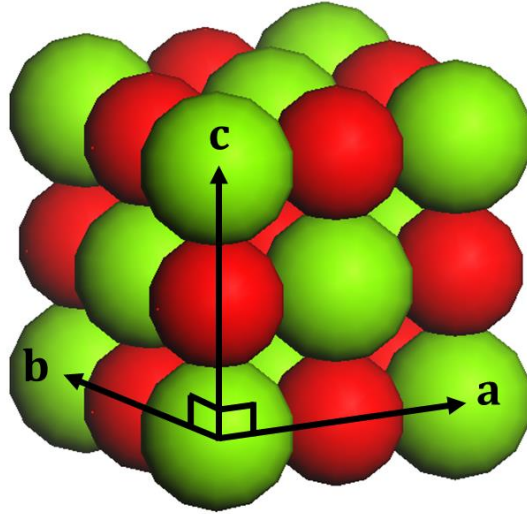
Figure 9 – Illustration of an MgO unit cell. Magnesium atoms are represented by

green spheres and oxygen atoms by red spheres

and (111) surfaces can be exposed using synthetic approaches (cutting and polishing) but are relatively unstable compared to the (100) facet and tend to reorient (Henrich 1976). The MgO(100) surface has 4-fold symmetry which differs from the hexagonal structures of the other substrates used in this study. The corrugation of the MgO surface potential is also greater than both graphite and hBN since the interaction between magnesium and oxygen involves Coulombic forces. The penta-coordinated oxygen atoms at the surface of MgO react strongly with atmospheric moisture producing surface hydroxyls. The presence of surface hydroxyls changes the reactivity (chemical and physical) and smoothness of the (100) surface. Thus, MgO is hygroscopic and must be kept in an inert/dry atmosphere to preserve surface quality. The MgO powders produced for this study are advantageous over other materials because of their superior elemental purity and surface homogeneity. Furthermore, the nanocube particle size distribution is tunable with minimal dispersion. The simple crystalline structure and ionic bonding in MgO make this material prototypical for determining the influence of electrostatic forces in physical adsorption.

### *Graphite*

Early physisorption measurements utilized graphitic substrates since surface homogeneity and purity exceeded that of other materials available at the time. Graphite is a solid made up of layered honeycomb-shaped carbon networks with P6$_3$/*mmc* space group symmetry and lattice parameters of **a** = **b** = 2.46 Å and **c** = 6.8 Å (McKie 1986). Bernal refined the structure for one of the common
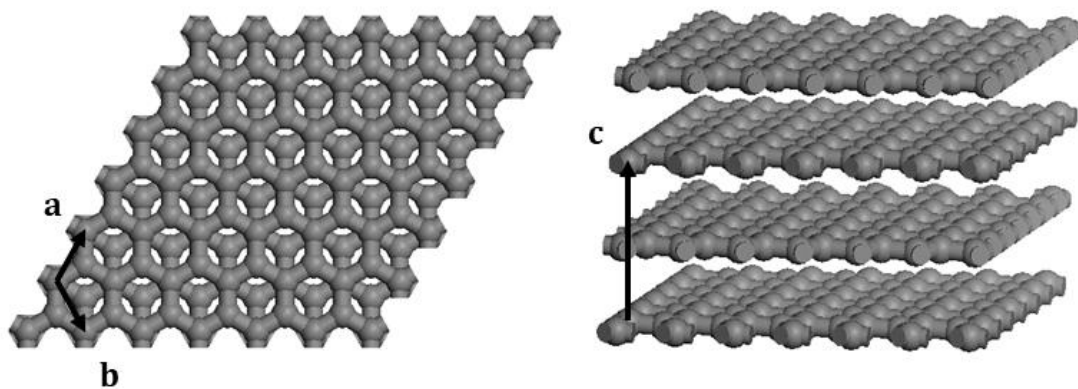
Figure 10 – Crystalline structure of graphite with AB-stacking

stacking sequences for a sample of graphite (AB-stacking), where the (n-1) layer projects a carbon within the hole in the $n$th layer (see Figure 10) (Bernal 1924). Bonding between adjacent carbons in the graphite layer is purely covalent where each carbon contributes three sp$^2$-hybrid orbitals. A lone electron contained within the P$_z$-orbital which is partially delocalized about the surface plane. This gives rise to graphite's unique electronic properties which are similar to a semiconductor with a narrow band gap. The purely covalent bonding between adjacent carbons in graphite results in a shallow corrugation of the surface potential when compared with the other substrates used in this study. Since graphite interacts with alkane molecules primarily through van der Waals intermolecular forces, it is an ideal substrate for studying fundamental physical adsorption.

### Hexagonal Boron Nitride

Hexagonal boron nitride (hBN) is isostructural with graphite having only a two percent (larger) difference in lattice parameters (**a** = **b** = 2.51 Å; **c** = 6.69 Å). In comparison with the covalent bonding network between carbon atoms in graphite, hBN exhibits a partial ionic character due to the difference in electronegativity between boron and nitrogen atoms. Electron density is thus higher in the vicinity of nitrogen resulting in a partial negative charge. This ionic behavior is responsible for hBN's insulating electrical properties with an indirect band gap of 4.027 eV (Liu 2003). There is disagreement in the literature about the true value of this band gap due to variations in the interplanar hBN structure.
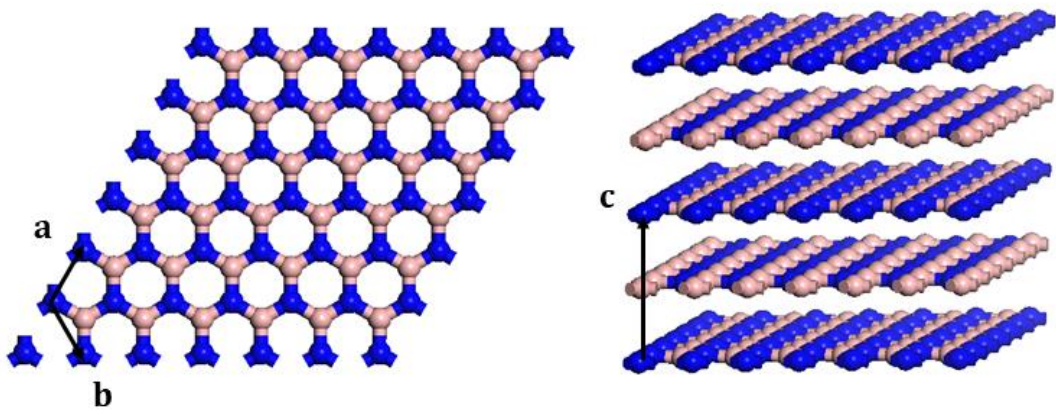
Figure 11 – Crystalline structure for the AA'-stacking sequence of hBN
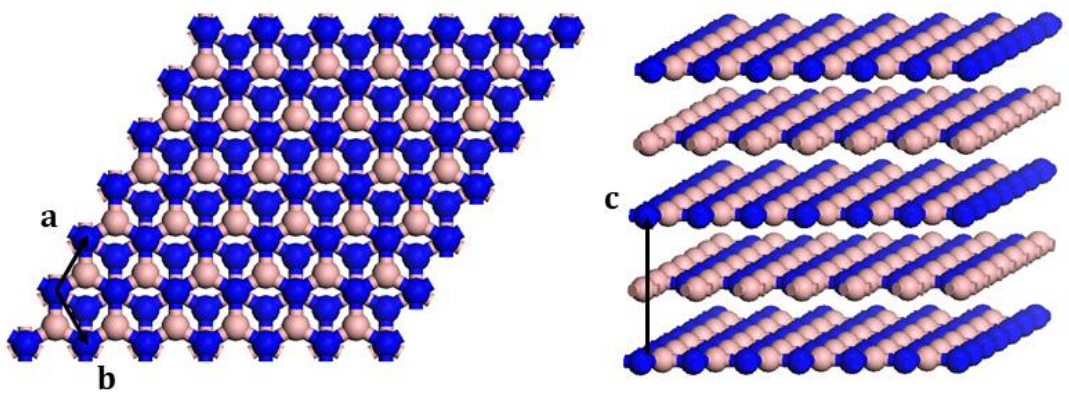


Figure 12 – Crystalline structure for the AB-stacking sequence of hBN

Similar to graphite, hBN has multiple stacking sequences that are energetically stable. The AA' and AB sequences (See Figure 11 and Figure 12) are two of the most stable structures of hBN; however a combination of these stacking sequences is likely to be found in a sample of hBN powder. The hBN crystal with AA' stacking (Brager 1937) exhibits P6$_3$/*mmc* space group symmetry where each plane is aligned perfectly along the c-direction. In the alternating sequence of layers, boron atoms lay directly beneath nitrogen atoms (and vice versa) resulting in an AA' alternation. The structure of hBN with AB stacking (Kurakevych 2007) has P3*m*1 space group symmetry and is more similar in structure to graphite where adjacent layers project a nitrogen atom within the hexagonal vacancy shown in Figure 12. In physical adsorption, this difference in stacking structure should be negligible since the out-of-plane lattice vector is nearly three times as large as the in-plane lattice vector and only weakly bound by van der Waals intermolecular forces.

## Properties of Normal Alkanes

The homologous series of n-alkanes is introduced to chemistry students as a textbook example at an early stage. They are fundamentally some of the most basic organic molecules exhibiting a simple zig-zag structure. In addition, these molecules are known for alternations in physical properties (e.g. melting point, density – see Figure 13) with increasing chain length resulting from odd and even numbers of carbon atoms in the molecular backbone. However, even
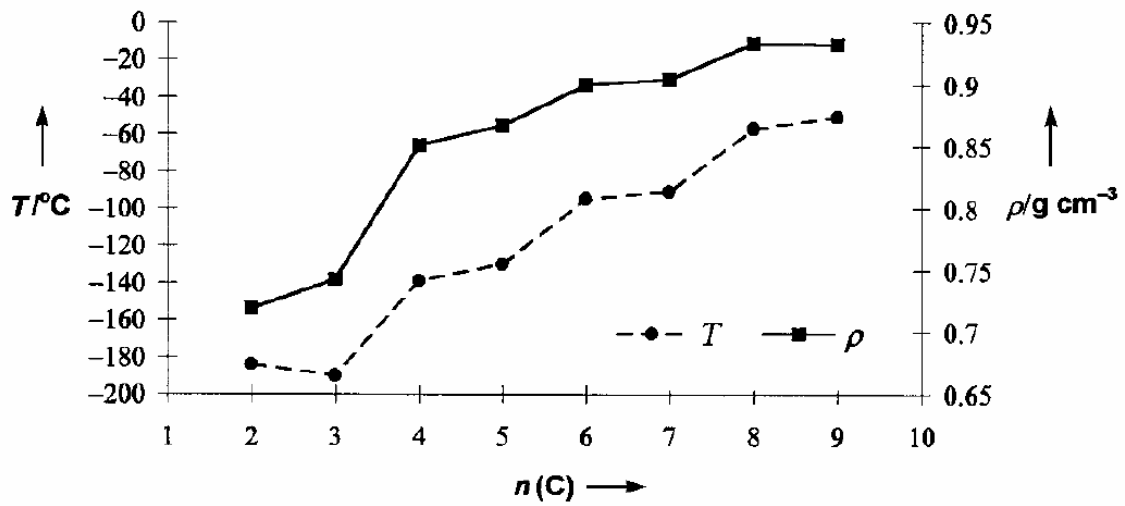
Figure 13 – Alternation in the trend of melting points and densities with increasing carbon number in *n*-alkanes  (Boese 1999)

for small chain alkanes, the boiling points show a monotonic increase with increasing chain length suggesting that the odd-even effect is minute in the liquid and gas phases. The alkanes also represent an interesting class of condensed phase materials where the intermolecular forces are weak. As a result, elusive entropic contributions to the total free energy are more readily observable. The structures, thermodynamics, and dynamics of bulk n-alkanes will be discussed in more detail in the following sections.

### *Structures of n-Alkanes*

The explanation for the odd-even alternation of properties is generally attributed to the packing of alkanes in the solid phase. Boese *et al.* determined the crystal structure for the *n*-alkanes propane through nonane (Boese 1999). Propane and butane exhibit a monoclinic crystal structure with space group $P2_1/n$ while pentane displays an orthorhombic structure with *Pbcn* symmetry. From hexane until nonane, the alkanes form an ordered triclinic crystal system with P-1 symmetry. For all the alkanes, the molecular planes of the alkanes organize in a planar manner. The 2D-projected shape of an alkane with an even number of carbons is approximated as a parallelogram as observed in Figure 14. Odd-numbered alkanes have a trapezoidal shape in their 2D projection. In a single layer of alkane molecules, the alkanes can align with a ribbon phase (Figure 14c) or centered rectangular structure (Figure 14d). For odd-numbered alkanes in the centered rectangular phase, the terminal groups interfere with a natural geometric structure resulting in gaps. This odd-even effect tends to become

47
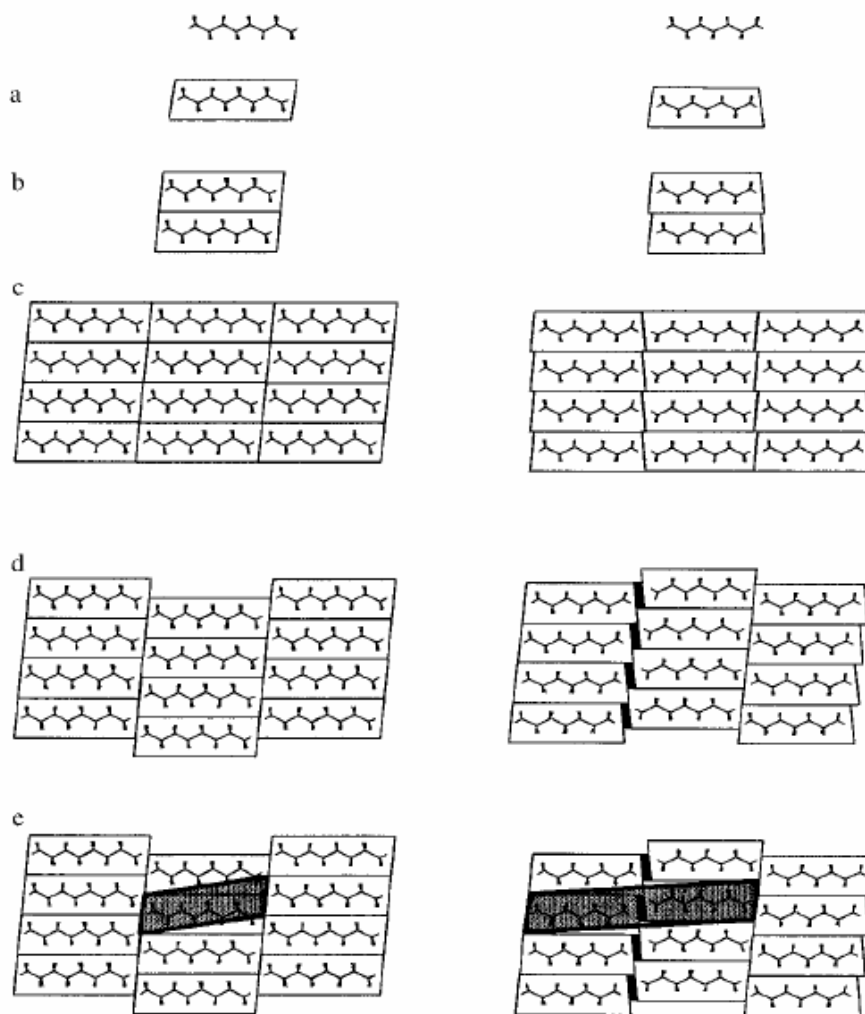
Figure 14 – 2D packing mechanism for *n*-hexane versus *n*-heptane (Boese 1999)

subtler for longer alkanes because the ratio between chain groups and terminal groups becomes more dramatic. For alkanes with nine or more carbon atoms in the backbone, a glassy, rotator phase exists in between the isotropic liquid and ordered solid phases (King Jr. 1993). This phase exhibits long range positional order but lacks rotational order. The alkanes can be structurally tilted with respect to their planar arrangements and have rotational motion about the long axis. This is one of the terms that contributes to the subtle configurational entropy.

### *Thermodynamics of n-Alkanes*

The thermodynamics of *n*-alkanes are known from calorimetric and pressure-temperature measurements and have been abundantly available in the literature for some time now. In 1962, Martin Broadhurst compiled a collection of these studies in an attempt to understand the behavior of solid paraffins as a function of increasing chain length (Broadhurst 1962). These measurements and more recent work have been collected and are available from NIST. The accuracy of previous thermodynamic results is pertinent to the success of our adsorption work since sample temperature is often determined from the saturated vapor pressure of the adsorbate. Further, the bulk enthalpies of vaporization provide a good comparison for the heats of adsorption calculated at saturation pressures. Thermodynamic properties associated with the solid state have been shown to reflect the odd-even alternation (e.g. sublimation enthalpy, solubility, and compressibility). As previously noted, the melting temperatures exhibit the odd-even dependence, but is lost in the boiling temperatures.

49

However, it will be discussed in one of the following sections how the liquid state exhibits odd-even effects in their transport coefficients near the melting point. These results suggest that there may be a subtle hint of the odd-even effect in the bulk thermodynamics.

### *Conformational Properties of n-Alkanes*

Alkanes with four or more carbon atoms in the molecular backbone contain what is known as a dihedral angle (see Figure 15). For the longer alkanes, these conformational motions contribute to a configurational entropy. Volkenstein developed the rotational isomeric state model (Volkenstein 1959) which was designed to compute configurational averages for large chain molecules (i.e. polymers). Flory and Yoon later computed scattering functions (Yoon 1978) for small angle neutron scattering measurements based on the rotational isomeric state model for $C_{16}H_{34}$ and $C_{36}H_{74}$. These measurements were in strong agreement with small angle neutron scattering measurements performed by Dettenmaier for alkanes in the liquid phase and in solution (Dettenmaier 1978), thus further validating the rotational isomeric state model applied to alkanes. The bulk alkanes have proven effective as a model for studying much larger chain molecules such as colloids, lipids, membranes, and polymers.
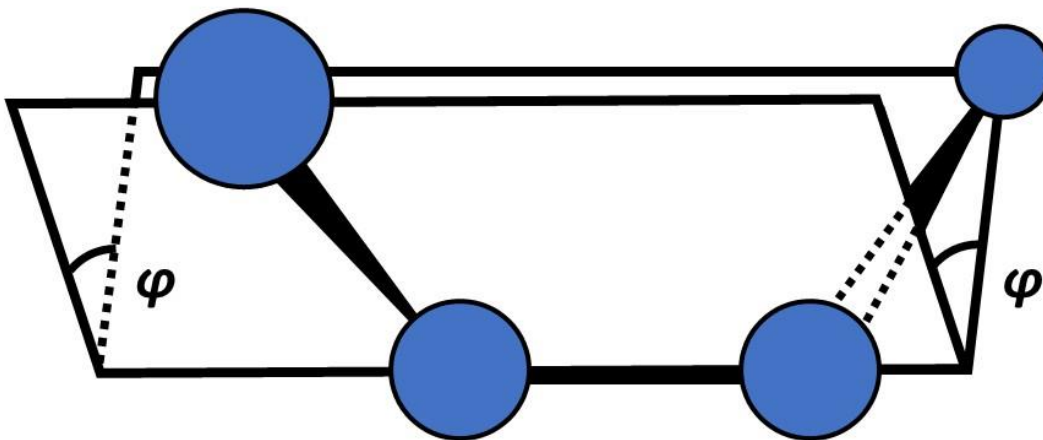
Figure 15 – Illustration of the dihedral angle ($\varphi$) in an *n*-butane molecule. The

hydrogen atoms have been left off to emphasize the dihedral angle in the

molecular backbone

### *Dynamics of n-Alkanes*

Since the odd-even effect is typically associated with packing effects the solid phase, the appearance of such a phenomenon was not thought to exist in the liquid phase. However, Yang *et al.* have performed a series of quasi-elastic neutron scattering (QENS) measurements which suggest the dynamic behavior of *n*-alkanes is dependent on odd-even variations in carbon number (Yang 2016). The QENS spectra were measured at temperatures ~3 K above the respective melting points to ensure the dynamics were not influenced by the alternation in melting temperatures. It was determined that the extracted translational relaxation times and stretching exponents alternate as a function of chain length where at the dynamics recorded differed by as much as a factor of 30 (octane vs. nonane). This provides evidence that the odd-even alternation is not exclusively caused by packing efficiencies in the solid phase but have a dependence on dynamics as well.

The inelastic neutron scattering spectrum was recorded for bulk alkanes by Hudson *et al.* (Braden 1999, Tomkinson 2002). These measurements recorded the presence of longitudinal acoustic modes (i.e. accordion oscillations) and tranverse acoustic modes. The homologous series of alkanes present an excellent model system for comparing experimental vibrational spectra to excitations calculated from density functional theory. These acoustic excitations are likely hindered in the adsorbed phase and present a potentially interesting study about how a surface potential influences the coherent molecular dynamics.

# CHAPTER TWO – MATERIALS AND METHODS

## Preparation of Adsorbate Solvents

### *Dehydration of Liquid Adsorbates*

The solvents used as adsorbates in these adsorption isotherm studies were obtained from commercial suppliers. In all cases, the purity was at least 99% or above as determined by the supplier assays. For the liquid adsorbates (pentane through decane), there was concern about the presence of water due to absorption of moisture from the atmosphere. These solvents were dried using a method outlined by Shriver and Drezdzon (Shriver 1986). The apparatus in Figure 16 was assembled and subsequently evacuated to nearly 200 mTorr. The system was backfilled with ultra-high purity argon gas to an atmosphere (~740 Torr). Fractional distillation was performed over freshly cut sodium metal through a column containing Dri-Rite which was then refluxed onto activated alumina micro sieves. The dry solvent was sealed in the glass vessel and moved into a glove bag filled with UHP argon. The solvent was transferred into a 50 mL stainless steel volume and sealed with a membrane valve. The stainless-steel volume was then added to a gas handling system for further purification.
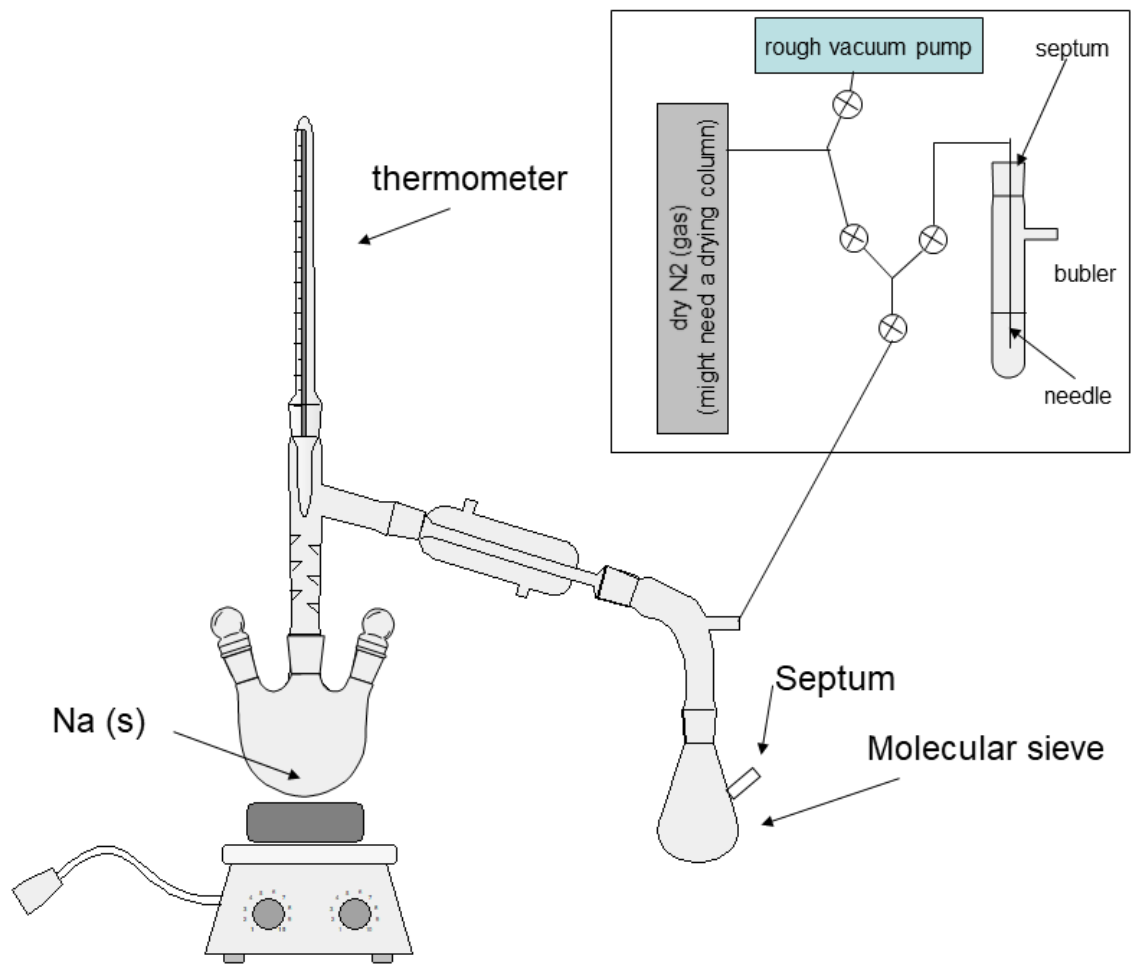
Figure 16 – Diagram for fractional distillation and reflux (Cook 2006)

### *Freeze-Pump-Thaw Distillation*

This procedure was designed to remove soluble gases present in the atmosphere (e.g. $N_2$, $O_2$, Ar, etc.) that dissolve into the adsorbates. For the alkanes, methane through butane, this was the first step in purification process since there was no possibility of absorbing moisture from the environment. In freeze-pump-thaw distillation, the gaseous or liquid adsorbates were cooled to liquid nitrogen temperatures and subsequently evacuated. The sample was allowed to cool until just prior to melting in order to pump away any gases that boil. The gases boiling off were monitored using an ionization gauge where increases in the pressure prior to melting were attributed to impurity gases. This procedure relies on the differences in melting temperature and vapor pressure between the soluble atmospheric gases and the adsorbate sample. The freeze-pump-thaw distillation process was performed multiple times until the only increase in pressure measured from the ionization gauge was the melting of the adsorbate.

## Preparation of Powder Substrates

### *Synthesis and Preparation of MgO for Adsorption Isotherm Studies*

Magnesium oxide was first synthesized using a metal vapor-synthesis route and later prepared for adsorption isotherm studies. The recipe used for synthesizing MgO was based on the method of Kunnmann and Larese first developed at Brookhaven National Laboratory (Kunnmann-Larese 2001). This

approach is advantageous over other methods for synthesizing metal oxides because the resulting MgO powders are highly pure, with tune-able size distribution, and almost exclusive exposure of the (100) surface. This method also produces large quantities (nearly 20 grams) of material upon completion. Figure 17 illustrates the general design for the vapor-phase synthesis of metal oxides.

The setup for the synthesis of MgO was relatively simple in design. The components were all enclosed within a three foot long quartz tube chimney. At the base of the chimney was a graphite crucible supported by glass cylinders through which argon gas flowed upward through the reaction chamber. The graphite crucible was surrounded by an open ceramic crucible. The ceramic crucible was surrounded by a thin glass cylinder. The coils for heating the carbon encircled the outer glass cylinder. A ring suspended above the graphite crucible was designed to introduce oxygen to the reaction.

Magnesium cubes (approximately 0.5 x 0.5 x 0.5 cm$^3$) were washed with dilute hydrochloric acid in order to clean the surface of any oxide formation. These cubes were then entrained within crushed graphite contained inside of a graphite crucible. A Lepel radio frequency generator was used as an induction furnace designed to resonate with the carbon material. A low flow of argon was introduced to the reaction chamber initially to flush the system of oxygen. As the induction furnace resonates with the carbon, heat is transferred to the magnesium where it eventually reaches its boiling point. The magnesium vapors

57
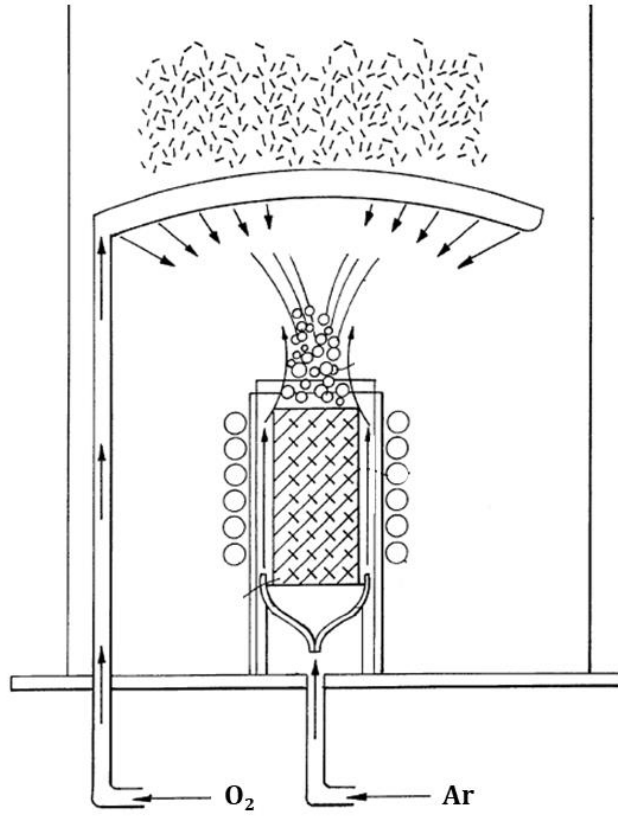
Figure 17 – Diagram for the metal oxide synthesis chamber (Kunnmann-Larese 2001)

react with the carbon to form reactive magnesium carbide. At this point, oxygen is introduced to the reaction chamber where the carbide reacts to form magnesium oxide. The MgO powder was collected from the interior wall of the quartz chimney while still warm and swiftly moved into an argon atmosphere to prevent the formation of surface hydroxyl groups.

Prior to adsorption studies, the MgO powder was sealed in a quartz tube and evacuated. These powders were kept under vacuum or in an inert atmosphere at all times since the material is hygroscopic and reactive with moisture. The powder material was heated in a Lindberg Blue tube furnace for nearly 48 hours at 950 °C. The base pressure reached $10^{-7}$ Torr in about 12 hours. Upon completion, the clean MgO powders were transferred to an argon glovebox where they were loaded into the copper sample cell.

### *Preparation of Graphite for Adsorption Isotherm Studies*

A form of flexible graphite (GTB grade) was obtained from Union Carbide Corp. This particular type of graphite is an exfoliated form of GRAPHOIL which is used industrially for fluid sealing applications. An amount of GTB grade graphite was transferred into a quartz tube, sealed, and subsequently evacuated. The powder was heated at 700 °C overnight where a base pressure of $10^{-7}$ Torr was achieved. Low energy electron diffraction (LEED) measurements have been performed in the past to illustrate that molecules that are physically bound to the surface of graphite are removed near 200 °C (Gay 1986). The heat-treated powder was transferred into an argon glovebox for loading in a sample cell.

59

### *Preparation of Boron Nitride for Adsorption Isotherm Studies*

Hexagonal boron nitride (hBN) was obtained from Momentive Performance Materials. The grade used was identified as AC6004. This type of hBN exhibits a lower surface area (2 $m^2$/g), and a larger mean particle size (12-13 μm). Preliminary studies performed by Migone *et al.* (Wolfson 1996) suggest that hBN materials with small surface areas have fewer high energy binding sites (and hence less surface heterogeneity) and smaller pore volume with sharper adsorption features than those with a larger surface area. hBN powders which have been left in open air for years have shown to exhibit less than 5% borate contamination. While these materials are only weakly reactive in open air, it was important to ensure the substrates were as homogenous as possible. Thus, the surfaces of these powders were cleaned before use in adsorption experiments. The procedure for cleaning these materials was influenced by the work of Migone *et al.* (Shrestha 1994). Soluble borates (boric oxide and boric acid) are the two most common impurities. Boric oxide ($B_2O_3$) reacts with atmospheric moisture to produce boric acid ($H_3BO_3$). The powder was initially washed in methanol and stirred for nearly three hours in order to convert the boric acid into trimethyl borate. The methanol was filtered from the hBN powder using a fine grade filter and the precipitate collected. The hBN powder dried in an oven for approximately four hours at 150 °C. The material was then transferred into a large quartz tube, sealed, evacuated, and heated to 900 °C in a Lindberg Blue tube furnace for 24 hours where a base pressure of $10^{-7}$ Torr was achieved. The purified hBN was

60

transferred to an argon glovebox where it was loaded into the OFHC copper sample cell.

## High-Resolution Volumetric Adsorption Isotherm Apparatus

### *Description of Adsorption Apparatus*

Unlike many other volumetric adsorption experiments which utilize commercial equipment, these experiments were performed on a custom-built adsorption system which was designed based on the model of Mursic and Larese (Mursic 1996) at Brookhaven National Laboratory. The general construct for this adsorption apparatus is shown in Figure 18. This multi-component system consists of five main parts: (1) a gas handling manifold with calibrated volumes separated by Swagelok B-4HK bellows sealed valves, (2) closed cycle helium cryostat refrigerator, (3) capacitance manometers, (4) high-vacuum turbo pump, and (5) a National Instruments LabView program designed to automate the operation of pneumatic actuators.

A few of the bellows valves on the gas handling manifold (V1, V2, V3, V4 in Figure 18) are automated by replacing the caps with pneumatic actuators. The opening and closing of these valves is then controlled by the LabView program. This allows for the automation of a series of doses in an adsorption experiment.

The closed-cycle helium cryostat (Air Products or Cold Edge) when used with a temperature controller (Neocera LTC-21 or CryoCon 32B) is designed to control the temperature of the sample cell, which is mounted on the second stage
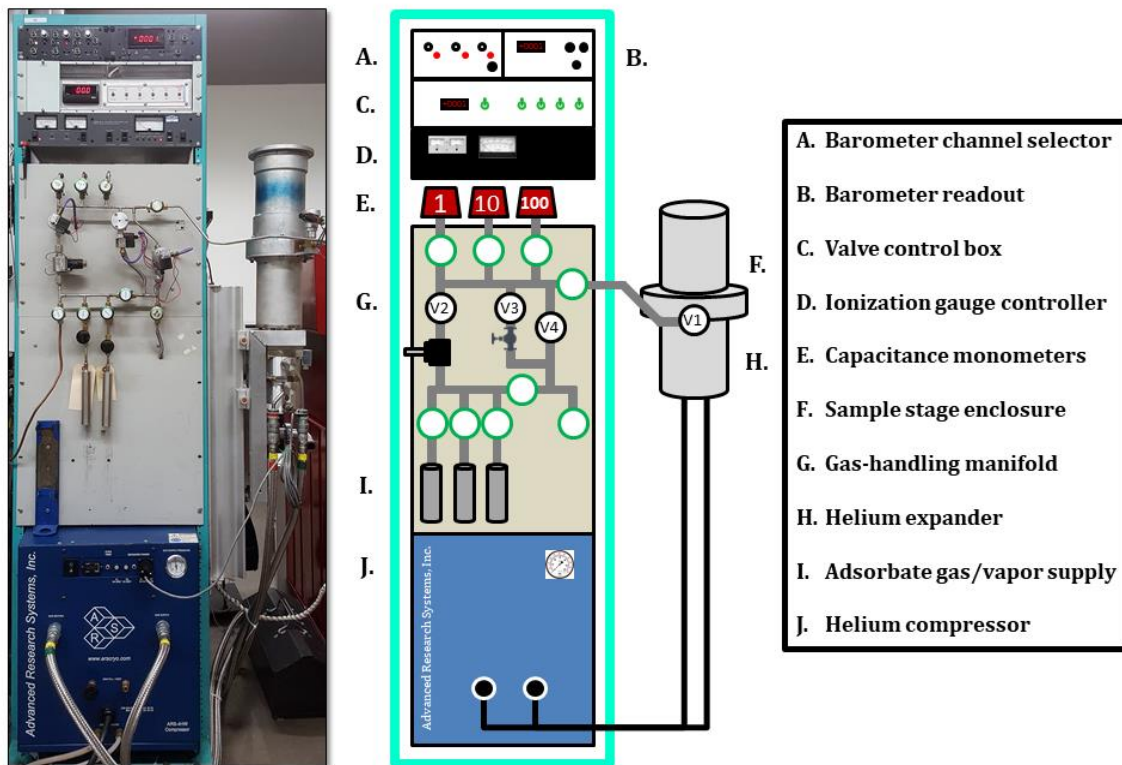
Figure 18 – Schematic for the design of a custom-built volumetric adsorption isotherm apparatus. The components shown in the diagram are listed to the right.

of the cold-finger (H in Figure 18). These cryostats have a temperature range of approximately 10 – 298 K with regulation of temperature fluctuations less than 2.5 mK.

The pressure transducers used were MKS Baratron capacitance manometers. These Baratrons have a full-scale pressure (in Torr) specified by the model. Figure 18 illustrates 1, 10, and 100 Torr manometers used in these experiments. The resolution of these manometers is $10^{-6}$ times the full-scale value, though this value is limited on the 1 Torr Baratron where fluctuations in pressure due to temperature tend to exceed the resolution.

An Agilent TPS Compact high vacuum pump (not shown in Figure 18) was used to evacuate the gas handling manifold and the sample cell prior to the adsorption isotherm experiments. The base pressure achieved within the adsorption apparatus was nearly $10^{-7}$ Torr before an experiment was started. The pressure of the manifold was monitored using a Bayard-Alpert ionization gauge.

The LabView software converted analog data from the Baratron manometers and temperature controller through an analog to digital converter. The in-house designed program contained multiple sub-programs. These programs included the ability to manually control pneumatic actuators, a pressure-temperature plot for leak checking, an interface for remotely operating the temperature controller, and a program designed to automate adsorption and subsequent desorption experiments.

In the typical adsorption experiment, valve two (V2) is briefly opened (with flow moderated by a proportional valve) and closed to allow an excess of adsorbate gas into the calibrated volume, contained in the volume within V1, V2, V3, and V4. Valve three (V3) is opened and the pressure of the gas in the calibrated volume is slowly reduced to a pre-specified dosing pressure. When the specified pressure is reached, V3 closes and V1 opens, expanding a known number of moles of gas into the sample cell at a given temperature. The decay in pressure resulting from the interaction of the adsorbate with the sample is recorded as a function of time. When the change in pressure is reduced to a defined threshold, V1 is closed and the process is repeated until the saturated vapor pressure of the adsorbate is reached at the sample temperature. The data is recorded as the sum over the changes in pressure from consecutive doses versus the equilibrium vapor pressure.

The sample temperature of each measurement was determined using semi-empirically determined coefficients for Antoine's equation. The coefficients used for the temperature range of the current set of measurements were obtained from NIST and the Landolt-Börnstein databases as shown in Table 4.

### *Calibration of the Gas-Handling Manifold Volume*

A calibration of the volume contained within the gas handling manifold is essential for performing accurate adsorption isotherm measurements. The volume of a glass bulb containing a ¼ inch Kovar opening was calibrated using the mass of ultra-pure distilled water. In this procedure, the glass bulb was

64

Table 4 – Coefficients used for the conversion of saturated vapor pressure to temperature using Antoine's equation

| Alkane [Ref.] | Temperature Range (K) | A | B (K) | C (K) |
|---|---|---|---|---|
| Methane [a] | 58 – 89 | 6.31972 | 451.64 | -4.66 |
| | 92 - 118 | 5.7687 | 395.744 | -6.469 |
| Ethane [a] | 90 – 133 | 6.0567 | 687.3 | -14.46 |
| | 133 - 198 | 5.95405 | 663.72 | -16.469 |
| n-Propane [a,b] | 85.5 – 167 | 6.6956 | 1030.7 | -7.79 |
| | 166.02 – 231.41 | 4.01158 | 834.26 | -22.763 |
| n-Butane [a] | 138 – 196 | 6.0127 | 961.7 | -32.14 |
| | 196 - 298 | 5.93266 | 935.773 | -34.361 |
| n-Pentane [a] | 143 – 219 | 6.6895 | 1339.4 | -19.03 |
| | 219 - 328 | 5.97786 | 1064.84 | -41.138 |
| n-Hexane [a] | 182 - 247 | 6.895378 | 1549.94 | -19.15 |
| n-Heptane [a] | 185 – 274 | 6.75691 | 1599.5 | -29.95 |
| | 274 - 385 | 6.02023 | 1263.91 | -56.718 |
| n-Octane [a] | 217 - 294 | 6.56398 | 1606.62 | -42.89 |
| n-Nonane [a] | 219.7 - 315 | 9.2671 | 3131.8 | 29.7 |
| n-Decane [b] | 243.49 – 310.59 | 0.21021 | 440.616 | -156.896 |

[a](Landolt-Börnstein)
[b](NIST)

cleaned with soap and water, followed by successive rinses with methanol and then acetone. The bulb was dried in an oven at 200 °C for two hours. The bulb was then filled with ultra-pure distilled water and ultra-sonicated (degassed) for one hour. The glass volume was filled with water past the neck where roughly a hemisphere of water protruded from the opening. This amount was accounted for by adding the volume of a hemisphere using the outer diameter of the Kovar tubing to determine the radius. The temperature of the sonication bath was assumed to be in thermal equilibrium with the water contained within the glass bulb and measured with a mercury thermometer. Upon completion of the degassing step, the exterior of the bulb was quickly dried using Kim-Wipes and the mass obtained using a top-loading balance. The density used to convert mass of water to volume was corrected based on the temperature of the water as determined by the sonication bath. Multiple trials of this procedure were performed, and the relative error was determined to be less than 0.6 percent. Using the calibrated glass bulb, gas expansions were performed on the isotherm station in order to determine the volume of the gas-handling manifold.

### *Sample Cell for Helium Cryostat*

Figure 19 shows one of the sample cells used in the closed-cycle helium cryostats designed in-house (Larese 2018). An aluminum ring was mounted in between the expander component of the cryostat and the vacuum jacket. Valve one (V1) was mounted on the outside of the aluminum ring and connected to the sample cell through a 1/16" o.d. capillary tube. The transfer line is designed to be
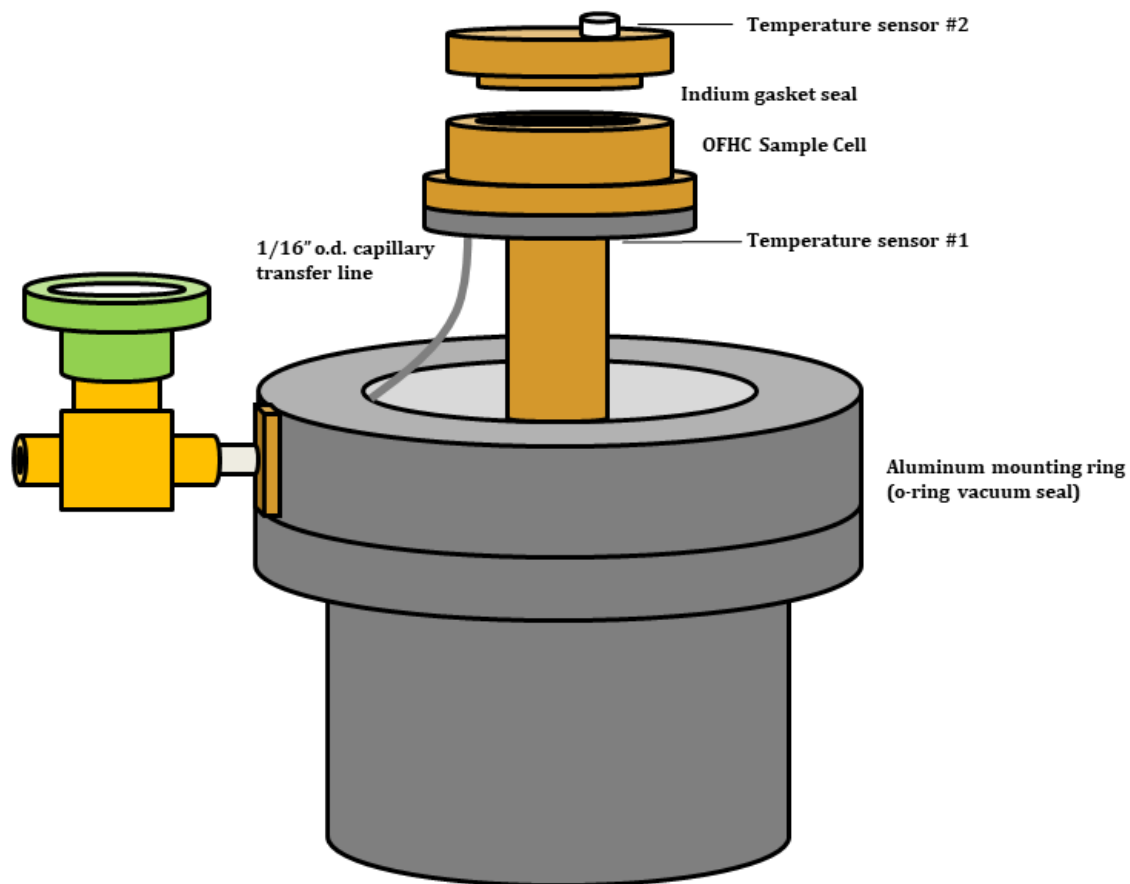
Figure 19 – Illustration of a sample cell mounted on the second stage of a closed-cycle helium cryostat

small so that the The sample cell and lid were made of OFHC and sealed with an indium gasket. The sample cell is mounted on the second stage of the helium cryostat. Two temperature sensors were used to monitor and control temperature. The first sensor was a calibrated Lakeshore Si-410DT silicon diode thermometer mounted at the tip of the cold finger. The second sensor, typically a platinum resistance or Cernox thermometer which was used to control the sample temperature, was mounted on the lid of the sample cell.

### Sample Cell for Water Bath

For measurements above 250 K, a custom sample cell was designed and constructed for use in a constant temperature water bath (Larese 2018). The design of this sample cell was necessary because many of the liquid alkanes tend to capillary condense in the helium cryostat sample cell transfer line described above. Additionally, the operation of these cryostats above 250 K is an inefficient process since resistance heaters are constantly operating near maximum power to control ~240 K above the base temperature of the cold-finger. A Thermo Neslab RTE 10 water bath was used to control the temperature for measurements exceeding 250 K. The design of the sample cell used in this setup is shown in Figure 20. A stainless-steel vacuum jacket enclosed the transfer line (either 1/8" or 1/16"outer diameter stainless-steel tube) in order to minimize heat transfer with the water bath. An OFHC sample cell was mounted at the bottom of the vacuum jacket and placed in the center of the water bath volume in order to minimize temperature fluctuations from the atmosphere. A pre-calibrated

68
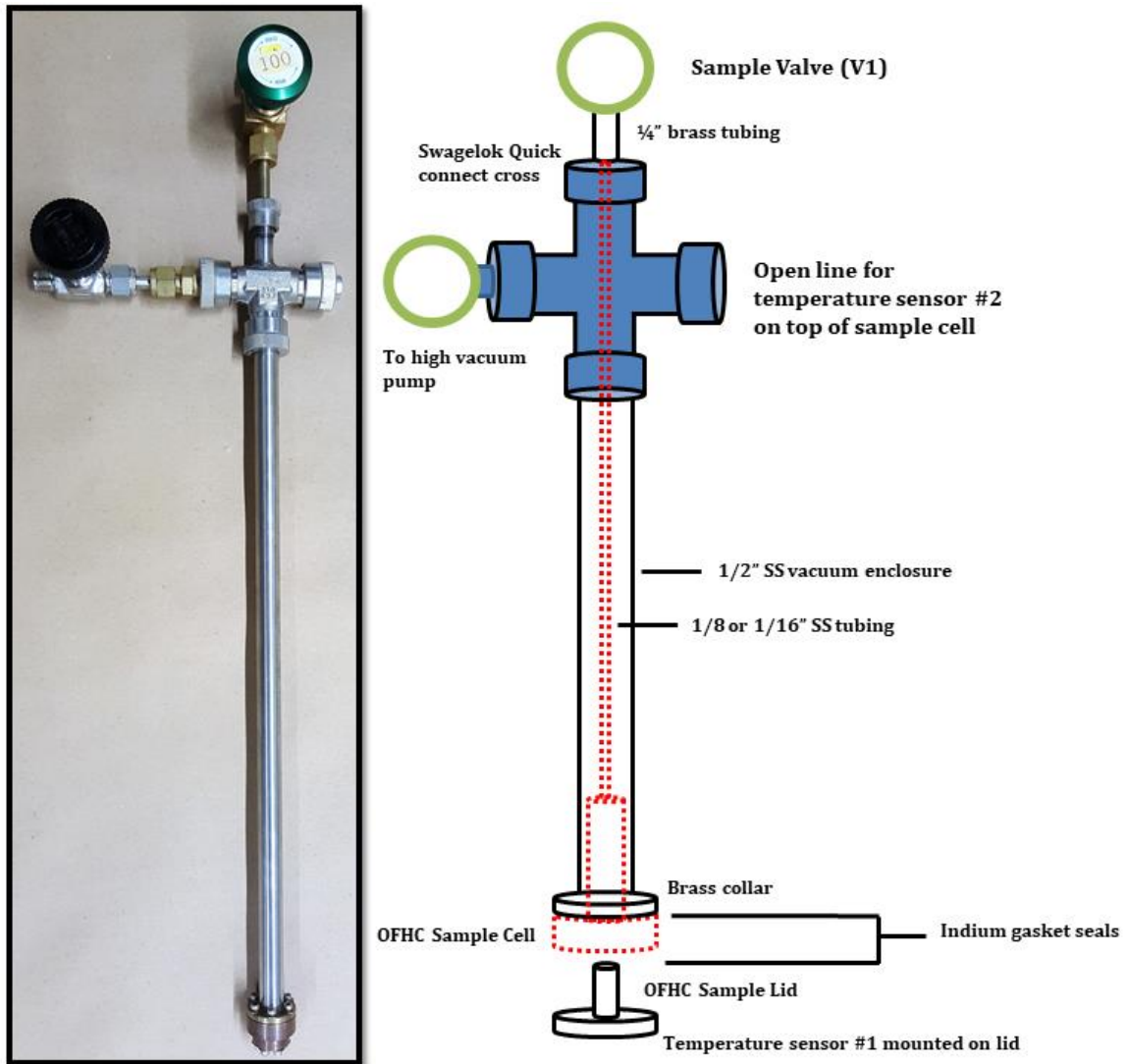
Figure 20 – Sample cell designed for volumetric adsorption isotherm measurements within a constant-temperature water bath.  The figure on the left is the sample cell used in the heptane measurements with a description of the components on the right.

platinum resistance thermometer was placed next to the sample cell in the bath to observe the fluctuations in 50/50 ethylene glycol/water mixture. The temperature of the bath at 250 K was maintained within 7.4mK. The temperature of the sample was ultimately calculated using empirically determined parameters for Antoine's equation to convert the saturated vapor pressure at a given set point to temperature. Variations in pressure over a two-hour period for a condensed sample of heptane were used to measure the fluctuations in sample temperature. At 250 K, the temperature fluctuations inside the sample cell were held within 6.2mK.

## Molecular Dynamics Calculations

### *Construction of the Substrates*

The coordinates for a unit cell of MgO, graphite, and hBN were obtained from literature values of refined x-ray diffraction data (Wyckoff 1963, McKie 1986, Kurakevych 2007). Supercells were constructed by replicating the unit cells in the **a**, **b**, and **c** directions. The crystal was cleaved in the z-axis (**c** vector direction) such that the substrate thickness was the equivalent of two unit cells. The surfaces of each of the three substrates were constructed having approximately the same surface area. An 80 Å vacuum slab was constructed along the **c** direction on both faces of the substrate. Periodic boundary conditions were implemented such that a molecule leaving the sample space in a particular direction would re-enter the space at the symmetrically opposite boundary. This

70

feature was important in eliminating behavior resulting from the interaction of molecules at the edges of the crystals. In the experimental systems, adsorption features resulting from edge effects are minute and, in most cases behavior is not measurable. The coordinates of the crystal substrates were also frozen in space since the predominant dynamics result from the adsorbate molecules and physisorbed molecules tend not to perturb the substrate.

### Dynamics Calculations

Molecular dynamics calculations were performed with the Accelrys' Materials Studio suite using the Forcite package (Accelrys Forcite). The dynamics were performed using the Canonical ensemble (constant NVT) with the Nose Hoover Langevin thermostat with a decay time of 2.5 ps. Periodic boundary conditions were implemented to conserve the number of molecules in the calculation. The calculations were performed for a total of 50 – 200 ps with 1 fs time steps (500-2000 steps) where fluctuations were minimized in energy and temperature after approximately 5 ps. The output of trajectory frames was modified between every 5 – 100 steps depending on the relaxation time of the dynamics of interest. Non-bonding energies were truncated at a cutoff distance of 15.5 Å. The inter- and intramolecular contributions to the total energy were calculated using the COMPASS and Universal force fields.

### *Trajectory Analysis*

The molecular trajectories resulting from dynamics runs between 50 -250 ps were used to calculate structural and dynamical quantities useful for interpreting molecular behavior in condensed phases. These quantities are also valuable for interpreting and guiding future experimental measurements. Table 5 below highlights the functions relevant to adsorption of alkanes on surfaces. Details regarding how these quantities were obtained are presented in the molecular dynamics background.

Table 5 – Useful quantities calculated from MD trajectories

| Quantity/Function | Program used to Calculate |
|---|---|
| *Structural* | |
| Radial Distribution Function (RDF) | Materials Studio Forcite |
| Concentration Profile (C(z)) | Materials Studio Forcite |
| 2-Dimensional Lineshape Program | 2DIM (in-house built) |
| *Dynamical* | |
| Mean Square Displacement (MSD) | Materials Studio Forcite |
| Velocity Autocorrelation Function (VACF) | Materials Studio Forcite |
| Dynamic Incoherent Scattering Function (DISF) | MDANSE |
| Rotational Autocorrelation Function (RACF) | Materials Studio Forcite |
| Angular Correlation Function (ACF) | MDANSE |

# CHAPTER THREE – THERMODYNAMIC AND MODELING STUDY OF N-OCTANE, N-NONANE, AND N-DECANE FILMS ON MGO(100)

My contributions to this paper include: 1) volumetric adsorption measurements and analysis for both nonane and decane on MgO and 2) performed and analyzed molecular dynamics simulations for all three molecules on MgO.

## Abstract

The thermodynamic properties of n-octane, n-nonane and n-decane adsorbed on the MgO(100) surface were investigated using high-resolution, volumetric adsorption isotherms in the temperature ranges of 225-295 K, 245-280 K and 250-310 K respectively. Two distinct molecular layers were observed in all isotherms. The heat, differential enthalpy, differential entropy, and isosteric heat of adsorption were determined. The temperature dependence of the two-dimensional compressibility was used to identify that two phase transitions occur for the first and second layers, respectively. The average area per molecule $137\pm5$ Å$^2$,$128\pm5$ Å$^2$ and $202\pm5$ Å$^2$ for octane, nonane and decane respectively, suggesting that the carbon backbone is preferentially oriented parallel to the MgO(100) surface. A substantial set of molecular dynamics (MD) temperature and coverage runs for all three molecules using the COMPASS force field were

used to calculate both the minimum energy configurations for individual molecules and near completed layers on the MgO(100) surface. These calculations support the thermodynamic evidence of the carbon backbone oriented parallel to the surface and additionally suggest a preferential alignment of the molecule along the <11> and <10> directions in the surface (100) plane. The MD simulations were used to evaluate the distribution of the molecules perpendicular to the MgO(100) surface as a function of temperature and nominal surface coverage. Evidence is also recorded that suggests that the interface broadens, the orientational order decreases and liquid-like layers appear as the temperature is increased. As observed earlier with the behavior of heptane on MgO(100) an entropic contribution to the free energy is apparent as a result of the odd number of carbon atoms in the nonane backbone. The near surface layer of all three molecules appears to remain orientational ordered (i.e. noticeably more planar) and stabilized (i.e. more solid like) at substantially higher temperatures when the second and third layers are observed to be liquid-like. This observation is consistent with earlier experimental observation of rare gases and alkanes on graphite that indicate that the near surface layer melts at temperatures above the bulk melting temperature.

## Introduction

Nanomaterials, especially those composed of metal oxides are currently of significant interest in materials science and engineering due to their widespread use in heterogeneous catalysis, optoelectronics, separation and purification, and

energy conversion/storage. Furthermore, understanding and controlling the behavior of molecules adsorbed on the surfaces of these nanoparticles has important applications in such areas as lubrication, adhesion, and corrosion. Developments in the automation of scientific instrumentation has improved our ability to characterize the thermodynamic and microscopic properties of these adsorbed systems over a wide range of temperatures and pressures (Mursic 1996). Further, the ability to synthesize MgO nanocubes with high purity, narrow particle size distribution, and almost exclusive exposure of the (100) surface makes this material suitable for high-accuracy experimental surface studies (Kunnmann-Larese 2001). Additionally, since an important assumption in modeling fundamental interfacial interactions is surface homogeneity, the experimental materials scale well to our computational models. These advanced experimental studies lead to refinement of models for describing molecule-surface interactions and more accurate theoretical descriptions of the potential energy surfaces which dictate the physico-chemical properties. We describe below the findings of our thermodynamic and companion modeling studies of the interaction of normal octane, nonane, and decane with the (100) surface of MgO. Magnesium oxide (MgO) serves as a prototypical system to study the adsorption properties of this class of materials because of its simple ionic rock-salt structure. These experiments are a subset of our ongoing investigation of the first ten members of the normal alkanes and serve as the foundation for future neutron and x-ray investigations of the microscopic structure and dynamics of alkane

77

adsorption on MgO(100) surfaces. The work described here is part of a much larger effort to investigate the phase transitions, adsorption, and wetting properties of normal alkanes with MgO (100) surfaces as a function of chain length (Freitag 2000, Arnold 2005, Felty 2008, Arnold 2006, Cook 2015, Yaron 2006, Fernandez-Canoto 2014).

From the technological perspective, the n-alkanes discussed below are important components in automobile (octane) ((B.P. 2010, Biello 2007, ASTM D4814) and aviation fuels (kerosene, i.e. nonane and decane) (ASTM D910). From an economic standpoint, the octane rating dictates whether or not a fuel can be used with high compression (high-performance) piston engines. Hence, there is a need for methods that improve the separation efficiency and selectivity of these molecules as well as understanding the interactions of nonane and decane with metal oxide surfaces for improvements in hydro-conversion (isomerization) catalysts (Kinger 2001, Welters 1995) on a large scale. From the fundamental point of view, adsorbed monolayer films of these molecules exhibit two-dimensional odd-even behavior similar to the homologous series of alkanes in three-dimensions. This phenomenon has been investigated using molecular dynamics simulations to illustrate the structure and dynamics of the adsorbed systems as a function of carbon number, temperature, and coverage.

## Experimental

The thermodynamic properties of these surface interactions were examined experimentally using a series of high-resolution volumetric adsorption isotherms. From these measurements, we determined the heats of adsorption, differential enthalpies, and differential entropies for all three molecules adsorbed on MgO(100). Potential phase transitions were identified using peak widths of the numerical derivatives obtained from the raw data as a function of temperature. The experimental results in addition to the structure and dynamics were modeled with classical molecular dynamics. Using the Forcite module contained within the Materials Studio software available from Accelrys Software, Inc., (Accelrys Forcite) the minimum energy configurations were computed for isolated molecules as well as stable structures in a two-dimensional solid monolayer phase. Additionally, we have modeled the mobilities of multilayer systems to provide information about phase transitions and the layer growth of the larger alkanes. Molecular distributions calculated from the simulation trajectories illustrated properties such as the dynamics of the molecules in the nearest layer and intra- and interlayer mobility in the adsorbed multilayers.

### *Volumetric Adsorption Isotherms*

The method for synthesizing, handling, and characterizing the MgO samples is described elsewhere (Kunnmann-Larese 2001, Freitag 2000). Nanocubes of uniform size distribution (200 nm edge length) with almost

exclusive exposure of the (100) face were produced using a patented synthetic route for metal oxides then heat-treated (950 °C) under high-vacuum (< $10^7$ Torr). For the octane measurements MgO powders were loaded into an indium sealed OFHC copper cell under argon to prevent hydroxylation of the surface from atmospheric moisture. The cell was then mounted on the second stage of a closed-cycle helium cryostat (APD Cryogenics). The temperature was regulated using a silicon diode sensor and secondary platinum resistance thermometer with a CryoCon 32B temperature controller for regulation of 2.5 mK. The nonane and decane measurements on MgO were performed with thin walled quartz tubes used as the sample cell. The quartz cells were subsequently placed in a Thermo RTE-10 recirculating water bath with temperature control of 10 mK read from a Pt thermometer. This procedure was employed for nonane and decane to eliminate the possibility of capillary condensation of the adsorbate that had been observed in the closed-cycle cryostat system. The automated adsorption apparatus (Mursic 1996) consists of a low pressure gas-handling system equipped with a turbo-molecular pump and capacitance manometers (MKS baratron). The distinct advantage of these measurements over others is the ability to maintain high-resolution at low temperatures and pressures. Furthermore, it should be emphasized that the measurements were performed under thermodynamic equilibrium conditions hence the chemical potential of the adsorbed/2D phase is equal to that of the 3D vapor phase. The MgO samples were monitored for degradation and regularly replaced with equal amounts of

80

material from the same synthesis batch; after approximately 2-3 isotherms the samples showed minor degradation and were replaced. MgO substrate integrity was established using methane isotherms at 77 K. As in the past, we use the number and uniformity of the steps in the methane isotherm to determine the surface quality and homogeneity of the nanocubes. The alkanes were obtained from Acros Organics (purity >99%). Before use, they were dehydrated with sodium metal distillation, filtered through Dri-Rite (primarily silica used as a desiccant), and condensed over micro sieves. The alkanes were then further purified using a series of freeze-pump-thaw distillation cycles to remove any trace of soluble gaseous impurities. Approximately 25 isotherms were performed for each alkane spanning a temperature range of approximately 230-290 K for octane, 245-280 K for nonane, and 250-310 K for decane. The sample temperature of an individual isotherm was determined using published semi-empirical Antoine parameters for the saturated vapor pressures (SVP) from NIST (NIST). The temperature range of the measurements for each system was dictated by two factors; the ambient room conditions and the pressure resolution of the capacitance manometers which ultimately was the determining factor for the extent of the low pressure (low temperature) region.

### *Molecular Dynamics*

Modeling studies were performed using classical molecular dynamics (MD) with the Forcite Dynamics module contained in Material Studio. In this type

of simulation, a predetermined number of molecules are given a random set of initial trajectories and allowed to interact with each other based on a semi-empirical central forcefield, COMPASS (Sun 1998) The terms of the COMPASS forcefield that contribute to the total non-bonding energy of interaction are described as,

$$E_{non\text{-}bond} = E_{bond} + E_{angle} + E_{torsion} + E_{inversion} + E_{vdW} + E_{electrostatic} + E_{coupling} \quad (33)$$

During the simulation, Newton's equations of motion are iteratively solved for each atom per time step (user defined) for the duration of the total simulation time. A 16 x 16 x 2 (*a* x *b* x *c*) MgO supercell with lattice dimensions of $a = b = 67.38$ Å, $c = 8.424$ Å was constructed with periodic boundary conditions (in order to eliminate edge effects). The top and bottom of the simulated crystal were cleaved such that two equivalent (100) faces were exposed. Thus, the total available surface area from both surfaces of the MgO(100) plane was then found to be 9080 Å$^2$. The volume above and below the MgO surface was defined as vacuum space with 40 Å of headspace on each side available to the adsorbate molecules. This connected box was constructed in order to conserve the total number of molecules in the simulation. Hence, molecules in the 3D vapor phase whose trajectories would have caused them to leave upper (lower) head space region would appear in the lower (upper) head space region, though the size of the vacuum slab was chosen to minimize the probability of molecules moving to the adjacent surface. MD simulations were performed using the canonical ensemble (constant NVT) using the Nose-Hoover-Langevin (NHL) (Leimkuhler

2010) thermostat with a decay constant of 2.5 fs to regulate the temperature. The MgO substrate used in the MD simulations was built using the Accelrys Materials Studio crystal builder and then geometrically optimized (energetically relaxed) using the Smart algorithm, a hybrid of the steepest descent, quasi-Newton, and adapted basis Newton-Raphson (ABNR) minimizers. Before introducing the adsorbate molecules, the positions of the atoms that made up the MgO substrate were constrained to (frozen at) the geometrically optimized position for the duration of the MD simulations. Initially the adsorbate molecules were randomly added to the simulation volume until the desired effective surface coverage was obtained. The combined molecule/substrate system was subsequently heated to 1.5-2.5 times the bulk triple point. This step was performed to ensure the molecules were randomly located on the surface and the initial molecular configurations remained structurally unbiased. The MD simulations were performed for time intervals between 50-250 ps with 1.0 fs time steps. The fluctuations in energy and temperature were examined at the conclusion of every MD run. As a general observation, the system achieved equilibrium in both energy and temperature within the first 5 ps. The MD simulations were performed starting at temperature of 320 K (octane), 350 K (nonane), and 350 K (decane). Additional simulations were systematically run in decreasing temperature increments of 10-20 K. The resulting trajectories from the simulations were then used to calculate concentration profiles ($C(z)$) as a function of distance normal to the surface, mean square displacements, and velocity autocorrelation functions

to describe the dynamics of the molecules. In order to interpret the signals from the concentration profiles, single molecules were geometrically optimized and subsequently the internal modes were frozen. The isolated molecule was then placed on the surface and a concentration profile collected for each of the molecular orientations relative to the surface.

## Results and Discussion

### *Thermodynamics*

The monolayer capacities for all three molecules were determined using the Point B method (Emmett 1937) and the area per molecule (APM) were determined using a methane adsorption measurement as the fiducial. The APMs projected on the surface of MgO(100) for octane, nonane, and decane adsorbed on MgO were determined to be $137\pm9.7$ Å$^2$, $128\pm5$ Å$^2$, and $202\pm5$ Å$^2$ respectively. Representative adsorption isotherms and their numerical derivatives for these alkanes on MgO are shown in Figure 21, Figure 22, and Figure 23.

Several common features are worth noting about the adsorption behavior. First, evidence of two distinct layering "steps" with a third significantly less
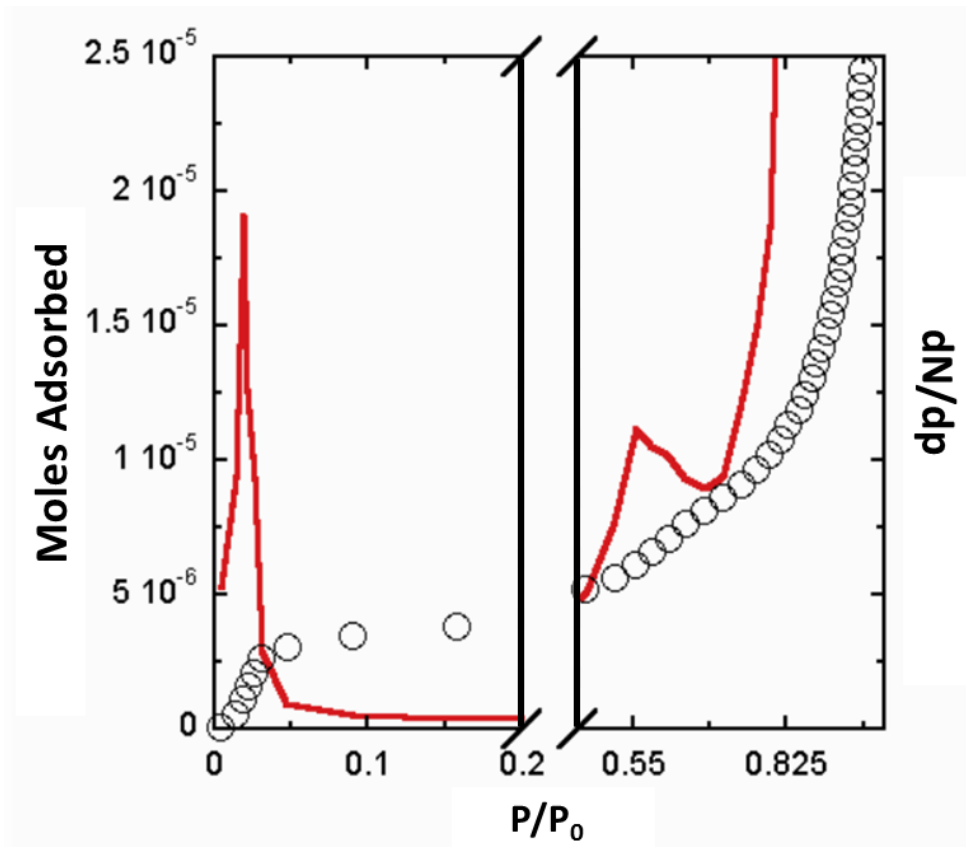
Figure 21 – Representative isotherm (circles) for octane on MgO(100) at 262.1 K in addition to the numerical derivative (red solid line) of the moles adsorbed with respect to equilibration pressure.
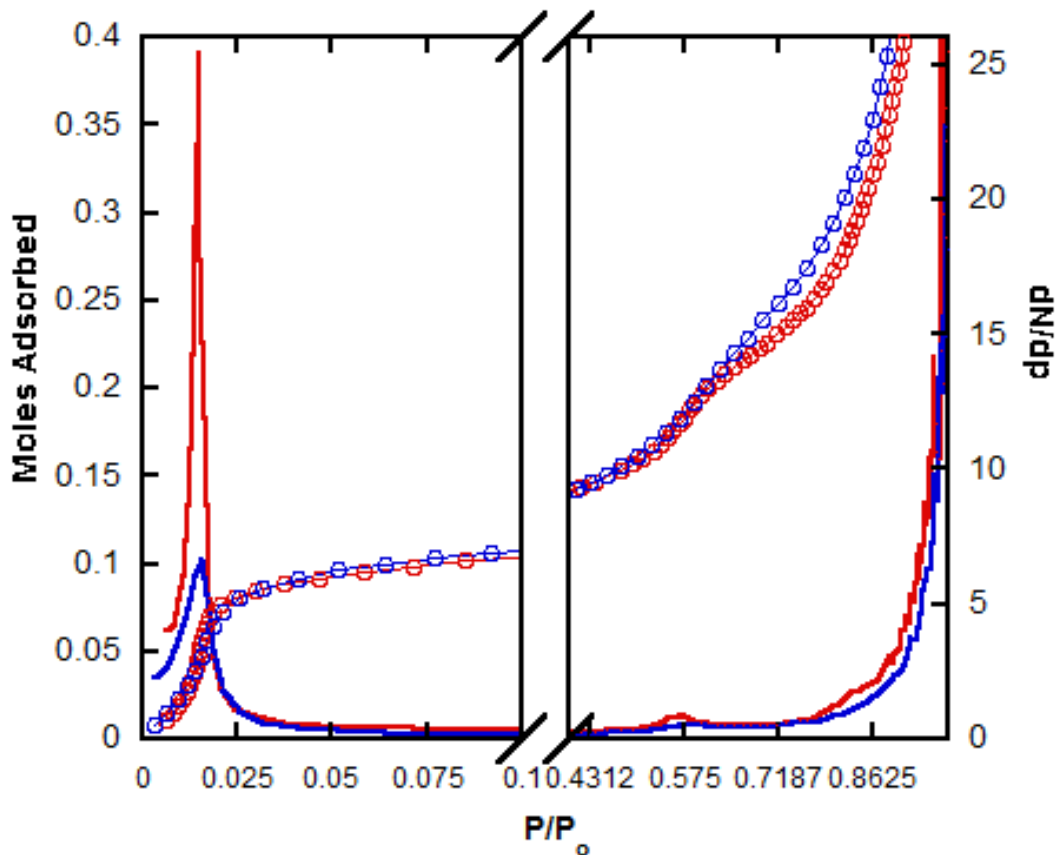
Figure 22 – Representative isotherms (circles) for nonane on MgO(100) at low temperature, 254 K (red), and high temperature, 275 K (blue), with their respective numerical derivatives (solid lines).
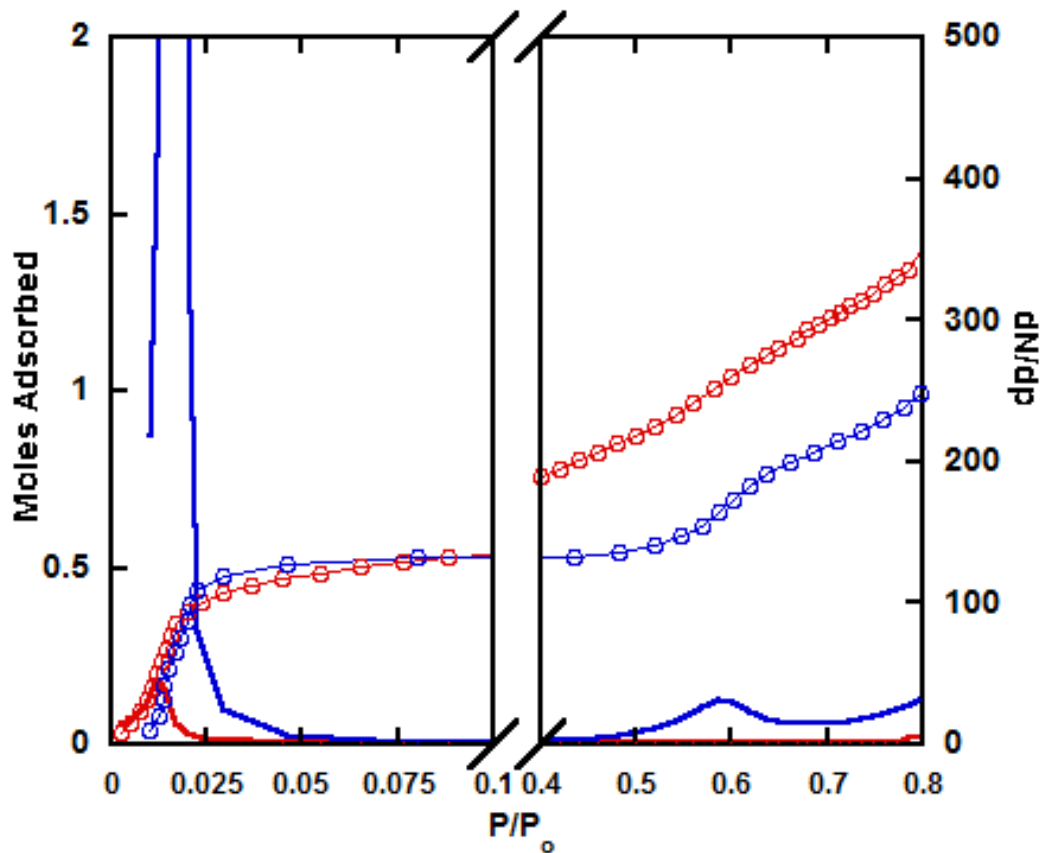
Figure 23 – Representative isotherms (circles) for decane on MgO(100) at low

temperature, 260 K (blue), and high temperature, 290 K (red), with their

respective numerical derivatives (solid lines).

pronounced step at the lowest temperatures for all three molecules were recorded. Second, the numerical derivatives of isotherms exhibit peaks that are sharp (narrow and tall) at low temperatures; as the temperature rises these peaks slowly decrease (increase) in height (width) until beyond a certain temperature. The numerical derivatives can be formally tied to the isothermal compressibility (Dash 1975) and as the peaks broaden they correspond to an increase in the mobility especially in the z-direction. The changes in interlayer mobility and associated loss of layer definition/sharpness and broadening of the film interface is illustrated later using still frames from the MD simulations. The numerical derivative data for each "layer" were fitted using Gaussians and the associated peak positions were then plotted as a function of inverse temperature.

Using a variant of the Clausius-Clapeyron equation, the slope (A(n)) and y-intercept (B(n)) can be used to obtain differential enthalpies and entropies relative to the bulk values as in previous studies (Freitag 2000, Arnold 2005, Felty 2008, Arnold 2006, Cook 2015, Yaron 2006, Fernandez-Canoto 2014).The heats of adsorption were calculated from the product of the slope and gas constant (R is 8.314 J K$^{-1}$ mol$^{-1}$). This approach was first suggested by Larher (Larher 1976) and is summarized in equations 34-36.

$$\Delta H^{(n)} = -R(A^{(n)} - A^{(\infty)}) \qquad (34)$$

$$\Delta S^{(n)} = -R(B^{(n)} - B^{(\infty)}) \qquad (35)$$

$$Q_{ads}^{(n)} = RA^{(n)} \qquad (36)$$

The tabulated quantities obtained from linear fits to these Clausius-Clapeyron data are presented in  even properties observed in bulk alkanes.

Table 6. $Q_{ads}$ incrementally increases as a function of carbon number because obviously the number of atoms binding to the surface increases with the increase in alkane chain length. In the limit of zero temperature and coverage the heat of adsorption is simply equal to the binding energy (Dash 1975). The $Q_{ads}$ values calculated for octane (Figure 24), nonane (Figure 25), and decane (Figure 26) fall in line with previous measurements for alkanes on MgO and continue to show an increase in $Q_{ads}$ with increasing carbon number as illustrated in Figure 27.

The differential enthalpies and entropies exhibit a similar increase in value for octane through decane as well. It is less straightforward to describe how these quantities respond to the change in carbon number. What is apparent is that with an increase in the number of carbons in the molecular chain, there are additional contributions to the total free energy of the adsorbed film. In an earlier publication, Fernández-Cañoto and Larese (Fernandez-Canoto 2014) pointed out that for odd members of the normal alkane series one needs to recognize that when the plane of the adsorbed molecule is normal to the surface plane there are two different orientations the molecule can assume (relative to the surface). One consequence of this additional term in the free energy is responsible for the odd-even properties observed in bulk alkanes.

89

Table 6 – Thermodynamic values from volumetric adsorption isotherm data for

octane, nonane, and decane on MgO

| Alkane | $n$ | $A^{(n)}$ | $B^{(n)}$ | $Q_{ads}^{(n)}$ (kJ/mol) | $\Delta H^{(n)}$ (kJ/mol) | $\Delta S^{(n)}$ (J/K·mol) |
|--------|-----|-----------|-----------|--------------------------|----------------------------|-----------------------------|
| Octane | 1 | 5384.9 ± 67.6 | 21.74 ± 0.27 | 44.77 ± 0.58 | −1.10 ± 0.02 | 27.88 ± 0.34 |
| | 2 | 5308.6 ± 22.9 | 24.76 ± 0.09 | 44.14 ± 0.20 | −0.47 ± 0.01 | 2.82 ± 0.02 |
| | ∞ | 5252.6 ± 3.0 | 25.09 ± 0.02 | 43.67 ± 0.03 | - | - |
| Nonane | 1 | 6137.8 ± 92 | 18.077 ± 0.34 | 51.03 ± 0.76 | −1.2796 ± 0.04 | 30.0984 ± 0.47 |
| | 2 | 6075 ± 46 | 21.514 ± 0.18 | 50.51 ± 0.38 | −0.7574 ± 0.01 | 1.5215 ± 0.02 |
| | ∞ | 5983.9 ± 74 | 21.697 ± 0.28 | 49.75 ± 0.62 | - | - |
| Decane | 1 | 6810.1 ± 70.16 | 18.88 ± 0.25 | 56.62 ± 0.58 | −3.4428 ± 0.04 | 24.1701 ± 0.31 |
| | 2 | 6506 ± 77.5 | 21.675 ± 0.28 | 54.09 ± 0.64 | −0.9146 ± 0.01 | 0.9312 ± 0.01 |
| | ∞ | 6396 ± 74.7 | 21.787 ± 0.27 | 53.18 ± 0.62 | - | - |
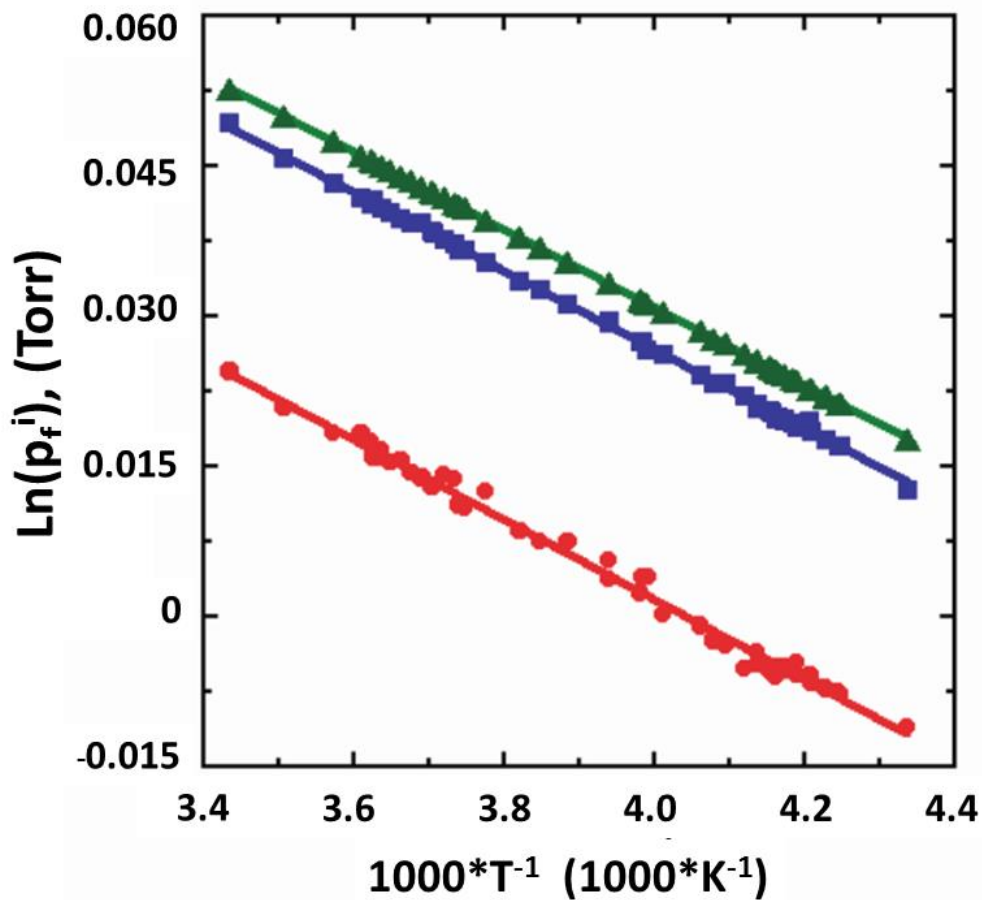
Figure 24 – Clausius−Clapeyron plot for octane on MgO. First layer (red circles), second layer (blue squares), and bulk (green triangles) data are available over the temperature ranges studied.
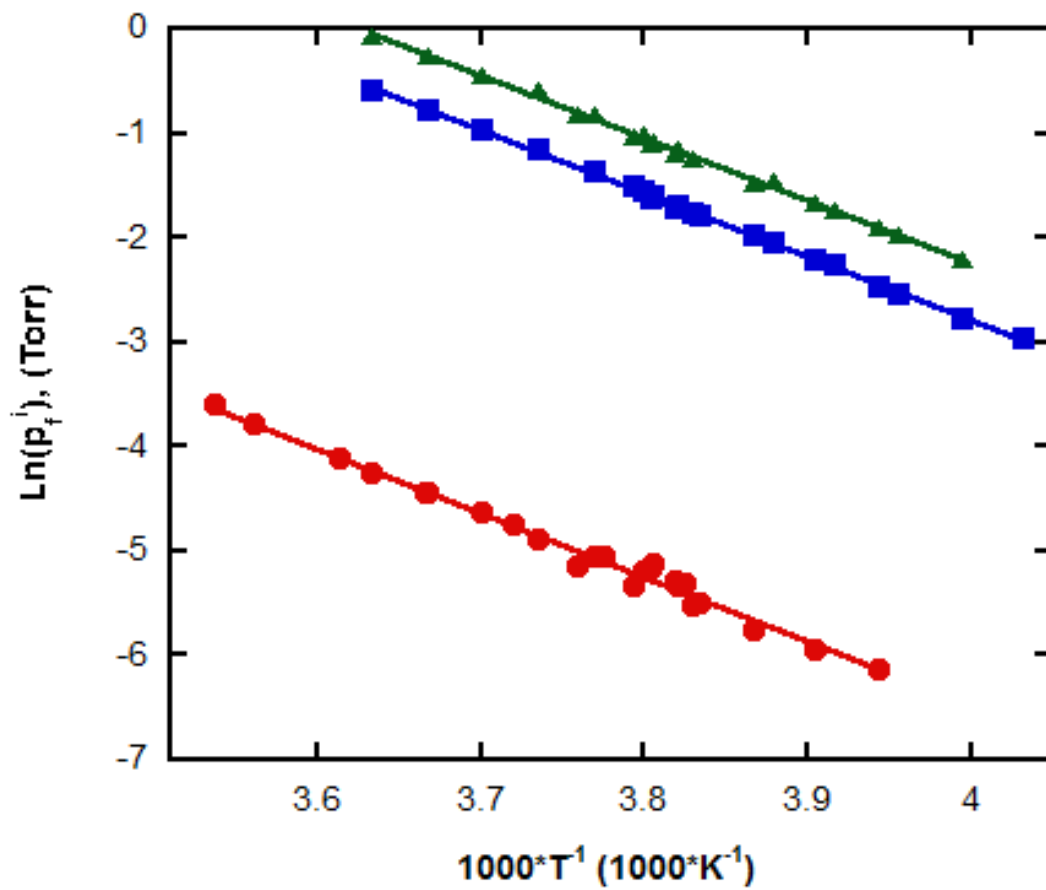
Figure 25 – Clausius−Clapeyron plot for nonane on MgO. First layer (red circles), second layer (blue squares), and bulk (green triangles) data are available over the temperature ranges studied.
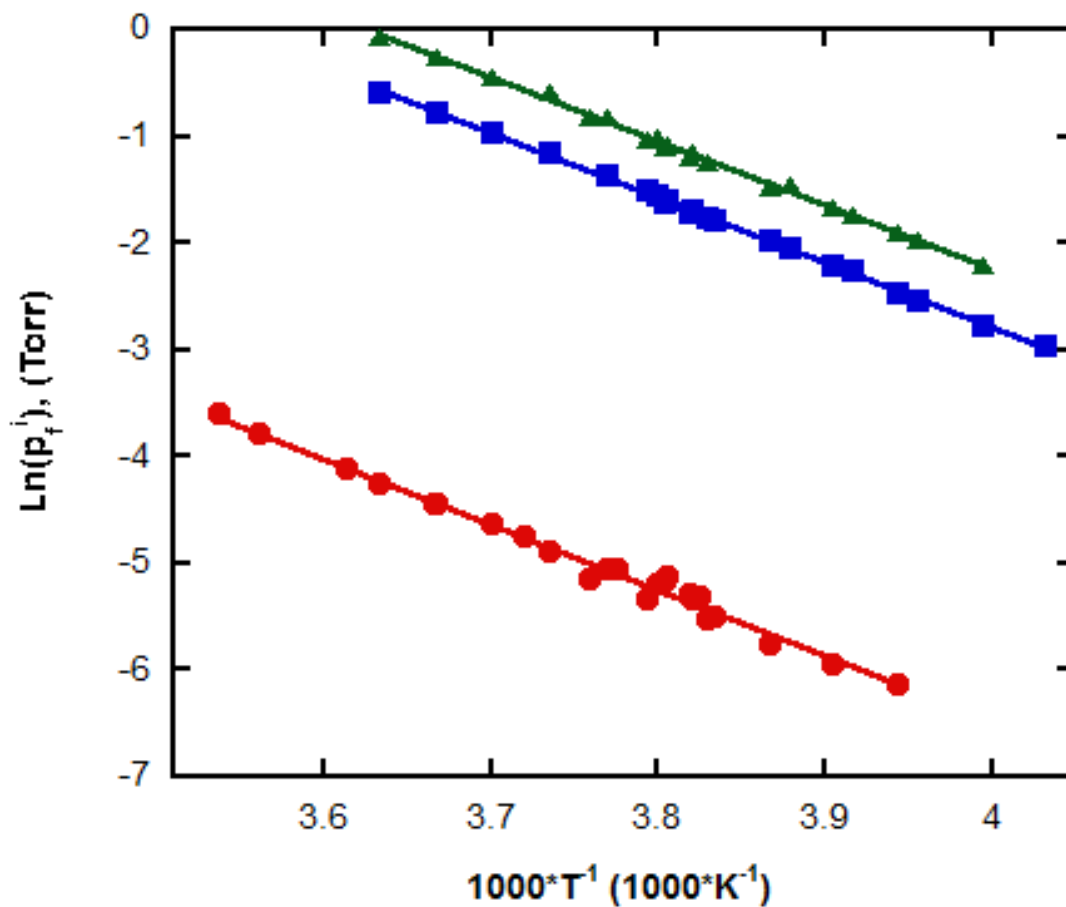
Figure 26 – Clausius−Clapeyron plot for decane on MgO. First layer (red circles), second layer (blue squares), and bulk (green triangles) data are available over the temperature ranges studied.
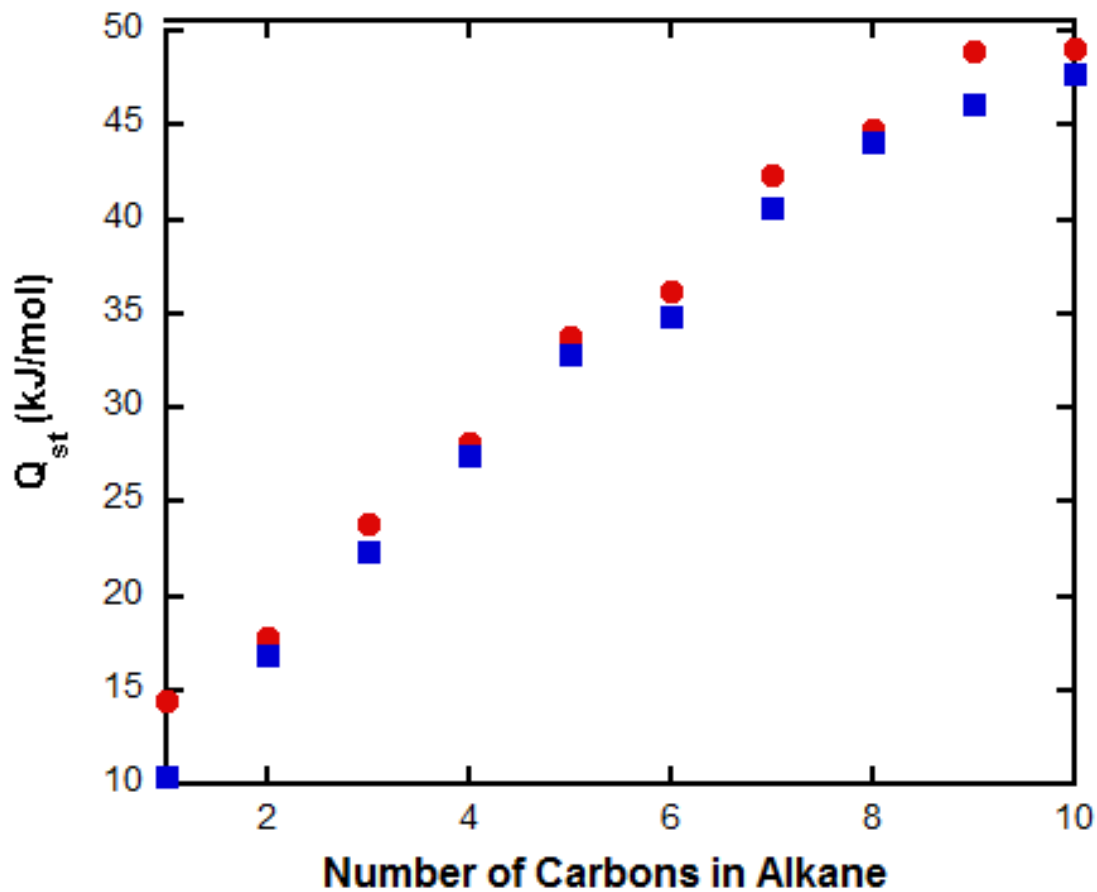
Figure 27 – Heats of adsorption for the homologous series of alkanes from methane to decane on MgO(100). The heats for the first layers are represented by red circles, and the second layers are represented by blue squares.

even properties observed in bulk alkanes.

Table 6 shows that the entropy of adsorption is observed to alternate with increasing chain length; most likely a consequence of the odd-even conformational effect in two-dimensions. Note, we are not referring to intramolecular conformational changes, i.e. intrachain backbone flexibility. Although such intramolecular effects are readily observed in our MD simulations for longer alkanes, i.e. where carbon number exceeds C20, we have not recorded evidence in our MD simulations for alkanes C10 and shorter. It is important to keep in mind the increasing importance of the intrachain conformational contribution to entropy as the number of internal degrees of freedom for larger normal alkanes (see Figure 28). This behavior becomes more important and relevant for systems with large fully-saturated carbon chains such as lipid bilayers where the carbon number is in the range of 14-18 (Bruch 2007).

Much can be said about the behavior of the phases of the layers from a careful evaluation of the shape of the isotherms and their corresponding numerical derivatives. Monolayer and submonolayer physisorbed films have been observed to exhibit melting transitions at 70% of the bulk triple point (Bruch 1997). Using this estimate as a guide, the studies discussed here have all been performed well above the "nominal" monolayer melting temperature suggesting that measurements at coverages below monolayer completion, the film is primarily in a liquid-like phase. Estimates from numerous monolayer studies also indicate that the two-dimensional critical temperature falls in the range of 0.3-0.5 times the bulk critical point. Hence our lower coverage measurements are in the
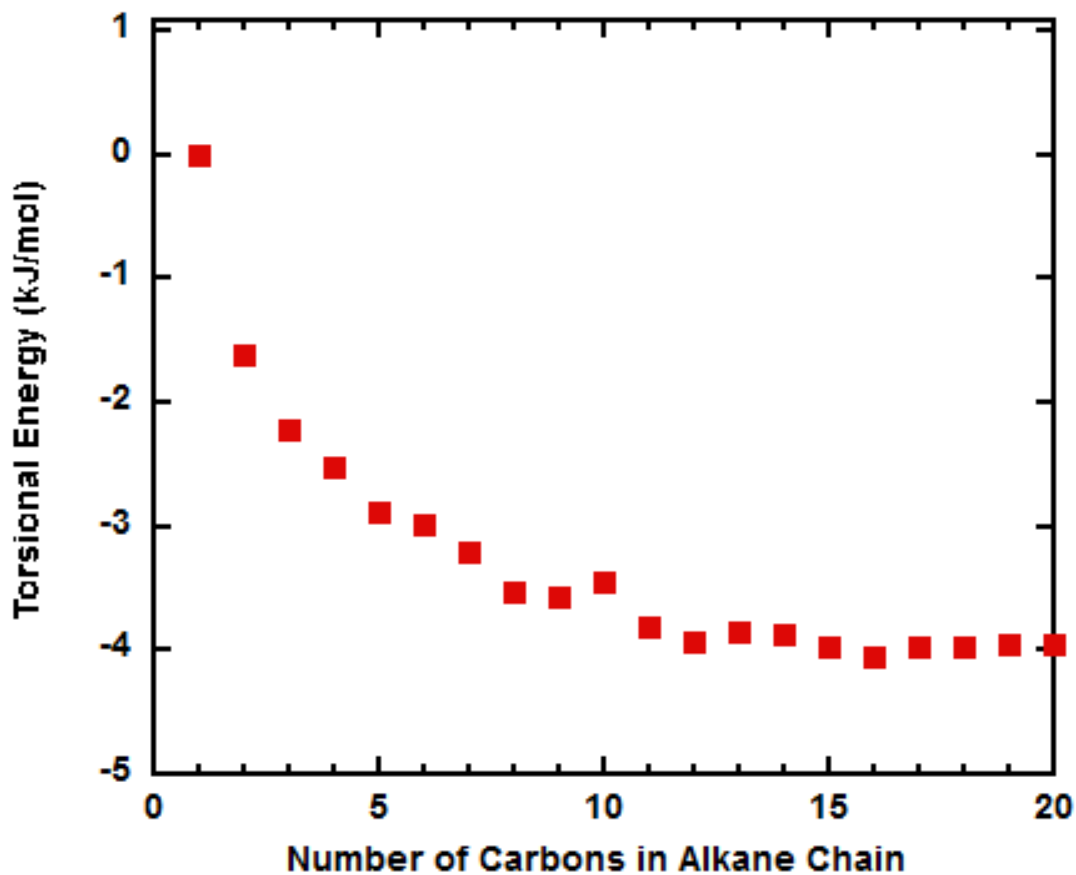
Figure 28 – Contribution to the total free energy from torsional motions (torsions about the dihedral angles) in the linear alkanes on MgO simulated using the COMPASS central force field. The torsional energies were obtained at temperatures of ~0.2 times the bulk triple point for each molecule.

neighborhood of the two-dimensional critical temperatures. We remind the reader that for the majority of our investigation it is reasonable to expect some type of liquid-liquid or 2D-liquid to hypercritical fluid phase transition may appear in the first layer within the temperature range presented here as can be seen in Figure 29, Figure 30, and Figure 31. We have previously used (Arnold 2006, Yaron 2006) the dramatic changes in the temperature dependent width of the numerical derivative to identify potential phase transitions. Similar increases in the width of the numerical derivative of the second layer feature has also been observed and presented in Figure 29, Figure 30, and Figure 31.

We now direct our attention to a discussion of the microscopic behavior that takes place at higher surface coverage. These comments below apply to all three of the alkane films we report in this paper. For example, when the film thickness is increased to two or more nominal layers and the temperature is such that the molecules that occupy the second layer are translationally mobile (i.e. liquid-like) it is worth discussing the influence these upper layers have on the physical status of the near surface layer. Although the more distant liquid-like layers are not as strongly attracted to the surface as the near surface layer the attraction to the surface is still greater than the molecule-molecule interaction. This added interaction acts as an effective pressure on the molecules closest to the surface restricting their spatial distribution and mobility; effectively stabilizing a solid-like near surface monolayer. This behavior was first described by Larese and Zhang for the behavior of multilayer argon on graphite (Larese 1995) and
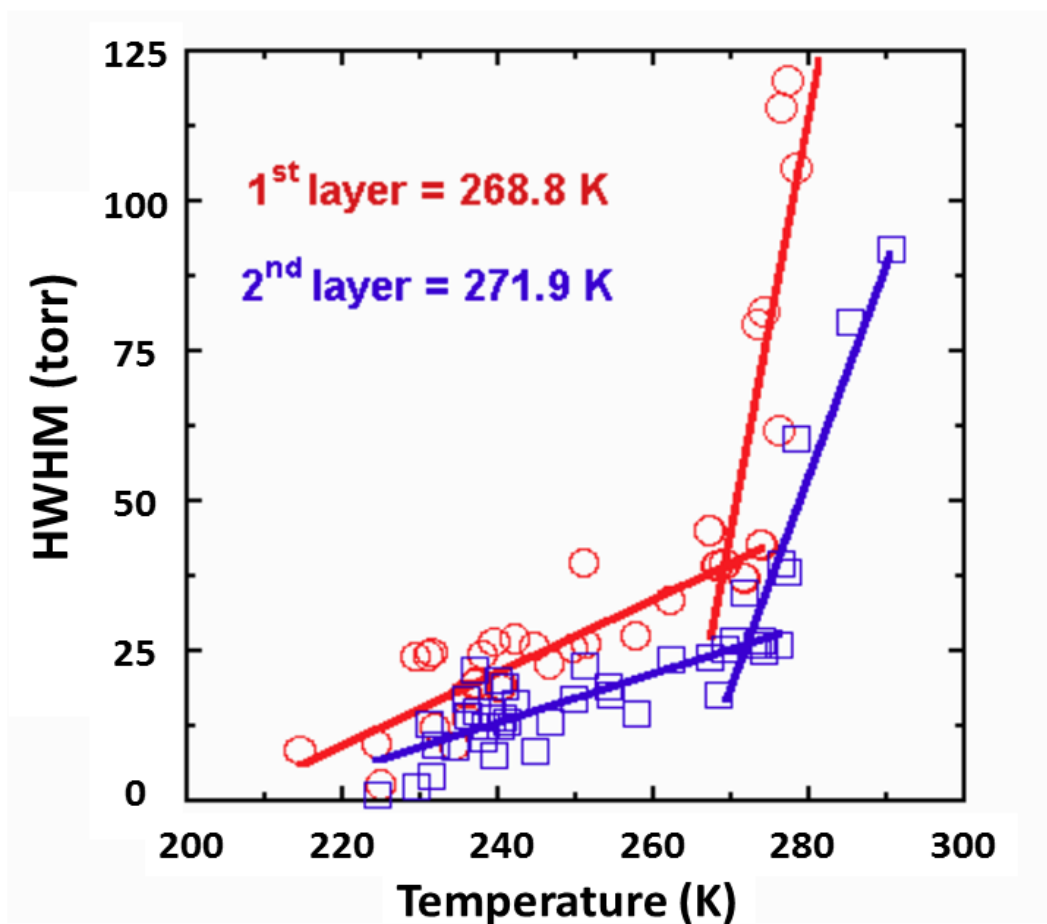
Figure 29 – Half-width at half-maximum (HWHM) for the fitted Gaussian function plotted against temperature for octane on MgO. Note the abrupt change in slope at 268.8 K for the first layer (red circles) and 271.9 K for the second layer (blue squares).
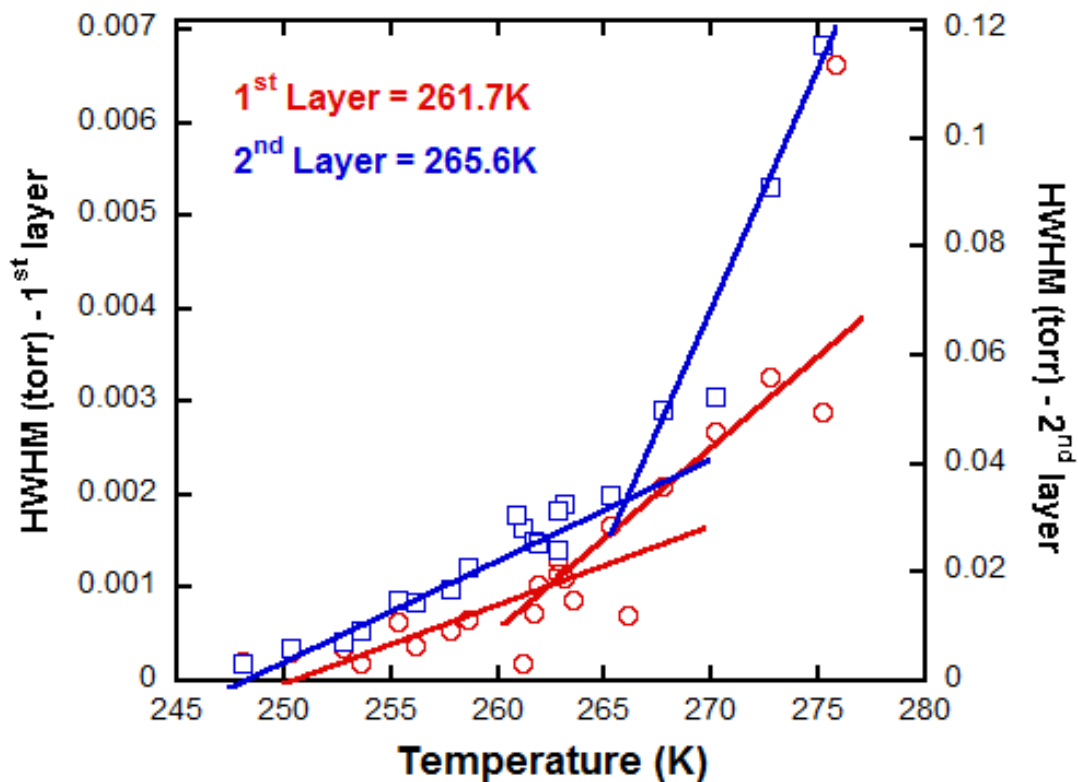
Figure 30 – Half-width at half-maximum (HWHM) for the fitted Gaussian functional plotted against temperature for nonane on MgO. Note the abrupt change in slope at 261.7 K for the first layer (red circles) and 265.6 K for the second layer (blue squares).
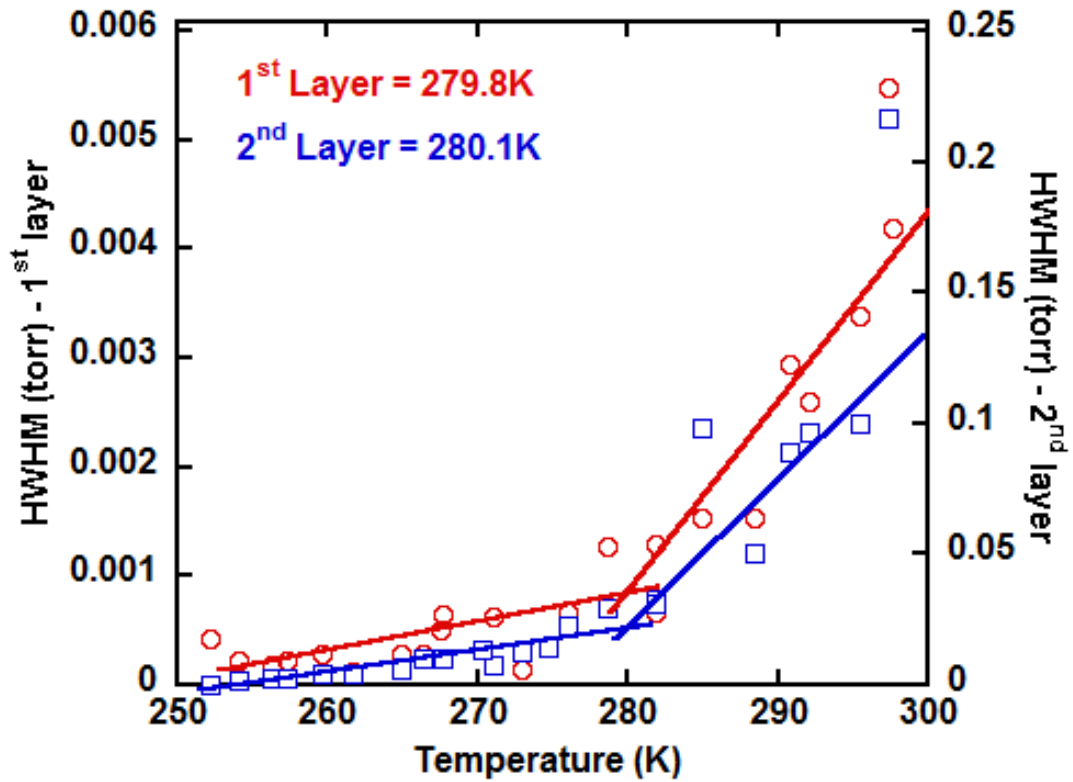
Figure 31 – Half-width at half-maximum (HWHM) for the fitted Gaussian functional plotted against temperature for decane on MgO. Note the abrupt change in slope at 279.8 K for the first layer (red circles) and 280.1 K for the second layer (blue squares).

more recently by Arnold et al. (Castro 1998) for the n-alkanes adsorbed on graphite. It is remarkable that for these multilayer films on graphite it was found that this solid-like near surface layer can coexist with the liquid-like upper layer(s) at temperatures 1.2 times the bulk melting point. Using these earlier studies as a guide, we note that the melting transition of a near surface layer solid in the multilayer regime for the octane, nonane, decane films on MgO would take place near the highest temperatures we investigated. The MD simulations described below appear to be consistent with this behavior. Neutron/x-ray diffraction as well as inelastic neutron scattering measurements are planned to explore whether such a stabilization of the near surface film takes place for alkane adsorption on MgO.

### *Molecular Dynamics*

As noted above, MD simulations using central forcefields have been performed to add a microscopic perspective to the thermodynamic investigations. In principle, such MD simulations can be used to explore any point in the phase diagram where experimental adsorption isotherms can be measured. However, a one to one correspondence between the experimental parameters of density, temperature and chemical potential and those in the simulation is not guaranteed. Hence, we performed simulations over a broader range of temperatures and at surface coverages that spanned those examined in the isotherm measurements to be sure we would get a representative picture of the microscopic behavior of each system. Analysis of the MD simulations included:

the molecular trajectories, the concentration profiles, C(z), normal to the MgO surface, the mean square displacements (MSD), and structural arrangement (i.e. the orientational ordering). In general, the information extracted from the MD simulations for such quantities as C(z) and the molecular mobility as a function of coverage and temperature are key ingredients for developing detailed knowledge about the alkane film growth. Additional insight concerning the dynamical behavior within the films can be obtained from the lateral concentration profiles. While there may be some uncertainties related to the proper choice of interaction potentials we have found that using central forcefields in the MD simulations for describing the interaction of hydrocarbons with MgO in previous studies have been generally reliable. Comparisons of the MD simulations with companion measurements using microscopic probes such as neutrons or x-rays help strengthen the reliability of the modeling results. In general, the simulations serve as a guide to better understand the microscopic trends within a given coverage/temperature regime. In the discussion that follows some comments related to the evolution of the film's growth properties as a function of the film thickness are presented. For example, the stratification of the layers tends to decrease/broaden and molecules within the film could potentially appear to be oriented with the molecular axis perpendicular to the surface. This we know to not be the case for previous modeling studies and certainly expect the same for these systems.

To simplify our initial understanding of the orientational states, the energies of isolated molecule stable structures were calculated in order to provide information about the additional odd/even microstates available to the quasi-two-dimensional adsorbed systems (Figure 32). The method used to explore the surface potential is provided in previous work (Yaron 2006). The resulting energies are provided in Table 7. We note that this represents the fundamental interaction of the isolated molecule with the surface. It is the gradual change in this interaction caused by greater molecule-molecule interactions from increasing coverage that is the basis for the behavior observed in two- and three-layer systems.

This method has been used in previous studies (Arnold 2006, Yaron 2006) and shows a narrowing between the difference in energies of the perpendicular states (for odd n-alkanes) on the surface with an increase in carbon number in the molecule. From the heptane on MgO data by Fernández-Cañoto and Larese there is a difference of 7 percent between the two orientations. The gap closes as the ratio of carbons in the two odd/even perpendicular states approaches unity. For decane on MgO this difference is reduced to below 5 percent. Ultimately, we might expect the orientational contribution to entropy to become less significant in larger alkanes and move toward a system dominated by configurational entropy with an increasing number of internal degrees of freedom. From preliminary simulations for higher n-alkanes such as icosane on MgO(100) the dilute submonolayer system exhibits "worm-like" dynamics where the

103
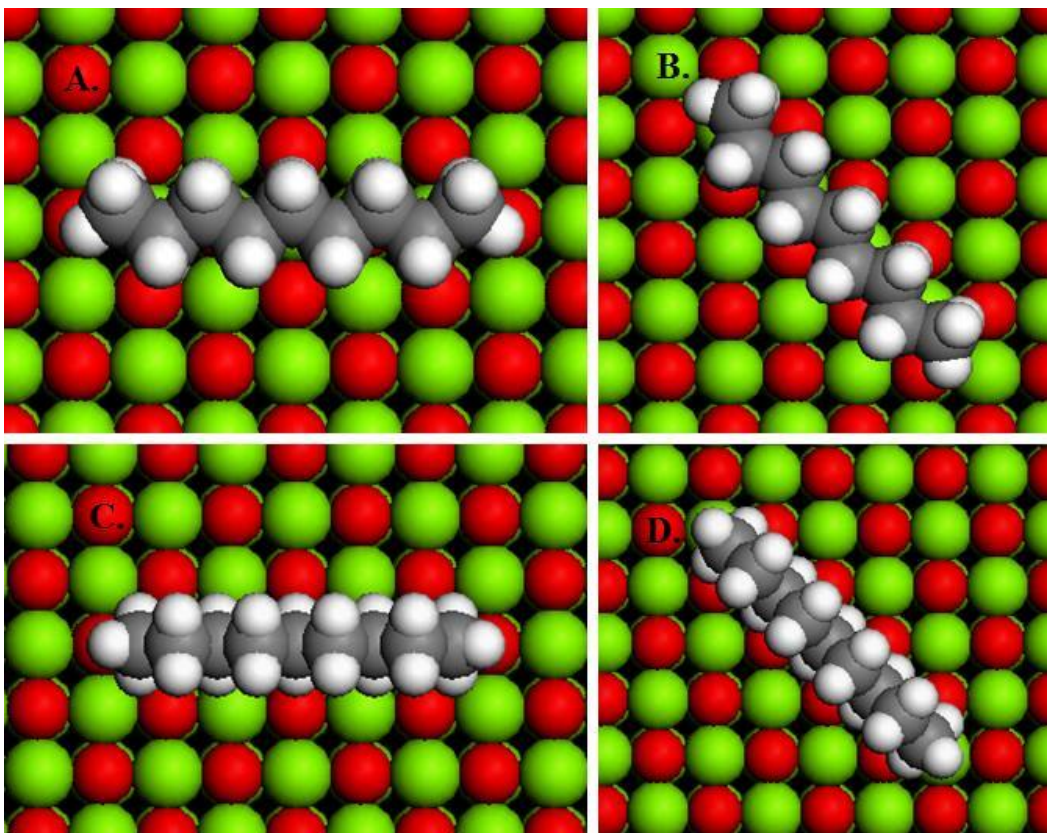
Figure 32 – Illustrations of the lowest energy single-molecule configurations for nonane on the surface of MgO (100). A and B correspond to the parallel and perpendicular orientations with the molecular plane (all carbons) in contact with the surface in the <10> and <11> directions, respectively. Further, C and D relate to the next highest energy configurations with the molecular plane perpendicular to the surface (five carbons in contact with the surface). Finally as illustrated in Table 7, the lowest energy, yet stable configuration is when the molecular plane is perpendicular to the surface with only four carbons in contact with the surface (not pictured).

Table 7 – Calculated binding energies for parallel and perpendicular molecular plane configurations relative to the MgO(100) surface with molecular axis orientations in the ⟨10⟩ and ⟨11⟩ directions

| Adsorbate | Carbons in Contact | Surface Orientation | Non-bonding Energy (kJ/mol) |
|---|---|---|---|
| Octane | C8 – parallel | <11> | -169.730 |
| | | <10> | -166.90 |
| | C4 – perpendicular | <11> | -161.08 |
| | | <10> | -156.81 |
| Nonane | C9 – parallel | <11> | -188.36 |
| | | <10> | -186.52 |
| | C5 – odd perpendicular | <11> | -180.72 |
| | | <10> | -178.04 |
| | C4 – even perpendicular | <11> | -175.42 |
| | | <10> | -175.75 |
| Octane | C10 – parallel | <11> | -210.67 |
| | | <10> | -206.88 |
| | C5 – perpendicular | <11> | -200.11 |
| | | <10> | -196.95 |

adsorbate tends to ignore the surface potential and molecule-molecule interactions dominate.

We now focus our attention on the more complicated system at higher coverages where molecule-molecule interactions play a crucial role. In order to obtain a more complete microscopic understanding of the alkane film growth and layering behavior we concentrated our MD simulations at film thicknesses of nominally one, two, and three layers thick. To completely understand the contributions to the overall concentration profiles, single isolated molecules with frozen internal modes were placed on the surface of MgO(100) in the orientational configurations discussed by Fernández-Cañoto and Larese. For the sake of clarity, the orientations will be labeled, "parallel" for a configuration where the molecular plane of the alkane lies parallel to the MgO(100) surface and likewise, "perpendicular" when the molecular plane is perpendicular to the surface. Further, for alkanes with an odd number of carbons, the "perpendicular" orientation is broken down into odd and even perpendicular orientations since there are two inequivalent states. An example of the description for the orientations and decomposition of the total concentration profiles is provided in

Figure 33 and Figure 34. Figure 35 A(B) displays the temperature dependence of the concentration profiles, C(z), for nonane(decane) films on MgO at approximately 0.7 times monolayer coverage between 40 and 280 K. Comparison of Figure 35 A(B) with

Figure 33 and Figure 34 clearly illustrates that the molecules adsorb with the molecular plane parallel to the MgO(100) surface
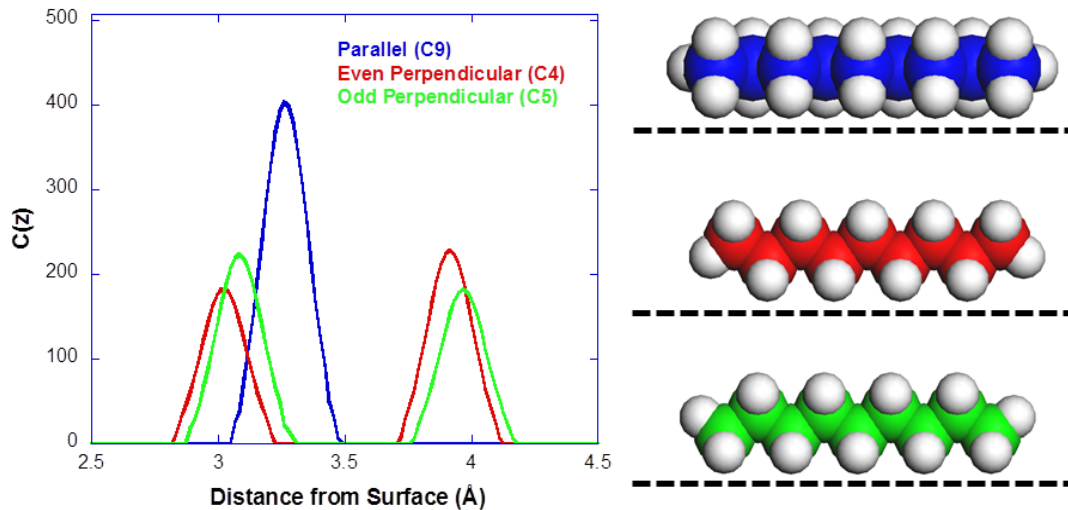


Figure 33 – Carbon atom concentration profiles as a function of the distance from the MgO(100) surface, C(z), for nonane on MgO. The three sets of peaks correspond to surface orientations of alkanes on MgO first discussed by Fernández-Cañoto and Larese shown on the right side of the figure.
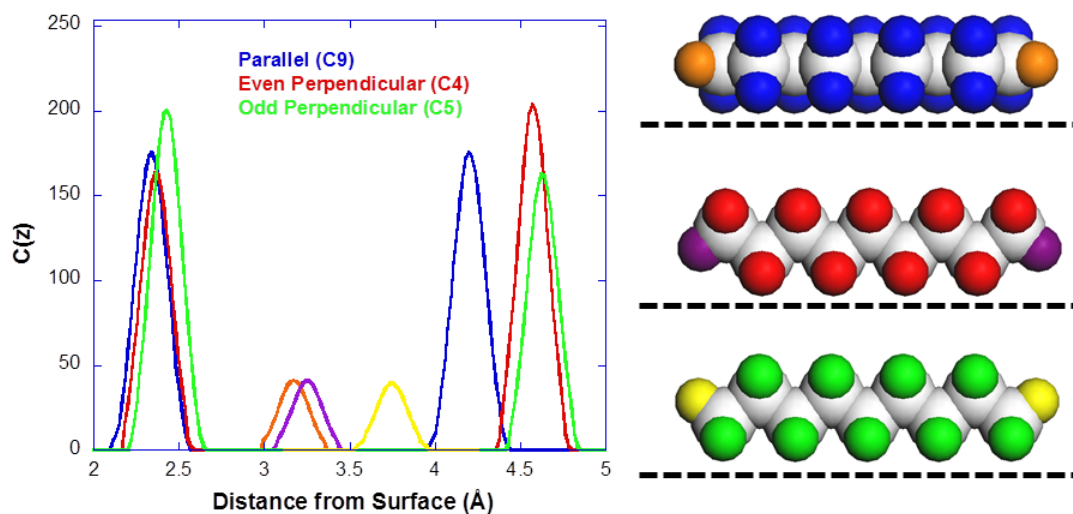
Figure 34 – Hydrogen atom concentration profiles as a function of the distance from the MgO(100) surface, C(z), for nonane on MgO. The three sets of peaks correspond to surface orientations of odd-numbered alkanes on MgO first discussed by Fernández-Cañoto and Larese shown on the right side of the figure.
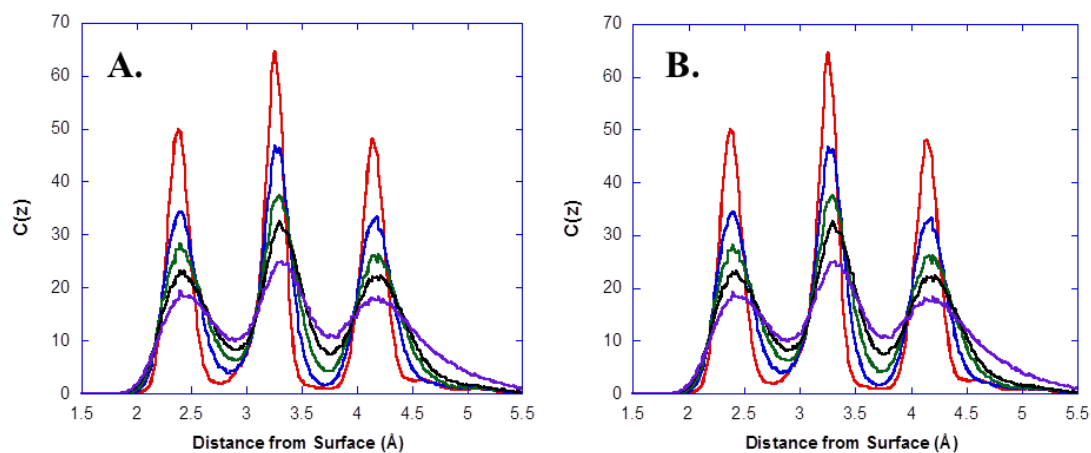
Figure 35 – Illustration of the concentration profiles, C(z), as a function of temperature for nonane (A) and decane (B) on MgO at near 0.7 times nominal monolayer coverage. The temperatures shown are as follows: 40 K (red), 100 K (blue), 160 K (green), 220 K (black), and 280 K (purple).

and that no molecules are promoted to a second layer. Figure 36 (Figure 37) and Figure 38 (Figure 39) show full concentration profiles, C(z) and snapshots of the sideview of the molecular distribution of nonane(decane) molecules calculated from the MD trajectories for adsorbed nonane(decane) at several different temperatures. A discussion of these figures provides valuable insight regarding the spatial distribution of the molecules perpendicular to the MgO(100) plane.

Figure 36 (Figure 37) and Figure 38 (Figure 39) shows the temperature dependence of C(z) for a two (three) layer film from 40 K to 280 K along with companion sideview snapshots at 40 K and 280 K. Comparison of these two sets of figures clearly illustrates the increased roughness (and spatial extent) of the adsorbed film interface as the nominal thickness grows from two to three layers. Several additional comments should first be made about the bilayer film. First, C(z) exhibits a three peak structure centered around 3.3 Å at all temperatures. It is followed by a broader second peak centered near 7.3 Å at 220 K that moves to 7.7 Å at 310 K. The essentially temperature independent, three-peaked structure indicates a significant degree of orientational order of the first layer molecules relative to the MgO surface from 220 K-310 K. Second, the location and breath of the second peak illustrates the increase in spatial distribution of carbon atoms beyond the near surface region as well as an increase in mean perpendicular distance of the center of mass for those molecules as temperature increases. Third, the molecular snapshots shown at the right of Figure 18 at the lowest and
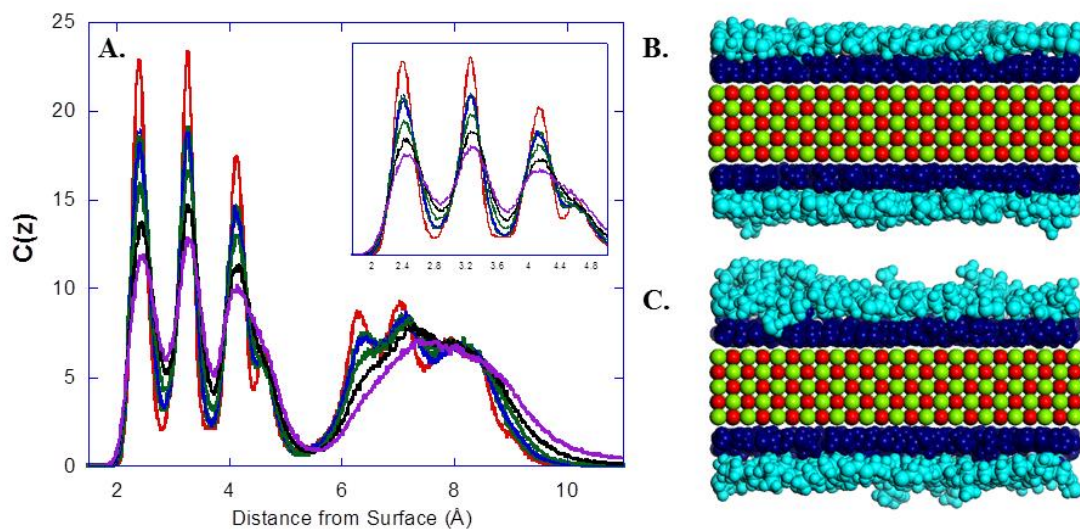
Figure 36 – (A) Representative selection of bilayer-coverage concentration profiles in the z direction, C(z), for nonane molecules on MgO(100). Inset: behavior of the layer nearest to the surface. The temperature profiles pictured are as follows with the temperature shown as a fraction of the bulk triple point in parentheses and color scheme in brackets: 40 K (0.18) [red], 100 K (0.46) [blue], 160 K (0.73) [green], 220 K (1.00) [black], and 280 K (1.28) [purple]. (B) (T = 40 K) and (C) (T = 280 K): snapshots of bilayer coverage nonane on MgO(100) with molecules in the nearest layer (dark blue) and bilayer (light blue) highlighted to show interlayer mobility as a function of temperature.
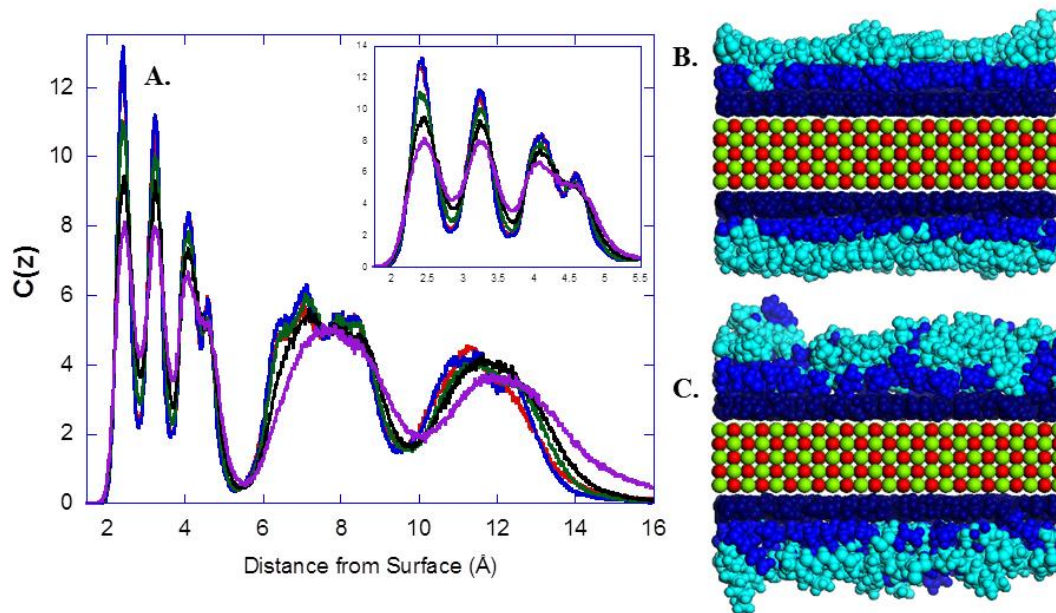
Figure 37 – (A) Representative selection of trilayer-coverage concentration profiles in the z direction, C(z), for nonane molecules on MgO(100). The inset highlights the behavior of the layer nearest to the surface. The temperature profiles pictured are as follows with the temperature shown as a fraction of the bulk triple point in parentheses and color scheme in brackets: 40 K (0.18) [red], 100 K (0.46) [blue], 160 K (0.73) [green], 220 K (1.00) [black], and 280 K (1.28) [purple]. (B) (T = 40 K) and (C) (T = 280 K): snapshots of trilayer coverage nonane on MgO(100) with molecules in the nearest layer (dark blue), bilayer (royal blue), and trilayer/bulk (light blue) highlighted to show interlayer mobility as a function of temperature.

Figure 38 – (A) Representative selection of bilayer-coverage concentration profiles in the z-direction, C(z), for decane molecules on MgO(100). The inset highlights the behavior of the layer nearest to the surface. The temperature profiles pictured are as follows with the temperature shown as a fraction of the bulk triple point in parentheses and color scheme in brackets: 40 K (0.16) [red], 100 K (0.41) [blue], 160 K (0.66) [green], 220 K (0.90) [black], and 280 K (1.15) [purple]. (B) (T = 40 K) and (C) (T = 280 K): snapshots of bilayer coverage nonane on MgO(100) with molecules in the nearest layer (dark blue) and bilayer (light blue) highlighted to show interlayer mobility as a function of temperature.

Figure 39 – (A) Representative selection of trilayer-coverage concentration profiles in the z direction, C(z), for decane molecules on MgO(100). The inset highlights the behavior of the layer nearest to the surface. The temperature profiles pictured are as follows with the temperature shown as a fraction of the bulk triple point in parentheses and color scheme in brackets: 40 K (0.16) [red], 100 K (0.41) [blue], 160 K (0.66) [green], 220 K (0.90) [black], and 280 K (1.15) [purple]. (B) (T = 40 K) and (C) (T = 280 K): snapshots of trilayer coverage nonane on MgO(100) with molecules in the nearest layer (dark blue), bilayer (royal blue), and trilayer/bulk (light blue) highlighted to show interlayer mobility as a function of temperature

114

highest temperature underscore this variation in molecular orientation (axial tilting) and interface roughness.

Beyond the bilayer thickness there is no evidence of layer-by-layer or stratified layer growth. Instead, with increasing coverage and temperature, the corrugation of the film becomes more rough. In the three layer case we see in Figure 39 how the film growth evolves. First, the essentially temperature independent triplet structure (near surface 1st layer) is still observed and the position of central peak is fixed at 3.3 Å. Second, we still observe the second broad peak (bilayer regime) that is now centered near 7.6 Å at 220 K and 8 Å at 310 K. Third, we now observe that an additional broad peak (trilayer regime) appears near 11.6 Å (at 220 K) that moves to 12 Å (at 310 K). Fourth, the breath of the COM distribution (or the mean perpendicular distance from the surface) or layer roughness can be gauged using the full width at half maximum of the layer associated peaks in C(z). We find that the FWHM remains constant at 2.4 Å for the 1st layer; increases to 2.9-3.4 Å for the bilayer peak and increases further to 3.2 - 3.6 Å for the third layer as the temperature rises from 220 K to 310 K. Furthermore, the significant intensity of C(z) at z >12 Å, underscores the fact that the spatial extent of the film as a function of increased temperature and film thickness has increased. The snapshots in the right panel of Figure 39 illustrate that the molecular axes are more randomly distributed (tilted) perpendicular to the surface plane, i.e. they exhibit a less planar, more 3D-like behavior beyond the ordered near surface layer. Examination of the molecular trajectories within

115

the MD simulations shows an increased interlayer mobility as a function of temperature. This behavior is also observed experimentally where the functional form of the isotherms exhibit an exponential increase to the saturated vapor pressure after the appearance of the second layer feature. At the lowest temperatures there is a weak indication that a third layer may be starting to form. From the concentration profiles in Figure 39, it is clear that the distribution of the molecular centers of mass in the z-direction appears to change as a function of coverage. Furthermore, in the first layer the molecules appear to be orientationally ordered about the long-axis of the molecule as illustrated by the three peak structure of C(z) in Figure 39. In higher layers (>1) this distribution becomes smoothed and it is clear the molecules are no longer constrained rotationally by the interaction with the attractive surface potential.

## Conclusion

Using a combination of thermodynamics and molecular modeling methods the adsorption properties and microscopic behavior of the normal alkanes octane, nonane and decane adsorbed on MgO(100) surfaces have been investigated. The high-resolution adsorption traces initially exhibit a more stepwise increase that corresponds to approximately two discrete layers over most the temperature range studied. At the lowest temperatures investigated weak evidence of a possible third layer appears. As the film thickness exceeds two nominal layers the volumetric adsorption exhibits an asymptotic approach

towards saturation (which suggests limited layer growth and a broadening of the film interface). Clausius-Clapeyron analysis of the adsorption data reveals a steady increase in the heat of adsorption $Q_{ads}$, while the differential entropy, dS, increases from octane (even) to nonane (odd) then decreases for decane (even). Energy minimization studies and molecular dynamics (MD) simulations were used to gain insight into the microscopic molecular behavior at the gas solid interface. Single molecule energy minimization studies revealed that in all cases single molecules adsorb with the molecular plane parallel to the MgO(100) surface. Alkanes with odd numbers of carbons in the backbone exhibit adsorption energy differences when the molecular plane is oriented perpendicular to the MgO(100) surface leading to an important entropic contribution when condensed single and multilayer films are formed. The MD simulations performed for all three molecules as a function of film thickness and temperature revealed that the spatial distribution C(z) of the molecules perpendicular to the MgO(100) surface was spatially more diffuse as the film thickness and temperature increased. Likewise the orientational (rotational) order and molecular mobility increased as the temperature and film thickness increased. Remarkably, for films two and three nominal layers thick, the molecular layer closest to the surface remained orientationally and spatially more ordered due to the stabilization effects of the upper (more liquid like) layers even to temperatures well above where the films that occupied the higher layers were both translationally and rotationally more mobile. Using snapshots from the MD simulations of the film of the microscopic

117

status of the multilayer films clearly shows evidence of a well ordered near surface layer and a roughening of the film profile as the temperature and film thickness increase. These results are in agreement with the existence of near surface first layer solid observed and reported for multilayer atomic and alkane films on the graphite basal plane. Structural and dynamical investigations using x-ray diffraction and inelastic and quasielastic neutron scattering methods are planned to verify these observations.

# CHAPTER FOUR – HIGH-RESOLUTION VOLUMETRIC ADSORPTION AND MOLECULAR DYNAMICS OF THE N-ALKANES ON THE SURFACE OF HEXAGONAL BORON NITRIDE

Authors: Nicholas Strange, J.Z. Larese

*(pre-print)*

## Abstract

High-resolution volumetric adsorption isotherm measurements were performed for the *n*-alkanes, methane through octane, on hexagonal boron nitride (hBN) in the vicinity of their bulk triple point temperatures. The shapes of the adsorption isotherm curves for these alkanes allows one to separate these molecules into sub-groups based on their geometries. The spherical molecules (methane) form six layers over a broad range of temperatures. The cigar-like molecules (ethane and propane) exhibit three layers where the first two steps are relatively steep. The larger alkanes (butane through octane) are more worm-like and show three transitions, but with shallower steps suggesting a less-ordered layering mechanism. The thermodynamics of adsorption were calculated using a variation of the Clausius-Clapeyron equation. The alkanes exhibit a relatively linear trend in heat of adsorption with increasing chain length. Molecular dynamics simulations were performed to provide microscopic information about the adsorption of these alkanes on hBN. Concentration profiles ($C(z)$) calculated normal to the surface plane support the conclusion that there is less stratification in discrete layers with increasing chain length. Fluid-like multilayers also were observed to stabilize the layer nearest to the surface near and above the bulk triple point.

120

## Introduction

Two-dimensional (2D) materials have recently drawn a considerable amount of technological and scientific interest because of their unique properties. This attention is enhanced by the fact that atomic/molecular deposition, chemical functionalization and doping can lead to precise control of their physico-chemical and optoelectronic properties. Although graphene is the most recognizable member of these 2D materials, hexagonal boron nitride (hBN) has been shown to exhibit unique electronic properties. hBN is a wide band gap (5.955 eV) semiconductor that is both chemically and thermally stable. Recent studies suggest that optical properties of hBN are determined by phonon assisted transitions (Cassabois 2015). Other members of the nitride-based 2D family include GaN and $Ca_2N$, which both exhibit crystalline structures (wurzite) and electronic properties different from those of hBN (Jacoby 2017). Successful engineering of these interesting 2D material's electronic properties requires a robust, molecular level understanding of the surface properties including the potential energy surfaces. Molecular adsorption is one way to effectively characterize the physical properties of a class of these materials providing thermodynamic (macroscopic) information such as binding energies, differential enthalpies/entropies, and locations of potential phase transitions. By combining the thermodynamic data with those obtainable from microscopic measurements such as neutron or x-ray scattering, a comprehensive understanding of 2D materials is possible. The adsorption properties of the n-alkanes (methane

through octane) on the surface of hBN using high-resolution volumetric isotherms are described below. Molecular dynamics simulations of all eight alkanes were performed in tandem with these thermodynamic measurements. The results reported here will serve as the basis for future neutron/x-ray scattering measurements aimed at examining the monolayer structures and microscopic dynamics of these alkanes on hBN.

Soon after the discovery of graphene (Novoselev 2004) it was quickly recognized that there were numerous materials that could be produced in single layers. hBN was one such material identified as an ideal layered material to investigate because of its structural similarity to the graphite basal plane. hBN is iso-structural and exhibits only a two percent (larger) difference in the inter-planar lattice constant. Beyond the fundamental scientific benefits of studying molecular adsorption on hBN, it is widely used in industry as a lubricant (Deepika 2014) and as a lubricant additive (Kimuraa 1999) (frequently referred to as white graphite), as a catalyst (Grant 2016, Nash 2016) and as machinable high-temperature ceramic (Saint-Gobain) NASA has also investigated the use of hBN in radiation shielding because of its stability under the ultra-high vacuum and temperatures in space as well as the large boron-10 isotope neutron absorption cross section (Thibeault 2012). A better understanding of various substrate-catalyzed hydrogenation reactions of paraffins can be achieved by examining the interfacial behavior of alkanes on hBN. For example, BN has recently shown promise as a metal-free catalyst for hydrocarbon conversion reactions (Grant 2016) and as a

catalyst support for the hydrogenation of olefins (Nash 2016). Hence as a result of this investigation the information needed to improve the current semi-empirical force fields used for describing interactions with hBN as well as the efficiency of industrially important catalytic processes and the selectivity in hydrocarbon separations now exist.

Extensive literature exists on atomic and molecular adsorption on the surface of graphite. A subset of this work has focused on the interaction of alkanes on the basal plane of graphite using heat capacity and diffraction measurements (Ferreira 1984, Bienfait 1990, Bomchil 1980, Kim 1984, Gay, 1986, Regnier 1981, Zhang 1990, Lee 1997, Alkhafaji 1996, Castro 1999, Krim 1985, Clarke 1999, Arnold 2002). In contrast, studies of adsorption on hBN are less substantial. Nearly four decades ago, Bockel *et al.* (Bockel 1979) published a limited set of adsorption isotherms of methane on hBN between 77 and 90 K. Based upon these measurements, they proposed a 2D critical temperature of ~77 K. Several years later, Tessier and Larher (TL) (Tessier 1982) extended the adsorption studies of Bockel *et al.* to lower temperatures and to include deuterated-methane on hBN. Based on these new measurements, TL suggested a refined 2D critical temperature of ~74 K. The adsorption measurements described here take advantage of newly developed synthetic methods that now produce hBN with improved surface homogeneity/quality and technological advances (e.g. pressure transducers of better stability and resolution, temperature regulation, and a computer-automated apparatus). Thus, the current

study aims to improve upon the accuracy of previously determined thermodynamic values and extend the fundamental knowledge of multilayer formation of methane film growth on hBN. Migone *et al.* have reported adsorption thermodynamics of argon and krypton on hBN (Alkhafaji 1991, Alkhafaji 1992, Migone 1993, Li 1996, Diama 1999) in order to make a comparison to their behavior on graphite and further, to improve the understanding of re-entrant layering in adsorption. Morishige *et al.* have performed complementary structural measurements for rare gases and nitrogen on hBN where it was discovered that Kr forms an incommensurate lattice prior to melting unlike that observed for Ar and Kr on hBN (Morishige 1996). Arnold and coworkers have performed multilayer scanning calorimetry (Arnold 2012) (hexane-hexadecane) and monolayer x-ray diffraction (Arnold 2014) structural studies of various alkanes adsorbed on hBN. As noted above, a portion of the work described here is an experimental investigation of the thermodynamics of *n*-alkanes on the surface of hBN using high-resolution volumetric adsorption isotherms. It complements a recently completed comprehensive thermodynamic and structural study of the *n*-alkanes on the surface of MgO(100). Thus, the current results allow one to examine how the adsorption behavior changes with a substrate of different chemical composition and surface symmetry. In the current study we have performed a series of volumetric adsorption isotherm measurements over a wide range of temperatures combined with molecular dynamics modeling to accurately describe the alkane-substrate interaction. Differential thermodynamics of

124

adsorption have been calculated from the isotherm measurements. The molecular dynamics calculations reveal microscopic phenomena important for interpreting future structural and dynamical measurements.

## Experimental

### *Volumetric Adsorption Isotherms*

The hBN used in the adsorption study was AC6004 grade produced by Momentive Performance Materials, Inc. (Momentive).  Previous measurements have shown that there is an inverse relationship between specific surface area and substrate quality (Wolfson 1996). Thus, AC6004 hBN was chosen because of its large particle size (12-13 μm) rather than its surface area (2 $m^2$/g). Before use, the known soluble surface impurities (primarily boric oxide and boric acid) were removed from the hBN powder. The hBN sample was prepared in the following way: a slurry of hBN was stirred in methanol for approximately two hours, then vacuum filtered using a fine-grade filter funnel and subsequently dried in an oven at 160 °C for approximately four hours. The dried powder was transferred to a quartz tube and then heated *in vacuo* to 900 °C until a base pressure of $10^{-7}$ Torr was achieved (~24 hours). The heat-treated hBN was transferred in an argon-filled glove box into an OFHC copper cell (methane-hexane) and then sealed with an indium wire gasket before being mounted on the second stage of an Air Products closed-cycle helium cryostat. In order to

avoid the possibility of capillary condensation with the longer alkanes (hexane-octane), the heat-treated hBN was sealed in a small quartz tube which was placed in a Thermo Neslab RTE water bath with temperature control of ±5 mK. As in the past, the isotherm measurements were performed using custom-built Lab-View based automated control system which is described elsewhere (Mursic 1996). The sample temperature of the cryostat-based measurements was regulated with a CryoCon model 32B temperature controller to ±2.5 mK using a silicon diode thermometer; a separate platinum resistance thermometer mounted on the top of the Cu sample cell lid monitored the sample temperature. The temperature of the water bath-based measurements was monitored with a platinum resistance thermometer. The vapor pressures were recorded using 1, 10, and 100 torr MKS capacitance manometers. The temperature ranges over which the measurements were made are provided in Table 8. Details regarding how the adsorbates were obtained and their purities are also contained in Table 8. The liquid alkane samples were distilled over freshly cut sodium metal, passed through a Dri-Rite filled distillation column, and subsequently refluxed over activated alumina microsieves to remove any moisture from the atmosphere. The distilled liquids were transferred into a stainless-steel container in an argon

126

Table 8 – Temperature ranges over which the adsorption measurements were carried out for the series of n-alkanes. The experimental temperature ranges attainable were determined by the vapor pressures of the bulk phases.

| Alkane | Temperature Range (K) | $T/T^{3D}_{trip}$ | Number of Measurements | Vendor (Purity) |
|--------|----------------------|-------------------|------------------------|-----------------|
| Methane | 60-90 | 0.66-0.99 | 43 | Air Gas (99.99%) |
| Ethane | 92-149 | 1.01-1.64 | 26 | Nat. Spec. Gases (99%) |
| *n*-Propane | 121-186 | 1.42-2.19 | 45 | Nat. Spec. Gases (99%) |
| *n*-Butane | 164-222 | 1.22-1.65 | 27 | Nat. Spec. Gases (99.5%) |
| *n*-Pentane | 187-231 | 1.30-1.61 | 39 | Fisher Scientific (>99%) |
| *n*-Hexane | 186-279 | 1.05-1.57 | 93 | Acros Organics (≥99%) |
| *n*-Heptane | 203-284 | 1.11-1.56 | 42 | Acros Organics (>99%) |
| *n*-Octane | 232-294 | 1.07-1.36 | 76 | Acros Organics (≥99%) |

atmosphere and then purified using a freeze-pump-thaw (FPT) distillation sequence with liquid nitrogen to remove soluble gases.

### *Molecular Dynamics*

In order to obtain complementary microscopic information about the adsorption properties, a series of molecular dynamics (MD) simulations were performed using Accelrys' Materials Studio Forcite (Accelrys) package. All eight of the alkanes on hBN over a broad temperature range were modeled using the canonical ensmeble (i.e. constant NVT) and periodic boundary conditions in order to eliminate edge effects. The Nose-Hoover Langevin thermostat (Leimkuhler 2010) was used with a 1.0 ps decay constant which results in a temperature regulation under ten percent of the setpoint value. The Universal force field (UFF) developed by Rappe *et al.* (Rappé 1992) was employed to describe interactions between atoms. The UFF includes contributions to the total energy as a sum of bond stretch, bond angle, dihedral angle, inversion, electrostatic, and van der Waals terms. Currently this is the only parameterized force field that includes interactions for boron with nitrogen, carbon, and hydrogen atoms. The UFF has been used effectively by Perim *et al.* in previous studies to describe the energetics of boron nitride nanoscrolls (Perim 2013).

The lattice parameters ($\mathbf{a} = \mathbf{b} = 2.49824$ Å, $\mathbf{c} = 6.6357$ Å) for the hBN unit cell were obtained from published x-ray diffraction data of Kurakevych *et al* (Kurakevych 2007). A 29 x 29 x 2 supercell (surface area = 4589 Å$^2$) with AB-stacking was constructed from the initial unit cell and then the atom positions of

the hBN substrate were held fixed throughout the MD simulations. We followed a procedure here that has been described elsewhere for alkane films on MgO (Strange 2016, Fernandez-Canoto 2014). Films one, two, and three equivalent monolayers thick were investigated by initially locating a uniform number of molecules randomly in each layer within the simulation box. Then, in order to eliminate any bias from the choice of initial configuration, MD simulations were first performed at sufficiently high temperatures such that the inter- and intra-layer traffic was observed, and the molecules exhibited both rotational and translational mobility (i.e. diffusion). After these preliminary high temperature MD runs were completed, subsequent calculations were performed in decreasing steps of 10-20 K until the rotational and translational motions were restricted (i.e. solid-like structure). Concentration profiles ($C(z)$) were calculated from the trajectories of each of the temperature runs. The MD simulations were performed for a total of 50 ps with 1.0 fs time steps. In order to ensure our simulations were performed long enough for the system to reach thermodynamic equilibrium, we monitored the temperature and total energy (both bonded and unbonded) fluctuations of each run as a function of run time and observed that the system equilibrium was reached (defined by energy and temperature) in approximately 5 ps.

Prior to performing the MD simulations, energy minimization calculations were performed for single alkane molecules on hBN to gain insight into the effects of the hBN substrate on the molecular orientation at the interface. In

particular we examined the difference in energy between parallel and perpendicular configurations of the molecular plane. The optimum orientation and location of an isolated molecular was determined by using the Accelrys Smart algorithm. The threshold for energy convergence was set at $< 2 \times 10^{-5}$ kcal/mol. Energies were calculated for each molecular configuration (parallel and perpendicular orientations) by initially locating the molecules over all the high-symmetry hBN surface sites (i.e. a top, hole, bridge) and then repeating the minimization process by rotating the initial molecular axis orientation by 15 degree increments until a representative sample of the surface symmetry was obtained. Naturally, using a single molecule energy minimization route is not suitable for structural determination, but the MD simulations described in the next section provide some insight into the effects of molecule-molecule interactions on the behavior of condensed states. Future calculations aim to enhance current understanding of lattice defects (domain walls, gauche conformers, and molecular plane configuration) and their effect on the formation and melting of the solid structure.

## Results and Discussion

### *Thermodynamics*

A set of volumetric adsorption isotherm measurements were performed for each of the *n*-alkanes (methane through octane) on hBN over the temperature ranges summarized in Table 8. As alluded to in the previous section, the

minimum experimental temperatures are limited by the low vapor pressures of the alkane adsorbates. The *n*-alkanes in this series can be organized by their molecular geometries into three groups: quasi-spherical, cigar-, and rod-like. Methane is the only member of this series that resembles a quasi-sphere. Ethane and propane can be classified as having cigar geometries. The longer molecular axes of butane through octane exhibit rod-like geometries. This classification of the alkanes by their geometries is reflected in the general shapes of the adsorption curves. Three adsorption isotherms representative of the geometric groups are shown in Figure 40, Figure 41, and Figure 42. Methane on hBN is the only system where the monolayer solid phase is measurable. It has been found that the monolayer melting temperature for atomic and simple molecular films on graphite takes place at ~0.7 times the bulk triple point temperature. For the other molecules in the study (ethane-octane), the experimental temperature range is above 70% of the bulk triple point (i.e. the suggested monolayer melting temperature). In this range of alkanes, two layers are easily resolved in the adsorption measurements. Only at the lowest experimental temperatures does a subtle third layer appear. It should be noted that the observed adsorption behavior for smaller alkanes (i.e. ethane and propane) is qualitatively different than that for the larger molecules, even though the measured temperatures are nominally within the same fractional range of their bulk triple points. The adsorption behavior of longer alkanes has been examined previously by Larese and coworkers for octane, nonane, and decane on MgO (Strange 2016). As the
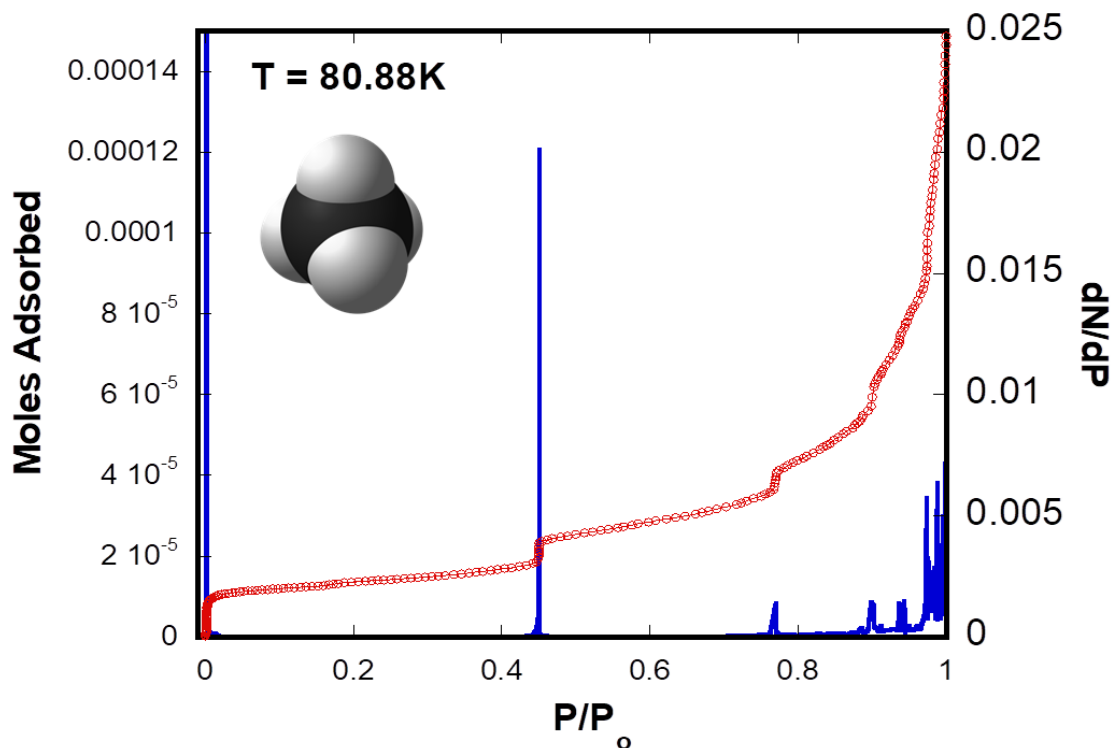
Figure 40 – Representative set of adsorption isotherm data for methane on hBN at 80.88 K ($T/T_{trip}$ = 0.89). The raw isotherm data for moles adsorbed (left y-axis) versus reduced equilibrium vapor pressure is provided in red with a line interpolated from point to point. The numerical derivative (right y-axis) of the raw data shown as dN/dP versus reduced equilibrium vapor pressure is provided in blue. The numerical derivative was used to locate the center of the stepwise transitions.
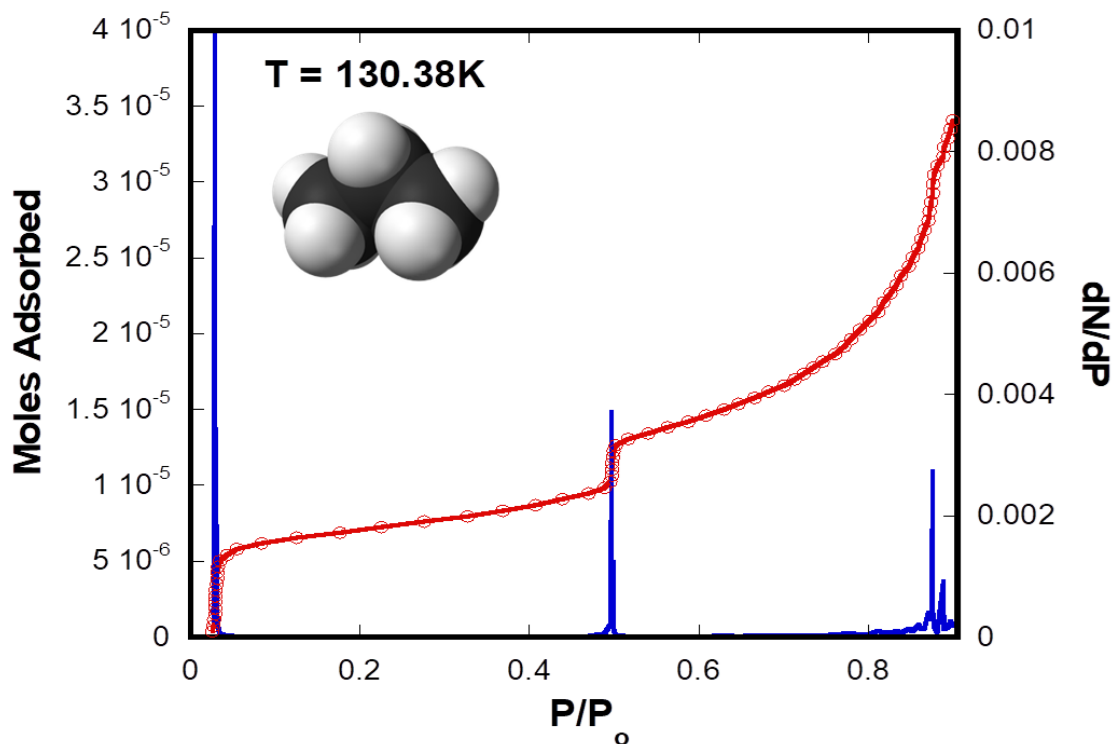
Figure 41 – Representative set of adsorption isotherm data for propane on hBN at 130.38 K ($T/T_{trip}$ = 1.53). The raw isotherm data for moles adsorbed (left y-axis) versus reduced equilibrium vapor pressure is provided in red with a line interpolated from point to point. The numerical derivative (right y-axis) of the raw data shown as dN/dP versus reduced equilibrium vapor pressure is provided in blue. The numerical derivative was used to locate the center of the stepwise transitions.
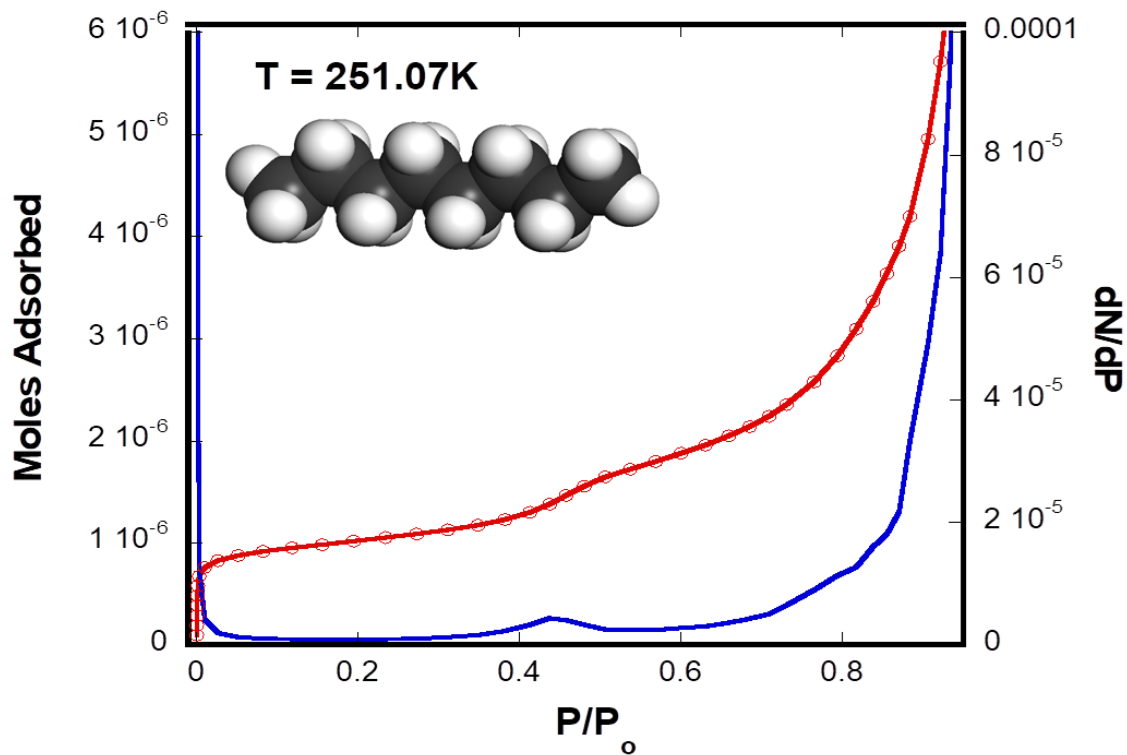
Figure 42 – Representative set of adsorption isotherm data for octane on hBN at 251.07 K ($T/T_{trip}$ = 1.16). The raw isotherm data for moles adsorbed (left y-axis) versus reduced equilibrium vapor pressure is provided in red with a line interpolated from point to point. The numerical derivative (right y-axis) of the raw data shown as dN/dP versus reduced equilibrium vapor pressure is provided in blue. The numerical derivative was used to locate the center of the stepwise transitions.

length of the carbon backbone increases, the molecule-molecule (MM) interaction tends to grow increasingly more important relative to the molecule-substrate interaction (MS). In a similar fashion to the *n*-alkane adsorption of MgO, the number of observable steps in the adsorption isotherms decreases as the molecular length increases (see Figure 40, Figure 41, and Figure 42).

The areas per molecule (APM) were also calculated using a methane isotherm as a fiducial as described in previous studies (Cook 2015). At 77 K, methane forms a √3 x √3 solid monolayer structure on graphite. Bockel *et al.* determined that the structures of methane on graphite and hBN should be identical by making a comparison of the monolayer concentrations. For ethane - octane, the APMs are averaged values since the monolayers exist in fluid phases. The APMs for the alkanes are listed in Table 9 below.

### *Methane on hBN Adsorption Isotherms*

A subset of the methane on hBN isotherms between 77 K and 90 K is shown in Figure 43a. The stepwise shape of the isotherm suggests that growth behavior is similar to that observed previously for rare gases on hBN (Alkhafaji 1992, Migone 1993, Grillet 1980, Dupont-Pavlovsky 1985) and methane on graphite (Bienfait 1990). This is not too surprising given the quasi-spherical geometry of methane and the structural similarity of hBN to graphite. Five layering transitions are clearly visible over much of the temperature range measured with a sixth layer discernible near 74 K. Two sub-steps can readily be identified in the monolayer regime: the first of these features (see Figure 43a)

Table 9 – APMs for the alkanes adsorbed on hBN in the temperature range of this study. The temperature at which the APM was obtained in addition to the temperature reduced by the bulk triple point are provided for reference.

| Alkane | Temperature (K) | $T/T_{trip}^{3D}$ | APM ($\text{Å}^2$/molecule) |
|---|---|---|---|
| Methane | 77 | 0.85 | 16.33 |
| Ethane | 112.65 | 1.24 | 21.74 |
| *n*-Propane | 137.16 | 1.61 | 28.42 |
| *n*-Butane | 162.24 | 1.21 | 39.08 |
| *n*-Pentane | 186.40 | 1.30 | 36.90 |
| *n*-Hexane | 202.18 | 1.14 | 48.76 |
| *n*-Heptane | 206.21 | 1.13 | 62.43 |
| *n*-Octane | 242.21 | 1.12 | 76.45 |
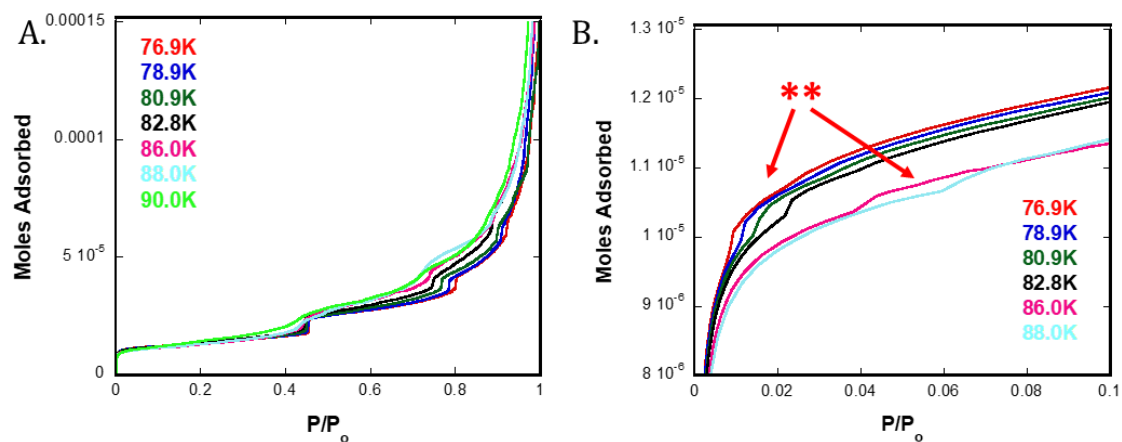
Figure 43 – (a.) Set of adsorption isotherms measured between 77 and 90 K for methane on hBN. Four steps correspond with layer formation over the entire range. A fifth step appears for T~77 K. (b.) illustrates the substep immediately following monolayer formation which corresponds nicely to a phase transition observed previously for the methane on graphite system (Bockel 1979).

corresponds to a 2D vapor to a 2D liquid phase; the second feature (see Figure 43b) has been attributed to the 2D liquid to 2D commensurate solid transition. Clear evidence of a third sub-step appears midway between the monolayer and the onset of the second layer formation (see Figure 44). While this feature has not been observed in earlier work, this sub-step corresponds to the solid commensurate - solid incommensurate phase transition similar to that observed for methane on graphite. Naturally, the more pronounced adsorption steps visible in Figure 43a correspond to additional discrete layer condensation. The thermodynamic values associated with these transitions were calculated based on the equations procedure introduced by Larher (Larher 1971). The details of how we employed this procedure have been described in our previous work (Strange 2016, Freitag 2000, Arnold 2005, Felty 2008, Arnold 2006, Cook 2015, Yaron 2006, Fernandez-Canoto 2014). The differential entropy and enthalpy and the heat of adsorption derived from the current study are given in Table 10. The thermodynamic values for the fifth and sixth layer formations are omitted because the steps are only visible over a narrow temperature range.

The thermodynamic results reported here agree reasonably well with those of TL. It is notable that the experimental results presented here cover a broader temperature range and employ a significantly larger number of data points than TL. We find that the "A" parameters for both the 2D gas to 2D liquid (i.e. G(2D) to L(2D)) and the L(2D) to CS(2D) (i.e. commensurate solid) are less than ten percent smaller than the TL values. However, the "B" parameters for
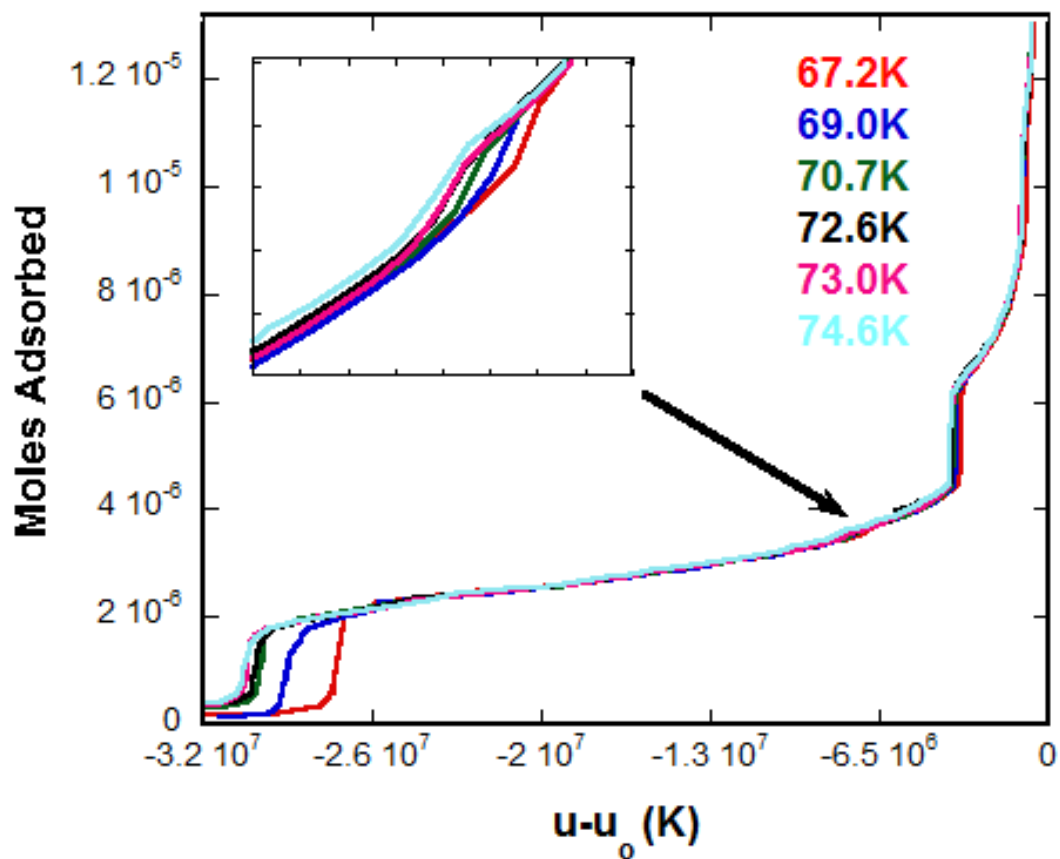
Figure 44 – Plot of moles adsorbed versus chemical potential for methane on hBN over the temperature range 77-88 K. The inset highlights the second substep located in between the monolayer and bilayer risers. This feature likely corresponds with the commensurate solid to incommensurate solid phase transition identified in the methane on graphite system.

Table 10 – Thermodynamic values for n-alkanes methane through octane on hBN calculated from volumetric adsorption isotherm measurements

| Alkane | (n) | A (kJ/mol) | B (J/mol K) | Q (kJ/mol) | ΔH (kJ/mol) | ΔS (J/mol K) |
|---|---|---|---|---|---|---|
| **Methane** | **1** | 1424.7±0.39 | 14.136±0.0052 | 11.8450±0.0032 | -1.9846±0.0105 | 28.6667±0.1478 |
| | **SS1** | 2064.5±0.42 | 24.248±0.0051 | 17.1642±0.0035 | -7.3038±0.0106 | -55.4045±0.1476 |
| | **SS2** | 1157.2±0.029 | 15.445±0.00039 | 9.6210±0.0002 | 0.2394±0.0100 | 17.7836±0.1414 |
| | **2** | 1189.5±0.0018 | 16.816±0.00003 | 9.8895±0.00002 | -0.0291±0.0100 | 6.3852±0.1434 |
| | **3** | 1176.1±0.0033 | 17.241±0.00005 | 9.7781±0.00003 | 0.0823±0.0100 | 2.8517±0.1413 |
| | **4** | 1172.8±0.004 | 17.328±0.00006 | 9.7507±0.00003 | 0.1097±0.0100 | 2.1284±0.1413 |
| | ∞ | 1186±1.2 | 17.584±0.017 | 9.8604±0.0100 | | |
| **Ethane** | **1** | 2463.7±0.43 | 15.984±0.003 | 20.4832±0.0036 | -3.2582±0.0106 | 18.3656±0.4995 |
| | **2** | 2078.6±0.023 | 17.752±0.0002 | 17.2813±0.0002 | -0.0565±0.010 | 3.6665±0.4988 |
| | **3** | 2058.9±0.023 | 17.975±0.0002 | 17.1177±0.0002 | 0.1073±0.010 | 1.8125±0.4988 |
| | ∞ | 2071.8±1.2 | 18.193±0.06 | 17.2249±0.0010 | | |
| **n-Propane** | **1** | 3156.4±0.29 | 16.576±0.0016 | 26.2423±0.0024 | -4.2709±0.0218 | 14.7241±0.1420 |
| | **2** | 2667.5±0.025 | 17.837±0.00017 | 22.1776±0.0002 | -0.2062±0.0216 | 4.2401±0.1413 |
| | **3** | 2596.6±0.021 | 17.895±0.00014 | 21.5881±0.0002 | 0.3833±0.0216 | 3.7579±0.1413 |
| | ∞ | 2642.7±2.6 | 18.347±0.017 | 21.9714±0.0216 | | |
| **n-Butane** | **1** | 3903.9±1.9 | 16.97±0.009 | 32.4570±0.01580 | -5.6668±0.0920 | 14.8987±0.5044 |
| | **2** | 3419.5±0.15 | 19.195±0.0087 | 28.4297±0.0012 | -1.6395±0.0910 | -3.6000±0.5041 |
| | **3** | 3154.2±1.4 | 18.14±0.009 | 26.2240±0.0116 | 0.5662±0.0914 | 5.1713±0.5044 |
| | ∞ | 3222.3±10.9 | 18.762±0.06 | 26.7902±0.0906 | | |
| **n-Pentane** | **1** | 4595.1±50 | 17.29±0.24 | 38.2037±0.4157 | -7.0627±0.4164 | 15.0567±2.000 |
| | **2** | 3841.1±25 | 18.851±0.12 | 31.9349±0.2079 | -0.7940±0.2092 | 2.0785±1.0044 |
| | **3** | 3546.5±99 | 17.865±0.52 | 29.4856±0.8231 | 1.6553±0.8234 | 10.2761±4.3248 |
| | ∞ | 3745.6±2.8 | 19.101±0.014 | 31.1409±0.0233 | | |
| **n-Hexane** | **1** | 5276.8±55 | 17.576±0.23 | 43.8713±0.4573 | -7.0860±0.4719 | 21.2090±1.9894 |
| | **2** | 4605.4±18 | 20.211±0.085 | 38.2893±0.1497 | -1.5040±0.1896 | -0.6984±0.8947 |
| | **3** | 4873.7±105 | 22.185±0.53 | 40.5199±0.8730 | -3.7346±0.8807 | -17.1102±4.4404 |
| | ∞ | 4424.5±14 | 20.127±0.066 | 36.7853±0.1164 | | |
| **n-Heptane** | **1** | 5551.3±88 | 16.505±0.34 | 46.1535±0.7316 | -6.0784±0.7359 | 29.8805±2.8453 |
| | **2** | 5030.9±26 | 20.256±0.54 | 41.8269±0.2162 | -1.7518±0.2301 | -1.3053±4.5013 |
| | **3** | 4995.5±113 | 20.685±0.54 | 41.5326±0.9394 | -1.4574±0.9428 | -4.8720±4.5013 |
| | ∞ | 4820.2±9.5 | 20.099±0.039 | 40.0751±0.0790 | | |
| **n-Octane** | **1** | 6295.8±102 | 17.269±0.38 | 52.3433±0.8480 | -8.1569±0.8503 | 26.9956±3.1685 |
| | **2** | 5549±46 | 20.657±0.17 | 46.1344±0.3824 | -1.9480±0.3874 | -1.17223±1.4338 |
| | ∞ | 5314.7±7.4 | 20.516±0.029 | 44.1864±0.0615 | | |

both transitions are approximately 25 percent greater than those of TL. We can determine the 2D triple point by making an extrapolation of the linear fit for the L(2D) - CS(2D) transition to the coexistence line for G(2D) - L(2D) (see Figure 45). Based on this extrapolation, we find the value of 64.22 K for the two-dimensional triple point. Both the TL and our triple point determination require extrapolations from the same coexistence curves, however, the current investigation employs a greater number of data points near the transition from which the linear fits were constructed as seen in Figure 45. Critical layering temperatures for methane on hBN are presented and discussed in a following section.

### Ethane – Octane on hBN Adsorption Isotherms

Given the similarities in structure between graphite and hBN, the results of previous structural and dynamical measurements for *n*-alkanes on graphite can serve as a useful guide for predicting the phases observed in the current set of adsorption experiments on boron nitride. The alkanes ethane through octane are grouped together because in these systems, the temperature ranges of our studies fall in a region where the monolayer phases that form are 2D liquids, in contrast with the monolayer solid formation observed for methane on hBN at lower temperatures. It is important to point out that while this group of hydrocarbons exhibits similar monolayer liquid phase behavior, the adsorption character differs significantly with increasing coverage. For example, the adsorption curves of ethane and propane on hBN increase smoothly toward

141
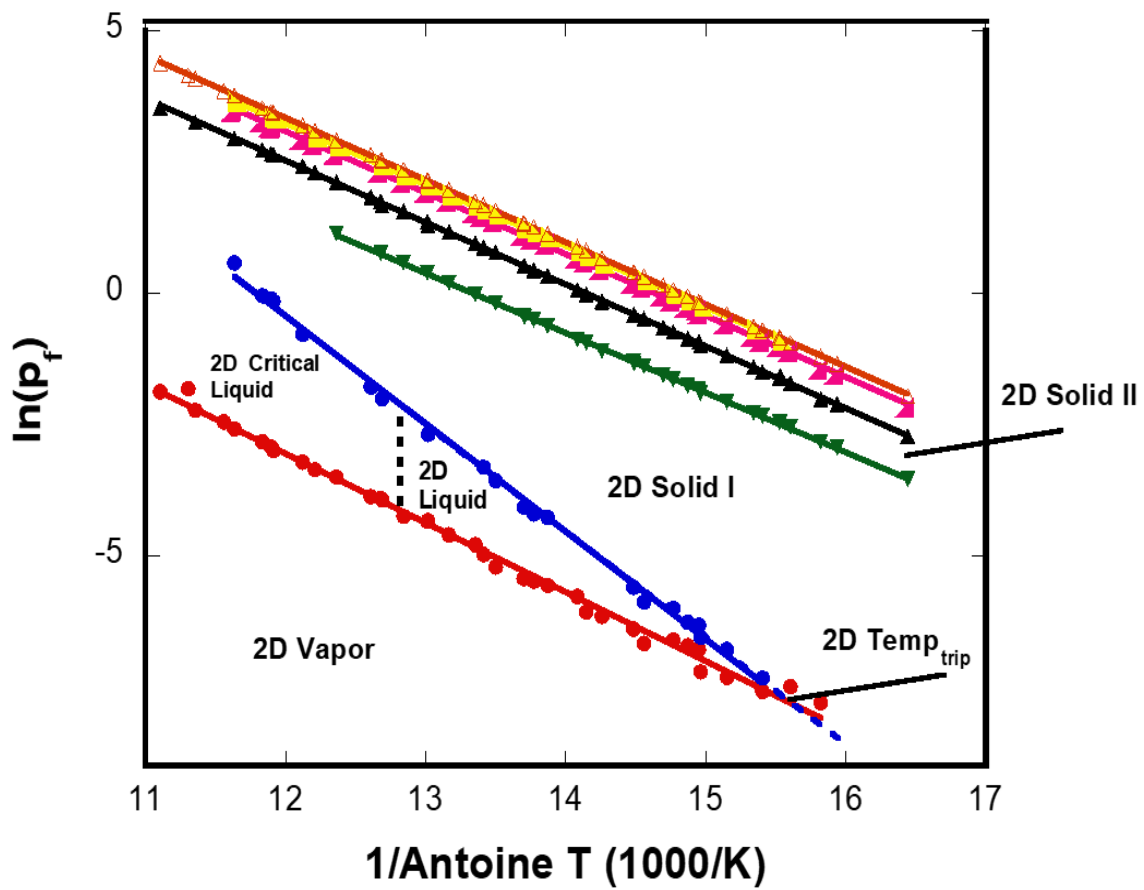
Figure 45 – Clausius-Clapeyron plot for methane adsorbed on hBN in the temperature range 60 - 90 K.

monolayer completion upon which they exhibit an abrupt, stepwise increase as the second layer begins to form (see Figure 41). In contrast, the adsorption curves for the longer alkanes butane through octane on hBN exhibit the same smooth increase toward monolayer completion but exhibit a more gradual bilayer riser (see Figure 42). Only at the lowest temperatures investigated do the adsorption curves for butane through octane exhibit a feature indicative of trilayer formation. The behavior of the numerical derivatives of the isotherm traces can be used to probe the microscopic status of the adsorbed layer. For example, the sharp, narrow derivative peaks associated with bilayer condensation of ethane and propane clearly suggests that the film is more stratified compared to the layering behavior observed for the longer alkanes on hBN (compare Figure 41 and Figure 42). Additional insight can be gained by considering earlier thermodynamic studies of ethane and propane films on graphite. It has been suggested that ethane exhibits an ordered liquid phase on graphite up to 95 K.

Migone *et al.* suggest that monolayer propane films have thermodynamic signatures consistent with an ordered fluid phase. Thus, it is quite possible that the abrupt stepwise increase in adsorption curves upon bilayer formation observed here for ethane and propane signals the formation of an ordered (second layer) fluid. There is no indication from previous work for butane through octane on graphite that an ordered fluid phase appears upon monolayer melting. Additional insight into the microscopic behavior for these multilayer adsorption systems can be obtained using MD simulations. The results of our MD

investigations will be discussed in the next section. In addition, these thermodynamic results when combined with diffraction studies of the alkane films performed in the same temperature ranges examined here could be quite valuable for elucidating the microscopic behavior.

The thermodynamic values for ethane through octane on hBN calculated from the adsorption isotherm measurements are summarized in Table 10. To our knowledge, no other thermodynamic values have been published for the adsorption *n*-alkanes on hBN, however, we can compare these values to a few results for alkanes on the basal plane of graphite. Gay, Suzanne, and Wang (GSW) performed a series of low energy electron diffraction measurements for ethane on graphite from 64 - 144 K. Based upon their LEED measurements, it is highly likely that our set of data for ethane on hBN exhibits monolayer and multilayer liquid phases. The results of GSW indicate that monolayer ethane on graphite binds 16% stronger than on hBN. This is consistent with our recent results for the adsorption of pentane and hexane on graphite (Larese 2018). However, the alkanes on hBN exhibit stronger binding in comparison with adsorption on MgO(100). It is clear from the comparison of adsorption of alkanes on graphite with hBN and MgO(100) that the presence of an electrostatic potential does not lead to a stronger MS interaction. This fact is not too surprising given the small magnitude of the static polarizability for *n*-alkanes (Williams 2004). The trend in heat of adsorption appears fairly linear over the range of alkanes measured (Figure 46). The second layer and bulk heats of adsorption
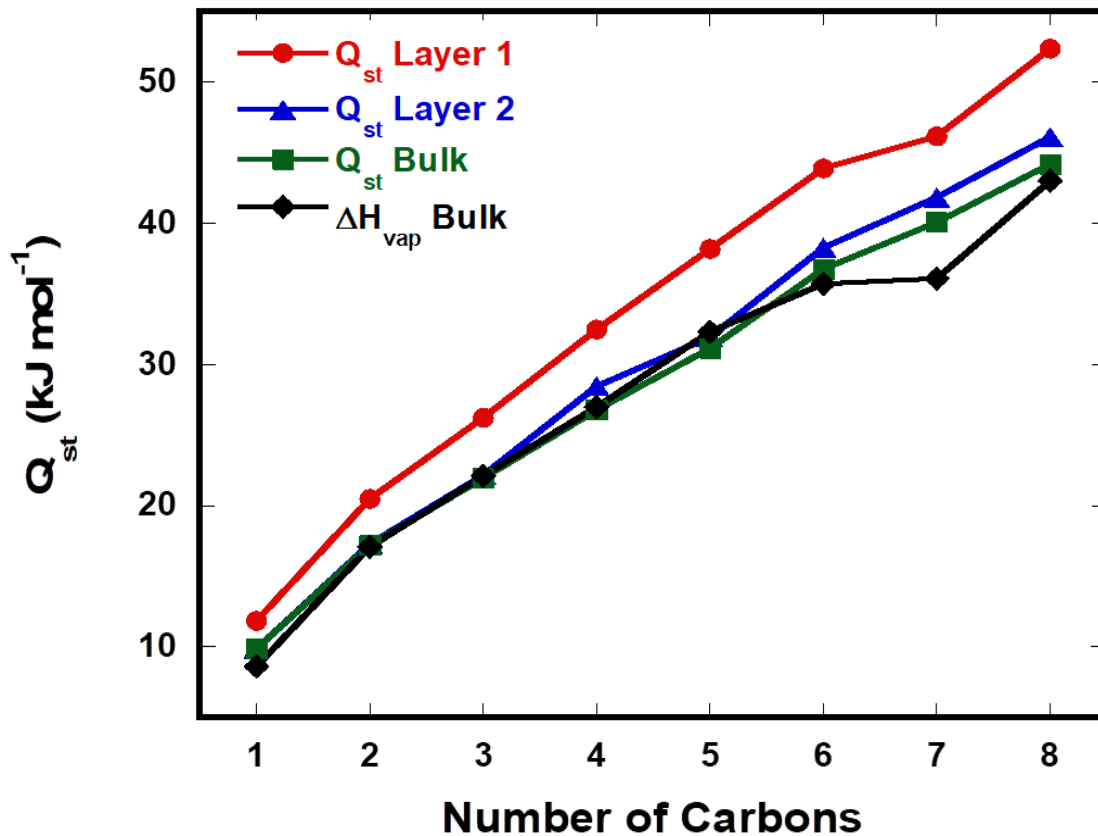
Figure 46 – Trend in carbon chain length of the heats of adsorption ($Q_{st}$) for the

first (red circles) and second (blue triangles) layering transitions in addition to the

heats of adsorption for the bulk phase (i.e. heat of vaporization) from the

experimental measurements (green squares). The heats of vaporization from

NIST are provided (black diamonds) for comparison. Error bars are present

behind the markers

show a slight alternation with increasing numbers of carbons suggesting

evidence of an odd-even effect. Surprisingly this odd-even behavior is not

observed in the monolayers. It is also apparent that the general shape of the

trend follows that of heats of adsorption for bulk alkanes in the literature, though

the monolayers require increasingly greater amounts of energy to move a

molecule away from the surface than their bulk counterpart.

Critical temperatures associated with layer condensation for the alkanes

on hBN were determined by applying a method used previously by Hess and

Nham (Nham 1988). This approach is based on the procedure developed by

Larher (Larher 1979) where a plot of the inverse slope of the riser from

adsorption measurements versus temperature was used to determine the critical

exponent for argon on cadmium chloride. Chan *et al.* (Kim 1984) have shown

that above the critical temperature the two-dimensional compressibility, $K_T$ can

be described using,

$$K_T^{-1} \propto \left(\frac{T-T_c}{T_c}\right)^{\gamma} \quad (37)$$

The two-dimensional compressibility has been shown to be related to the width of

the adsorption step by,

$$\Delta\mu_{HWHM} = \frac{\Delta n}{\left(\frac{\partial n}{\partial \mu}\right)_T} = \left(\frac{4}{\Delta n}\right) K_T^{-1} \quad (38)$$

The widths of the adsorption steps were evaluated by fitting a Gaussian function

to the numerical derivative of the data, plotted as moles adsorbed (n) versus

difference in chemical potential ($\Delta\mu$). Thus, if $\gamma$ is assumed to be equal to 7/4 based on the universality class of the two-dimensional Ising model it can be shown that,

$$\Delta\mu_{HWHM} = \Gamma(n)[(T - T_c)/T_c]^\gamma \quad (39)$$

The critical temperatures can be extracted from adsorption measurements by observing the behavior of $\Delta\mu_{HWHM}^{4/7}$ versus temperature. Above the triple point, equation 39 should yield a linear relationship between step width and temperature. The intersection of the linear fit in the high temperature regime with a fit to the low temperature data yields an approximate location for the layer critical temperatures. The locations for the critical phase transitions (provided in Table 11) can be determined more precisely using heat capacity measurements which have been shown to be less sensitive to surface heterogeneity and impurities. An example of this approach is applied in Figure 47. Larher and Gilquin have determined the critical temperatures for rare gas adsorption on the basal plane of graphite and made comparisons to the adsorption on lamellar halides. They determined that the reduced critical values ($T_c^{2D}/T_c^{3D}$) for a system with relatively small corrugations in the surface potential (i.e. Ar on graphite) are near 0.4. Reduced critical values determined from rare gases on lamellar halides were determined to be as great as 0.55. We find values in the range of 0.39 to 0.46, which suggests the alkanes exhibit a relatively smooth liquid-vapor equilibrium on the surface of hBN.

147

Table 11 – Experimentally determined critical temperatures for layer condensation of methane through heptane on hBN. Results for octane are absent because the range of temperatures for the adsorption measurements exceeded the predicted critical temperature.

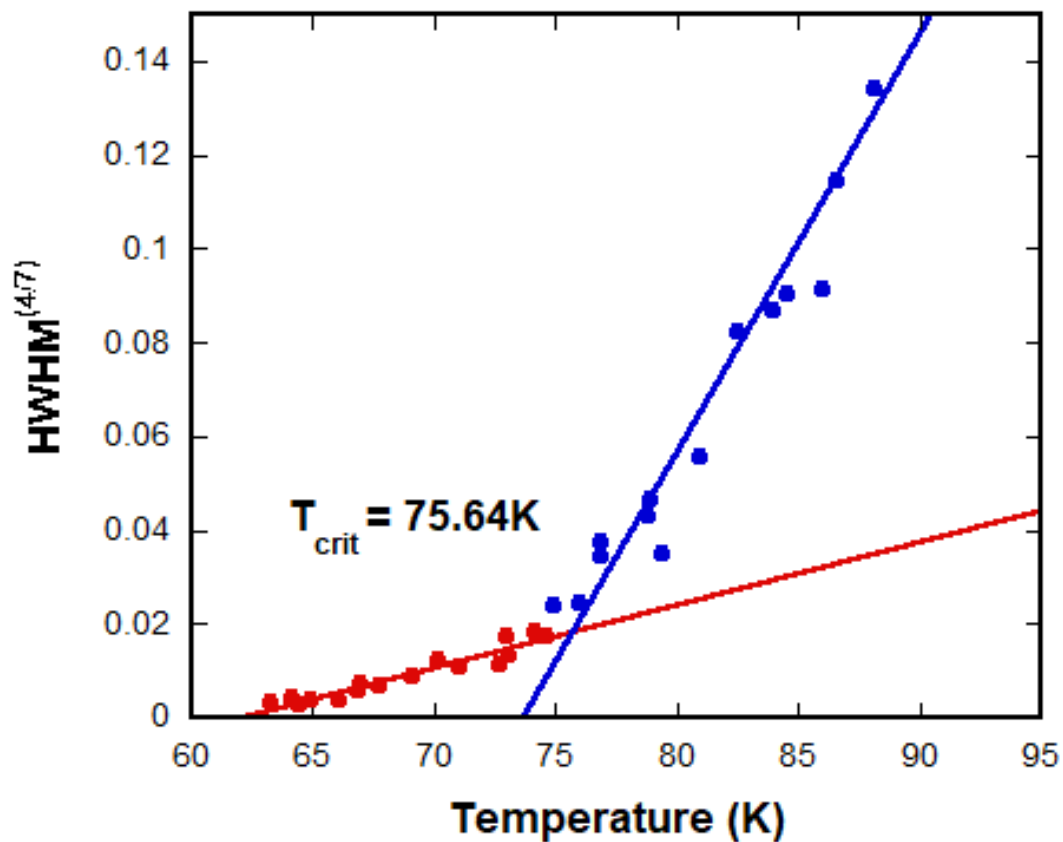| Alkane | Layer 1 (K) | L1 $T_c^{2D}/T_c^{3D}$ | Layer 2 (K) | Layer 3 (K) | Layer 4 (K) |
|---|---|---|---|---|---|
| Methane | 75.64 | 0.3969 | 78.28 | - | - |
| Ethane | 129.02 | 0.4226 | 127.50 | 116.22 | - |
| *n*-Propane | 155.54 | 0.4205 | 148.97 | 145.99 | - |
| *n*-Butane | 193.19 | 0.4546 | 179.23 | - | - |
| *n*-Pentane | 214.01 | 0.4555 | 199.29 | - | - |
| *n*-Hexane | 222.16 | 0.4377 | 197.88 | - | - |
| *n*-Heptane | 236.43 | 0.4378 | - | - | - |

Figure 47 – Plot of the half-width at half-maximum (HWHM) to the (4/7)th power for monolayer methane on hBN. The intersection of the two linear fits reveals the critical temperature for the first layer of methane on hBN. The fits for the remaining alkanes can be found in the Appendix.

### *Minimum Energy Configurations*

The first step in the characterization of the interaction of the alkanes on

hBN involves calculating the minimum energy configuration for a single molecule.

The purpose is to obtain information on how the molecule-surface (MS)

interaction evolves as a function of the chain length and those effects on the

molecules configuration as a function of the binding energy. Although the isolated

molecule study doesn't take into account the MM contribution to the overall

binding energy it nonetheless provides valuable insight into the preferred

adsorption sites and lowest energy molecular orientations of the alkane on the

hBN surface. Figure 48 highlights the adsorbed structures of molecular

configurations with the lowest energies for the alkanes adsorbed on hBN with

corresponding total energies provided in Table 12. For all the *n*-alkanes

measured in this study, the most stable configuration is when both the molecular

plane and backbone are parallel to the surface, i.e. where there are the greatest

number of contact points between the alkane and substrate. The six-fold

symmetry of the honeycomb-shaped surface results in three equivalent sub-

lattices differing by 120 degrees. The preferred orientation of the long axis is

along the <10> direction or either of the two symmetry equivalent directions.

Careful inspection of Figure 48 shows that the carbon and hydrogen atoms tend

to share the position above the hexagonal lattice hole. This particular adsorption

site represents a region where the electrostatic potential results from the

contribution of the partially negative nitrogen and partially positive boron. When

150
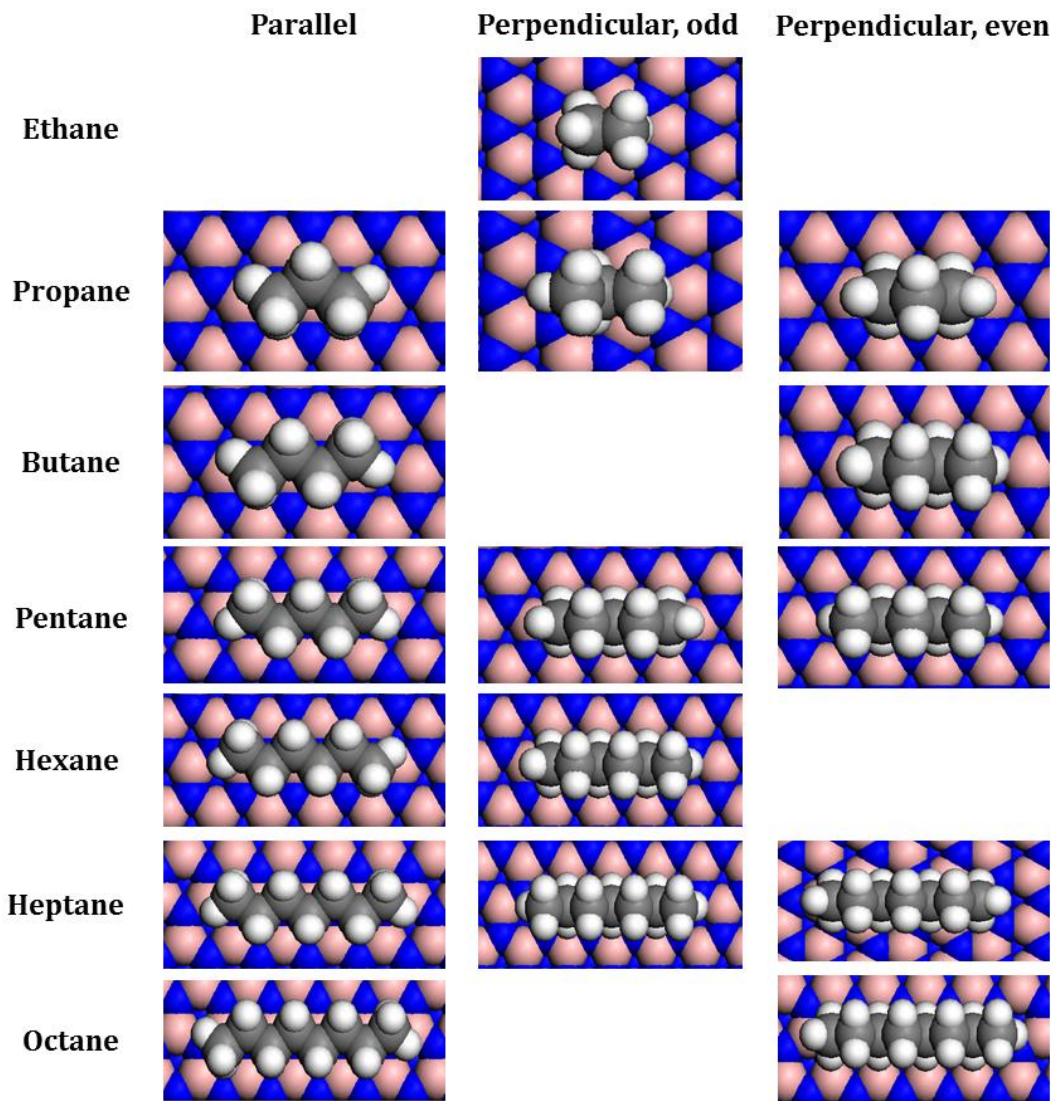
Figure 48 – Minimum energy configurations calculated for *n*-alkanes on hBN using the Universal Forcefield. The first column represents the minimum energy configurations for an alkane with the molecular plane parallel to the surface of hBN. The second and third columns represent the minimum energy structure for an alkane with the molecular plane perpendicular to the surface with odd and even numbers of carbons closest to the surface respectively

151

Table 12 – Calculated energy values for minimum energy configurations of single

molecules on the surface of hBN

| Alkane | Surface Orientation | Parallel Energy (kcal/mol) | Perpendicular – odd Energy (kcal/mol) | Perpendicular – even Energy (kcal/mol |
|---|---|---|---|---|
| Ethane | <10> | N/A | -7.9947140 | N/A |
| *n*-Propane | <10> | -10.254057 | -8.4596360 | -9.7693720 |
| *n*-Butane | <10> | -12.726140 | N/A | -11.100066 |
| *n*-Pentane | <10> | -15.266144 | -14.020718 | -12.213764 |
| *n*-Hexane | <10> | -17.795932 | -15.314118 | N/A |
| *n*-Heptane | <10> | -20.348575 | -18.332241 | -16.534104 |
| *n*-Octane | <10> | -22.883222 | N/A | -19.620060 |

an alkane resides in this arrangement, the molecule is slightly compressed similar to an accordion and undergoes a carbon-carbon bond angle decrease of two-percent when compared with the isolated ground-state molecule. This perturbation of the alkane geometry accounts for a seven percent difference between the energy from non-bonded interactions and the total energy.

There are different aspects that the presence of orientational states can introduce in film growth. While the above single molecule calculations suggest weaker binding for the perpendicular states, in a 2D film the perpendicular orientation allows for a greater packing fraction by reducing the area projected on the surface and simultaneously increasing the number of contact points between adjacent alkanes. This feature could play a significant role in layer growth especially during the onset of bilayer formation. Furthermore, work by Larese *et al.* has suggested that melting of hydrocarbons (i.e. the onset to translational diffusion) involves the reduction of the area projected on the surface by molecular reorientation.

The results of the present study indicate that the difference in energies between the molecules plane oriented parallel and perpendicular to the hBN surface gradually increase from propane through octane. Additionally, for alkanes where the perpendicular state has both an odd and even configuration, the relative difference in energies between these orientations remains constant with increasing carbon number. This should not be too surprising because the interaction is additive and there is always a difference of one carbon between the

binding energies of these two states. As the chain length increases, this constant

difference in energy becomes a smaller fraction of the total energy, thereby

reducing the surface contribution to the odd-even effect for longer alkanes. This

particular series of *n*-alkanes is ideal for illustrating this behavior because

published results for bulk alkanes show that as the chain length becomes

significantly great, the odd-even effect becomes increasingly more important and

the molecular interaction is defined by an average along the carbon backbone.

### *Molecular Dynamics Simulations*

The results of previous studies have suggested interesting behavior when

the molecule-surface interaction is greater than the molecule-molecule

interaction. It is important to note that the melting temperature of monolayer

hydrocarbon films physisorbed on most substrates is lower than that of the bulk

material. This idea is perhaps not too surprising given the reduced coordination

of molecules in the 2D phase. However, when the coverage is increased well

beyond the monolayer regime, the melting temperature of the solid layer closest

to the surface has been found to increase substantially, in certain cases above

the bulk. In fact (Arnold 2012), when layers are added, the near surface layer can

be stabilized to temperatures nearly 1.25 times the bulk triple point temperature!

The results of our MD simulations concur with these experimental observations.

The molecular trajectories generated by the MD simulations have been shown in

the past to accurately represent the microscopic behavior of alkanes adsorbed

on substrates (Strange 2016, Fernandez-Canoto 2014). The results discussed

154

below are representative of the behavior for the three types of adsorbate geometry discussed previously (i.e. quasi-spherical, cigar, and rod-like).

In this portion of the investigation, concentration profiles (C(z)) perpendicular to the substrate plane (**ab** plane) were generated to examine the molecular distribution within the adsorbed film. Particular attention was given to the behavior of fluid-like multilayers on the layer nearest to the substrate. The molecular concentrations can be separated into their atomic components (i.e. individual C and H distributions). To facilitate the calculation of C(z), the volume of the simulation box in the c-direction is divided into 5000 equivalent slabs/bins. C(z) for a particular atom in one of these bins can be determined from the atomic fraction (atoms in bin/total atoms) multiplied times the total volume (total number of bins). When averaged over the total simulation time, the C(z) becomes a probability density function where the probability of finding atom *i* at position *z* is determined by the surface normal vector. The basal plane of hBN was chosen as the zero reference. Figure 49, Figure 50, and Figure 51 show C(z) corresponding with the isotherms shown above (i.e. methane, propane, and octane on hBN; Figure 40, Figure 41, and Figure 42 respectively). The C(z) for ethane on hBN is shown in Figure 52 because it reveals interesting re-orientation behavior. Coverages of the C(z) were limited to three layers since adsorption measurements indicated the formation of only two or three layers for alkanes greater than ethane.

155

Figure 49 – Molecular concentration profiles calculated from MD trajectories for nominal trilayer coverage methane on hBN. The temperature range is as follows: 1 K (red), 30 K (blue), 60 K (green), 90 K (black), 140 K (magenta), and 200 K (purple). The temperature reduced by the 3D bulk triple point temperature is provided for reference to other systems.

Figure 50 – Molecular concentration profiles calculated from MD trajectories for nominal trilayer coverage propane on hBN. The temperature range is as follows: 10 K (red), 30 K (blue), 60 K (green), 90 K (black), 140 K (magenta), and 200 K (purple). The reduced temperature scaled to the bulk triple point is provided for reference to other systems
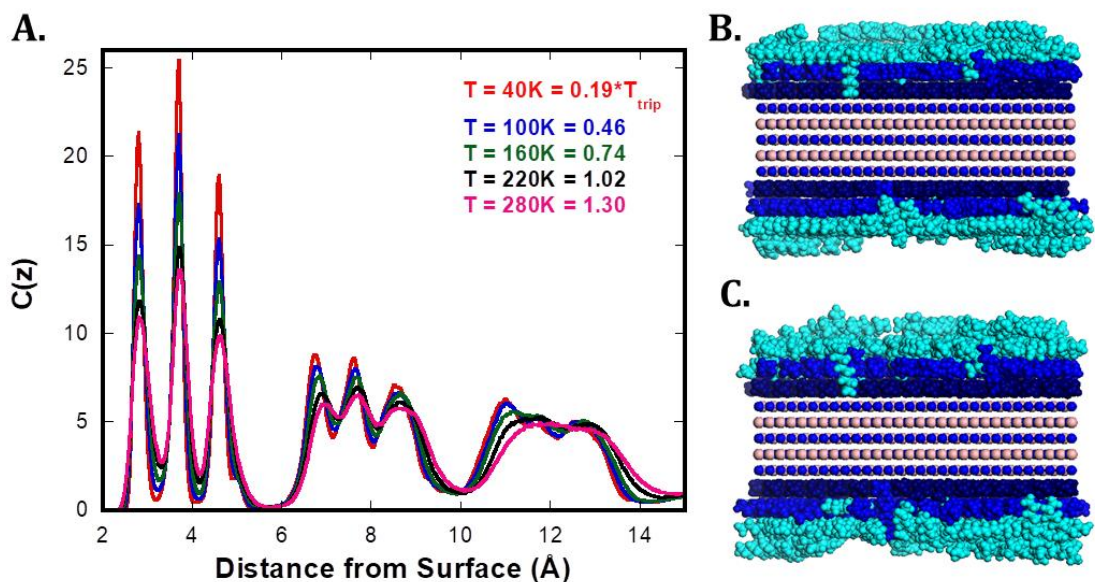
Figure 51 – A. Molecular C(z) calculated for nominal trilayer coverage octane on hBN. The temperature range is as follows: 40 K (red), 100 K (blue), 160 K (green), 220 K (black), and 280 K (magenta). The temperatures reduced by the 3D bulk triple point temperature is provided for reference to other systems. The interlayer motions of octane molecules are illustrated at (b.) 40 K and (c.) 280 K. In these figures, the molecules in each layer were highlighted at the beginning of the simulation and the final frames are provided in (b.) and (c.).
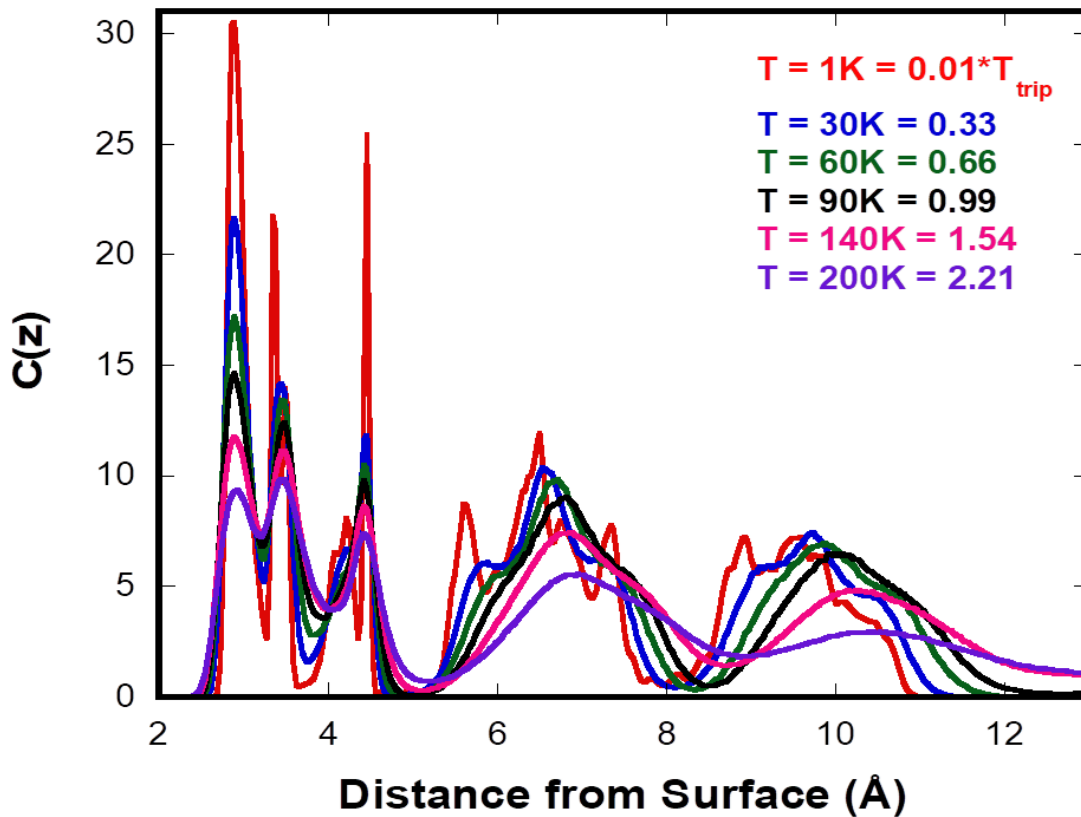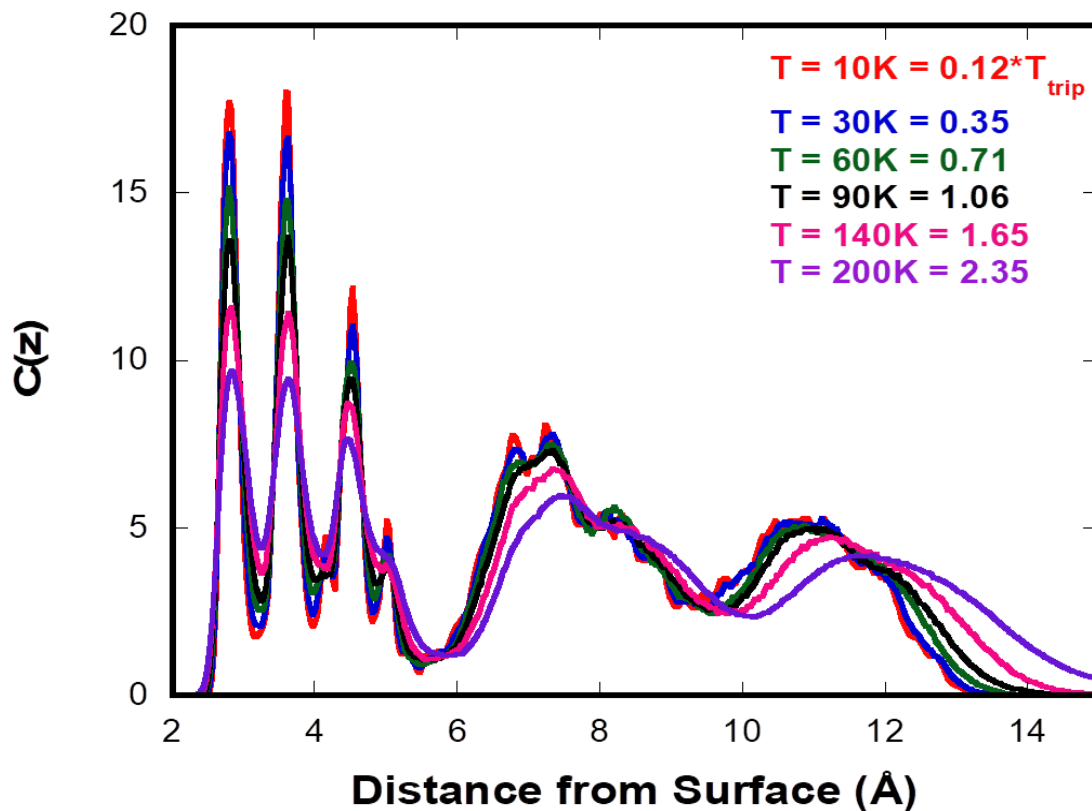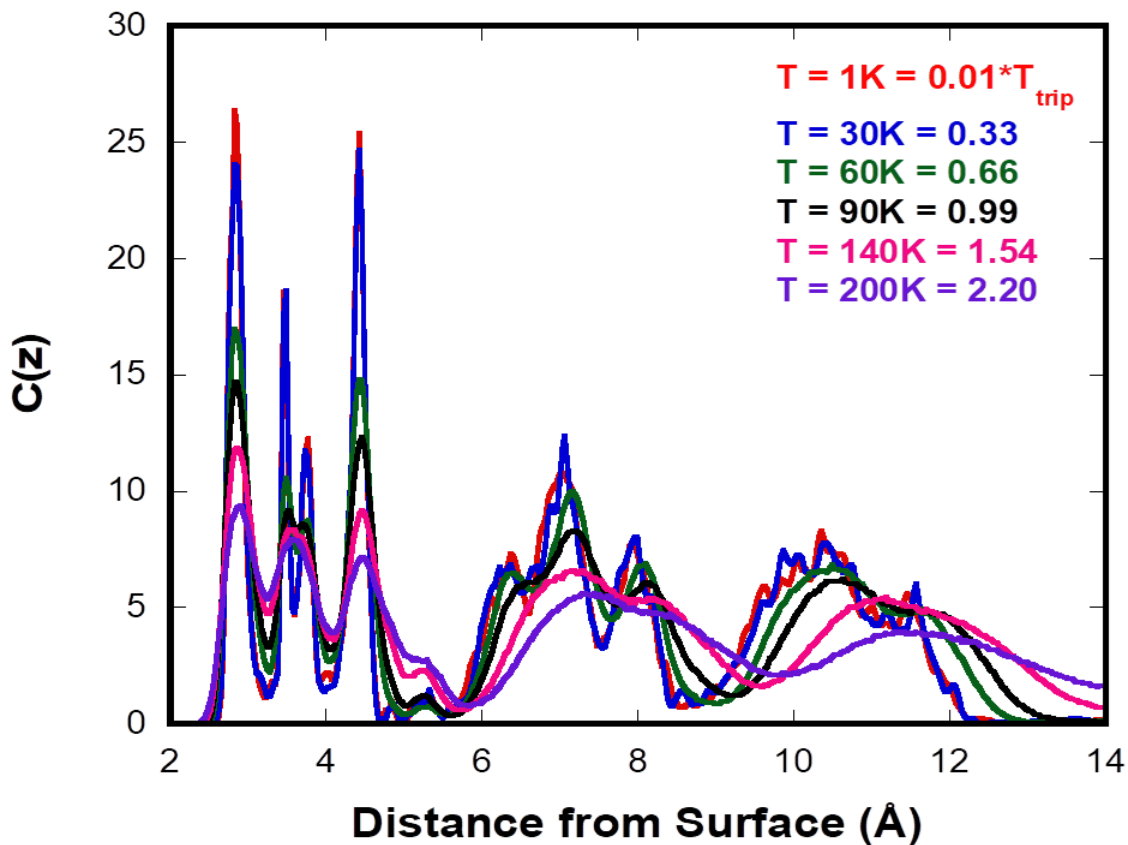
Figure 52 – Molecular concentration profiles calculated from MD trajectories for
nominal trilayer coverage ethane on hBN. The temperature range is as follows:
40 K (red), 100 K (blue), 160 K (green), 220 K (black), and 280 K (magenta). The
reduced temperature scaled to the bulk triple point is provided for reference to
other systems.

The C(z) are a valuable tool for investigating multilayer behaviors of these systems in numerous ways. The locations of the hydrogen atoms reveal information about rotational/re-orientational motion since they reside on the exterior of the molecule (i.e. behave similar to a lever arm). Next, the locations of the carbon atoms (which form the molecular backbone of *n*-alkanes) serve as an accurate indicator for the molecular centers of mass. Examination of the average position and breadth of the carbon peaks is a valuable avenue for identifying the degree of film stratification as well as quantifying the relative populations of orientational states (e.g. parallel vs. perpendicular) and can reveal the presence of chain defects (gauche conformers). By combining the C(z) data with the mean-square displacement (MSD) and the pair distribution function (PDF) analysis in a future publication, a more comprehensive understanding of the microscopic behavior of alkane adsorption on hBN is attainable.

*Methane*

The C(z) for trilayer coverage methane on hBN are provided in Figure Figure 49. Figure 53a and Figure 53b illustrate the individual atomic concentration profiles of methane for carbon and hydrogen atoms. The mean centers of mass for methane appear to remain constant in the first layer over the entire temperature range studied as indicated in Figure 53a. The average distribution of methane is wider (i.e. much less confined) in the multilayers where the carbon peaks exhibit significant broadening with an increase in temperature. The hydrogen atom distributions in Figure 53b suggest that the

160

Figure 53 – Atomic concentration profiles for (a.) carbon and (b.) hydrogen calculated from MD trajectories for nominal trilayer coverage methane on hBN. The temperature range is as follows: 1 K (red), 30 K (blue), 60 K (green), 90 K (black), 140 K (magenta), and 200 K (purple). The reduced temperature scaled to the bulk triple point is provided for reference to other systems.
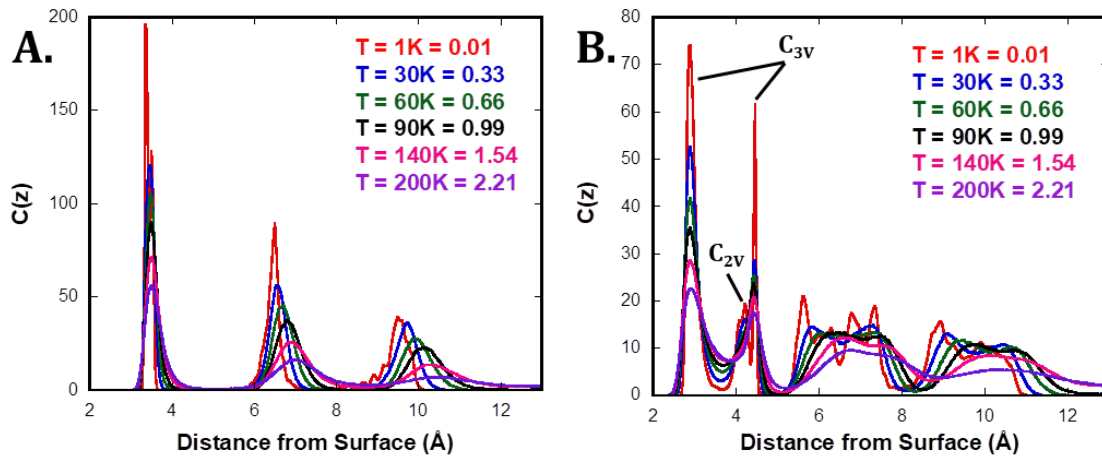
predominant structure of methane molecules in the layer nearest to the surface is one where the molecule has $C_{3V}$ point-group symmetry with respect to the surface. The shouldering peak at ~4.1 Å illustrates that only a small population of methane molecules exhibit an orientation with $C_{2V}$ symmetry. Additionally, the increase in the baseline near 3.75 Å indicates onset of rotational motion in the layer nearest the surface at low temperatures (~30 K). It is worth noting that these hydrogen peaks remain resolved even at high temperatures suggesting re-orientational motions between $C_{3V}$ and $C_{2V}$ oriented methane molecules. The rotational abilities of the molecules in the layer nearest to the surface support the conclusion that greater molecular size enhances the stabilization effect. However, interlayer translation for methane molecules in the first layer remains restricted even at the highest temperatures. The observed behavior of methane molecules in the multilayers is drastically different than that of molecules in the first layer. For most of the temperatures studied, the multilayer molecules have nearly free rotation as indicated by the smooth peaks representing the second and third layers, though interlayer traffic between the second and third layers isn't observed until approximately 1.5 times the bulk triple point.

*Ethane*

The C(z) for trilayer coverage ethane on hBN reveals interesting behavior as well. In the layer closest to the surface, most of the ethane molecules lay with their carbon-carbon bond roughly parallel to the surface. There are only a few ethane molecules were the molecular axis is oriented perpendicular. As the

temperature of the system is increased, the population of ethane molecules orthogonal to the surface becomes greater as identified by the peak at ~5.2 Å such that the area projected on the surface is reduced and the total energy is minimized. This supports experimental measurements for ethane on graphite that suggest there are multiple solid phases prior to melting (Gay 1986). Additionally, Larese and coworkers (Larese 1988(2)) observed this behavior for ethylene on graphite. This is intriguing since the first layer is confined by both the substrate and multilayers. Similar to that observed for methane, the multilayer ethane molecules exhibit nearly free rotation and strong interlayer motions at higher temperatures.

*Propane*

The $C(z)$ for trilayer coverage propane on hBN is shown in Figure 50. This molecular system is unique since the molecules in the layer nearest to the surface appear frustrated between parallel and perpendicular states (see Figure 54). Typically, the perpendicular state in the first layer is restricted by the presence of multilayers. The perpendicular states show up in the $C(z)$ at 4.1 and 5.0 Å and are observable even at the highest temperatures simulated. Translational motion between the second and third layers is prominent even at the lowest temperatures simulated. The widths of the multilayer peaks also indicate nearly free rotation at temperatures near the bulk triple point. Though it is weak, propane on hBN is the first system in this series of alkanes to exhibit behavior that suggests fluid multilayers stabilize the layer nearest to the surface.
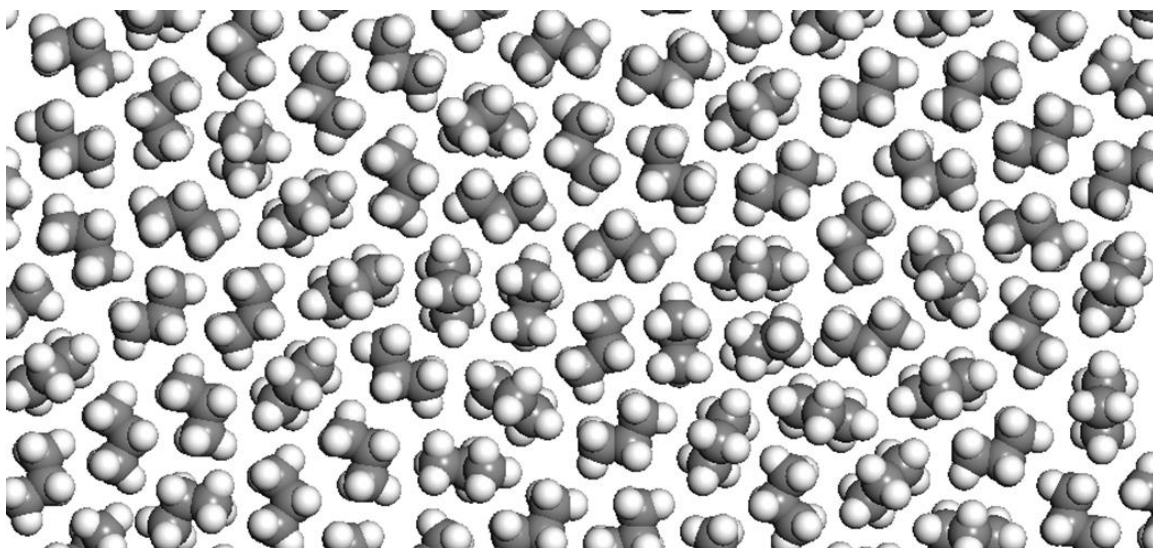
Figure 54 – Propane molecules in the layer nearest to the surface at 1 K at

trilayer coverage.

*Octane*

Figure 51a shows the C(z) for octane on hBN at a coverage of nominally three layers thick. The first layer is highly stratified in comparison with the second and third layers. The distribution in between these layers also reveals that there is essentially no interlayer traffic from the first layer to the multilayers. Between the second and third layers, the distribution is non-zero even at the lowest temperatures. Increased peak widths in the multilayers relative to the layer nearest to the surface indicates that the octane molecules have the ability to reorient. Thus, the multilayers exhibit behavior more similar to bulk octane. It is also interesting that the octane multilayers retain partial molecular order even at the highest temperatures. In the smaller alkanes, the multilayers lose order at lower temperatures.

The C(z) for layers nearest to the surface in octane on hBN are provided in Figure 55. At monolayer coverages, the C(z) reveal that octane possesses a measurable quantity of alkanes in the perpendicular state as identified by the peak at 5.0 Å and the increased intensity in the peak near 2.8 Å which correspond to the position of hydrogen atoms in a perpendicular orientation relative to the surface. Comparatively, when the coverage is near three layers, the perpendicular states appear to be minimized by the presence of multilayers (see Figure 55 b). At both coverages, it is clear that the potential from the substrate hinders the possibility of rotational/re-orientational motions as the individual contributions to the C(z) from carbon and hydrogen atoms remain

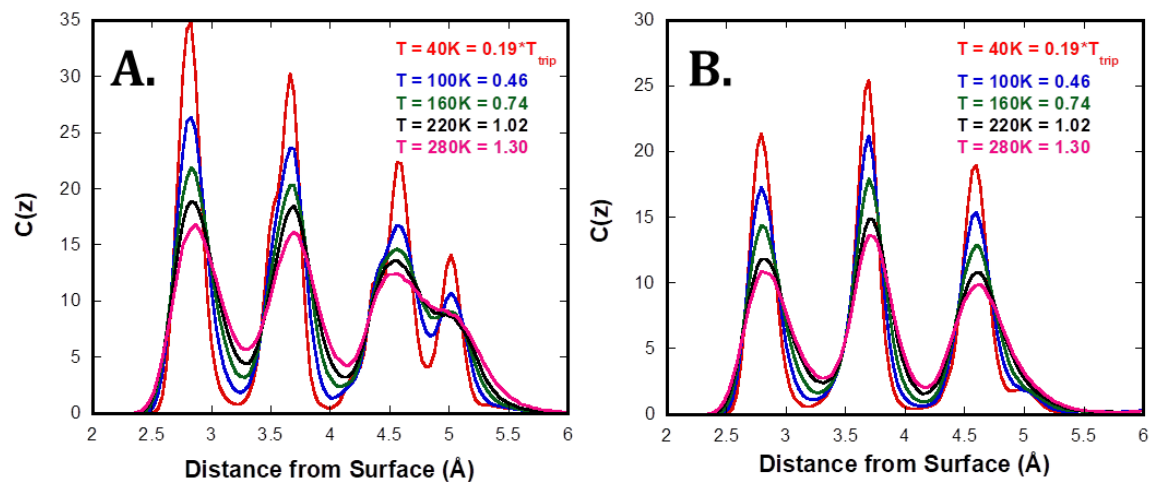Figure 55 – Molecular C(z) for the layer nearest to the surface for monolayer (a.) and trilayer (b.) coverage octane on hBN. The temperature range is as follows: 40 K (red), 100 K (blue), 160 K (green), 220 K (black), and 280 K (magenta). The reduced temperature scaled to the bulk triple point is provided for reference to other systems.

resolved even at higher temperatures. The depths of the wells in between the peaks also suggest that the motions of octane molecules are more restricted and hence stabilized by the effective pressure from fluid multilayers. When this feature is compared with the C(z) from smaller alkanes, it is apparent that the increase in molecular size/length enhances the stabilization of the layer nearest to the surface.

## Conclusion

Adsorption properties for the normal alkanes methane through octane on hexagonal boron nitride were examined using volumetric adsorption isotherm measurements in the vicinity and above their bulk triple points. Methane was the only molecule which formed a solid in the adsorbed phase as determined from earlier diffraction studies. In addition, the adsorption isotherm for methane exhibited five steps over much of experimental temperature range corresponding with the formation of discrete adsorbed layers. Ethane and propane displayed three distinct stepwise features, while for the remaining alkanes, a third layer was measured, but much more subtle in appearance. The APMs for each of the alkanes were calculated using a methane isotherm as a fiducial. A near linear increase in APM was observed as expected. The thermodynamics of adsorption were calculated using a variation of the Clausius-Clapeyron equation. The calculated heats of adsorption as a function of alkane chain length increase linearly. However, the second and third layers exhibit an odd-even oscillatory

behavior not observed in the first layer. Additionally, the trend in the heat of adsorption for the first layer is similar to that observed in the bulk enthalpy of vaporization with an anomaly at heptane. The critical phase transitions for each of the layers were located using a plot of the change in inverse compressibility with increasing temperature. Molecular dynamics simulations were also performed in order to provide microscopic details about the layering behavior with increasing chain length. It was shown how smaller alkanes can exhibit rotational motions in the layers nearest to the surface even at coverages of three equivalent monolayers. The larger alkanes display much less layer stratification at higher coverages compared with smaller alkanes. However, as a result of the enhanced attraction to the substrate for larger alkanes, these multilayers tend to stabilize the layer nearest to the surface to temperatures near 25 percent above the bulk triple point. Future scattering experiments aim to provide additional microscopic insight into this phenomenon. Structural and dynamical quantities obtained from the MD simulations have been calculated and will be presented in a future publication.

# CHAPTER FIVE – ADSORPTION OF PENTANE AND HEXANE THIN FILMS ON THE SURFACE OF GRAPHITE(0001)

Authors: Nicholas Strange, J.Z. Larese

*(pre-print)*

## Abstract

The thermodynamics of adsorption were obtained for *n*-pentane and *n*-hexane adsorbed on the basal plane of graphite in the temperature ranges 190-235 K and 230-280 K respectively using high-resolution volumetric adsorption isotherms. These molecules exhibit a vdW interaction with the surface of graphite and yield and overall greater binding than on boron nitride and MgO(100). The areas per molecule calculated for the fluid monolayer phases were determined to be 52.03 and 61.35 $Å^2$ for pentane and hexane respectively. These values are in agreement with previous diffraction measurements performed for the monolayer solid. MD calculations were performed in order to provide additional microscopic insight. The MD simulations revealed that the stabilization of the layer nearest to the surface by fluid multilayer takes place, however, it is less effective than observed for adsorption on boron nitride and MgO.

## Introduction

Surface adsorption is important in a variety of industrial and technological processes. As a result, there is a growing need for advancing the current understanding of fundamental interactions that govern these types of processes. One approach utilizes volumetric adsorption isotherm measurements in order to determine the thermodynamic quantities of a film-substrate interaction. The results of these measurements provide a useful guide for complimentary atomic-scale investigations using neutron/x-ray scattering and diffraction techniques. Using this multi-faceted approach, a comprehensive understanding of roles played by both the adsorbate and adsorbent in physisorption can be obtained. The current study focuses on the interaction between the normal-alkanes pentane and hexane on the basal plane of graphite (0001). A series of adsorption isotherm measurements have been performed over a temperature range of 30 K, where the differential thermodynamics were calculated for each layer. Classical molecular dynamics (MD) simulations were performed to enhance our understanding of the multilayer growth mechanism observed in the adsorption isotherms.

Graphite is an ideal material to use as a substrate in this study because of its simple layered hexagonal structure and bonding network combined with its prominence in the electronics industry (Park 2012). Graphite has also drawn interest from industry since it has been shown to be useful as a catalyst support (Coq 1995, Otsuka 2004) Graphite in its natural form is defined as a semi-metal

171

due to aromaticity resulting from delocalized pi-bonding. However, graphite's electrical properties and surface reactivity can be easily tuned by surface functionalization. Many of the approaches used in functionalizing graphite rely on a fundamental understanding of the surface and how it reacts with a variety of small molecules. The *n*-alkanes pentane and hexane are two simple chain molecules where characterizing their interaction with graphite could be useful. Fundamentally, pentane and hexane are the smallest molecules in the homologous series of linear alkanes to exhibit observable conformational changes. From an industrial perspective, pentane and hexane represent two of the most commonly used solvents in synthesis with production exceeding 1 million pounds in the United States alone. These two alkanes are also commonly used as fuels and fuel additives. Independently, pentane is used as a blowing agent in forming polymer foams. Hexane is commonly found in textile solvents, furniture varnishes, and adhesives. Furthermore, ring-opening reactions which can be catalyzed on a support are important reactions in industry.

Previous experiments involving pentane and hexane adsorbed on graphite include results from calorimetry (Castro 1998), ellipsometry (Krutchen 2005), neutron diffraction (Castro 1998, Krutchen 2005, Arnold 2002) and molecular dynamics (Wexler 2009, Hansen 1993). It was found that a solid monolayer of pentane melts at approximately the same temperature as its bulk phase. This was in contrast with behavior observed for other alkanes on graphite, where the monolayer melting temperature exceeded the bulk melting temperature. The

172

structure of the solid monolayer was determined to be centered rectangular which is consistent with the other odd-numbered members of the homologous series. However, the hexane monolayer solid was determined to exhibit a herringbone rectangular structure which is characteristic of the even-numbered linear alkanes. The MD and ellipsometry measurements revealed that the solid monolayer melts by reducing the areal density by re-orienting and decreasing the area projected on the surface. The current set of results in this study aim to complement previous measurements by providing a set of high-resolution thermodynamic data outside the temperature ranges previously investigated. Additionally, the results from this investigation can used to determine the influence of the substrate on the adsorption behavior. Larese *et al.* have performed a comprehensive study of pentane on MgO(100) using volumetric adsorption isotherm measurements combined with neutron diffraction and molecular dynamics simulations. Adsorption measurements for pentane and hexane on hexagonal boron nitride have also recently been completed and provide a unique opportunity to compare two substrates with similar structure (and symmetry), but with different chemical composition.

The work described below is centered on the interaction of *n*-pentane and hexane with graphite using high-resolution volumetric adsorption isotherms combined with molecular dynamics simulations. Isotherm measurements were performed for pentane and hexane over the temperature ranges 190-235 K and 230-280 K respectively. The differential thermodynamics were calculated in these

173

temperature ranges using a variation of the Clausius-Clapeyron equation. Isosteric heats of adsorption were calculated for both alkanes near the lowest temperatures measured. Potential phase transitions were identified using the height of the layering transitions (proportional to inverse compressibility) as a function of temperature. Classical molecular dynamics simulations were calculated over a broad range of temperatures in order to provide additional information about the dynamics and the multilayer growth. Our hope is that these measurements will be used to enhance fundamental understanding of small molecules on surfaces. The values from the thermodynamics also aim to improve/validate current semi-empirical molecular force fields for modeling these types of systems.

## Experimental

Exfoliated graphite obtained from Union Carbide (GTB grade) was used in these experiments. This form of GRAFOIL is a standard industrial grade produced for fluid-sealing applications. The material was prepared for adsorption measurements by sealing a quantity of graphite within a quartz tube which was subsequently evacuated and heated at 700 °C until a base pressure of $10^{-7}$ Torr was achieved (generally overnight). The treated graphite was transferred to an OFHC Cu sample cell in an argon atmosphere. The sample cell was then loaded onto the second stage of a closed cycle helium cryostat. The temperature of the cryostat was maintained to ±2.5 mK using a CryoCon model 32B temperature

controller. *n*-pentane and *n*-hexane were obtained from Fisher Scientific and Acros Organics respectively with greater than 99% purity for both solvents.

The adsorption measurements were performed on an "in-house" constructed isotherm system based on the Mursic and Larese design (Mursic 1996). Each dosing sequence was controlled using a LabView-based program for automating the operation of pneumatic switches. Equilibrium vapor pressures were recorded using 1 and 100 Torr MKS Baratrons (capacitance manometers). Hexane measurements above approximately 160 K were performed in a Pyrex tube contained within a modified water bath with temperature regulation of ±10mK. Actual experimental temperatures were determined using empirical data for Antoine's equation applied to the saturated vapor pressures of each run. Methane adsorption was performed before and after a series of alkane measurements to ensure the graphite sample quality was maintained throughout the experiment.

MD simulations were performed using Accelrys' Materials Studio Forcite package (Accelrys Forcite). A graphite unit cell was imported from refined structural measurements (McKie 1986) and subsequently frozen in space (i.e. all carbon atoms in graphite constrained). A 22 x 22 x 2 (**a** x **b** x **c**) supercell was constructed from the unit cell. The surface was cleaved in the **c**-direction with an 80 Å vacuum slab above and below the substrate. Periodic boundary conditions were implemented to eliminate behavior resulting from edge effects. Thus, a molecule leaving the cell in the c-direction would re-appear in the vacuum slab

175

on the opposite side of the substrate. Nominal coverages of one, two, and three equivalents of a monolayer were initially loaded onto the surface. Bias from the starting positions of the adsorbate molecules was minimized by performing a dynamics calculation at a temperature were all molecules were rotationally and translationally mobile. Dynamics calculations were performed for 50 ps in a 1 fs time step (frame output every 100 steps for a total of 501 trajectories). MD calculations were performed in decreasing 10-20 K increments. The intermolecular forces between molecules and the substrate were described by the COMPASS (Sun 1998) semi-empirical force field. The calculations were performed using the NVT ensemble with the Nosé Hoover Langevin thermostat (Leimkuhler 2010) to regulate the temperature below ten percent the absolute value.

## Results and Discussion

### *Adsorption Isotherm Measurements*

A set of more than 30 adsorption isotherm measurements were performed for both pentane and hexane on the surface of graphite. The results of previous calorimetry and neutron diffraction measurements (Castro 1998, Krutchen 2005) suggest that the monolayer is an isotropic fluid phase in this temperature regime. A representative selection of the isotherms measured for pentane and hexane adsorbed on graphite is provided in Figure 56 and Figure 57. In both systems,
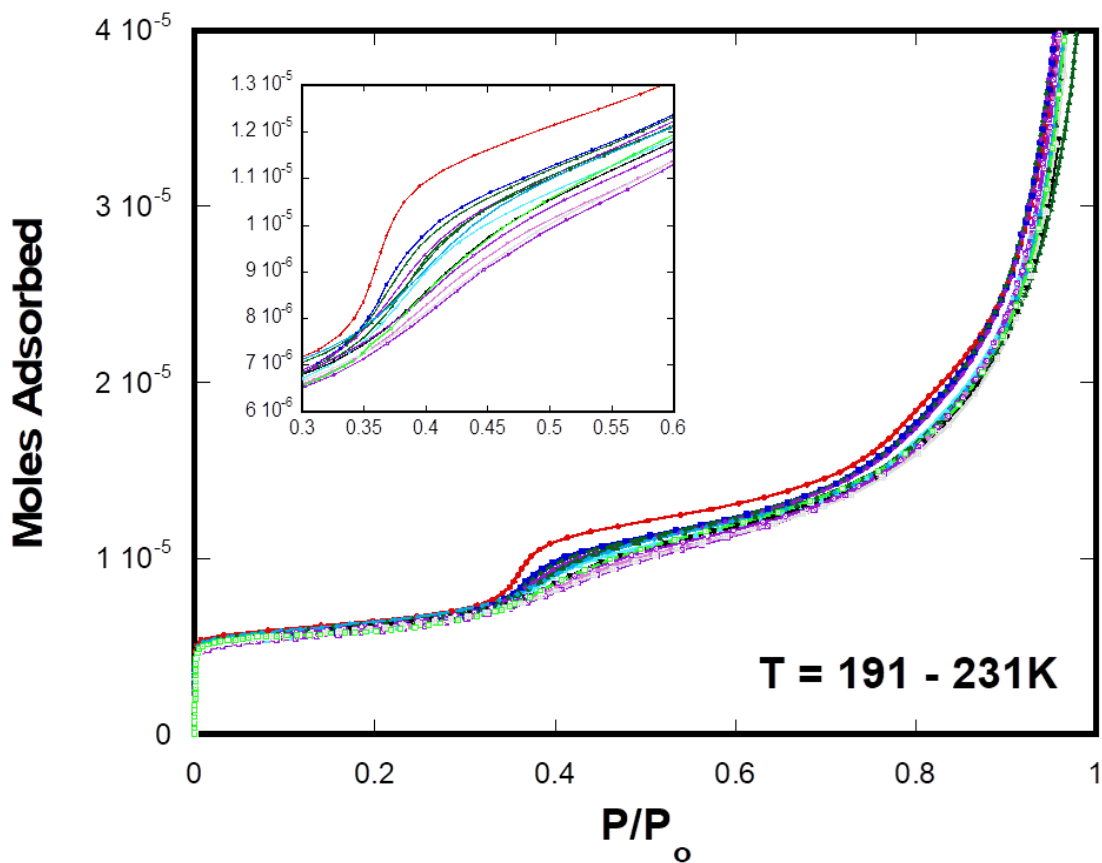
Figure 56 – Plot of moles adsorbed versus reduced vapor pressure (P/P$_o$ = equilibrium vapor pressure/saturated vapor pressure) for pentane adsorbed on graphite in the temperature range, T = 191-231 K.
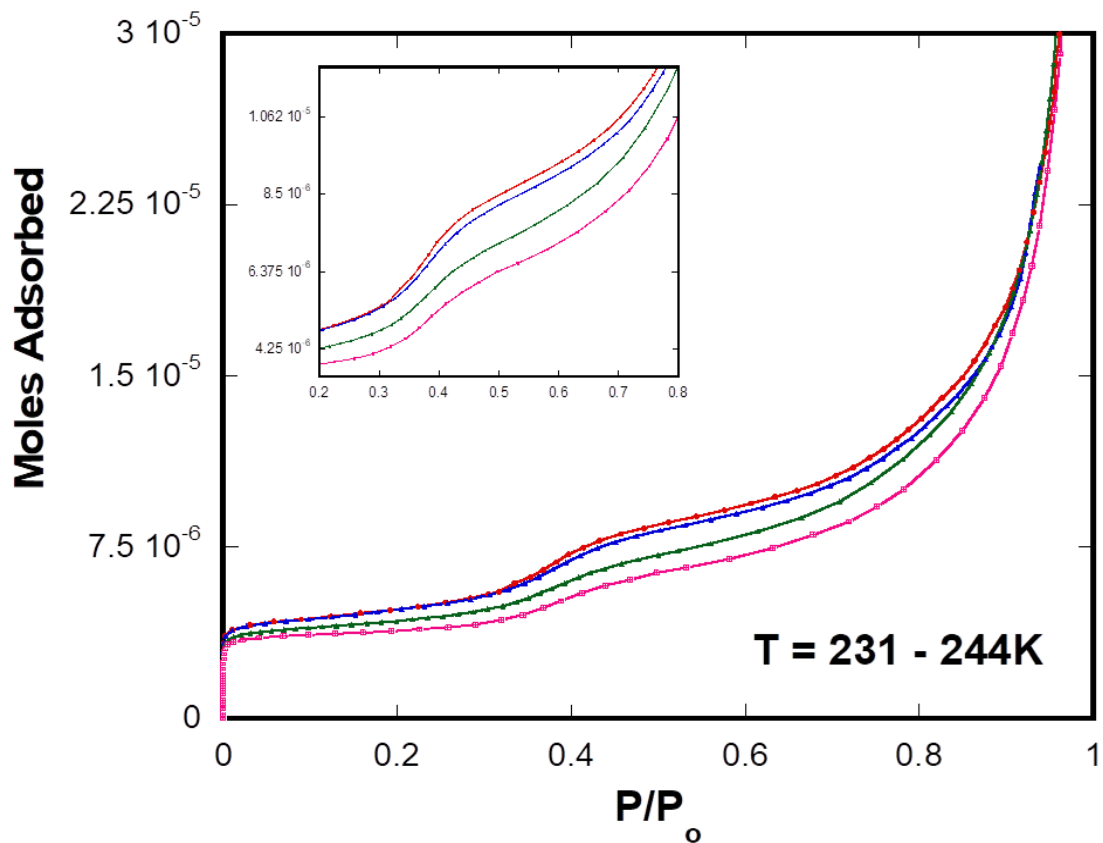
Figure 57 – Plot of moles adsorbed versus reduced vapor pressure (P/P$_o$ = equilibrium vapor pressure/saturated vapor pressure) for hexane adsorbed on graphite in the temperature range, T = 231-244 K.

the formation of the monolayer is accompanied by a relatively steep increase in amount adsorbed as a function of chemical potential. Between the completion of the monolayer and onset of bilayer formation, the system exhibits an abrupt increase in chemical potential while relatively few molecules are introduced to the adsorbed phase. The bilayer that follows appears as a smooth riser with less definition as compared to the monolayer. The intensity and breadth of the numerical derivatives indicate that the behavior of these two layers is inherently different. The MD simulations discussed below reveal the cause of this difference. For both pentane and hexane, a third layer appears for both alkanes only at the lowest of adsorption measurement temperatures. In Figure 56 and Figure 57, the third layer is identified by the subtle increase in molecules adsorbed near $P/P_o$= 0.8.

The averaged areas per molecule (APM) for pentane and hexane on graphite were determined to be 52.03 and 61.35 $Å^2$ respectively.  A methane adsorption measurement at 77 K was taken in order to calculate the surface area of the sample. From the results of Larese and coworkers (Larese 1988), the areal density of methane on graphite at 77 K is 0.0636 molecules $Å^2$. The number of molecules in the monolayer was evaluated using the Point B method and can be seen in Figure 58 and Figure 59. Since the monolayer phase in these experiments was a two-dimensional liquid, the quoted APMs are only the mean values. Compared to the solid structures determined from neutron diffraction data, the liquid APM is approximately 41% larger for pentane and 35% larger for
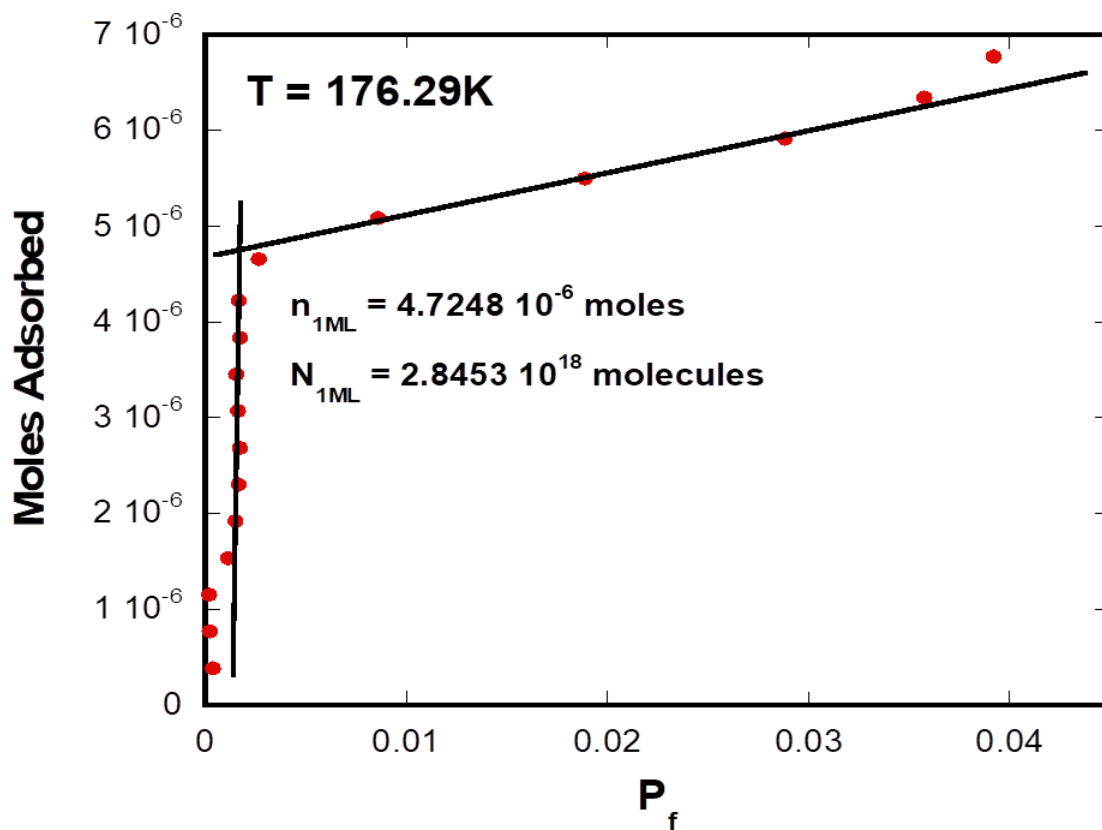
179

Figure 58 – Plot of moles adsorbed versus equilibrium vapor pressure in the

monolayer regime for pentane adsorbed on graphite at 176 K. The number of

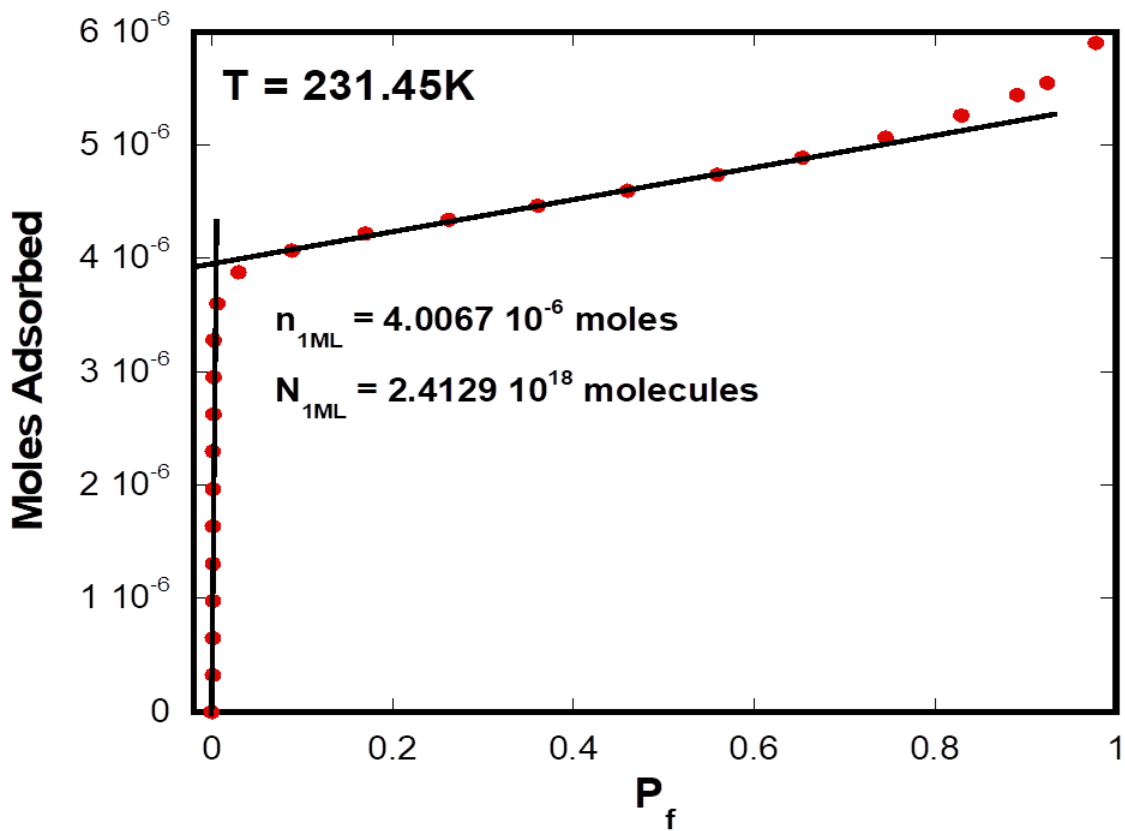moles in one monolayer was determined using the Point B method.

Figure 59 – Plot of moles adsorbed versus equilibrium vapor pressure in the monolayer regime for hexane adsorbed on graphite at 231 K. The number of moles in one monolayer was determined using the Point B method.

hexane on graphite. APMs were previously determined in the same temperature regime for pentane and hexane on MgO(100) (Yaron 2006, Cook 2015). In comparison, pentane on graphite appears to be less dense than its liquid phase on MgO(100), while hexane on graphite is more dense than observed on MgO(100).

The thermodynamics of adsorption were calculated using a variation on the Clausius-Clapeyron equations developed by Larher (Larher 1971). In this formalism, the numerical derivative from the raw isotherm plot is used to identify the location of adsorption layers in terms of equilibrium vapor pressure. The natural logarithm of these locale is plotted versus inverse temperature and the standard form of the Clausius-Clapeyron equation is used. Clausius-Clapeyron plots for pentane and hexane on graphite are shown below in Figure 60 and Figure 61. The thermodynamic values determined from these figures are contained in Table 13. In comparison with the thermodynamic values obtained for these alkanes on MgO(100) using the same method, the overall interaction of pentane and hexane with graphite is stronger than on MgO(100) as illustrated by the greater heats of adsorption.

Since the widths from the numerical derivatives of the raw data are proportional to the inverse 2D compressibilities, phase transitions can often be identified by observing abrupt changes or discontinuities in the full width at half maximum. However, for pentane and hexane on graphite, the locations of critical phase transitions are at temperatures lower than can be presently measurements
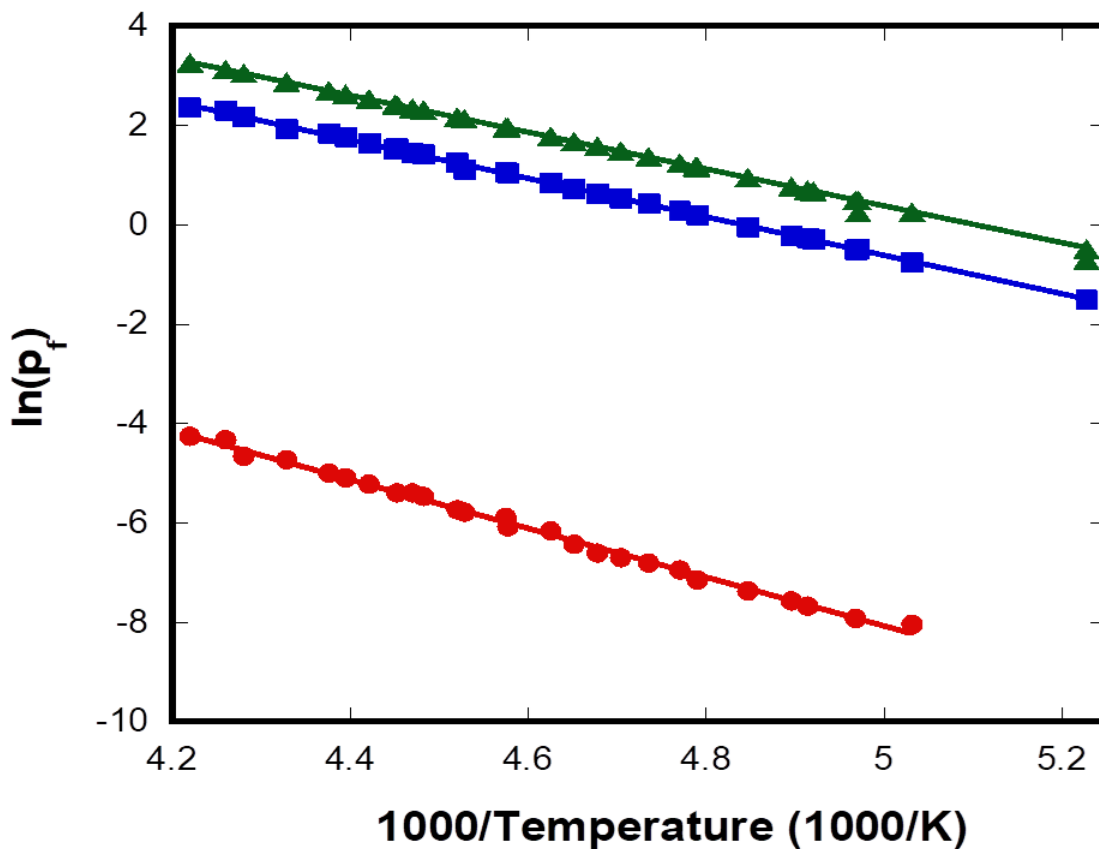
182

Figure 60 – Clausius-Clapeyron plot for *n*-pentane adsorbed on the surface of graphite. The individual layers are represented by red circles (1st layer), blue squares (2nd layer), and green triangles (3rd layer).
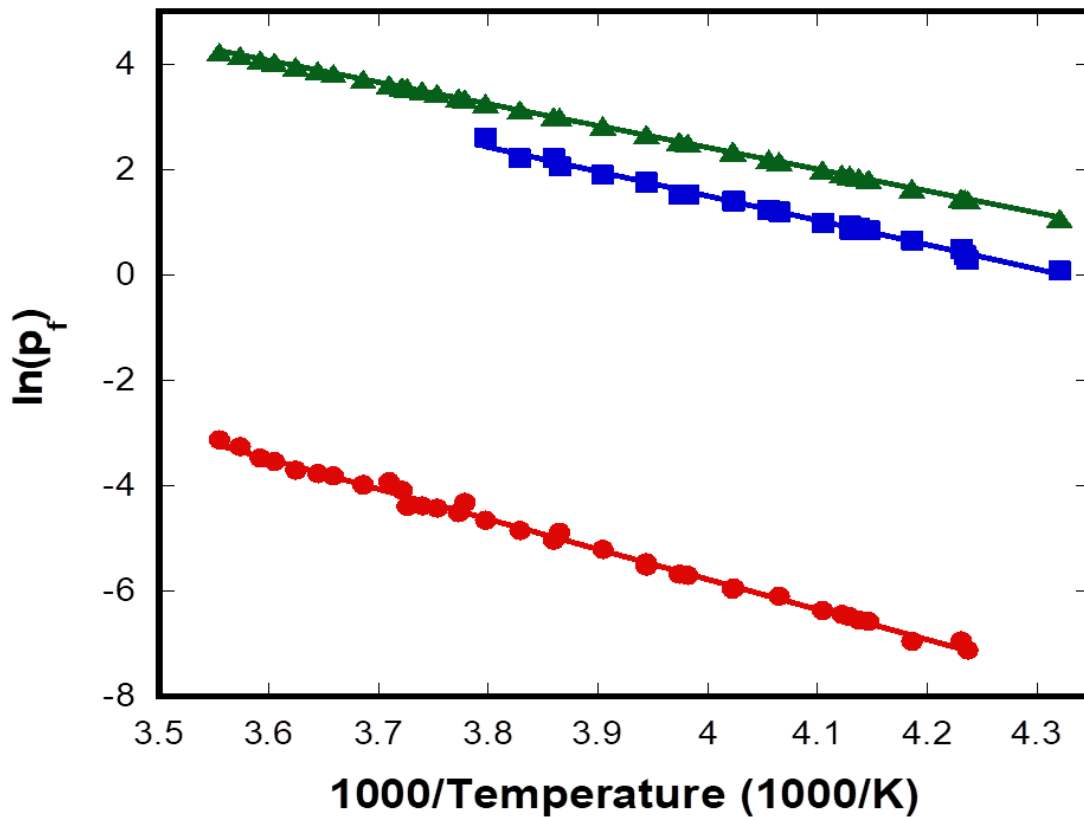
Figure 61 – Clausius-Clapeyron plot for *n*-hexane adsorbed on the surface of graphite. The individual layers are represented by red circles (1st layer), blue squares (2nd layer), and green triangles (3rd layer).

Table 13 – Thermodynamic values for n-pentane and n-hexane on graphite calculated from the Clausius-Clapeyron equation

| Alkane | | $A^{(n)}$ | $B^{(n)}$ | $Q^{(n)}_{ads}$ (kJ/mol) | $\Delta H^{(n)}$ (kJ/mol) | $\Delta S^{(n)}$ (J/mol K) |
|---|---|---|---|---|---|---|
| Pentane | 1 | 4914.9±67 | 16.497±0.31 | 40.8625±0.5570 | -9.9677±0.5768 | 20.4691±2.5827 |
| | 2 | 3874.3±22 | 18.76±0.10 | 32.2109±0.1829 | -1.3161±0.2363 | 1.6545±0.8314 |
| | ∞ | 3716±18 | 18.959±0.02 | 30.8948±0.1497 | - | - |
| Hexane | 1 | 5708.7±68 | 17.067±0.26 | 47.4621±0.5654 | -13.1902±0.5688 | 16.2040±2.1750 |
| | 2 | 4632.7±98 | 18.834±0.40 | 38.5163±0.8148 | -4.2443±0.8172 | 1.5131±3.3343 |
| | ∞ | 4122.2±7.5 | 19.016±0.03 | 34.272±0.0624 | - | - |

using volumetric methods due to small equilibrium pressures. Locating these types of transitions was possible for adsorption of these alkanes on MgO(100) and hexagonal boron nitride because the binding energies were lower, resulting in higher overall equilibrium vapor pressures for the same temperature ranges used in this experiment.

### *Molecular Dynamics Simulations*

The minimum energy structures/orientations for single molecules were calculated for both pentane and hexane on graphite in order to provide a fundamental understanding about how the alkane interacts with the graphite surface. The most stable orientations are provided in Figure 62 with corresponding energies shown in Table 14. For both molecules, the most stable configuration is one where the long molecular axis is parallel to the surface. Additionally, the plane of the molecule lies parallel to the surface where the optimal number of carbons are nearest to the surface. As previously observed for large alkanes on MgO(100), (Fernandez-Canoto 2014, Strange 2016) there are molecular orientations where the plane of the molecule is perpendicular to the surface. Normal alkanes with an odd number of carbons (e.g. pentane) have two inequivalent perpendicular "states" where the orientation with the most carbons nearest to the surface exhibits a stronger binding energy. It has been suggested that this behavior may contribute to the well-known "odd-even" effect observed for bulk alkanes in the two-dimensional adsorbed state. It is possible that the perpendicular states are important in the melting mechanism where the molecule
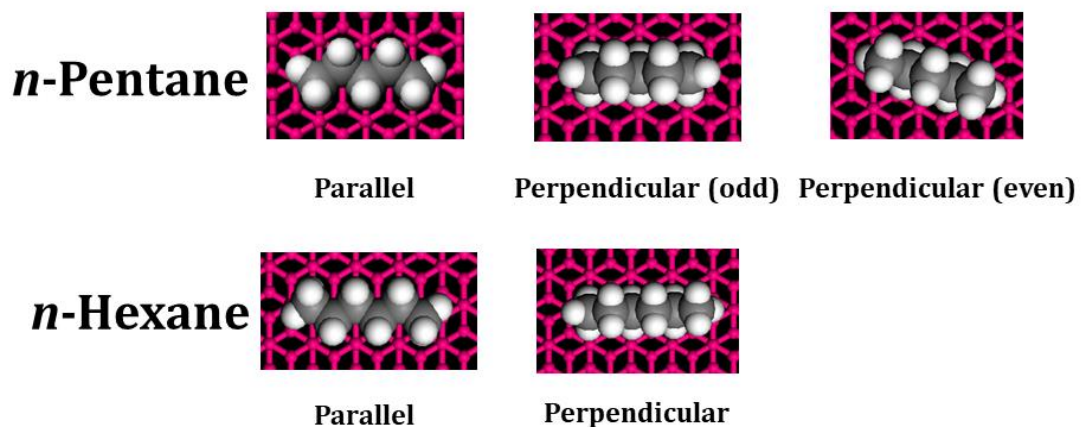
186

Figure 62 – Minimum energy configurations for pentane and hexane adsorbed on the basal plane of graphite

Table 14 – Calculated energy values for minimum energy configurations of single molecules on the surface of graphite

| Alkane | Surface Configuration | Surface Orientation | Energy (kcal/mol) |
|---|---|---|---|
| Pentane | Parallel | <10> | -21.6157 |
| | Perpendicular – odd | <10> | -20.8002 |
| | Perpendicular - even | | -19.9503 |
| Hexane | Parallel | <10> | -26.6307 |
| | Perpendicular - odd | <10> | -25.2031 |

could re-orient to reduce its area projected on the surface. An interesting comparison could be made by determining the relative population of perpendicular states and their ability to re-orient on surfaces with different chemical composition and symmetry.

C(z) at a coverage of approximately three layers for pentane and hexane adsorbed on graphite are shown in Figure 63 and Figure 64 respectively. These distributions are qualitatively similar to those observed in previous work for octane, nonane, decane on MgO(100) (Strange 2016). The layer nearest to the surface remains relatively well ordered and stratified as identified by the set of peaks centered at 3.0 Å. Interlayer traffic between the first and second layers is mostly restricted as shown by the deep well near 6.0 Å. The second and third layers are rotationally and translationally mobile since the representative carbon and hydrogen peaks cannot be resolved except for at the lowest temperature.

As previously noted the adsorption measurements and single molecule calculations for pentane and hexane on graphite suggest that alkanes bind the strongest to graphite in comparison with MgO(100) and hexagonal boron nitride substrates. Surprisingly, both pentane and hexane exhibit only a weak stabilization of the layer nearest to the surface by the fluid multilayers. Figs. Figure 65 and Figure 66 demonstrate how the rotational and translational order with respect to distance from the surface in the first layer evolves with an increase in temperature. The left-most C(z) represents the first layer at monolayer coverage while the figures on the right are for coverages of nominally
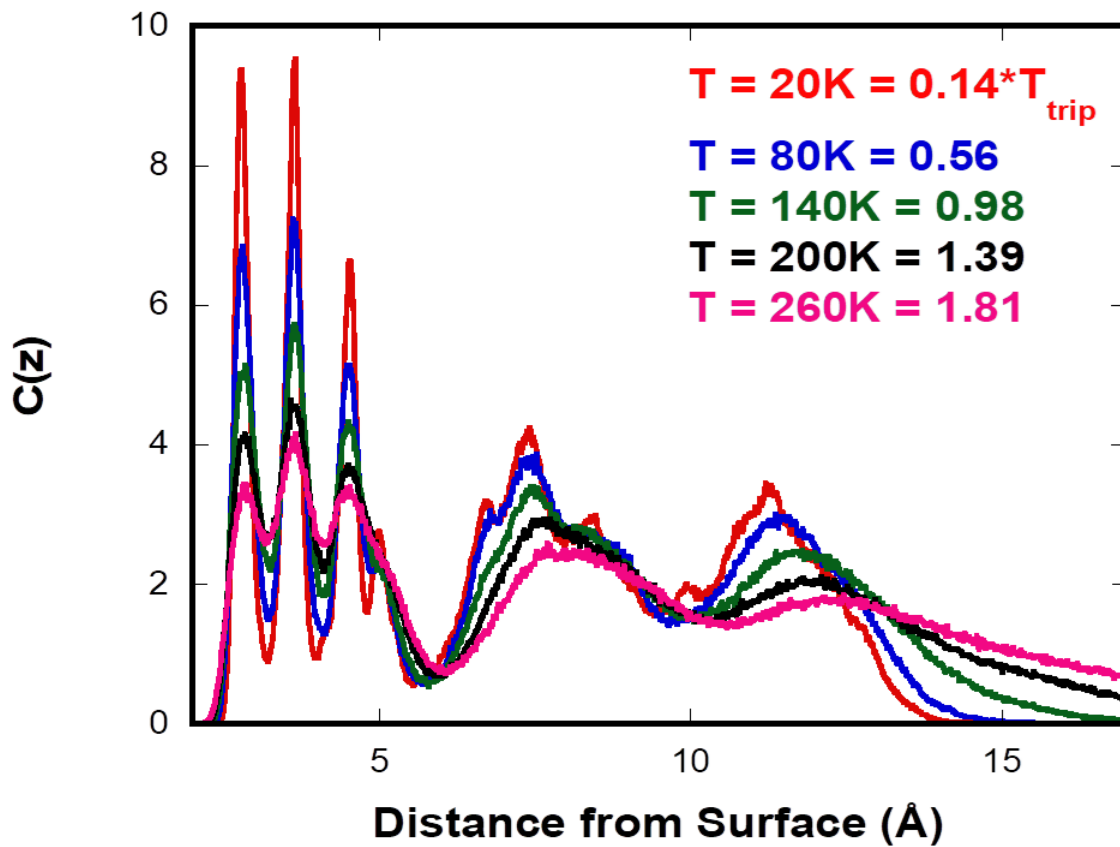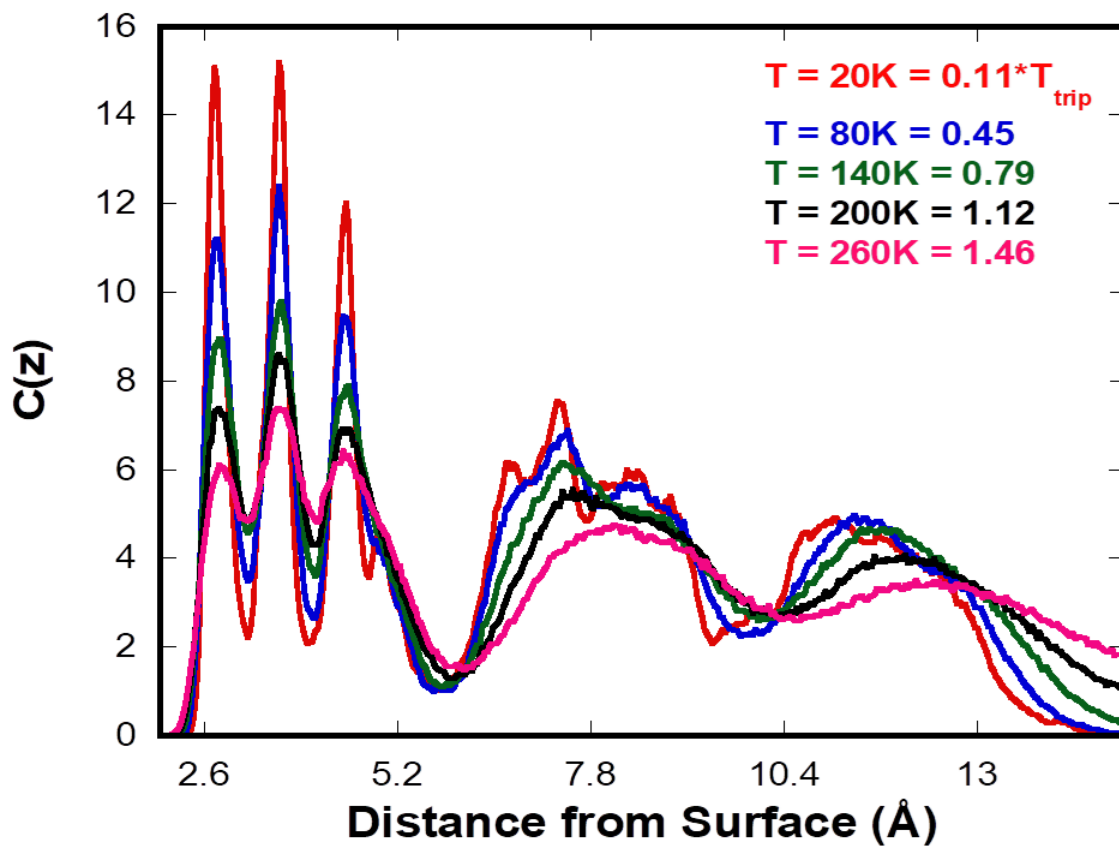
188

Figure 63 – C(z) for trilayer pentane on graphite.
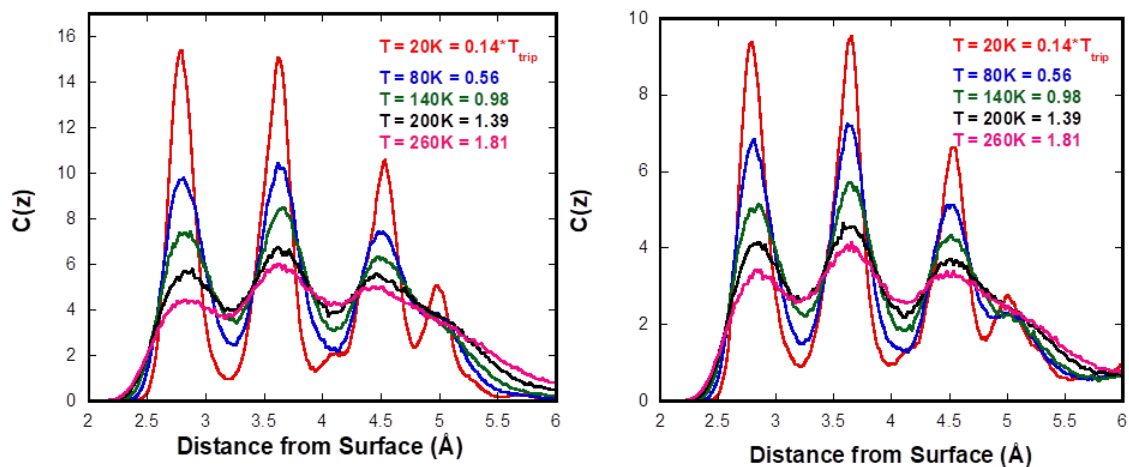
Figure 64 – C(z) for trilayer hexane on graphite.

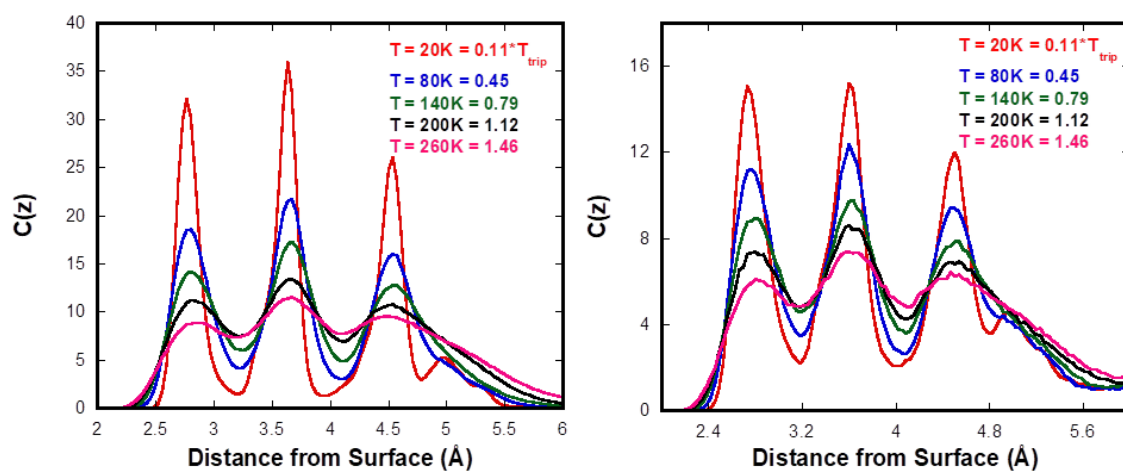Figure 65 – C(z) for monolayer pentane on graphite compared to trilayer coverage



Figure 66 – C(z) for monolayer hexane on graphite compared to trilayer coverage

three layers thick. The C(z) peak widths at both monolayer and trilayer coverages are relatively similar. For alkanes on MgO(100) and boron nitride, C(z) at trilayer coverages exhibited narrower peaks over a greater temperature range when compared to monolayer coverages. Additionally, for pentane and hexane on graphite, it appears as though there is an appreciable distribution of atoms between the first and second layers at trilayer coverage. These observations provide a question regarding the origin of the first layer stabilization by fluid multilayers. For both alkanes, the height of the peak near 2.8 Å indicates that there are alkane molecules in the perpendicular orientation with respect to the surface. It may be important to note that the population of perpendicular orientations is slightly greater for pentane than for hexane on graphite.

## Conclusion

High-resolution volumetric adsorption isotherm measurements were performed for *n*-pentane *n*-hexane on graphite in order to determine the thermodynamics of adsorption. These measurements revealed that pentane and hexane molecules interact stronger on graphite compared to MgO(100) and hBN. The averaged areas per molecule in the liquid phase were observed to be nearly 30 percent larger than observed for the monolayer solid. MD simulations were used to provide additional microscopic insight about the layering behavior of the alkanes on graphite. Compared with previous calculations performed for alkanes on MgO, adsorption on graphite seemingly has a lesser stabilization of the layer

nearest to the surface. Future structural and dynamical measurements aim to

provide supporting evidence for this phenomenon.

# CHAPTER SIX – INELASTIC NEUTRON SCATTERING STUDY OF ETHANOL ADSORBED ON TRANSITION PHASE ALUMINAS

Authors: Nicholas Strange, Sourav Adak, J.Z. Larese

(*pre-print)*

## Abstract

A combination of temperature programmed desorption (TPD) and inelastic neutron scattering (INS) measurements were performed in order to investigate the surface-catalyzed reaction of ethanol on the surface of transition phase aluminas. The TPD measurements provided preliminary information about the optimal temperatures for the formation of the ethylene product. The surface reaction and subsequent desorption on γ-alumina proceeds at lower temperatures than for θ-alumina. However, the θ-phase results in minimal formation of a diethyl ether byproduct. Inelastic neutron scattering measurements revealed the presence of surface-bound ethanol and other reaction intermediates. The surface species were identified by comparison to previous spectroscopic measurements.

## Introduction

Adsorption plays a key role in many technologically important processes including lubrication, gas separations, and catalysis. In particular, heterogenous catalysis often relies on solid substrates that either act as a catalyst or catalyst support. In order for a heterogenous catalyst to be effective, a reactant molecule must first adsorb to the substrate. In some cases, the adsorbed molecule must diffuse along the surface to a catalytically active site followed by a chemical

reaction. Upon completion of the reaction, the product can then potentially diffuse across the surface and finally end the process with desorption. While this cycle is simple to describe in an elementary way, the underlying phenomena that occur in each step are much more complex. Investigating the stages of catalysis using surface sensitive measurements can provide a more complete understanding of how the reactant molecules interact with the substrate before, during, and after the chemical reaction. This can be achieved using a combination of volumetric adsorption isotherms, temperature programmed desorption (TPD), and spectroscopic methods. In the current study, we have employed inelastic neutron scattering (INS) as a sensitive probe for investigating the dehydration reaction of ethanol on the surface of transition phase aluminas.

Alumina ($Al_2O_3$) has been widely used as a catalyst and catalyst support for a large number of organic reactions for a number of years (Pines 1960, Peterson 2014). The alumina powders used in these industrial processes are often derived from minerals present in the aluminum ore, Bauxite. Some of the more common minerals used to produce alumina are Gibbsite, Boehmite, and Bayerite. These minerals are essentially hydroxylated aluminas that transition through a variety metastable phases upon thermal treatment before ultimately rearranging to form the highly stable corundum phase (α-alumina). Figure 67 illustrates some of the intermediary transition aluminas that can be derived from the aforementioned minerals. The structures of the transition aluminas are
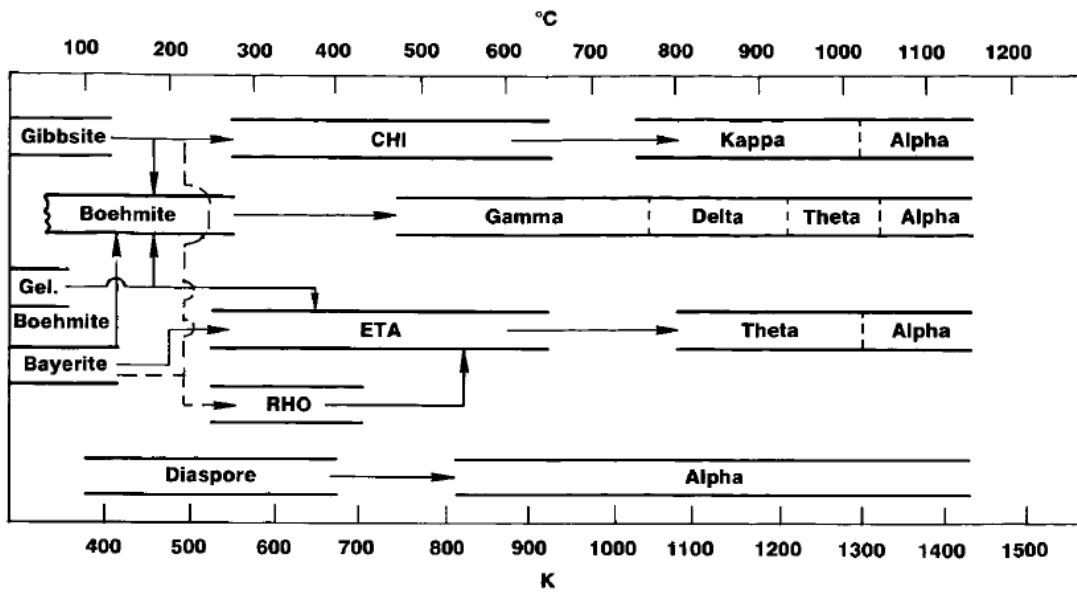
196

Figure 67 – Calcination sequence for a variety of aluminum oxide hydroxide starting materials from Wefers and Misra (Wefers 1987)

strongly dependent on the impurities and defects of the starting minerals. As a result, there is disagreement in the literature about the bulk and surface structures of the transition aluminas.

In an effort to better understand the transition alumina structures and their relationship with catalytic efficiency, new studies have been performed aimed at determining the identity and quantity of reactive surface sites on transition aluminas. Reports by Peden *et al.* (Kwak 2011) suggest that Lewis and Brønsted acid sites on the alumina surface contribute to the catalytic dehydration of alcohols. Unsaturated penta-coordinated $Al^{3+}$ atoms on the (100) surface of alumina were identified as the Lewis acid sites while hydroxyl groups function as the corresponding Brønsted acid.

The use of INS in catalysis has only recently attracted considerable attention for studying these types of surface-mediated reactions. This approach is advantageous over other spectroscopic techniques due to its sensitivity to hydrogen atom motions (in particular, hydroxyl/methyl vibrations and torsions). The inelastic incoherent scattering cross section for hydrogen in the thermal neutron energy range is an order of magnitude higher than any other element (Sears 1992). Thus, INS provides a unique and sensitive probe for studying the reactants, intermediates, and products in a surface-catalyzed reaction. The results of INS experiments can also be accurately modeled with molecular dynamics and density functional theory.

198

## Experimental

The mineral boehmite was obtained in powdered form from BASF (BASF G-250 catalyst substrate). All the alumina samples used in these studies were derived from the same starting boehmite batch. Specifically, the transition aluminas (γ, θ) and the final corundum phase (α) were calcined using a Lindberg Blue top loading furnace in open air. The temperature programs for the calcination of Boehmite to the transition aluminas are provided in Table 15. The resulting alumina materials were thoroughly characterized using x-ray diffraction (XRD), solid state NMR (SS-NMR), thermogravimetric analysis with differential scanning calorimetry (TGA-DSC), and adsorption isotherm techniques. Our characterization of the alumina powders was guided by the work of Peden *et al.* (Kwak 2008, Kwak 2009, Kwak 2011). The combined results of these measurements verified the identity and nature of the alumina powders used in the subsequent temperature programmed desorption (TPD) and inelastic neutron scattering (INS) experiments.  A brief summary of these characterization steps is given below.

*X-ray Diffraction*

XRD measurements were performed on a Panalytical Empyrean power diffractometer with a Cu-kα source and rotating sample stage. All XRD patterns were obtained in open air at room temperature. The resulting patterns for the γ- and θ-phases in comparison to the starting boehmite material are provided in Figure 68. The structures of the various transition aluminas were determined

Table 15 – Calcination temperatures and times for conversion of boehmite into the transition aluminas. Note: In each case, the starting material is boehmite

| Alumina Phase | Calcination Temperature (°C) | Time (hrs) |
|---|---|---|
| Boehmite | N/A | N/A |
| γ-Alumina | 600 | 8 |
| γ-Alumina with additional penta-coordinated $Al^{3+}$ sites | 600, 800, 600, | 8, 2, 2, |
| θ-Alumina | 1050 | 8 |
| α-Alumina | 1200 | 8 |
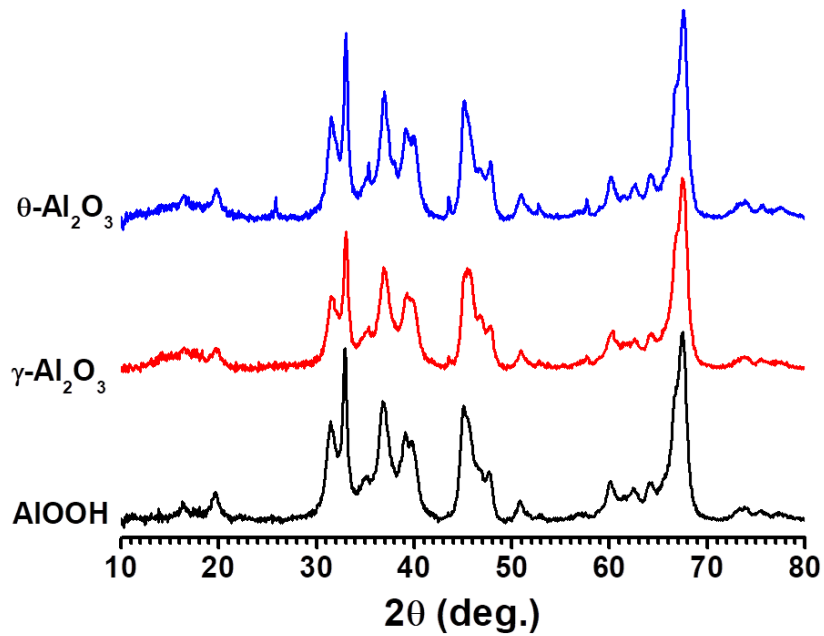


Figure 68 – XRD patterns for Boehmite in addition to γ- and θ-alumina phases calcined from the raw material

using the Rietveld refinement using GSAS (Larson 2000) and were found to be in agreement with values reported in the literature.

*Solid State NMR*

[27]Al solid state magic angle spinning (SS MAS) NMR experiments were performed on a Varian INOVA 400 MHz NMR. The NMR spectra are shown in Figure 69, Figure 70, and Figure 71 below. Figure 69 illustrates the change in aluminum coordination as a function of temperature. The octa-coordinated aluminum signal identified near 0 ppm is present in all the alumina phases. The structural reorganization that accompanies the γ-phase formation is demonstrated by the blue spectrum at 600 °C. The peak in the spectrum appearing near 60 ppm indicates the formation of tetrahedrally coordinated aluminum sites. The γ- and θ-alumina NMR spectra can be viewed with greater detail in Figure 70 and Figure 71. As the temperature of these phases is increased near 800 °C, a third peak becomes apparent at 25 ppm corresponding to increased numbers of penta-coordinated aluminum sites which appear at the (100) surfaces of γ- and θ-alumina.

*TGA-DSC*

TGA-DSC measurements were performed using a Netzsch Jupiter STA-449 instrument. The TGA recorded the percent mass lost during the calcination process and the DSC reveals the completion of the phase transitions. For all the TGA-DSC measurements, a linear temperature ramp was employed until the calcination temperature was reached. At this point, the temperature was fixed in
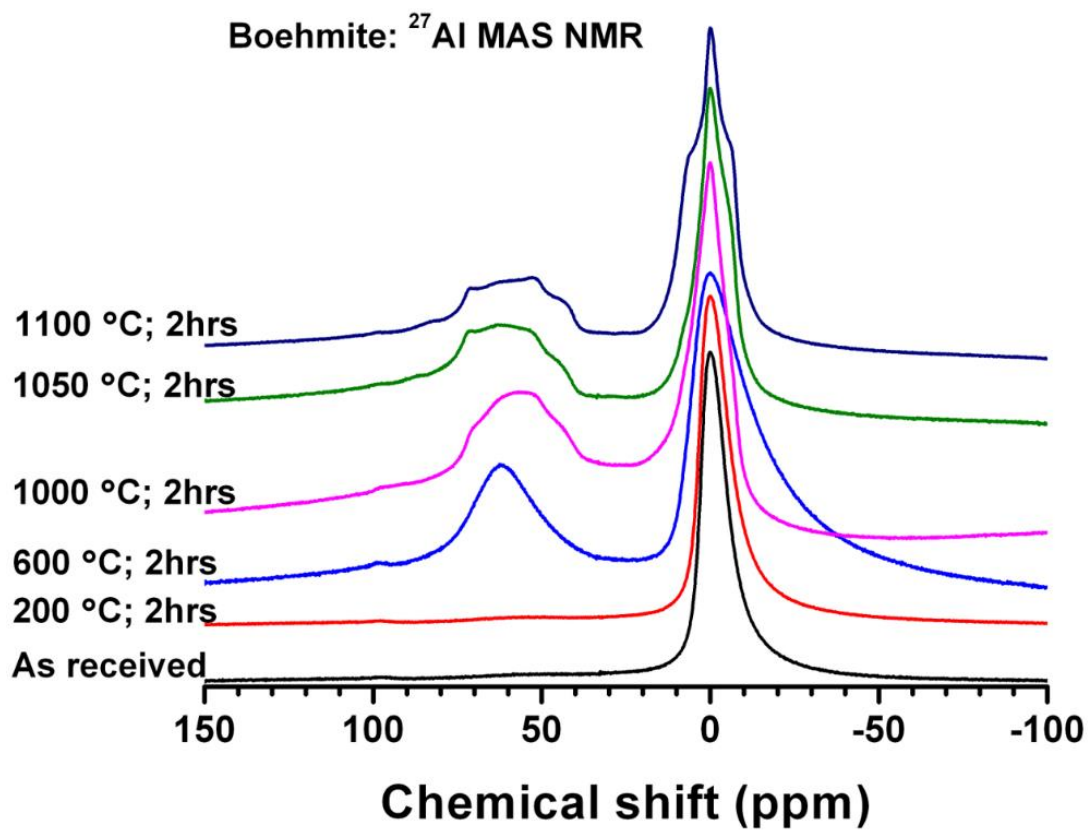
Figure 69 – Solid State NMR for the thermal treatment of the Boehmite starting material as a function of temperature.
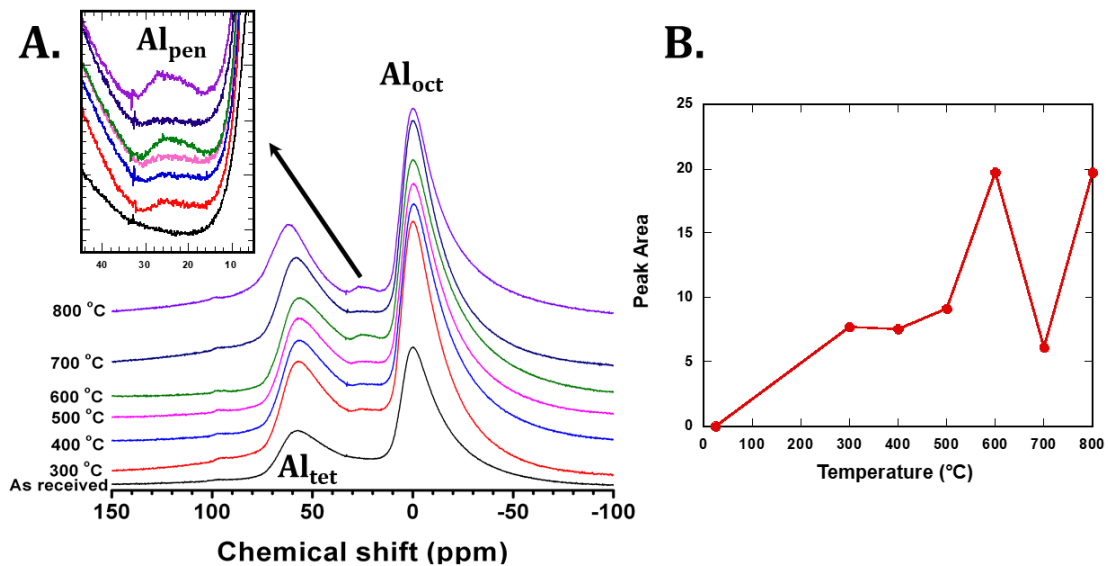
Figure 70 – (a) Solid State NMR for the thermal treatment of γ-alumina as a function of temperature. (b.) Peak area of penta-coordinated aluminum sites with increasing temperature.
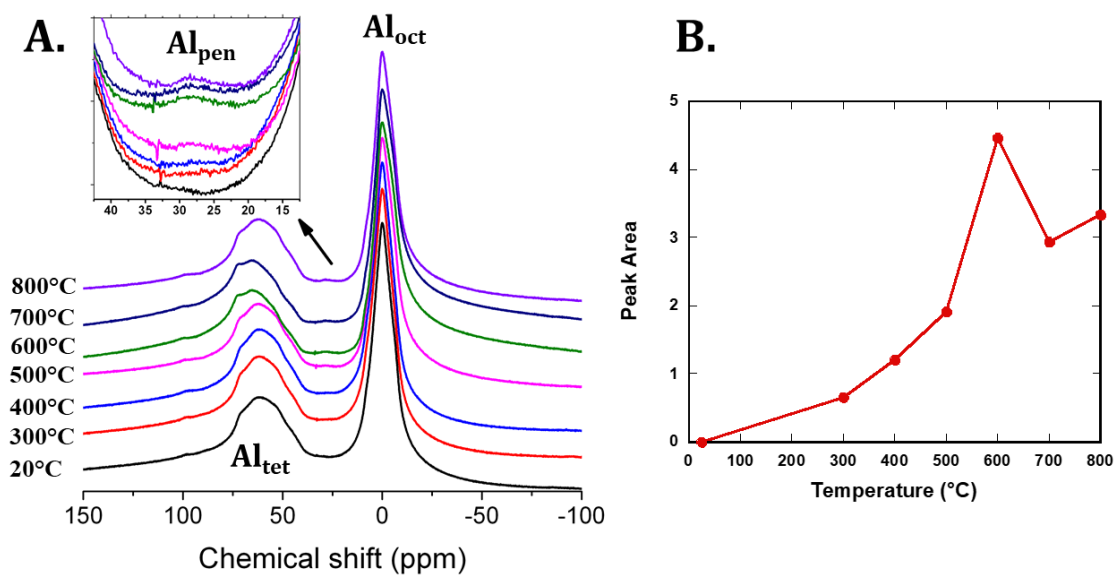
Figure 71 – (a) Solid State NMR for the thermal treatment of θ-alumina as a function of temperature. (b.) Peak area of penta-coordinated aluminum sites with increasing temperature.

order to observe the time dependence of mass loss and phase completion. The calcination scheme for γ-alumina containing additional penta-coordinated $Al^{3+}$ exhibited multiple temperature ramps. The boundaries of the temperature ramps are indicated by vertical dashes in Figure 72, Figure 73, and Figure 74. During the transformation to γ-alumina, about 13% of the initial mass was lost (see Figure 72). This decrease in mass likely resulted from a loss of hydroxylation and other physisorbed gases during the formation of the γ-phase. An exothermic turnover in the DSC trace can be observed just before the calcination temperature is reached indicating a crystalline phase transition. The formation of additional penta-coordinated aluminum sites noted above in the NMR spectra can be observed in Figure 73. Upon calcination at 600 °C, the TGA-DSC mimics that observed for γ-alumina. However, the DSC exhibits a second exothermic feature suggesting a new phase forms when heated to 800 °C. This new phase is similar in bulk crystal structure to γ-alumina with greater numbers of penta-coordinated aluminum surface sites similar to θ-alumina. These findings offer further support to our above NMR results. The γ-alumina sample was used as the starting material for the calcination to the θ-phase, hence the smaller decrease in percent mass. This thermal treatment can be viewed in Figure 74. Upon completion of the θ-alumina phase, the powder loses nearly 20% of its starting Boehmite mass. Another exothermic feature in the DSC indicates the formation of the θ-alumina phase.
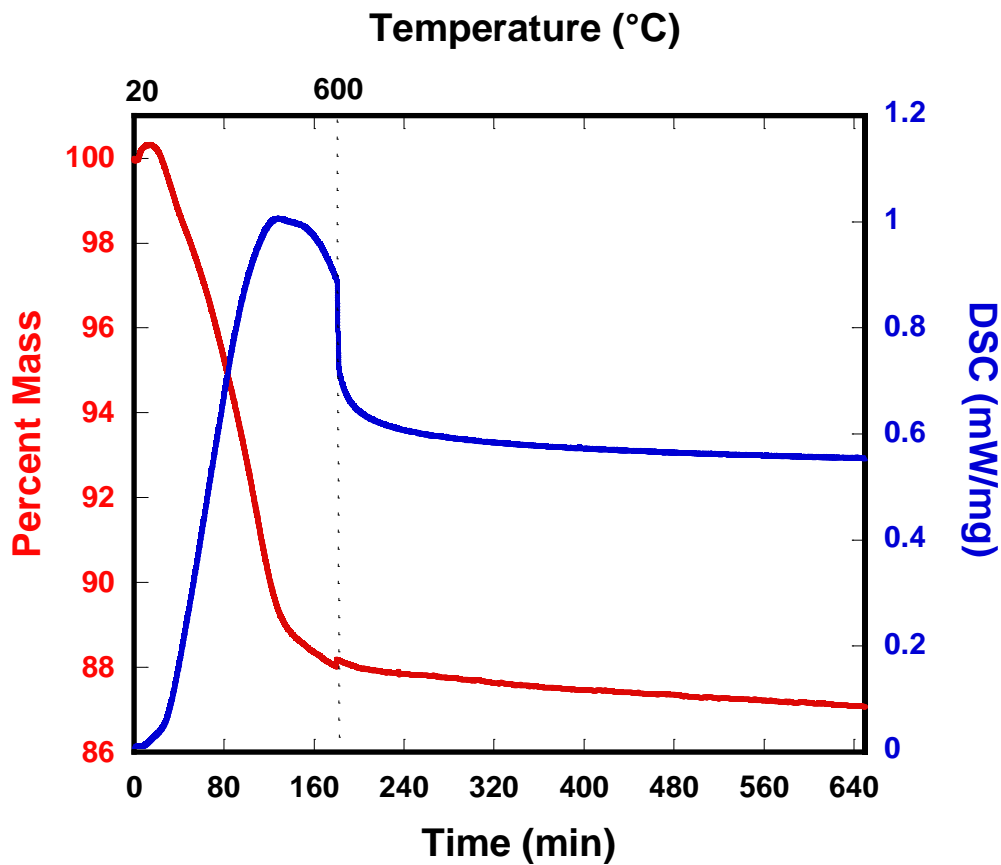
Figure 72 – TGA-DSC for the calcination of Boehmite to γ-alumina. The red trace (left axis) represents the percent mass loss from the starting material. The corresponding DSC is shown in blue (right axis).
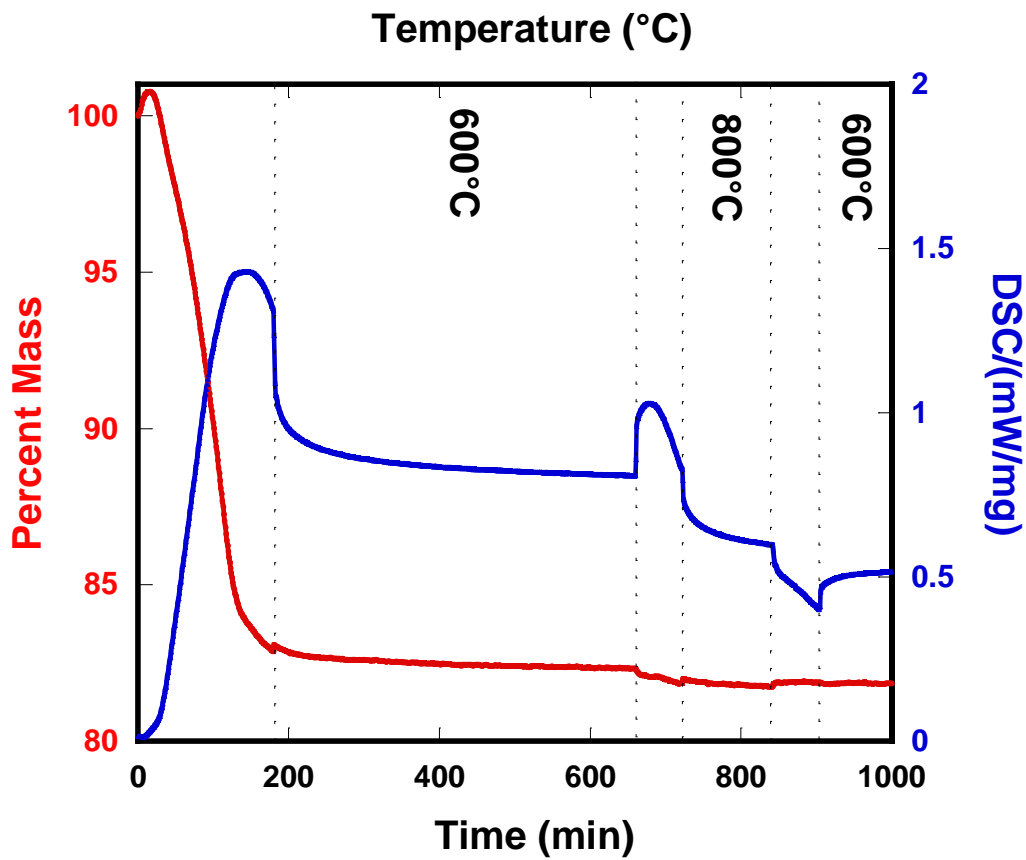
Figure 73 – TGA-DSC for the calcination of Boehmite to γ-alumina with additional penta-coordinated aluminum sites. The red trace (left axis) represents the percent mass loss from the starting material. The corresponding DSC is shown in blue (right axis).
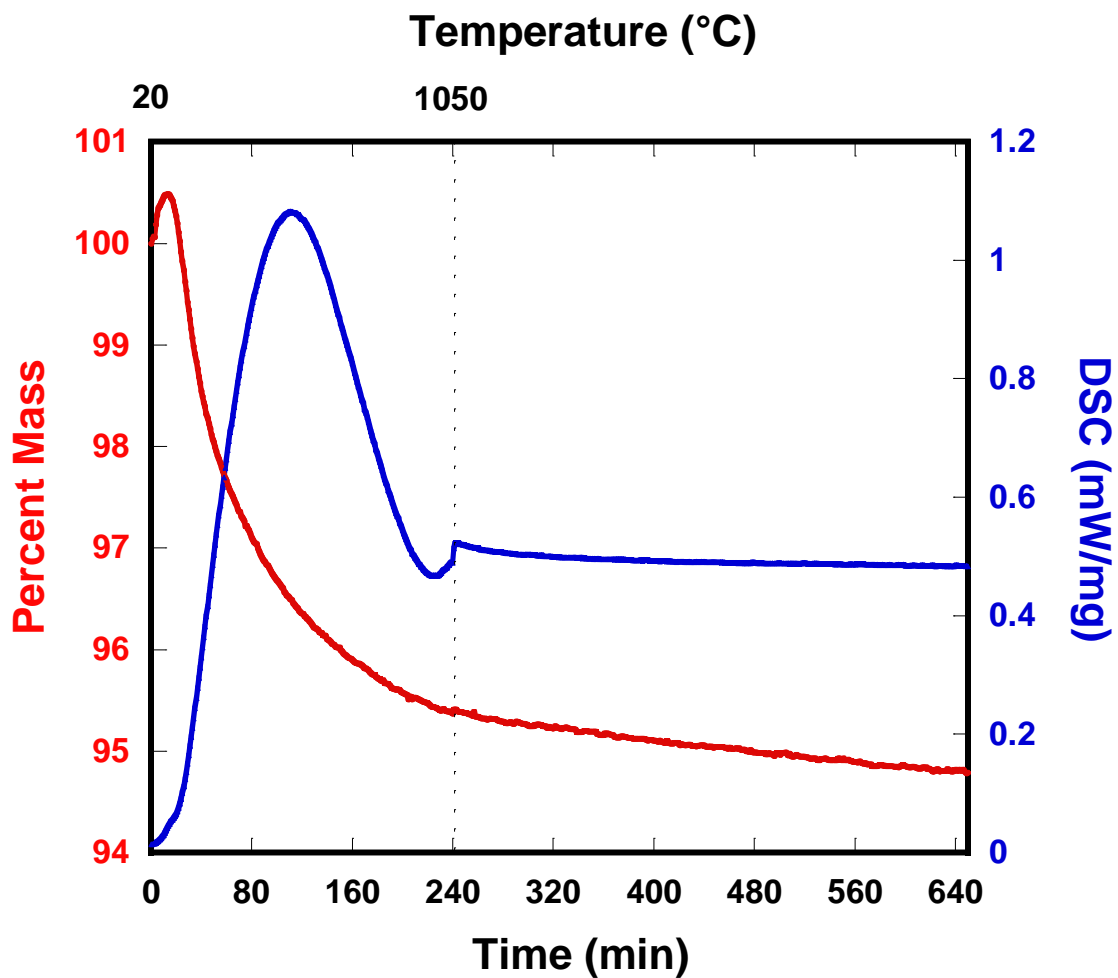
Figure 74 – TGA-DSC for the calcination of Boehmite to θ-alumina. The red trace (left axis) represents the percent mass loss from the starting material. The corresponding DSC is shown in blue (right axis).

*Adsorption Isotherm Measurements*

Volumetric adsorption measurements were performed on the transition alumina samples using an in-house design and developed adsorption apparatus described elsewhere (Mursic 1996). Methane adsorption isotherms at 77 K were used as a standard to determine the surface quality and relative surface areas of the alumina powders. Figure 75 illustrates the methane adsorption in the monolayer regime for each of the alumina phases. The Point-B method (Emmett 1937) was used to determine the number of molecules in an adsorbed monolayer, the relative decrease in adsorption capacity was plotted as a function of calcination temperature (see Figure 76). 190-proof ethanol was purchased from Fischer Scientific and azeotropically distilled to remove any water content. The purified ethanol was subsequently further distilled using a freeze-pump-thaw distillation cycle to remove any remaining soluble gases from the liquid. The absence of impurities in the ethanol was verified using the gas chromatography prior to use in adsorption measurements. Ethanol adsorption was performed at room temperature and allowed to continue until just before reaching the saturated vapor pressure. Once again, the Point-B method was used to determine the relative adsorption capacity for adsorption of ethanol on the aluminas at room temperature. New alumina samples were prepared after each adsorption measurement because slow adsorption kinetics suggested a chemical reaction occurs at the temperature where these adsorption measurements were performed.
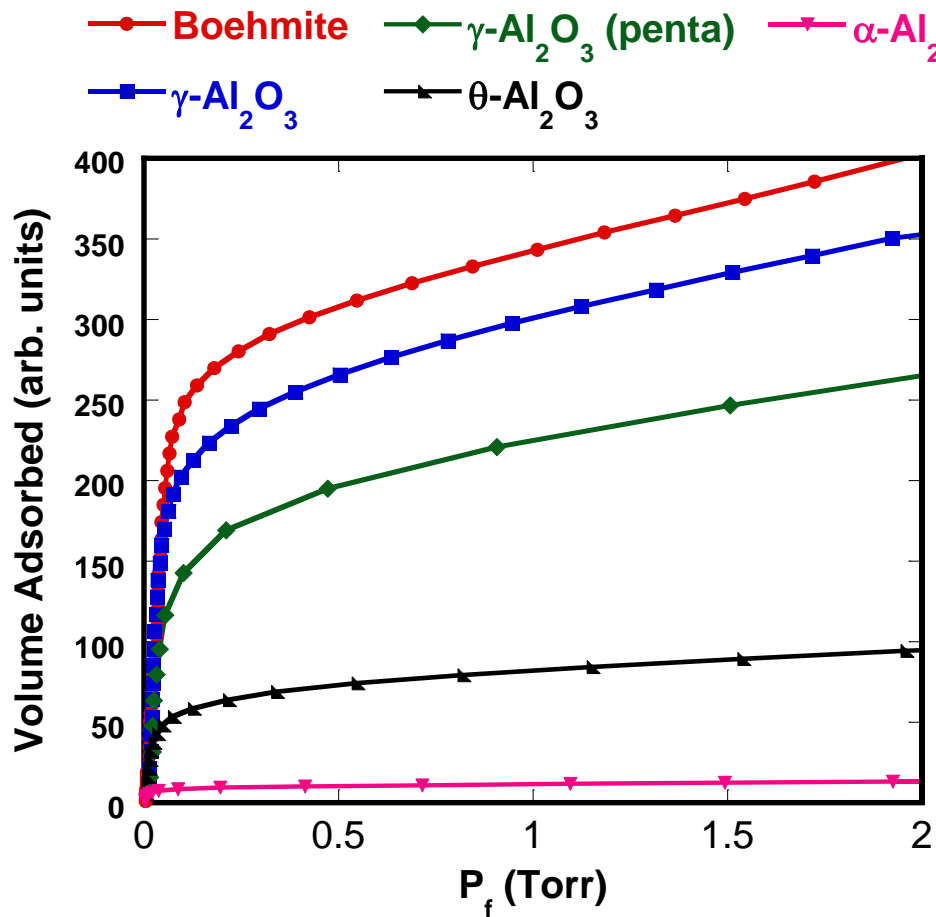
Figure 75 – Adsorption isotherms of methane on the surface of the aluminas at

77 K. Monolayer coverages were identified by the Point B method, i.e. the

intersection between a linear fit to data in the low-pressure region (vertical) and a

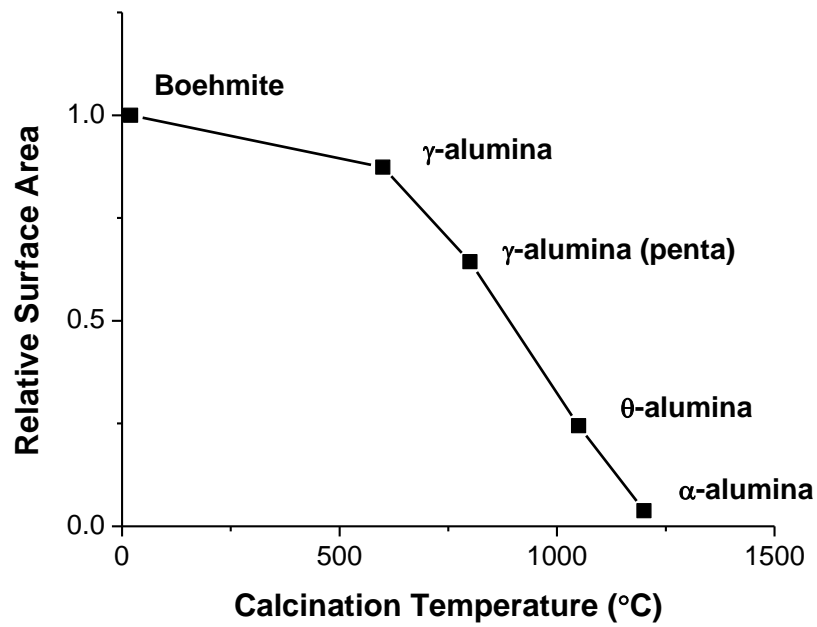linear fit to data in the high-pressure region (horizontal)

Figure 76 – Decrease in alumina surface area with increasing thermal treatment

*Temperature Programmed Desorption (TPD)*

The transition aluminas with monolayer coverage ethanol adsorbed were examined using a modified approach to standard temperature programmed desorption (TPD) methods. The setup for TPD included a temperature calibrated top-loading furnace, custom-built gas-handling manifold, Stanford Research Systems residual gas analyzer mass spectrometer (RGA), and an HP 5890 gas chromatogram with a thermal conductivity detector. The column used in the GC was a 2m long, 2.2 mm inner diameter stainless steel column packed with Hayesep T porous polymers. Additional parameters for the GC are provided in Table 16. In these measurements, the vapor phase of the ethanol on alumina system was sampled at discrete temperatures between room temperature and 300 °C in 25-degree increments. Throughout the entire TPD measurement, less than 1% of the total ethanol molecules initially adsorbed were removed and sampled. This feature was by design in order to maintain a fixed coverage-dependent chemical potential. At each temperature, a ten-minute waiting period was employed to ensure thermal equilibrium.

*Inelastic Neutron Experiments*

Three identical aluminum sample cans (i.d. = 9.7mm; wall thickness = 0.5mm) were prepared with approximately 2.3 grams of θ-alumina in an inert atmosphere. The samples were mounted on a sample stick similar to those described by Koehler and Larese (Koehler 2000) and subsequently evacuated. The first sample can was used as a background sample, while the remaining two

Table 16 – Relevant parameters for GC-TCD temperature programmed desorption

| Gas Chromatography Parameters | Value |
|---|---|
| Stationary Phase | L = 2m, I.D. = 2.2 mm column packed with Hayesep T porous polymers |
| Mobile Phase | UHP Helium |
| Mobile Phase flow rate (mL/sec) | 0.529 |
| Inlet Head Pressure (kPa) | 58 |
| Reference Gas flow rate (mL/sec) | 2.53 |
| Initial Oven Temperature (°C) | 140 |
| Initial Oven Hold Time (min) | 1.5 |
| Temperature Ramp Rate (°C/min) | 40 |
| Final Oven Temperature (°C) | 250 |
| Final Oven Hold Time (min) | 5 |
| Detector Temperature (°C) | 175 |

were loaded with monolayer coverage ethanol. One of the ethanol-dosed samples was heat treated to 300 °C in a top loading furnace. INS measurements were performed on VISION (Seeger 2009) at the Spallation Neutron Source (ORNL). The samples were measured near 5 K for approximately 4 hours. The signal from the background θ-alumina sample was subtracted from the ethanol and heat-treated ethanol samples in order to isolate the signal from the adsorbate and vapor phase molecules. The details of obtaining these types of difference spectra are provided elsewhere (Larese 2008).

## Results and Discussion

### *Temperature Programmed Desorption (TPD)*

TPD measurements were performed for monolayer coverage ethanol adsorbed on the transition aluminas. The results of these measurements served as a guide for determining the optimal temperatures for initiating a chemical reaction at the surface for later INS measurements. It should be noted that the purpose of these measurements was to examine the identity and relative abundance of reactant and product molecules in the vapor phase rather than determine the desorption quantity as a function of temperature in standard TPD measurements. Our measurement technique results in a constant surface coverage throughout the entire measurement by sampling less than 1% the total molecules initially adsorbed on the surface. Figure 77a illustrates the gas
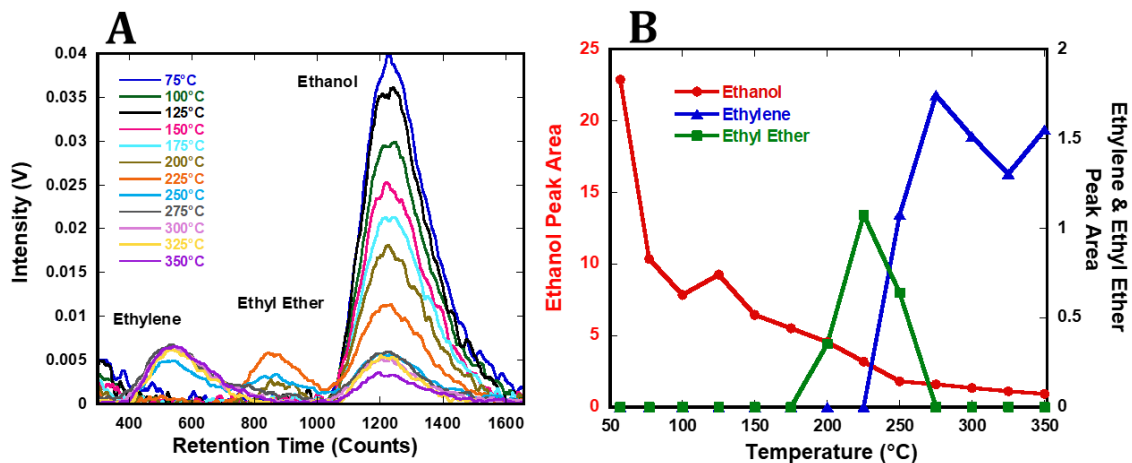
Figure 77 – (a) TPD of monolayer ethanol on the surface of γ-alumina as a function of temperature. (b) Numerically integrated areas obtained from the TPD peaks as a function of temperature.

chromatogram as a function of increasing sample temperature. A significant signal from unreacted ethanol desorbing from the surface is visible until 225 °C. At this point, ethyl ether appears to form until the onset of ethylene formation at 250 °C. The results of these measurements agree with those made previously by Peden *et al.* for ethanol on γ-alumina.

In Figure 78, the TPD for ethanol on the surface of γ-alumina containing additional penta-coordinated $Al^{3+}$ sites suggests that the formation of ethyl ether and ethylene mimics the behavior observed previously for regular γ-alumina. However, in the low temperature regime, the ethanol signal is drastically reduced in comparison. In fact, on the γ-alumina with additional penta-coordination, the ethanol signal gradually increases until a plateau near 175 °C. This indicates that there are more sites on this material with a greater overall binding energy in comparison with the regular γ-alumina material. This is expected since the penta-coordinated aluminum sites are known to be active Lewis acid sites in the hydration reaction.

The TPD for monolayer ethanol on θ-alumina is shown in Figure 79. From the integrated areas in Fig 79(b), the surface of θ-alumina exhibits the strongest binding and the narrowest temperature range for ethyl ether formation. Additionally, ethylene doesn't form until 275 °C where the concentration abruptly increases. These shifts in temperature suggest that the surface sites and reactivities are different for θ-alumina as compared to the γ-aluminas. From the results of the TPD measurements, it was determined that 300 °C was a
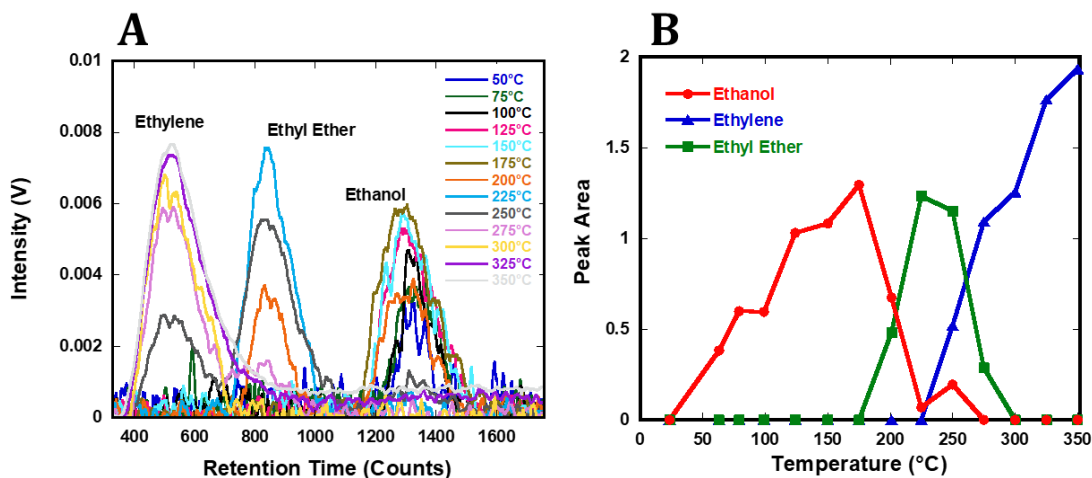
216

Figure 78 – (a.) TPD as a function of temperature of monolayer ethanol on the surface of γ-alumina containing additional alumina penta-coordinated sites. (b.) Numerically integrated areas obtained from the TPD peaks as a function of temperature.
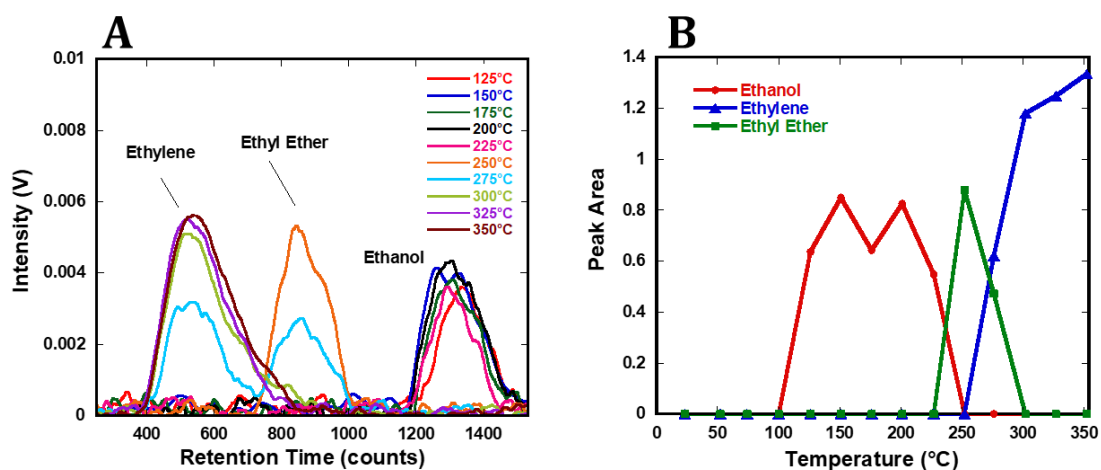


Figure 79 – (a.) TPD of monolayer ethanol on the surface of θ-alumina as a function of temperature. (b.) Numerically integrated areas obtained from the TPD peaks as a function of temperature.

sufficiently high temperature for initiating a surface reaction of ethanol on θ-alumina.

### *Inelastic Neutron Scattering (INS)*

The INS spectrum recorded for θ-alumina represents the first presentation to our knowledge of a comprehensive and high-resolution spectrum that includes all excitations (i.e. no selection rules) between 0 and 4000 cm$^{-1}$. The bulk and surface structures of θ-alumina are not well characterized in the literature and additional modeling studies are required before making absolute conclusions about the vibrational spectrum. As a result, the peaks in the θ-alumina INS spectrum were identified by comparison to previous IR and Raman studies (see Figure 80 and Figure 81).

Since the surface of the θ-alumina is modified during chemisorption, the signal of the background could not be effectively subtracted to isolate the adsorbate signal. The spectrum from the monolayer adsorbed ethanol was compared with the background alumina signal in Figures 80-83. In the range of 0-120 cm$^{-1}$, there is one substantial difference accompanied by a few additional minor peaks. After the adsorption of ethanol, a strong signal at 93 cm$^{-1}$ is observed. This feature is likely a downshifted hydroxyl torsional mode associated with a chemisorbed ethoxide molecule. Hydroxyl torsions in bulk ethanol are reported in the literature around 200 cm$^{-1}$ with frequency shifting of 30 cm$^{-1}$ for the deuterated variety (Barnes 1970).

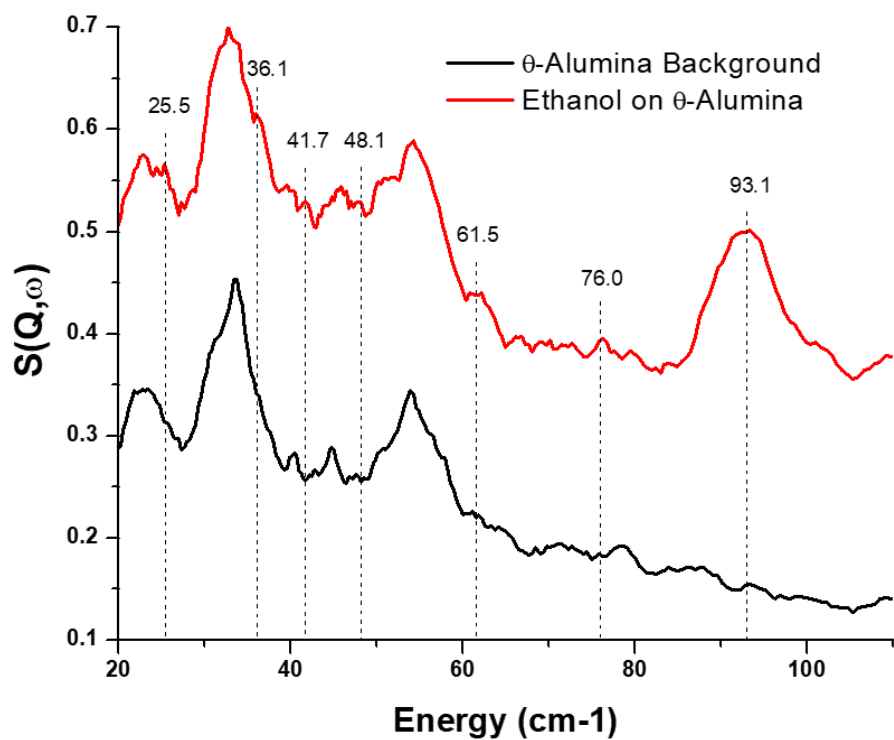Figure 80 – Comparison of the INS spectra for monolayer ethanol adsorbed on θ-alumina (red) vs. the θ-alumina background (black) in the energy range, 20-150 cm$^{-1}$.
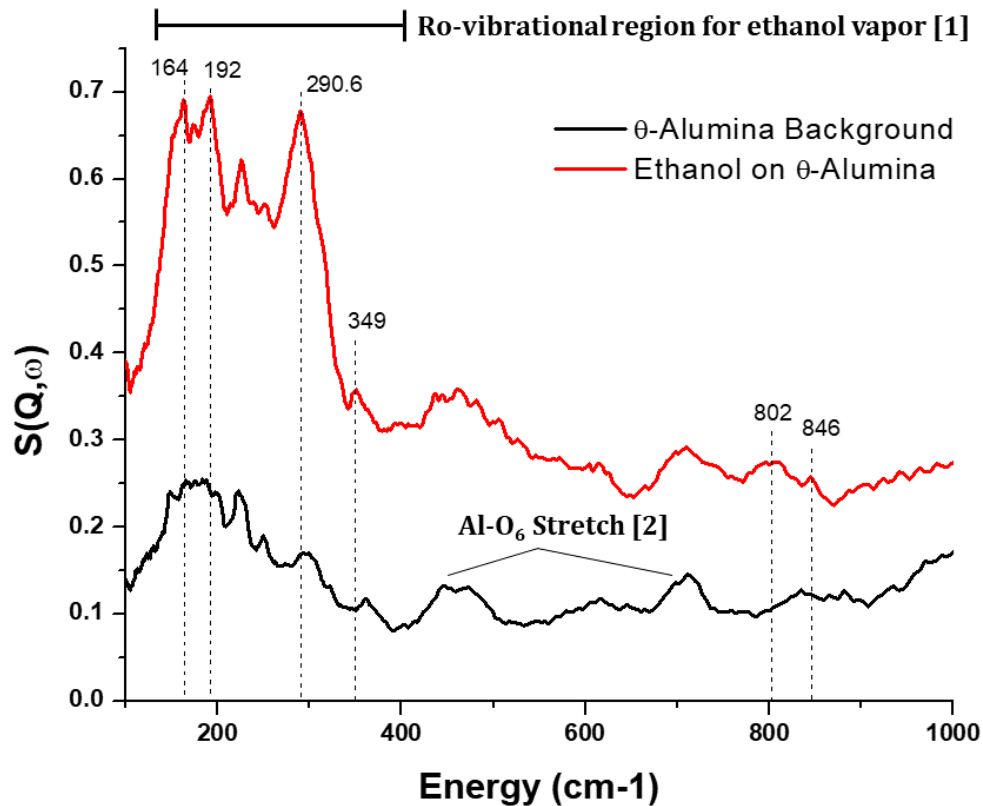
Figure 81 – Comparison of the INS spectra for monolayer ethanol adsorbed on θ-alumina (red) vs. the θ-alumina background (black) in the energy range, 150-1000 cm-1. Torsional modes for bulk ethanol were identified from Durig and Larsen (Durig 1989) [1]. Alumina modes were identified from Saniger (Saniger 1995) [2].
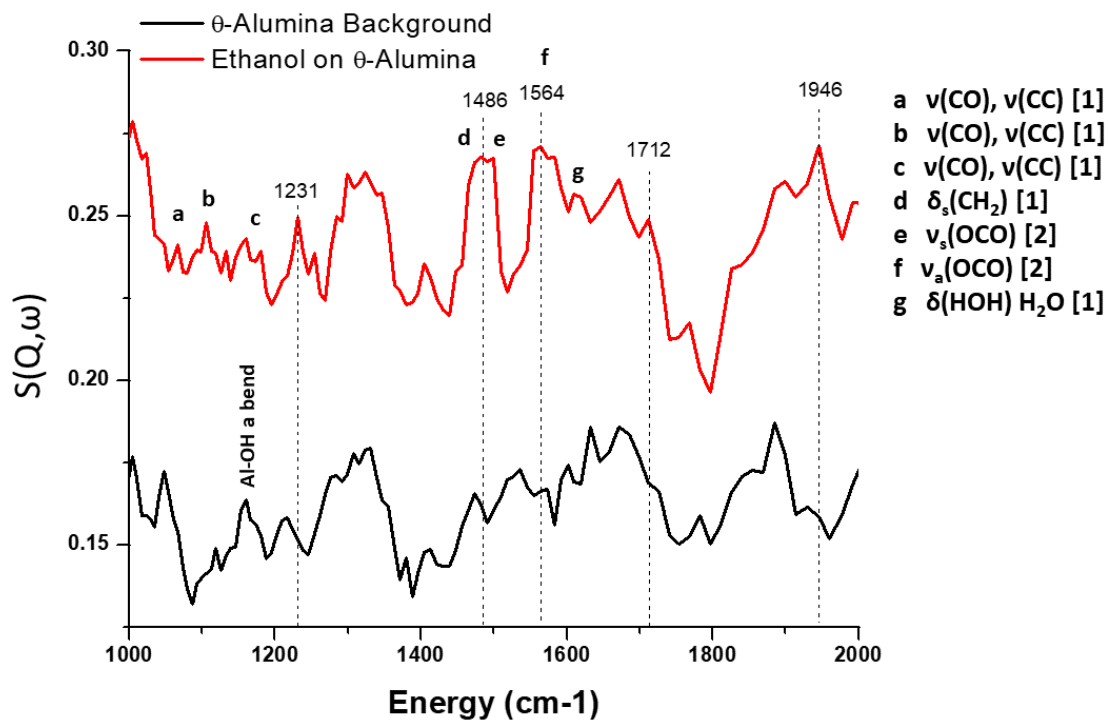
Figure 82 – Comparison of the INS spectra for monolayer ethanol adsorbed on θ-alumina (red) vs. the θ-alumina background (black) in the energy range, 1000-2000 cm$^{-1}$. Modes identified from Hussein (Hussein 1991) [1] and Knözinger (Knözinger 1978) [2]
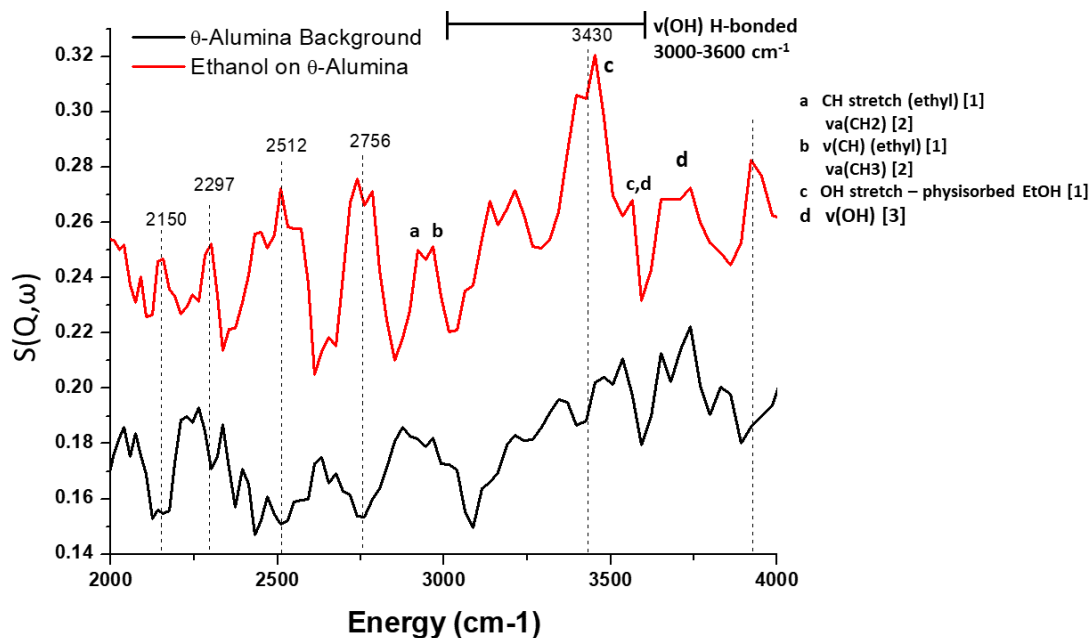
Figure 83 – Comparison of the INS spectra for monolayer ethanol adsorbed on θ-alumina (red) vs. the θ-alumina background (black) in the energy range, 2000-4000 cm$^{-1}$. Modes from the adsorbed species were identified from DeCanio (DeCanio 1992) [1], Hussein (Hussein 1991) [2], and Knözinger (Knözinger 1978) [3].

Figure 81 illustrates ethanol adsorbed on θ-alumina the spectral range of 150-1000 cm$^{-1}$. In this range there are three notable peaks which propagate in the vicinity of the bulk *trans* ethanol hydroxyl torsion fundamental. These peaks likely represent ethyl and hydroxyl torsional modes (Barnes 1970) from ethanol chemically bound to the alumina surface. Complex alumina lattice modes from coupled Al-O$_4$ and Al-O$_6$ centers can be seen between 400 and 750 cm$^{-1}$ (Saniger 1995).

At higher energies (1000-2000 cm$^{-1}$), the vibrational modes of chemically bound intermediates appear. The bands labeled *a-c* in Figure 82 correspond to C-O and C-C stretching modes in an ethoxide group bound to the surface. Peak *d* is attributed to a scissoring bend from the hydroxyl group in ethanol. Near 1500 cm$^{-1}$, deformations of CH and CH$_2$ in ethyl groups are observed. Peaks *e* and *f* come from OCO symmetric and asymmetric stretches respectively. Finally, the peak at 1630 is attributed to an HOH bend in H$_2$O and hints at the formation of adsorbed water from the dehydration reaction.

The highest spectral region (2000-4000 cm$^{-1}$) recorded is more complex due to the overlap between surface hydroxyl modes from the alumina surface and hydroxyl modes from chemisorbed ethanol. However, upon adsorption of ethanol, considerable increases in signal were readily identified and differentiated from the alumina hydroxyls. Literature suggests that surface hydroxyls of θ-alumina can be observed in the frequency range from 3000-3600 cm$^{-1}$ which is apparent in our measurement. Near 3430 cm$^{-1}$, a strong band appears that

DeCanio has suggested to occur from OH stretches in physisorbed ethanol. The appearance of the previously reported peaks in the monolayer ethanol sample confirm that the ethanol reacts with the alumina surface in a variety of ways including both physical and chemical interactions.

The sample containing monolayer ethanol on alumina which was heat treated at 300 °C for 1 hour exhibited several notable changes when compared with the non-heat-treated sample (see Figure 84 and Figure 85). First, the strong band near 93 cm-1 corresponding to ethanol decreased dramatically in intensity after heat treatment. Concomitantly, three peaks appear in the spectrum which align well with the bulk ethylene reference spectrum in Figure 84. In addition, the ethanol peaks in the bulk torsional range (150-200 $cm^{-1}$) decrease in intensity where the ethylene librational mode is expected to appear. In the higher frequency regime (see Figure 85), the peaks at 1500, 2750, and 3400 $cm^{-1}$ all decrease upon heating. The loss of the strong ethanol bands in the heat-treated spectra suggest that the dehydration reaction proceeds at 300 °C. Additionally, from the appearance of peaks in the low frequency spectrum, it appears ethylene is the main product in the dehydration on θ-alumina. Bulk ethylene has no strong excitations in the higher energy region, thus no statement can be made about the appearance of reaction products. A reference INS spectrum for diethyl ether was obtained from Parker *et al.* (Bennett 2015) The heat-treated sample did not contain any peaks that corresponded with the formation of diethyl ether.
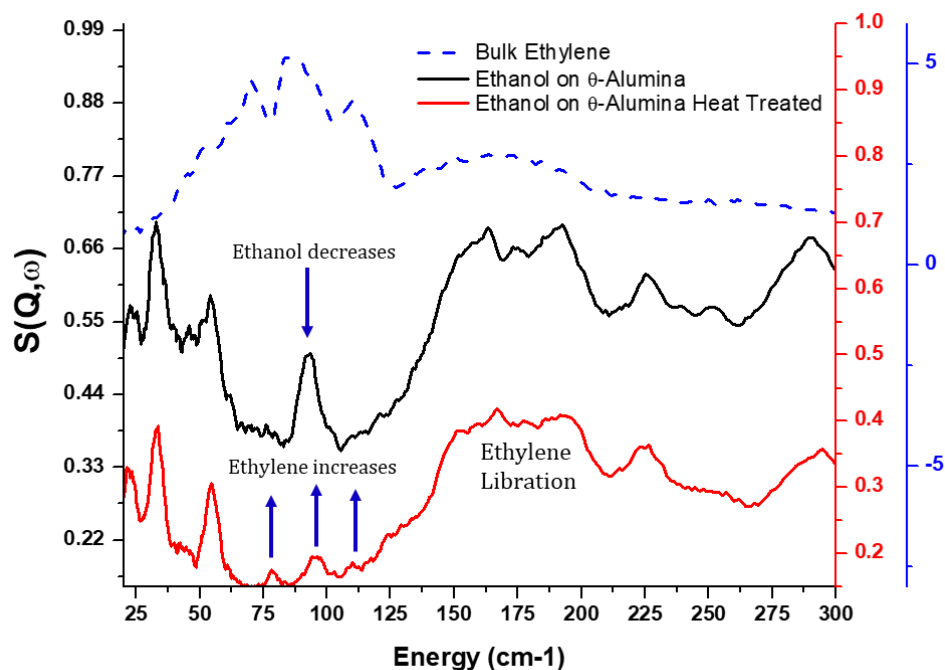
Figure 84 – INS spectrum of monolayer ethanol on θ-alumina (black) compared with the heat-treated ethanol on alumina (red) in the low energy regime (20-300 cm$^{-1}$). A INS spectrum of bulk ethylene (blue dash) is provided for reference (Lennon *et al.* (Lennon 2000))
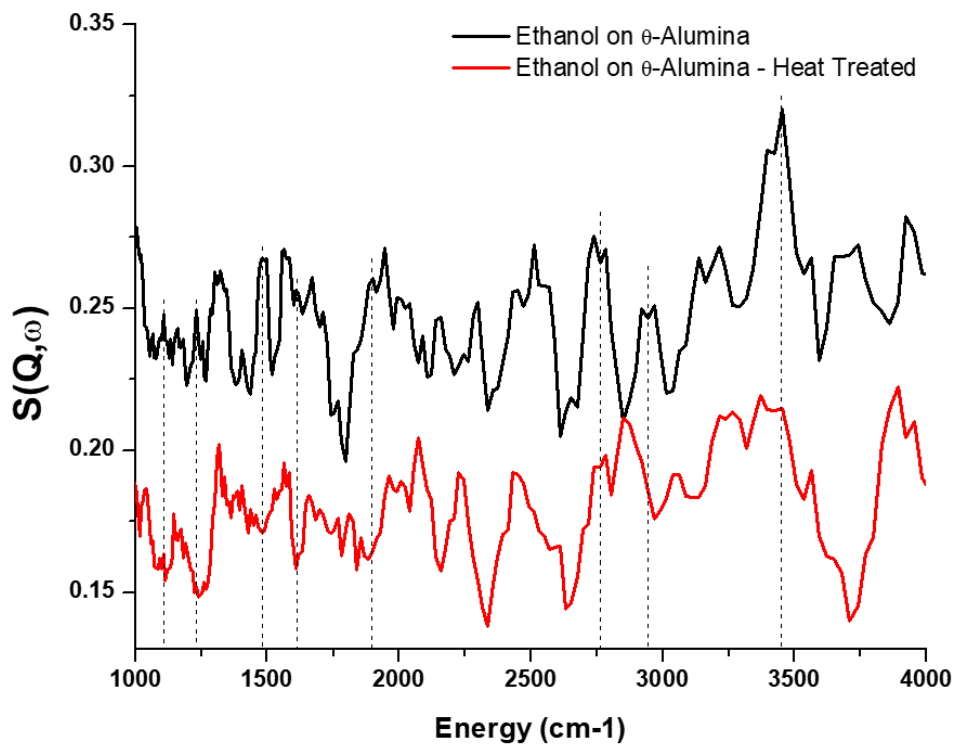
Figure 85 – INS spectrum of monolayer ethanol on θ-alumina (black) compared with the heat-treated ethanol on alumina (red) in the high energy regime (1000-4000 cm$^{-1}$).

## Conclusion

The adsorption, TPD, and INS measurements performed provided a bulk and microscopic understanding of the acid-catalyzed dehydration of ethanol on the surface of transition phase aluminas. Adsorption isotherm measurements revealed a decrease in available surface area with increasing calcination temperatures. The temperature programmed desorption measurements indicated that the dehydration reaction proceeds around 200 °C for γ-aluminas and nearly 300 °C for θ-alumina and beyond. This feature provided direct evidence that the surface reactivities are notably different for γ- and θ-alumina phases. INS is a technique which has only recently seen use in heterogenous catalysis. The sensitivity of INS to providing information about surface-catalyzed reactions can yield a potentially significant breakthrough in this realm. Our inelastic neutron scattering measurements confirmed that the ethanol chemically reacted with the alumina surface where a variety of intermediate ethoxide and surface hydroxyl species were observed. Due to the limited beam time provided for the INS measurements, our results do not justify the full potential of this technique. Further INS measurements and calculations performed on the interaction of ethanol with alumina are required before a comprehensive determination of the surface species can be made. The geometry optimized structures can be used to generate normal vibrational modes based on the classical GF-method using the program aClimax. Additional INS measurements are also planned for investigating the interaction of ethanol with other transition-phase aluminas.

# CHAPTER SEVEN – CONCLUSIONS AND FUTURE WORK

The physical adsorption of normal alkanes was examined on the surfaces of MgO(100), graphite, and hBN using volumetric adsorption isotherms and MD simulations. These results provide thermodynamic and microscopic insight into the influence of substrate symmetry and chemical composition on the adsorption properties of $n$-alkanes. The alkanes interact with these substrates primarily through weak vdW intermolecular forces. The thermodynamics of adsorption suggest that $n$-alkanes bind the strongest with the basal plane of graphite, followed by hBN and MgO(100) respectively. The weaker interaction with hBN indicates that the presence of a partial electrostatic potential does not increase the binding energy via polarization of alkane electrons. This was not too surprising considering the static polarization of alkanes is low. Using the homologous series of $n$-alkanes as adsorbates in a systematic study revealed that there is a relatively linear increase in the heat of adsorption with an increase in chain length on hBN and MgO(100). The critical phase transitions were identified using the change in 2D compressibility as a function of temperature. The precise location of these transitions can be improved in subsequent experiments using calorimetric methods. The MD showed how the geometry of the adsorbate molecule influences its layering behavior. The C(z) for methane, ethane, and propane revealed that there are rotational dynamics even in confined layers. The C(z) for longer alkanes indicated that there is less layer stratification in the multilayers, but the overall attraction to the surface results in a stabilization of the layer nearest to the surface at temperatures above the bulk

229

triple point. Structural and dynamical quantities were calculated from the MD trajectory; however, the analysis of these functions will be performed in a later publication. Additionally, neutron and x-ray diffraction experiments have been proposed in order to clarify the monolayer solid structures of alkanes on hBN and graphite. Future inelastic neutron scattering experiments aim to provide information about how the substrate's potential hinders rotational/configurational motions as well as the propagation of longitudinal and transverse acoustic modes previously observed in bulk alkanes.

In a secondary study, the chemical adsorption of ethanol was studied on the surface of transition aluminas. Upon adsorption, the ethanol was catalytically dehydrated to produce ethylene by surface Lewis and Brønsted acid sites. The dehydration reaction was studied *in-situ* using temperature programmed desorption and inelastic neutron scattering. The TPD measurements revealed that the surface reactivities differ between the γ- and θ-alumina phases where ethylene desorbs from the surface at higher temperatures on θ-alumina. Additionally, the side reaction that forms diethyl ether was minimized on the surface of θ-alumina. The INS measurements indicated that 1) the ethanol chemically binds to the surface, 2) the dehydration reaction proceeds near 300 °C, and 3) bulk ethylene is formed. The INS spectra were analyzed by making comparisons to previous spectroscopic measurements of surface bound ethanol. Future studies involve modeling the reaction intermediates on the surface of the transition aluminas. This has proven difficult in the past since the surface

structures of transition aluminas are not well defined and it is unclear how surface charges are redistributed from the undercoordinated surface atoms. Upon design of an accurate surface model for transition aluminas, density functional theory can be used to optimize the structure of a chemically-bound species and produce coordinates and force constants for normal mode analysis. The program aClimax (Ramirez-Cuesta 2004) can be used to produce a neutron vibrational density of states from the normal modes.

Finally, these studies underscore the value of INS techniques for the investigation of surface mediation of chemical reactions. Although the study described here is brief, the results clearly indicate that INS will play an important role in understanding the microscopic underpinnings of chemical reactions at interfaces.

# LIST OF REFERENCES

(Accelrys Forcite) Biova Products page. http://www.accelrys.com/products/datasheets/forcite.pdf (accessed Jun 6, 2014).

(Alder 1959) Alder, B.J.; Wainwright, T.E. Studies in Molecular Dynamics. I. General Method. *J. Chem. Phys.* **1959**, *31*, 459

(Alkhafaji 1991) Alkhafaji, M.T.; Migone, A.D. Vapor-pressure Study of the Melting of Two-Dimensional Argon Adsorbed on BN. *Physical Review B.* **1991**, *43*, 8741-8743

(Alkhafaji 1992) Alkhafaji, M.T.; Migone, A.D. Multilayer Adsorption Isotherm Study of Ar Films on Boron Nitride. *Physical Review B.* **1992**, *45*, 8767-8770

(Alkhafaji 1996) Alkhafaji, M.T.; Migone, A.D. Heat-capacity Study of Butane on Graphite. *Physical Review B.* **1996**, *53*, 11152-11155

(Arnold 2002(1)) Arnold, T.; Dong, C.C.; Thomas, R.K.; Castro, M.A.; Perdigon, A.; Clarke, S.M.; Inaba, A. The Crystalline Structures of the Odd Alkanes Pentane, Heptane, Nonane, Undecane, Tridecane, and Pentadecane Monolayers Adsorbed on Graphite at Submonolayer Coverages and from the Liquid. *Physical Chemistry Chemical Physics.* **2002**, *4*, 3430-3435

(Arnold 2002(2)) Arnold, T.; Thomas, R.K.; Castro, M.A.; Clarke, S.M.; Messe, L.; Inaba, A. The Crystalline Structures of the Even Alkanes Hexane, Octane, Decane, Dodecane and Tetradecane Monolayers Adsorbed on Graphite at Submonolayer Coverages and from the Liquid. *Physical Chemistry Chemical Physics.* **2002**, *4*, 345-351

(Arnold 2005) Arnold, T.; Cook, R. E.; Larese, J. Z. Thermodynamic Investigation of Thin Films of Ethane Adsorbed on Magnesium Oxide. *J. Phys. Chem. B.* **2005**, *109*, 8799-8805

(Arnold 2006) Arnold, T.; Chanaa, S.; Clarke, S. M.; Cook, R. E.; Larese, J. Z. Structure of an n-Butane Monolayer Adsorbed on Magnesium Oxide (100) *Phys. Rev. B.* **2006**, *74*, 85421

(Arnold 2012) Arnold, T.; Parker, J.E.; Macdonald, P. Investigation of the Adsorption of Alkanes on Hexagonal Boron Nitride from Their Liquids and Binary Mixtures. *Journal of Physical Chemistry C.* **2012**, *116*, 10599-10606

(Arnold 2014) Arnold, T.; Forster, M.; Fragkoulis, A.A.; Parker, J.E. Structure of Normal-Alkanes Adsorbed on Hexagonal Boron Nitride. *Journal of Physical Chemistry C.* **2014**, *118*, 2418-2428

(ASTM D4814) ASTM D4814-16b Standard Specification for Automotive Spark-Ignition Engine Fuel, ASTM International, West Conshohocken, PA, **2016**, http://dx.doi.org/10.1520/D4814-16B

(ASTM D910) ASTM D910-16 Standard Specification for Leaded Aviation Gasolines, ASTM International, West Conshohocken, PA, **2016**, http://dx.doi.org/10.1520/D0910-16

(Barnes 1970) Barnes, A.J.; Hallam, H.E. *Trans. Faraday Soc.*, **1970**, *66*, 1932

(Bennett 2015) Bennett, E.; Wilson, T.; Murphy, P.J.; Refson, K.; Hannon, A.C.; Imberti, S.; Callear, S.K.; Chass, G.A.; Parker, S.F. *Inorg. Chem.* **2015**, *54*, 2213.

(Bernal 1924) Bernal, J.D. The Structure of Graphite. *Proc. Royal Soc. A.* **1924**, *106*, 749

(Biello 2007) Biello, D. Fact or Fiction?: Premium Gasoline Delivers Premium Benefits to Your Car. *Scientific American.* **2007**.

(Bienfait 1980) Bienfait, M. Two Dimensional Phase Transitions in Classical van der Waals Films Adsorbed on Graphite. *Phase Transitions in Surface Films.* Dash, J.G., Ruvalds, J. Eds.; Springer, **1980**, Vol. 1, pp 29-64

(Bienfait 1999) Bienfait, M.; Zeppenfeld, P.; Gay, J.M.; Palmari, J.P. Surface Melting on the Close-Packed (111) Face of Methane Thin Films Condensed on Graphite. *Surface Science.* **1990**, 226, 327-338

(Bockel 1979) Bockel, C; Thomy, A.; Duval, X. Étude Comparée de la Premiére Couche D'Adsorption de Méthane Sur Nitrure de Bore et Graphite. *Surface Science.* **1979**, *90*, 109-120

(Bomchil 1980) Bomchil, G.; Huller, A.; Rayment, T.; Roser, S.J.; Smalley, M.V.; Thomas, R.K.; White, J.W. The Structure and Dynamics of Methane Adsorbed on Graphite. *Philosophical Transactions of the Royal Society of London B.* **1980**, *290*, 537-552

(B.P. 2010) B.P. Australia Ltd. Fuel, Octane, and Power. *Fuel News* [Online] **2010**, http://www.bp.com/content/dam/bp-country/en\_au/media/fuel-news/fuel-octane-power.pdf (accessed Jan 14, 2016).

(Braden 1999) Braden D.A.; Parker, S.F.; Tomkinson, J.; Hudson, B.S. Inelastic Neutron Scattering Spectra of the Longitudinal Acoustic Modes of the Normal Alkanes from Pentane to Pentacosane. *J. Chem. Phys.* **1999**, *111*, 429-437

(Brager 1937) Brager, A. An X-Ray Examination of the Structure of Boron Nitride. *Acta Physicochimica (USSR)*, **1937**, *7*, 699-706

(Broadhurst 1962) Broadhurst, M.G. An Analysis of the Solid Phase Behavior of the Normal Paraffins. *Journal of Research of the NBS – A. Phys. and Chem.* **1962**, *66A*, 241-249.

(Bruch 1997) Bruch, L. W.; Cole, M. W.; Zaremba, E. *Physical Adsorption: Forces and Phenomena*; Oxford University Press, **1997**.

(Bruch 2007) Bruch, L. W.; Diehl, R. D.; Venables, J. A. Progress in the Measurement and Modeling of Physisorbed Layers. *Rev. Mod. Phys.* **2007**, *79*, 1381−1454.

(Brunauer 1940) Brunauer, S.; Deming, L.S.; Deming, W.E.; Teller, E. On a Theory of the van der Waals Adsorption of Gases. *J. Amer. Chem. Soc.* **1940**, *62*, 1723

(Brunauer 1938) Brunauer, S.; Emmett, P.H.; Teller, E. Adsorption of Gases in Multimolecular Layers. *J. Am. Chem. Soc.* **1938***, 60*, 309-319

(Cassabois 2015) Cassabois, G.; Valvin, P.; Gil, B. Hexagonal Boron Nitride is an Indirect Bandgap Semiconductor. *Nature Photonics*. **2015**, *10*, 262-266

(Cassie 1944) Cassie, A.B.D. Multimolecular Absorption. *Trans. Faraday Soc.* **1945**, *41*, 450-458

(Castro 1998) Castro, M. A.; Clarke, S. M.; Inaba, I.; Arnold, T.; Thomas, R. K. Competitive Adsorption of Simple Linear Alkane Mixtures onto Graphite. *J. Phys. Chem. B* **1998**, *102*, 10528−10534.

(Castro 1999) Castro, M.A.; Clarke, S.M.; Inaba, A.; Arnold, T.; Thomas, R.K. Anomalous Behavior of Pentane Adsorbed at the Graphite/Liquid Interface. *Physical Chemistry Chemical Physics*. **1999**, *1*, 5203-5207

Clarke, S.M.; Inaba, A.; Arnold, T.; Thomas, R.K. Calorimetric Investigation of the Monolayers Formed at Solid-Liquid Interface. *Journal of Thermal Analysis and Calorimetry*. **1999**, *57*, 643-651

(Coq 1995) Coq, B.; Figuéras, F.; Hub, S.; Tournigant, D. Effect of the Metal-Support Interaction on the Catalytic Properties of Palladium for the Conversion of Difluorodichloromethane with Hydrogen: Comparison of Oxides and Fluorides as Supports. *J. Phys. Chem.* **1995**, *99*, 11159-11166

(Cook 2006) Cook, R.E. Thermodynamic and Neutron Structural Studies of Hydrocarbon Adsorption on MgO Nanocubes. Ph.D. Thesis, University of Tennessee. **2006**

(Cook 2015) Cook, R. E.; Arnold, T.; Strange, N.; Telling, M.; Larese, J.Z. Pentane Adsorbed on MgO(100) Surfaces: A Thermodynamic, Neutron, and Modeling Study. *J. Phys. Chem. C.* **2015**, *119*, 332-339

(Dash 1975) Dash, J. G. *Films on Solid Surfaces*; Elsevier Science & Technology Books, **1975**.

(DeCanio 1992) DeCanio, E.C.; Nero, V.P.; Bruno, J.W. *J. Catal.* **1992**, *135*, 444.

(Deepika 2014) Deepika; Li, L.H.; Glushenkov, A.M.; Hait, S.K.; Hodgson, P.; Chen, Y. High-Efficient Production of Boron Nitride Nanosheets via an Optimized Ball Milling Process for Lubrication in Oil. *Scientific Reports.* **2014**, *4*

(Dettenmaier 1978) Dettenmaier, M. *J. Chem. Phys.* **1978**, *68*, 2319

(Diama 1999) Diama, A.; Migone, A.D. Multilayer Kr Films Adsorbed on BN. *Physical Review B.* **1999**, *60*, 16103-16108

(Dubinin 1952) Dubinin, M.M. Adsorption of Gases and Vapors and Structure of Adsorbents. *Uspeckhi Khimii*, **1952**, *21*, 513-533

(Dupont-Pavlovsky 1985) Dupont-Pavlovsky, N.; Bockel, C.; Thomy, A. Adsorbed Gases on (0001) Graphite and Boron Nitride: Specific Behavior of Krypton. *Surface Science*, **1985**, *160*, 12-22

(Durig 1989) Durig, J.R.; Larsen, R.A. *J. Mol. Struc.* **1989**, *238*, 195.

(Egami 2003) Egami, T.; Billinge, S. Underneath the Bragg Peaks. Pergamon, **2003**, Vol. 1

(Emmett 1937) Emmett, P.H.; Brunauer, S. The Use of Low Temperature van der Waals Adsorption Isotherms in Determining the Surface Area of Iron Synthetic Ammonia Catalysts. *J. Am. Chem. Soc.* **1937**, *59*, 1553-1564

(Felty 2008) Felty, M. Adsorption of Propane on the Magnesium Oxide (100) Surface and Synthesis of Anodized Aluminum Oxide. Ph.D. Thesis, University of Tennessee, December, **2008**

(Fernández-Cañoto 2014) Fernández-Cañoto, D.; Larese, J. Z. Thermodynamic and Modeling Study of Thin n-Heptane Films Adsorbed on Magnesium Oxide (100) Surfaces. *J. Phys. Chem. C.* **2014**, *118*, 3451-3458

(Ferreira 1984) Ferreira, O.; Colucci, C.C.; Lerner, E.; Vilches, O.E. The Two-Dimensional Liquid-Vapor Coexistence Line of Methane Adsorbed on Graphite. *Surface Science.* **1984**, *146*, 309-317

(Flory 1974) Flory, P.J. Foundations of Rotational Isomeric State Theory and General Methods for Generating Configurational Averages. *Macromolecules.* **1974**, *7*, 381-392

(Freitag 2000) Freitag, A.; Larese, J. Z. Layer Growth of Methane on MgO: An Adsorption Isotherm Study. *Phys. Rev. B.* **2000,** *62,* 8360-8365

(Freundlich 1930) Freundlich, H. *Kapillarchemie,* Leipzig, **1930**

(Gay 1986) Gay, J.M.; Suzanne, J.; Wang, R. Phase Transitions, Thermodynamics, and Structural Analysis of Ethane Films Adsorbed on Graphite. *Journal of the Chemical Society, Faraday Transactions 2.* **1986,** *82,*1669-1684

(Goret 2016) Goret, G.; Aoun, B.; Pellegrini, E. MDANSE: An Interactive Analysis Environment for Molecular Dynamics Simulations. *J. Chem. Inf. Model.* **2016**, *57*, 1-5

(Grant 2016) Grant, J.T.; Carrero, C.A.; Goeltl, F.; Venegas, J.; Mueller, P.; Burt, S.P.; Specht, S.E.; McDermott, W.P.; Chieregato, A.; Hermans, I. Selective Oxidative Dehydrogenation of Propane to Propene Using Boron Nitride Catalysts. *Science.* **2016**, *354*, 1570-1573

(Grillet 1980) Grillet, Y.; Rouquerol, J. Two-Dimensional Phase Changes of Argon Adsorbed on Boron Nitride at 77 K. *Journal of Colloid and Interface Science.* **1980**, *77*, 580-582

(Hansen 1993) Hansen, F. Y. Molecular Dynamics Studies of the Melting of Butane and Hexane Monolayers Adsorbed on the Basal-Plane Surface of Graphite. *J. Chem. Phys.* **1993**, *98*, 4128-4141.

(Henrich 1976) Henrich, V.E. Thermal Faceting of (110) and (111) Surfaces of MgO. *Surface Science*, **1976**, *57*, 385--392

(Hussein 1991) Hussein, G.A.M.; Sheppard, N.; Zaki, M.I.; Fahim, R.B. *J. Chem. Soc. Faraday Trans*. **1991**, *87*, 2661.

(IUPAC 1985) International Union of Pure and Applied Chemistry. Reporting Physisorption Data for Gas/Solid Systems with Special Reference to the Determination of Surface Area and Porosity (Recommendations 1984). *Pure & Appl. Chem.* **1985**, *57*, 603-619

(Jacoby 2017) Jacoby, M. 2-D Materials Go Beyond Graphene *Chemical and Engineering News.* **2017**, *95*,} 36-40

(Jones 1924) Jones, J.E. On the Determination of Molecular Fields. – II. From the Equation of State of a Gas. *Proc. Royal Soc. A.* **1924**, *106*, 463-477

(Kayser 1881) Kayser, H. *Wied Ann. Phys.* **1881**, *12*, 526

(Kim 1984) Kim, H.K.; Chan, M.H.W. Experimental Determination of a Two-Dimensional Liquid-Vapor Critical-Point Determination. *Phys. Rev. Lett.* **1984**, *53*, 170-173

(Kimuraa 1999) Kimuraa, Y.; Wakabayashia, T.; Okadab, K.; Wadac, T.; Nishikawad, H. Boron Nitride as a Lubricant Additive. *Wear*, **1999**, *2*, 199-206

(King Jr. 1993) King Jr., H.E.; Sirota, E.B.; Shao, H.; Singer, D.M. A Synchrotron X-Ray Scattering Study of the Rotator Phases of the Normal Alkanes. *J. Phys. D: Appl. Phys.* **1993**, *26*, B133-B136

(Kinger 2001) Kinger, G.; Vinek, H. n-Nonane Hydroconversion on Ni and Pt containing HMFI, HMOR, and HBEA. *Applied Catalysis*, **2001**, *218,* 139-150

(Knözinger 1978) Knözinger, H; Stubner, B. *J. Phys. Chem.* **1978**, *82*, 1526.

(Koehler 2000) Koehler III, C.F.; Larese, J.Z. *Rev. Sci. Instrum.*, **2000**, *71*, 324.

(Kosterlitz 1972) Kosterlitz, J.M.; Thouless, D.J. Long Range Order and Metastability in Two Dimensional Solids and Superfluids. (Application of dislocation theory). *Journal of Physics C: Solid State Physics*, **1972**, *5*, L124

(Krim 1985) Krim, J.; Suzanne, J.; Shechter, H.; Wang, R.; Taub, H. A LEED and Neutron Diffraction Study of Hexane Adsorbed on Graphite in the Monolayer Range: Uniaxial Commensurate-Incommensurate Transition. *Surface Science*. **1985**, *162*, 446-451

(Krutchen 2005) Kruchten, F.; Knorr, K.; Volkmann, U. G.; Taub, H.; Hansen, F. Y.; Matthies, B.; Herwig, K. W. Ellipsometric and Neutron Diffraction Study of Pentane Physisorbed on Graphite. *Langmuir*. **2005**, *21*, 7507-7512

(Kunnmann-Larese 2001) Kunnmann, W.; Larese, J. Z. Novel Method for the Generation of High Density (Pure and Doped) Magnesium Vapors Which Bypass the Liquidus Phase. U.S. Patent 6,179,897, January 30, 2001

(Kurakevych 2007) Kurakevych, O.O.; Solozhenko, V.L. Rhombohedral Boron Subnitride, B13N2, by X-ray Powder Diffraction. *Acta Cryst. C.* **2007**, *63*, 80-82

(Kwak 1992) Kwak, J.H.; Peden, C.H.F.; Szani, J. *J. Phys. Chem. C.* **2011**, *115*, 12575.

(Kwak 2008) Kwak, J.H.; Hu, J.; Lukaski, A.; Kim, D.H.; Szanyi, J.; Peden, C.H.F. *J. Phys. Chem. C.* **2008**, *112*, 9486.

(Kwak 2009) Kwak, J.H.; Hu, J.; Mei, D.; Yi, C.W.; Kim, D.H.; Peden, C.H.F.; Allard, L.F.; Szanyi, J. *Science*, **2009**, *325*, 1670.

(Kwak 2011) Kwak, J.H.; Mei, D.; Peden, C.H.F.; Rousseau, R.; Szanyi, J. *Catal. Lett.*, **2011**, *141*, 649.

(Landolt-Börnstein) Subvolume A 'Vapor Pressure and Antoine Constants for Hydrocarbons, and S, Se, Te, and Halogen Containing Organic Compounds' of Volume 20 'Vapor Pressure of Chemicals' of Landolt-Börnstein - Group IV Physical Chemistry.

(Larese 1988(1)) Larese, J. Z.; Harada, M.; Passell, L.; Krim, J.; Satija, S. Neutron-Scattering Study of Methane Bilayer and Trilayer Films on Graphite. *Phys. Rev. B.* **1988**, *37*, 4735-4742

(Larese 1988(2)) Larese, J.Z.; Passell, L.; Heidemann, A.D.; Richter, D.; Wicksted, J.P. Melting in Two Dimensions: The Ethylene-on-Graphite System. *Phys. Rev. Lett.* **1988**, *61*, 432-435

(Larese 1995) Larese, J. Z.; Zhang, K. M. Phase Transitions of Argon Multilayer Films on Graphite: Evolution from Multilayer Film to Bulk Solid. *Phys. Rev. B: Condens. Matter Mater. Phys.* **1995**, *51*, 17023−17027.

(Larese 2008) Larese, J.Z.; Arnold, T.; Frazier, L.; Hinde, R.J.; Ramirez-Cuesta, A.J. *Phys. Rev. Lett.*, **2008**, *101*, 165302.

(Larese 2018) Larese, J.Z. Private Communication, **2018**.

(Larher 1971) Larher, Y. PhD. Thesis. Universite de Paris (France) Contribution a l'etude de la structure des phases physisorbees par analyse thermodynamique des isothermes a marches du krypton, du xenon, de l'argon et du methane sur la face de clivage d'halogenures a structure lamellaire **1971**

(Larher 1976) Larher, Y. Chaleurs Isosteriques Et Entropies D'Adsorption Pour Des Systemes Presentant Des Changements De Phase Bidimensionnels (2D). *Journ. Calorim. Anal. Therm.* **1976**, 1−11.

(Larher 1979) Larher, Y. The Critical Exponent β Associated with the Two-Dimensional Condensation in the Second Adlayer of Argon on the Cleavage Face of Cadmium Chloride. *Mol. Phys.* **1979**, *38*, 789-795

(Larson 2000) Larson, A.C.; Von Dreele, R.B. "General Structure Analysis System (GSAS)", *Los Alamos National Laboratory Report* LAUR 86-748 **2000**.

(Li 1996) Li, W.; Shrestha, P.; Migone, A.D.; Marmier, A.; Girardet, C. Monolayer Kr Films Adsorbed on BN. *Physical Review B.* **1996**, *54*, 8833-8843

(Liu 2003) Liu, L.; Feng, Y.P.; Shen, Z.X. Structural and Electronic Properties of *h*-BN. *Physical Review B.* **2003**, *68*, 104102-1-8

(Lee 1997) Lee, M.A.; Alkhafaji, M.T.; Migone, A.D. Heat Capacity Study of Monolayer Propane on Graphite. *Langmuir.* **1997**, *13*, 2791-2794

(Leimkuhler 2010) Leimkuhler, B.; Noorizadeh, E.; Penrose, O. Comparing the efficiencies of stochastic isothermal molecular dynamics methods. *Heriot-Watt Mathematics Report.* **2010**, *30*

(Lennon 2000) Lennon, D.; McNamara, J.; Phillips, J.R.; Ibberson, R.M.; Parker, S.F. *Phys. Chem. Chem. Phys.* **2000**, *2*, 4447.

(McBain 1909) McBain, *J.W. Phil. Mag.* **1909**, *18*, 916

(McKie 1986) McKie, D.; McKie, C. *Essentials of Crystallography*. Blackwell Scientific, 2nd edition **1986** p. 6-8

(Migone 1993) Migone, A.D.; Alkhafaji, M.T.; Vidali, G.; Karimi, M. Thermodynamic Study of Argon Films Adsorbed on Boron Nitride. *Physical Review B.* **1993**, *47*, 6685-6696

(Momentive) Momentive Performance Materials Condensed Product Bulletin. https://momentive.com/products/.../BN-Powder-Grades-AC6004--26amp-3b-AC6069/

(Morishige 1996) Morishige, K.; Inoue, K.; Imai, K. X-ray Study of Kr, Xe, and $N_2$ Monolayers on Boron Nitride. *Langmuir.* **1996**, *12*, 4889-4891

(Mursic 1996) Mursic, Z.; Lee, M. Y. M.; Johnson, D. E.; Larese, J. Z. A Computer Controlled Apparatus for Performing High Resolution Adsorption Isotherms. *Rev. Sci. Inst.* **1996** *67* 1886-1890.

(Nash 2016) Nash,D.J.; Restrepo, D.T.; Parra, N.S.; Giesler, K.E.; Penabade, R.A.; Aminpour, M.; Le, D.; Li, Z.; Farha, O.K.; Harper, J.K.; Rahman, T.S.; Blair, R.G. Heterogeneous Metal-Free Hydrogenation over Defect-Laden Hexagonal Boron Nitride. *ACS Omega.* **2016**, *1*, 1343-13543

(Nham 1988) Nham, H.S.; Hess, G.B. Layer Critical Points of Multilayer Ethane Adsorbed on Graphite. *Phys. Rev. B.* **1988**, *38*, 5166-5169

(NIST) NIST Chemistry Webbook. http://webbook.nist.gov

(Novoselev 2004) Novoselov, K.S.; Geim, A.K.; Morozov, S.V.; Jiang, D.; Zhang, Y.; Dubonos, S.V.; Grigorieva, I.V.; Firsov, A.A. Electric Field Effect in Atomically Thin Carbon Films. *Science.* **2004**, *306*, 666-669

(Otsuka 2004) Otsuka, K.; Abe, Y.; Kanai, N.; Kobayashi, Y.; Takenaka, S.; Tanabe, E. Synthesis of Carbon Nanotubes on Ni/carbon-fiber Catalysts Under Mild Conditions. *Carbon.* **2004**, *42*, 727-736

(Park 2012) Park, J.; Nam, S.; Lee, M.; Lieber, C. Synthesis of Monolithic Graphene-Graphite Integrated Electronics. *Nature Materials*. **2012**, *11*, 120-125

(Perim 2013) Perim, E.; Paupitz, R.; Galvão, D.S. Controlled Route to the Fabrication of Carbon and Boron Nitride Nanoscrolls: A Molecular Dynamics Investigation. *Journal of Applied Physics*. **2013**, *113*, 54306 1-5

(Peterson 2014) Peterson, E.J. *et al. Nat. Comm.* **2014**, *5*, 1-11.

(Pines 2014) Pines. H; Haag, W.O. *J. Am. Chem. Soc.* **1960**, *82*, 2471.

(Polanyi 1914) Polanyi, M. *Verh. Deutsch Phys. Ges.* **1914**, *16*, 1012

(Ramirez-Cuesta 2004) Ramirez-Cuesta, T. aCLIMAX 4.0.1, The New Version of the Software for Analyzing and Interpreting INS Spectra. *Computer Phys. Comm.* **2004**, *157*, 226-238

(Rappé 1992) Rappé, A.K.; Casewit, C.J.; Colwell, K.S.; Goddard III, W.A.; Skiff, W.M. UFF, A Full Periodic Table Force Field for Molecular Mechanics and Molecular Dynamics Simulations. *J. Am. Chem. Soc.* **1992**, *114*, 10024-10035

(Regnier 1981) Regnier, J.; Menaucourt, J.; Thomy, A.; Duval, X. Proprietes Thermodynamiques du Film D'Ethane Adsorbe Sur Graphite. *Journal de Chimie Physique*. **1981**, *78*, 629-633

(Saint-Gobain) Saint-Gobain Materials Data Sheet. http://www.bn.saint-gobain.com/sites/imdf.bn.com/files/combat-bn-solids-ds.pdf

(Saniger 1995) Saniger, J.M. *Mat. Lett.*, **1995**, *22*, 109.

(Sears 1992) Sears, V.F. *Neutron News*, **1992**, *3*, 29-37.

(Seeger 2009) Seeger, P.A.; Daemen, L.L.; Larese, J.Z. *Nucl. Instr. Meth. Phys. Res. A*, **2009**, *604*, 719.

(Shrestha 1994) Shreshta, P; Alkhafaji, M.T.; Lukowitz, M.M.; Yang, G.; Migone, A.D. Adsorption Studies on Boron Nitride Substrates. *Langmuir*, **1994**, *10*, 3244-3249

(Shriver 1986) Shriver, D.F.; Drezdon, M.A. The Manipulation of Air-Sensitive Compounds. John Wiley & Sons, 1st Ed. **1986**

(Strange 2016) Strange, N.; Fernández-Cañoto, D.; Larese, J. Z. Thermodynamic and Modeling Study of N-Octane, N-Nonane, and N-Decane Films on MgO(100). *J. Phys. Chem. C.* **2016**, *120*, 18631-18641

(Stokes 1997) Stokes, D.E. *Pasteur's Quadrant.* Brookings Institution Press, Washington, D.C. **1997**, 46-49

(Sun 1998) Sun H. COMPASS: An ab initio Force-Field Optimized for Condensed-Phase Applications – Overview with Details on Alkane and Benzene Compounds. *J. Phys. Chem. B.* **1998**, *102*, 7338-7364

(Tessier 1982) Tessier, C.; Larher, Y. Isotope Effect in the Melting of Monolayers of Tetradeuterated Methane Adsorbed on Boron Nitride. *Adsorption at the gas-solid and liquid-solid interface* **1982**, 503-509

(Thibeault 2012) Thibeault, S.A.; Fay, C.C.; Lowther, S.E.; Earle, K.D.; Sauti, G.; Kang, J.H.; Park, C. Radiation Shielding Materials Containing Hydrogen, Boron, and Nitrogen: Systematic Computational and Experimental Study - Phase I. *NIAC Final Report* September 30, 2012 https://www.nasa.gov/directorates/spacetech/niac/thibeault\_radiation\_shielding.html

(Tomkinson 2002) Tomkinson, J.; Parker, S.F.; Braden, D.A.; Hudson, B.S. Inelastic Neutron Scattering Spectra of the Transverse Acoustic Modes of the Normal Alkanes. *Phys. Chem. Chem. Phys.* **2002**, *4*, 716-721

(Tswett 1990) Tswett, M.S. Chromatographic Adsorption Analysis: Selected Works. Elis Horwood Ltd., **1990**

(Volkenstein 1959) Volkenstein, M.V. Configurational Studies of Polymeric Chains. Interscience, New York, N.Y. **1963**

(Veldhuizen 2000) Veldhuizen, E.J.A.; Haagsman, H.P. Role of Pulmonary Surfactant Components in Surface Film Formation and Dynamics. *Biochimica et Biophysica Acta*, **2000**, *1467*, 255-270

(Wefers 1987) Wefers, K.; Misra, C. Oxides and Hydroxides of Aluminum, *Alcoa Technical Paper*, **1987**, 19, 47.

(Welters 1995) Welters, W. J. J.; van der Waerden, O. H.; Zandbergen, H. W.; de Beer, V. H. J.; van Santen, R. A. Hydrocracking of N-Decane over Zeolite-Supported Metal Sulfide Catalysts. 1. CaY-Supported Transition Metal Sulfides. *Industrial & Engineering Chemistry Research,* **1995**, *34*, 1156-1165

(Wexler 2009) Wexler, C.; Firlej, L.; Kuchta, B.; Roth, M. W. Melting of Hexane Monolayers Adsorbed on Graphite: The Role of Domains and Defect Formation. *Langmuir*. **2009**, *25*, 6596-6598

(Williams 2004) Williams, G.J.; Stone, A.J. Transferable Polarizabilities for the Alkanes. *Molecular Physics*. **2004**, *102*, 985-991

(Wolfson 1996) Wolfson, R.A.; Arnold, L.M.; Shrestha, P.; Migone, A.D. Comparative Study of the Substrate Quality of BN Powders. *Langmuir*. **1996**, *12m*, 2868-2871

(Wyckoff 1963) Wyckoff, R.W.G. *Crystal Structures – Volume 1*. Interscience Publishers, New York. **1963**, 2nd Ed.

(Xinghua 2010) Xinghua, Z.; Tiejun, W.; Longlong, M.; Chuangzhi, W. Aqueous-Phase Catalytic Process for Production of Pentane from Furfural over Nickel-Based Catalysts. *Fuel*, **2010**, *80*, 2697-2702

(Yang 2016) Yang K.; Cai, Z.; Jaiswal, A.; Tyagi, M.; Moore, J.S.; Zhang, Y. Dynamic Odd-Even Effect in Liquid *n*-Alkanes near Their Melting Points. *Angew. Chem. Int. Ed.*, **2016**, *55*, 14090-14095

(Yaron 2006) Yaron, P. N.; Telling, M. T. F.; Larese, J. Z. Thermodynamic Investigation of n-Hexane Thin Films Adsorbed on Magnesium Oxide. *Langmuir*, **2006**, *22*, 7203-7207

(Yoon 1978) Yoon, D.Y.; Flory, P.J. Small Angle Neutron Scattering by *n*-Alkanes Chains. *J. Chem. Phys.* **1978**, *69*, 2536-2538

(Zeldovich 1934) Zeldovich, Y.B. *Acta Physicochimica URSS*. **1934**, *1*, 961-974

(Zhang 1990) Zhang, S.; Migone, A.D. Heat-Capacity Study of Bilayer Ethane Films Adsorbed on Graphite. *Physical Review B*. **1990**, *42*, 8674-8677

(Zhang 2012) Zhang, Y.G.; He, H.Y.; Pan, B.C. Structural Features and Electronic Properties of MgO Nanosheets and Nanobelts. *J. Phys. Chem. C*. **2012**, *116*, 23130-23135

**APPENDIX**
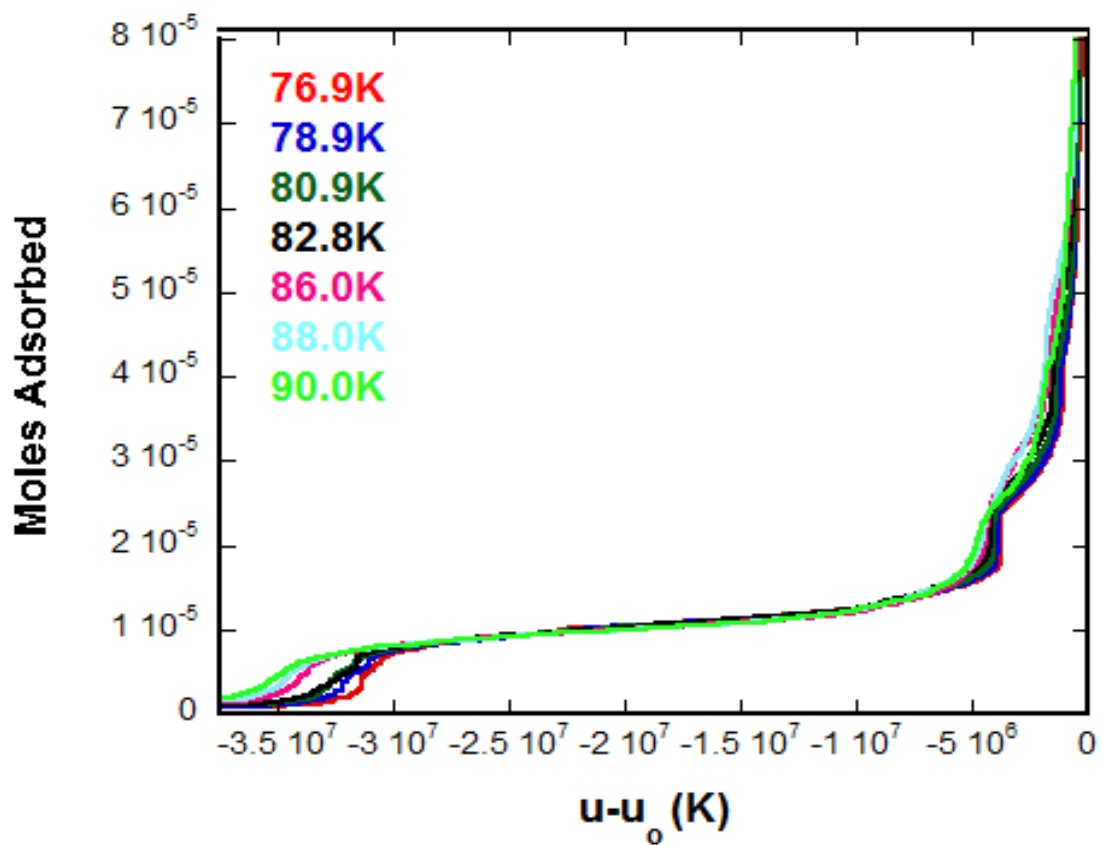
Figure 86 – Series of isotherms (chemical potential vs. moles adsorbed for methane on hBN.
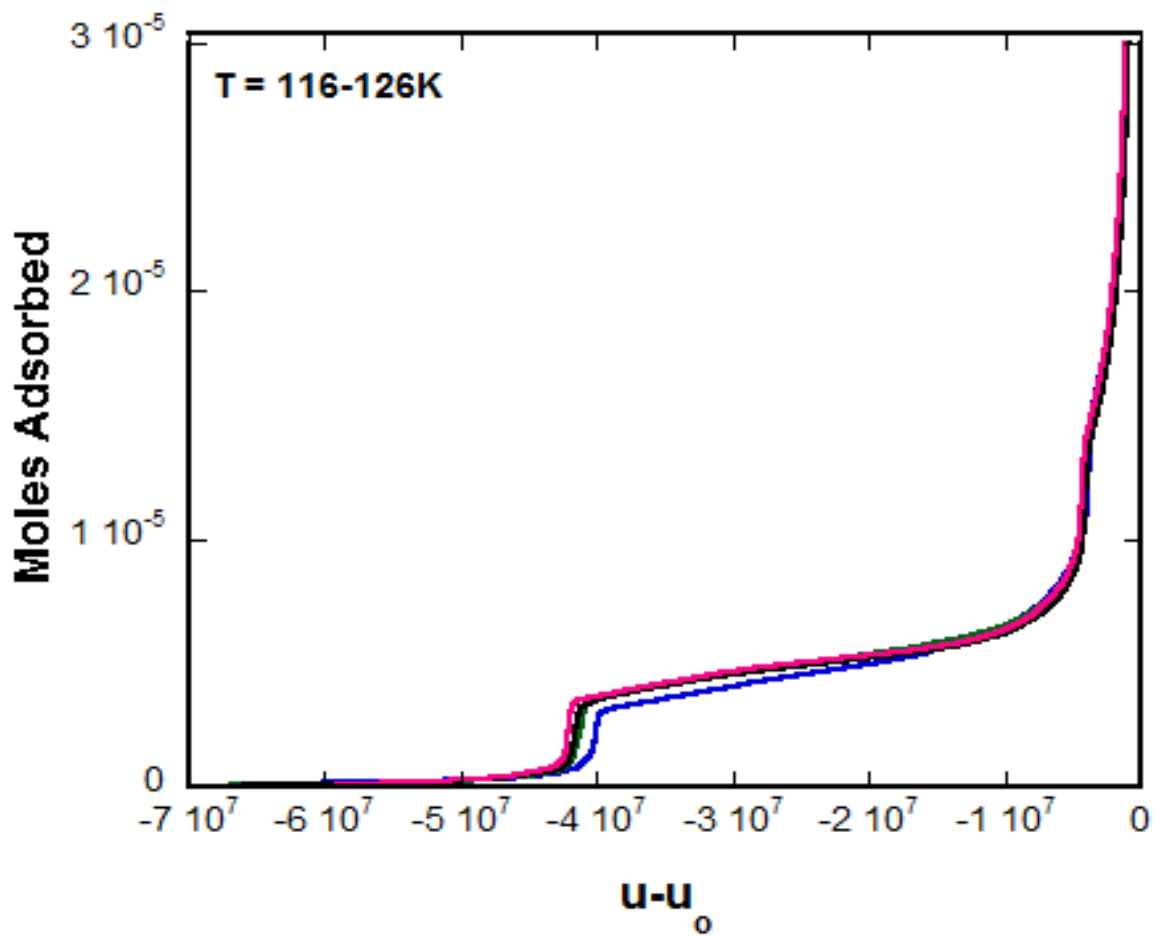
Figure 87 – Series of isotherms (chemical potential vs. moles adsorbed for ethane on hBN
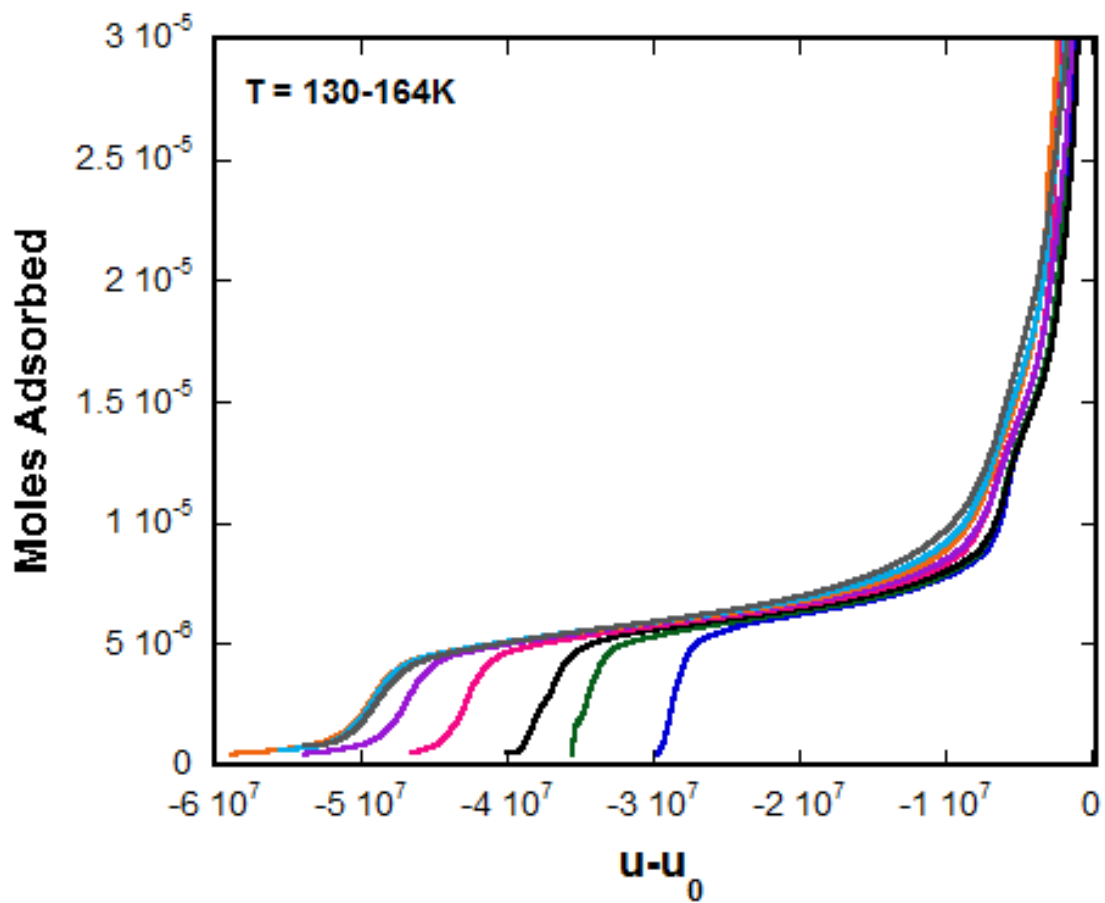
Figure 88 – Series of isotherms (chemical potential vs. moles adsorbed for propane on hBN
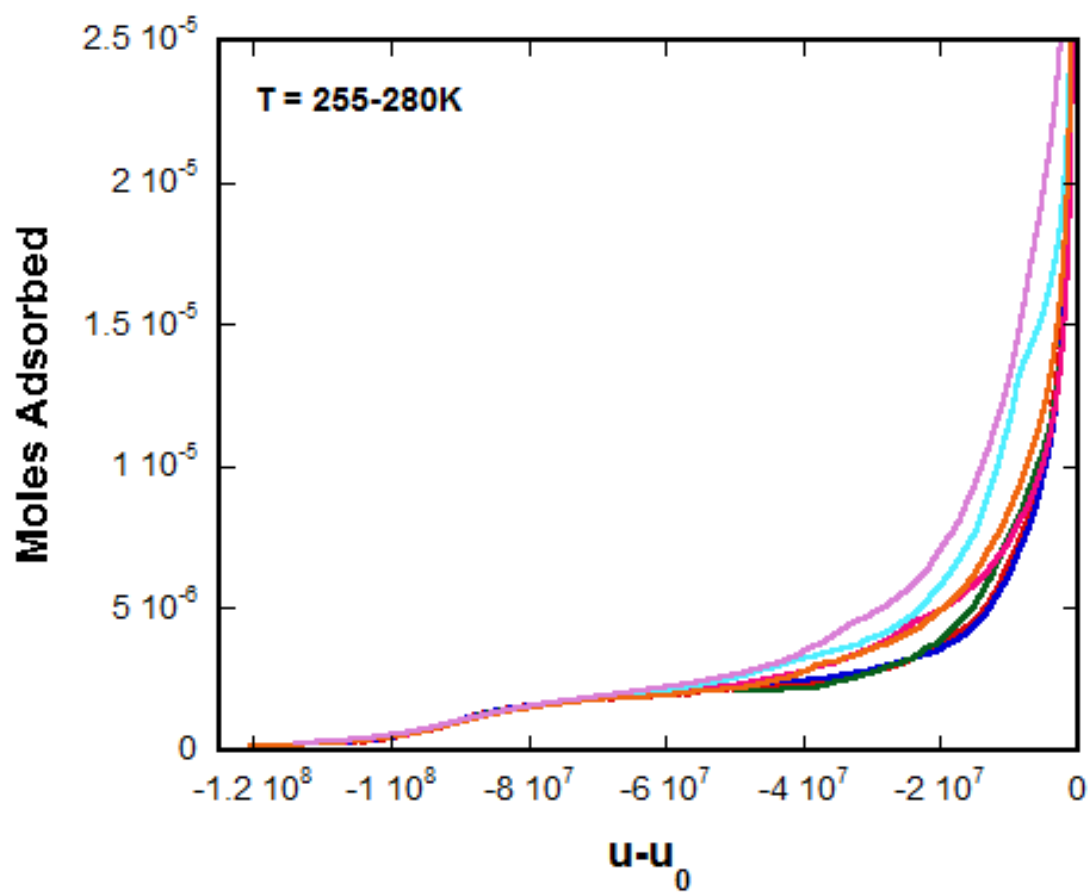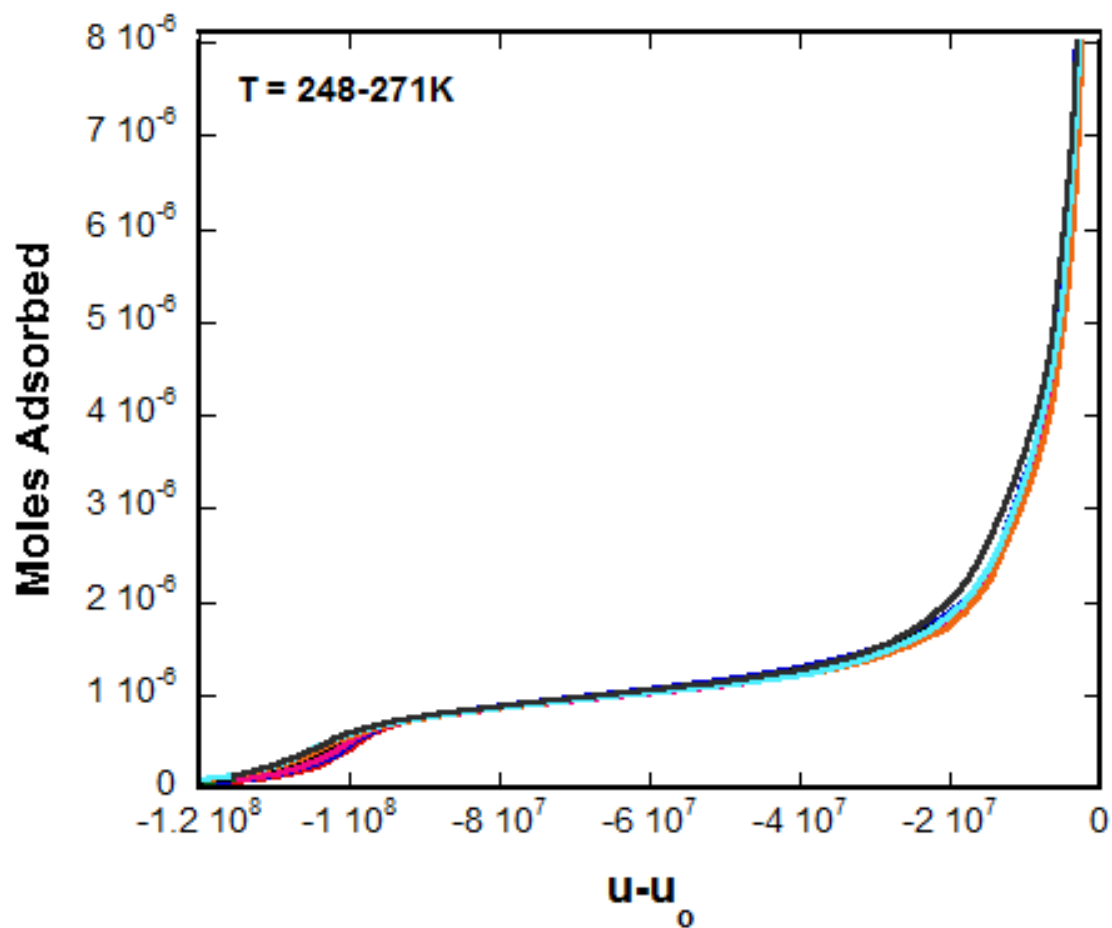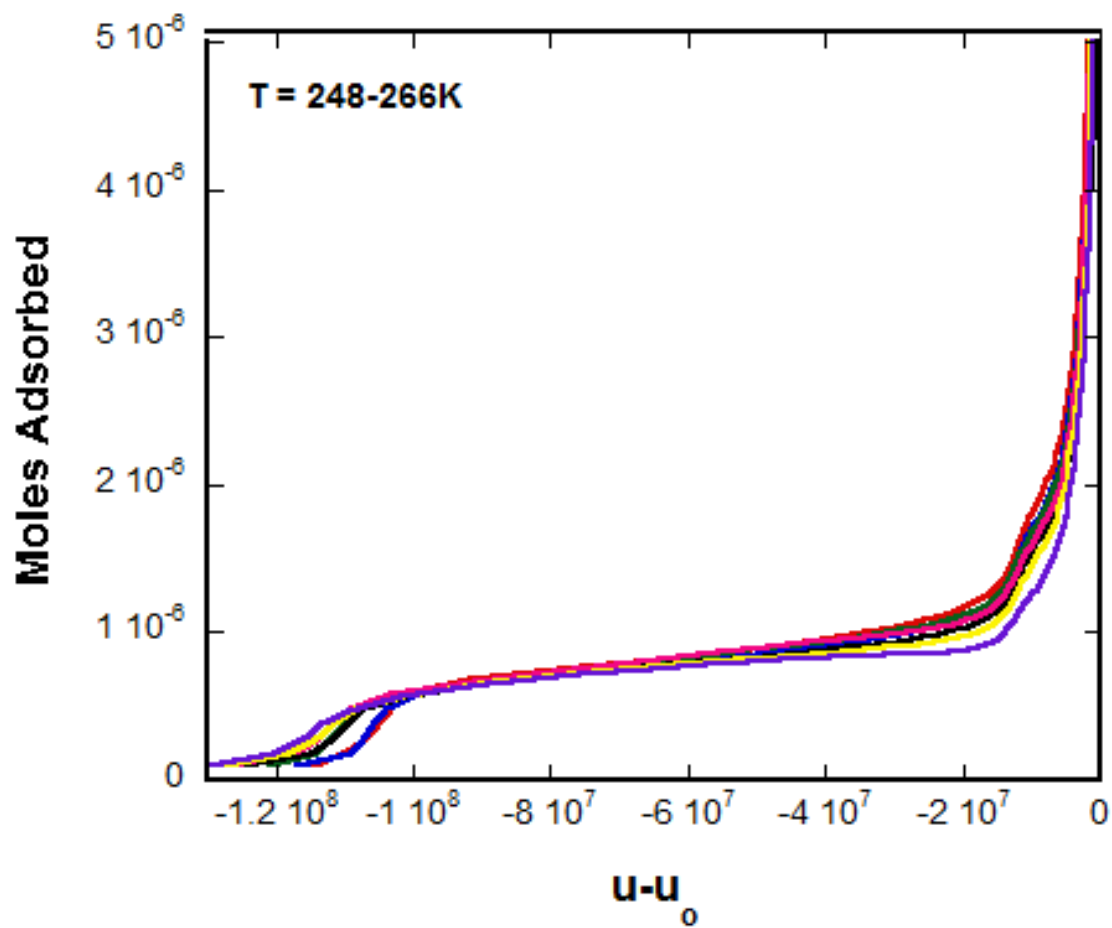
248
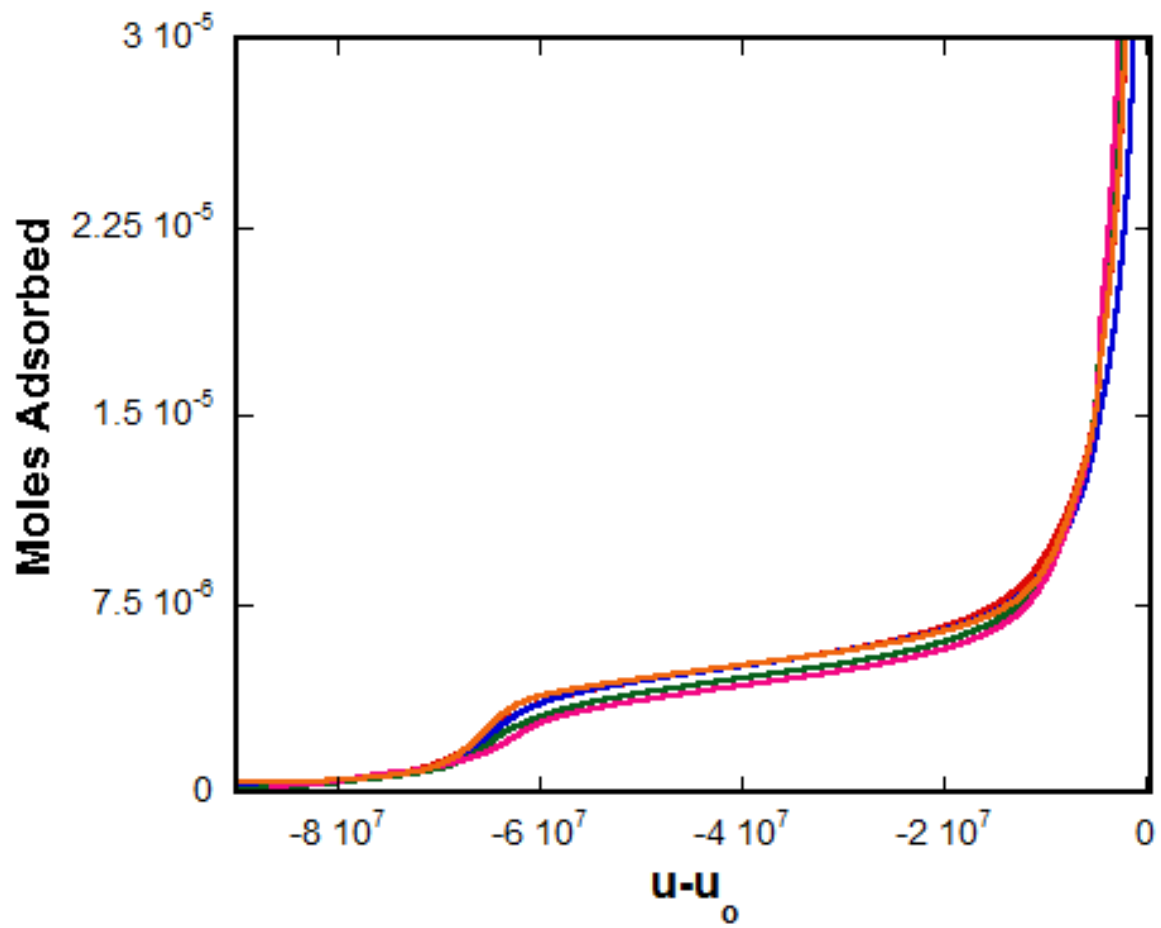
Figure 89 – Series of isotherms (chemical potential vs. moles adsorbed for

butane on hBN
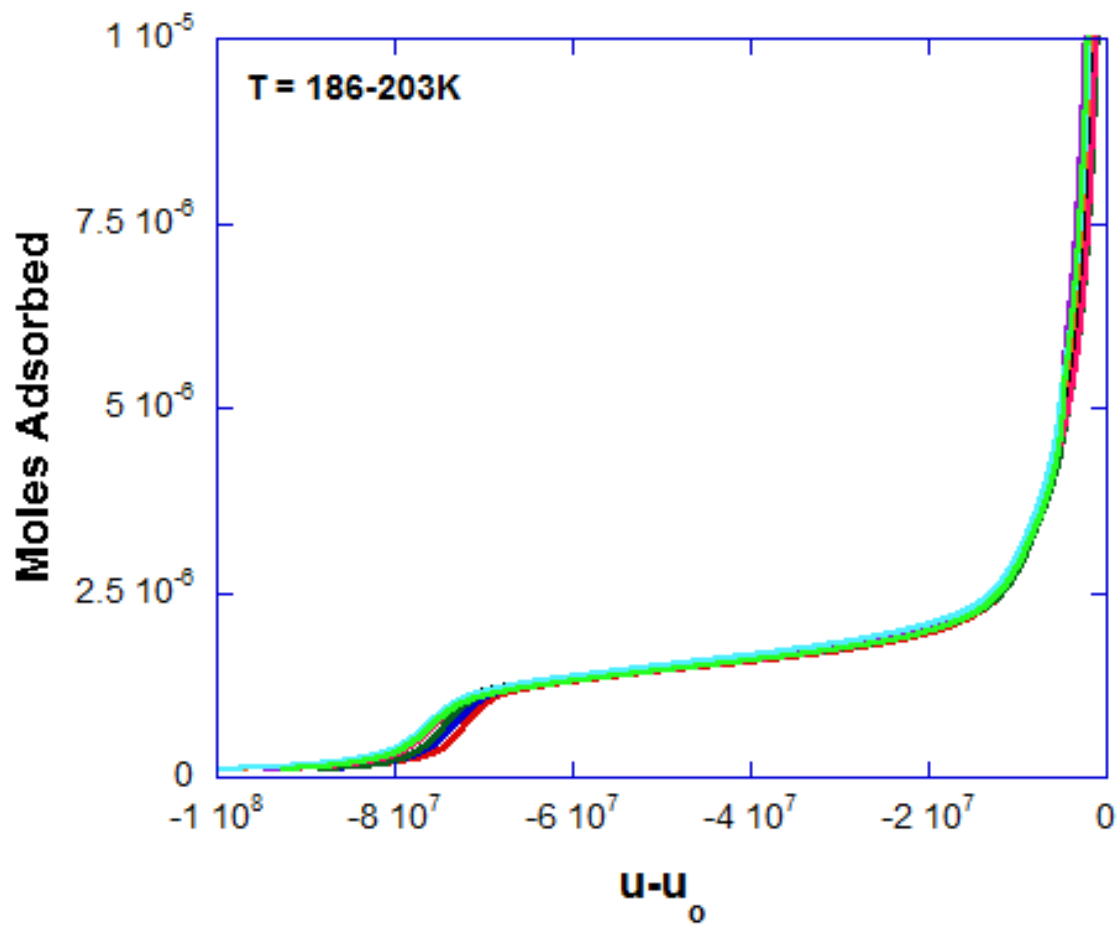
Figure 90 – Series of isotherms (chemical potential vs. moles adsorbed for

pentane on hBN

Figure 91 – Series of isotherms (chemical potential vs. moles adsorbed for hexane on hBN

Figure 92 – Series of isotherms (chemical potential vs. moles adsorbed for heptane on hBN

252

Figure 93 – Series of isotherms (chemical potential vs. moles adsorbed for octane on hBN
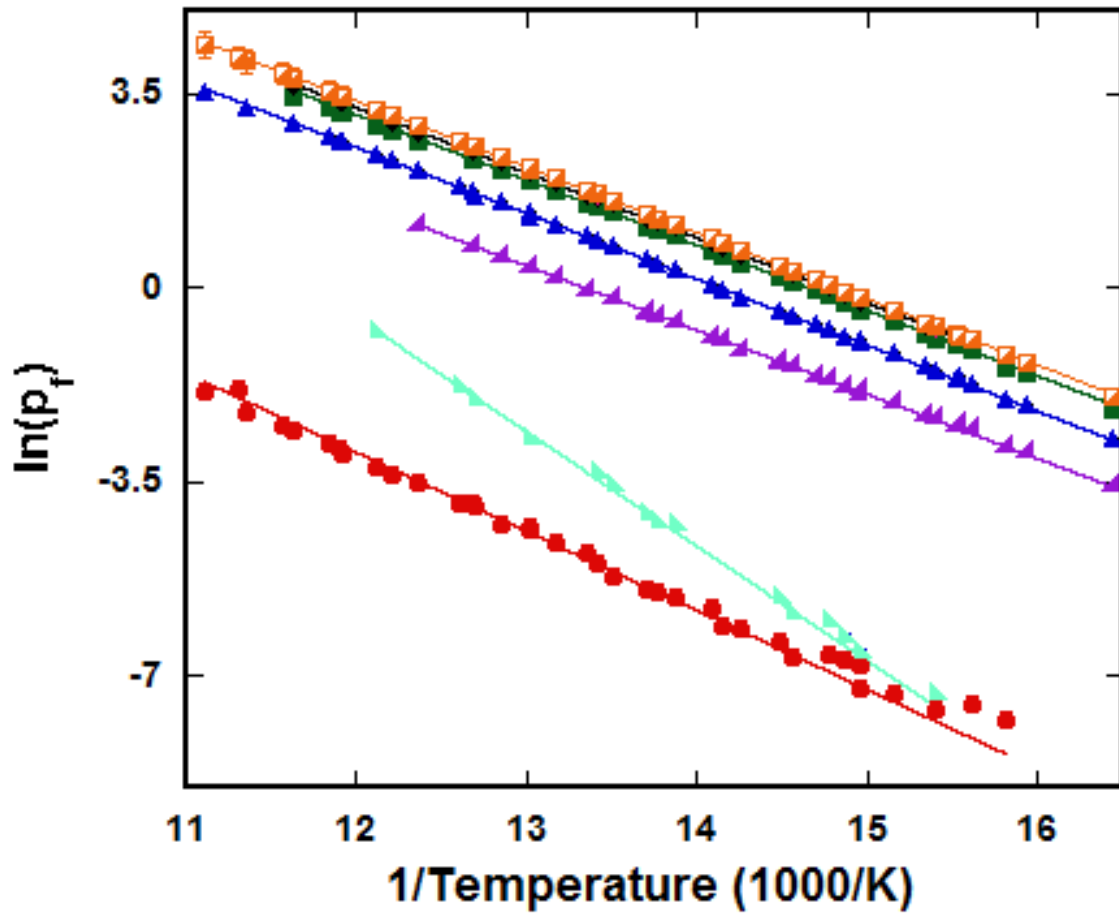
Figure 94 – Clausius-Clapeyron plot for methane adsorbed on hBN
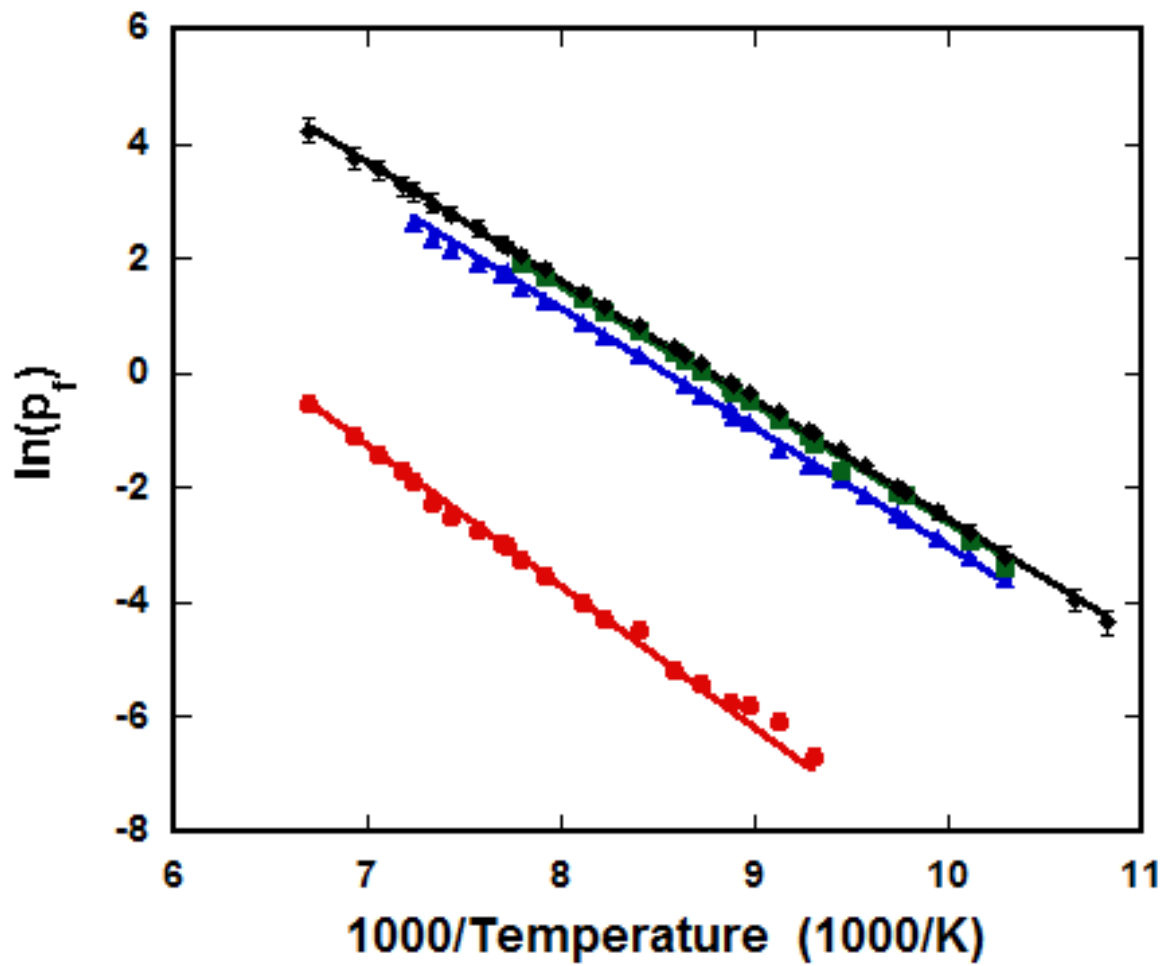
Figure 95 – Clausius-Clapeyron plot for ethane adsorbed on hBN
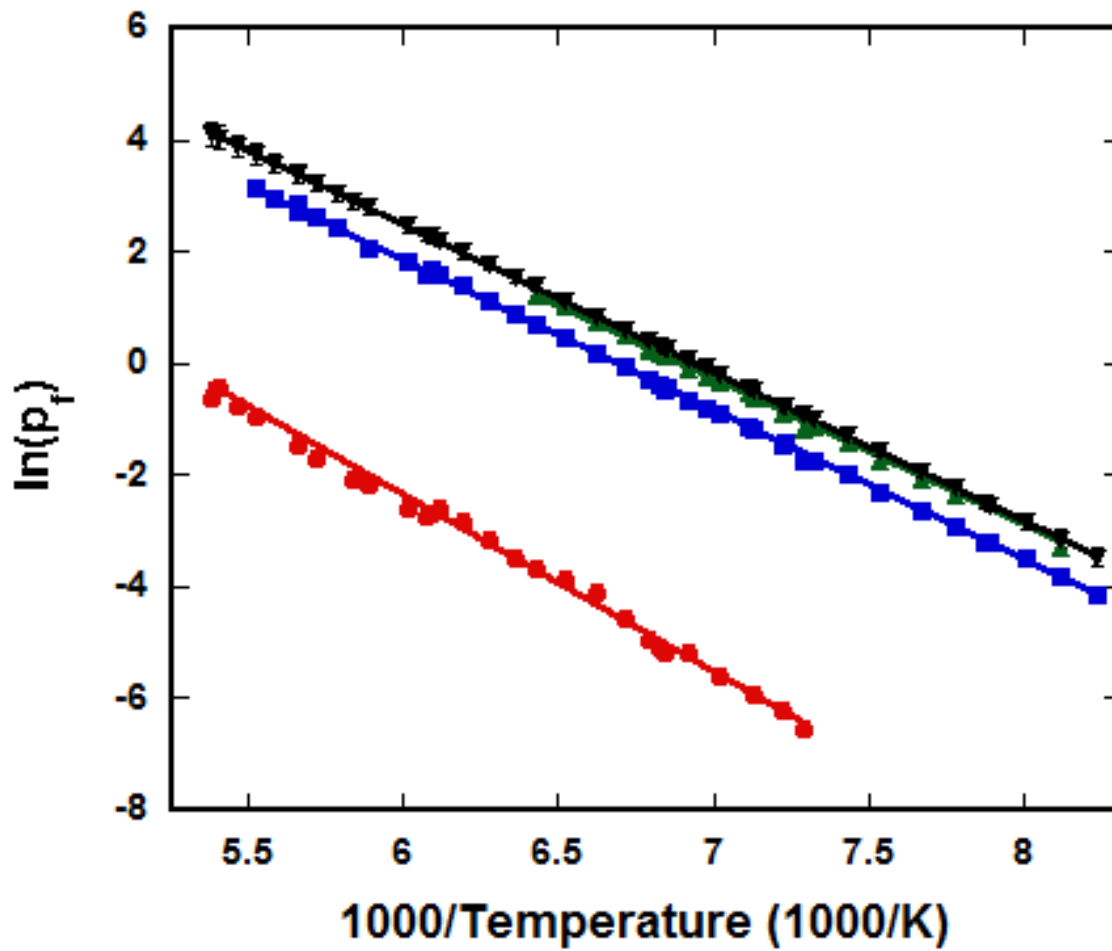
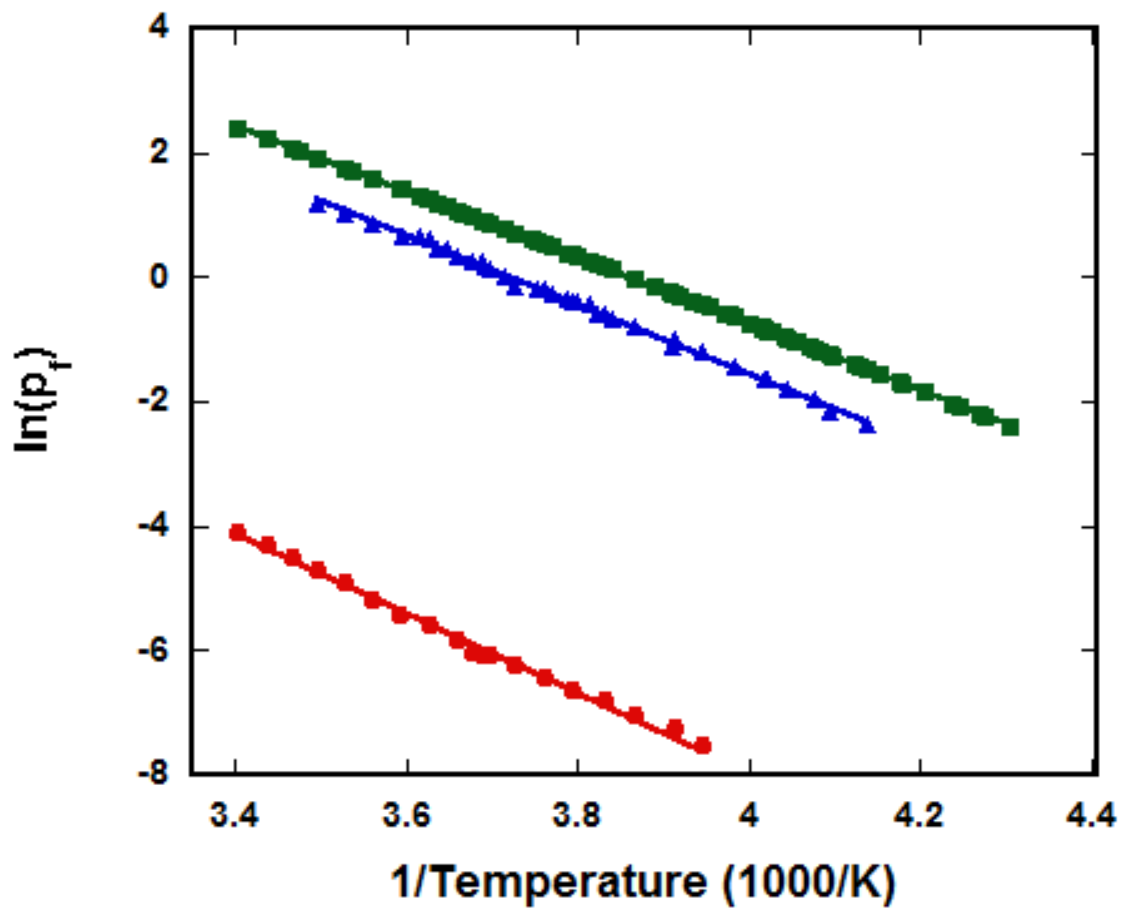Figure 96 – Clausius-Clapeyron plot for propane adsorbed on hBN
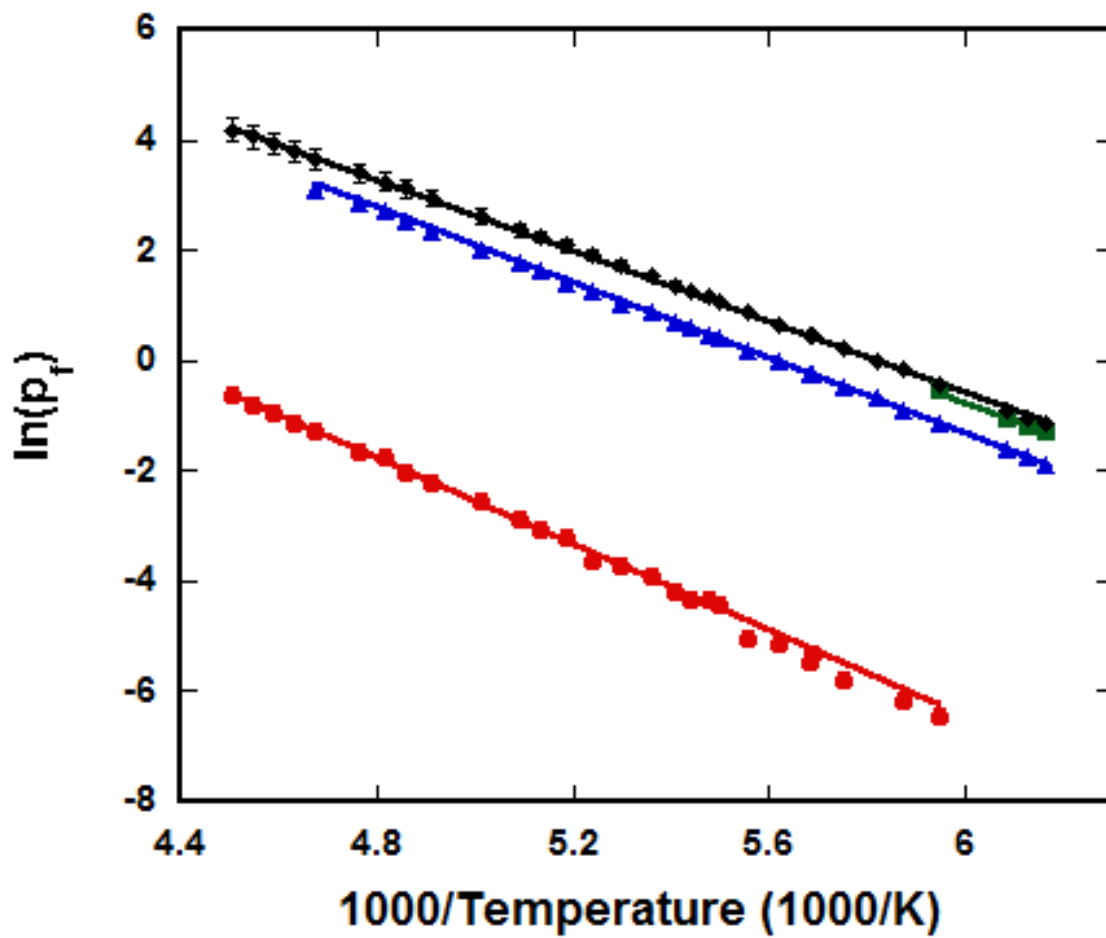
Figure 97 – Clausius-Clapeyron plot for butane adsorbed on hBN
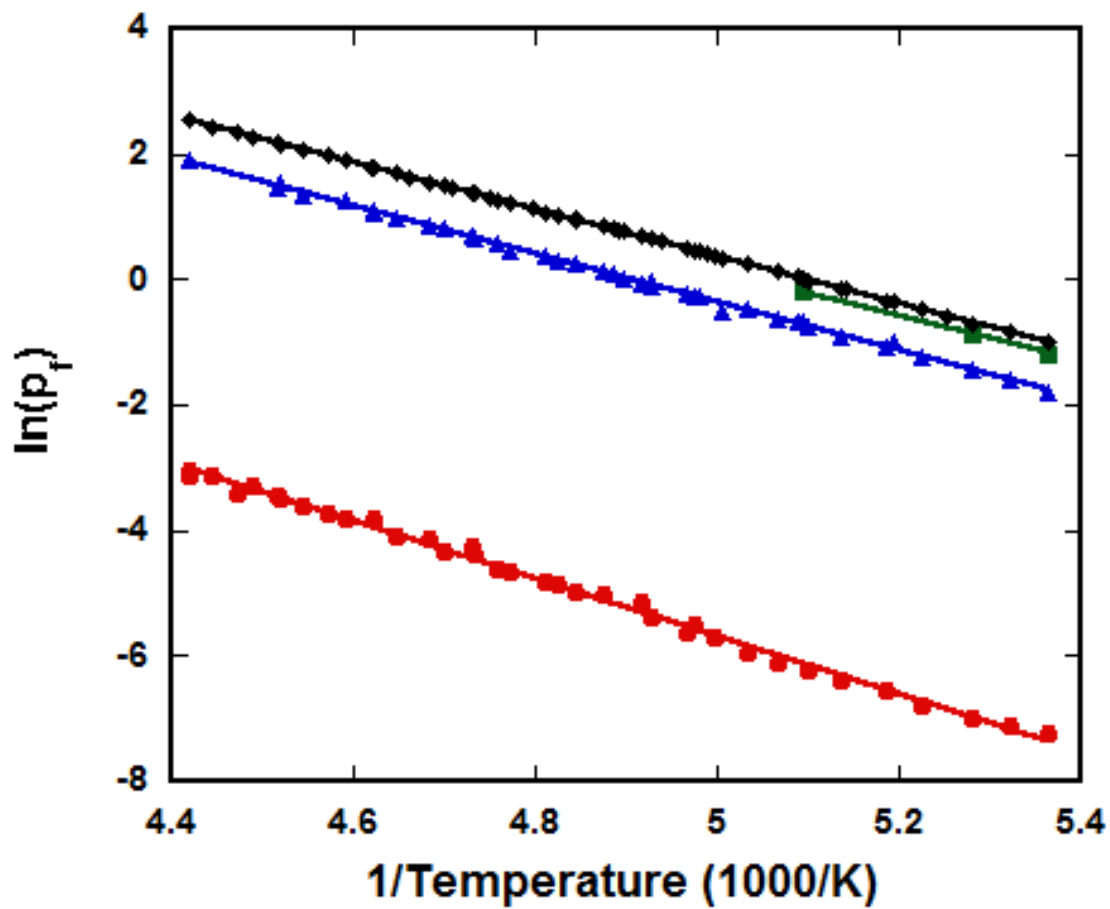
Figure 98 – Clausius-Clapeyron plot for pentane adsorbed on hBN
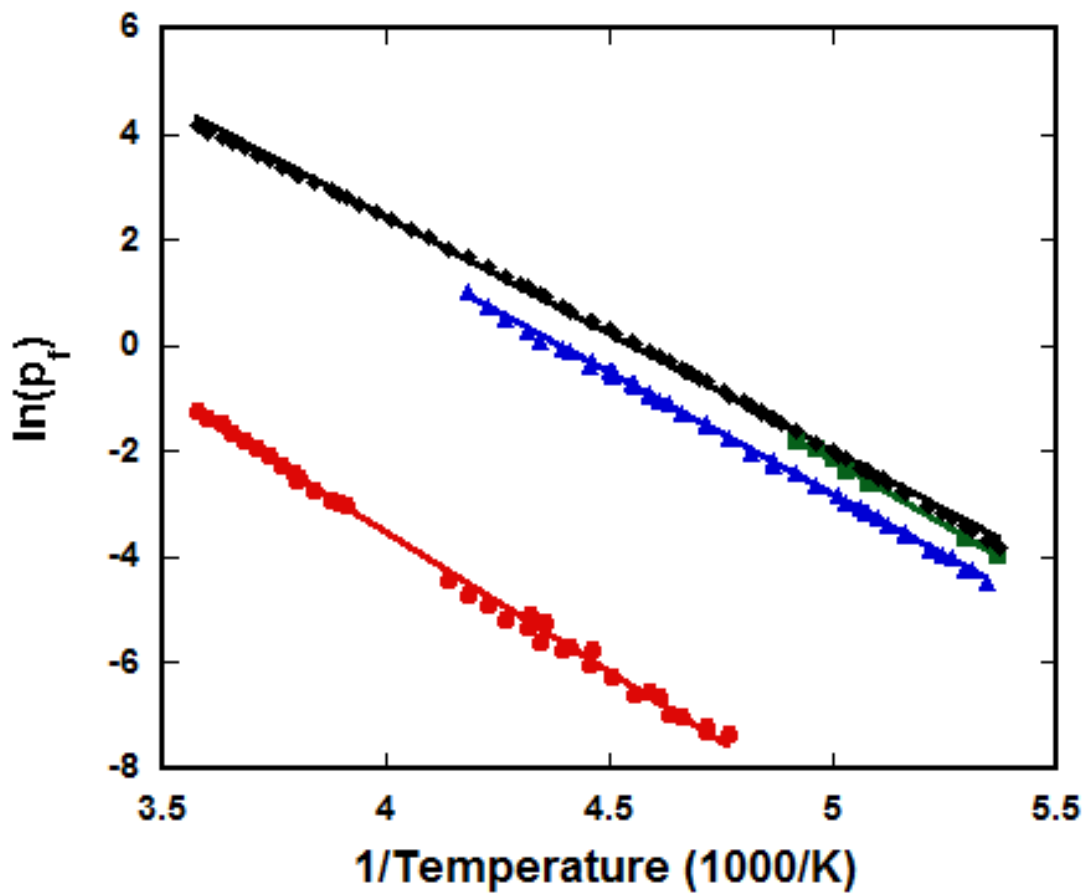
Figure 99 – Clausius-Clapeyron plot for hexane adsorbed on hBN
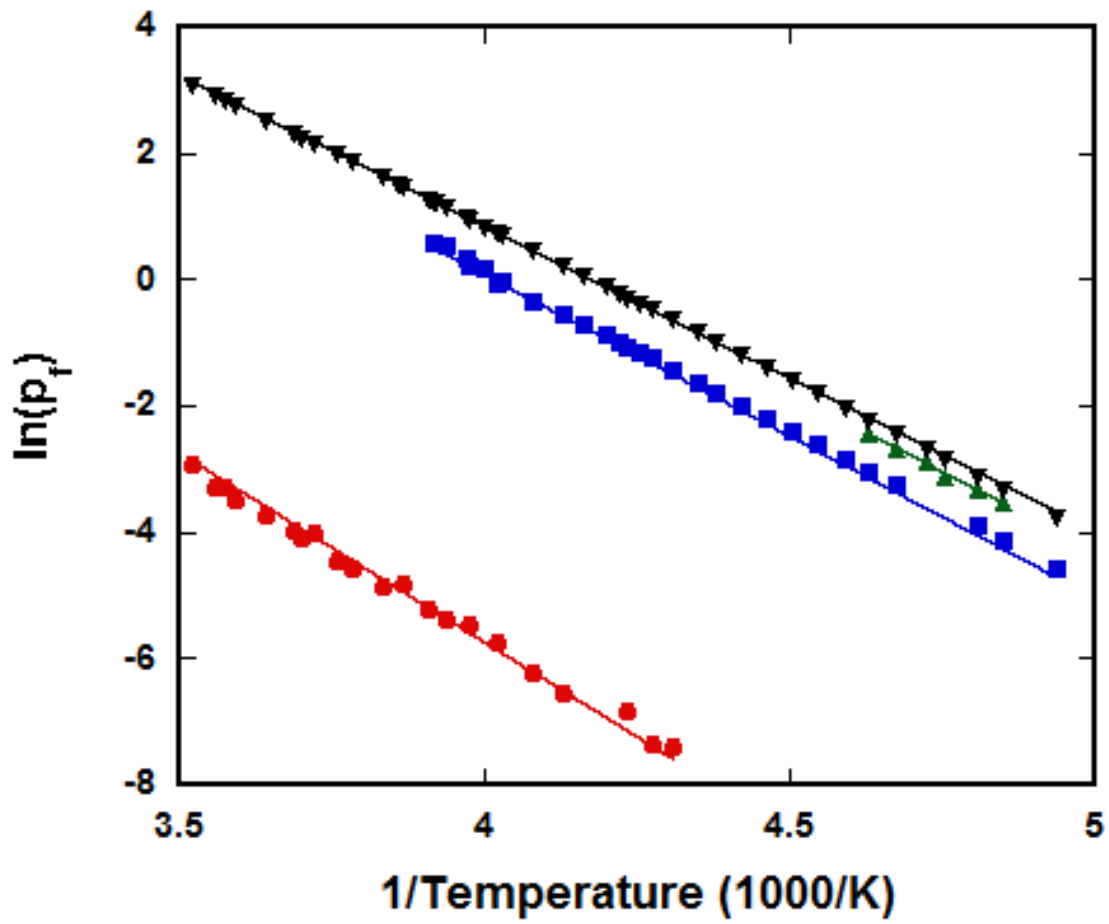
Figure 100 – Clausius-Clapeyron plot for heptane adsorbed on hBN

Figure 101 – Clausius-Clapeyron plot for octane adsorbed on hBN
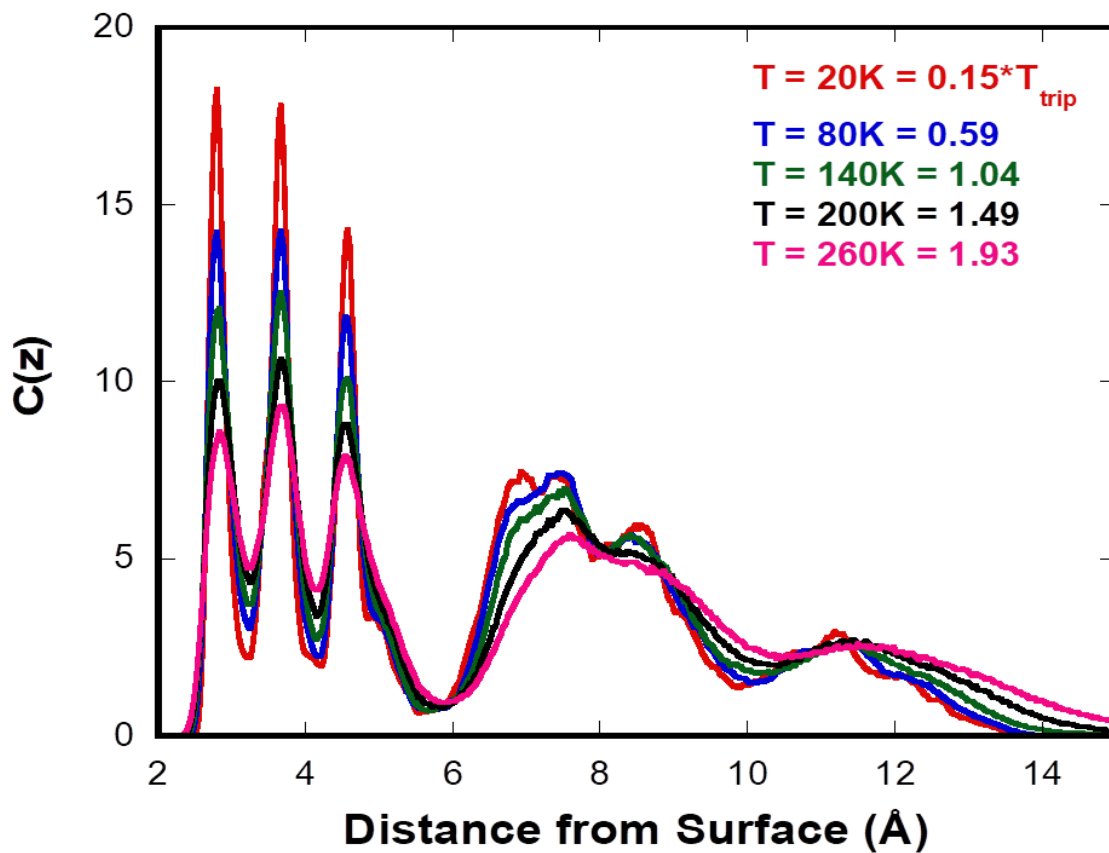
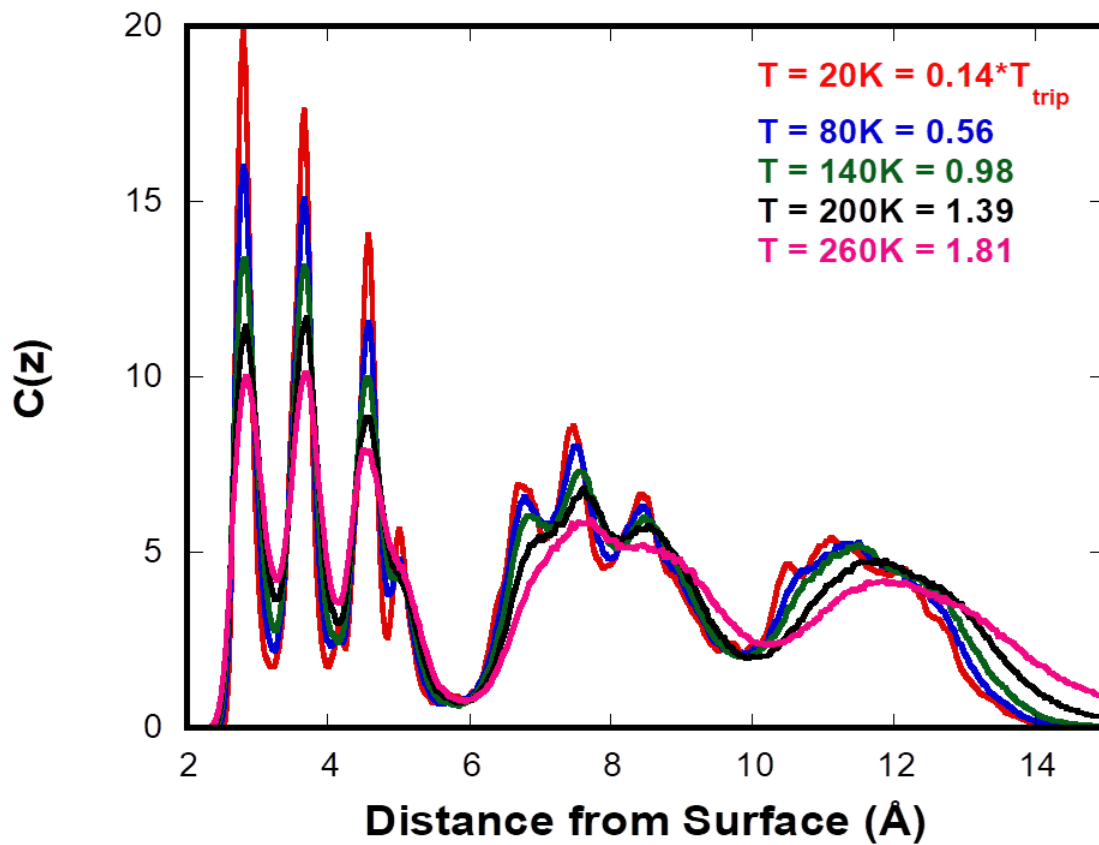Figure 102 – C(z) for trilayer coverage *n*-butane adsorbed on hBN

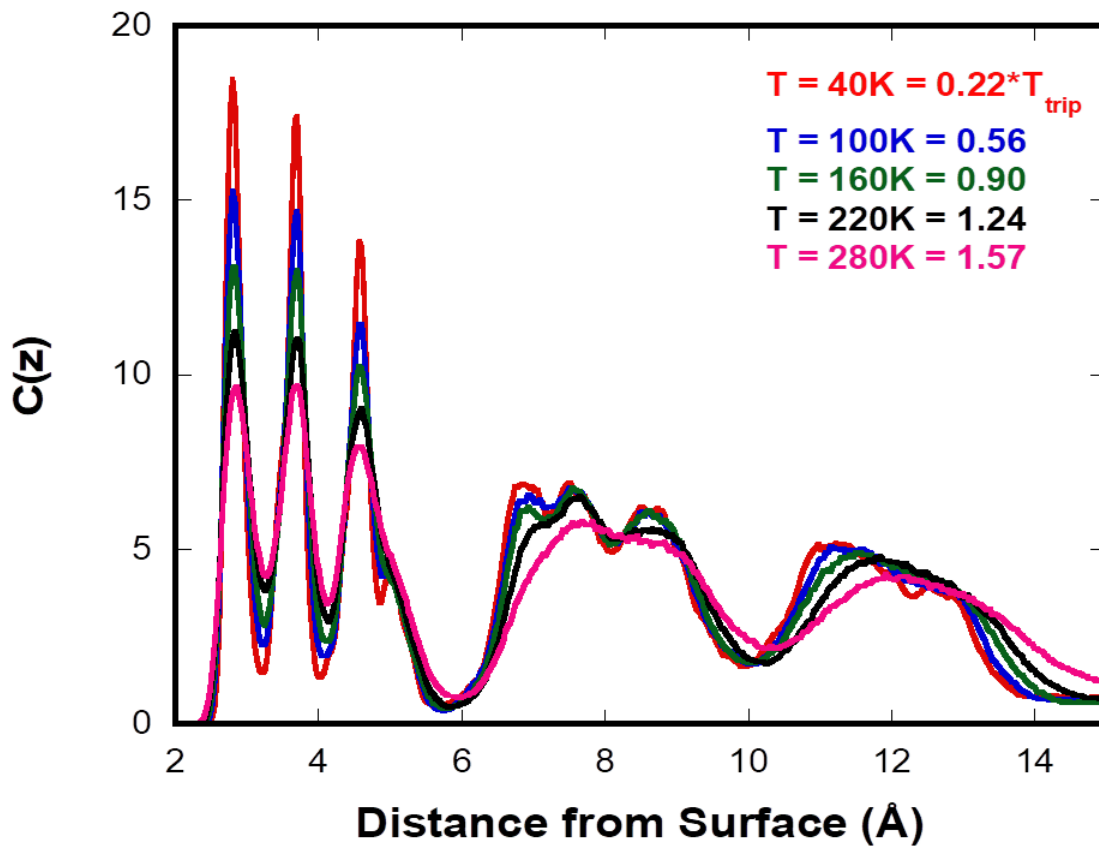Figure 103 – C(z) for trilayer coverage *n*-pentane adsorbed on hBN

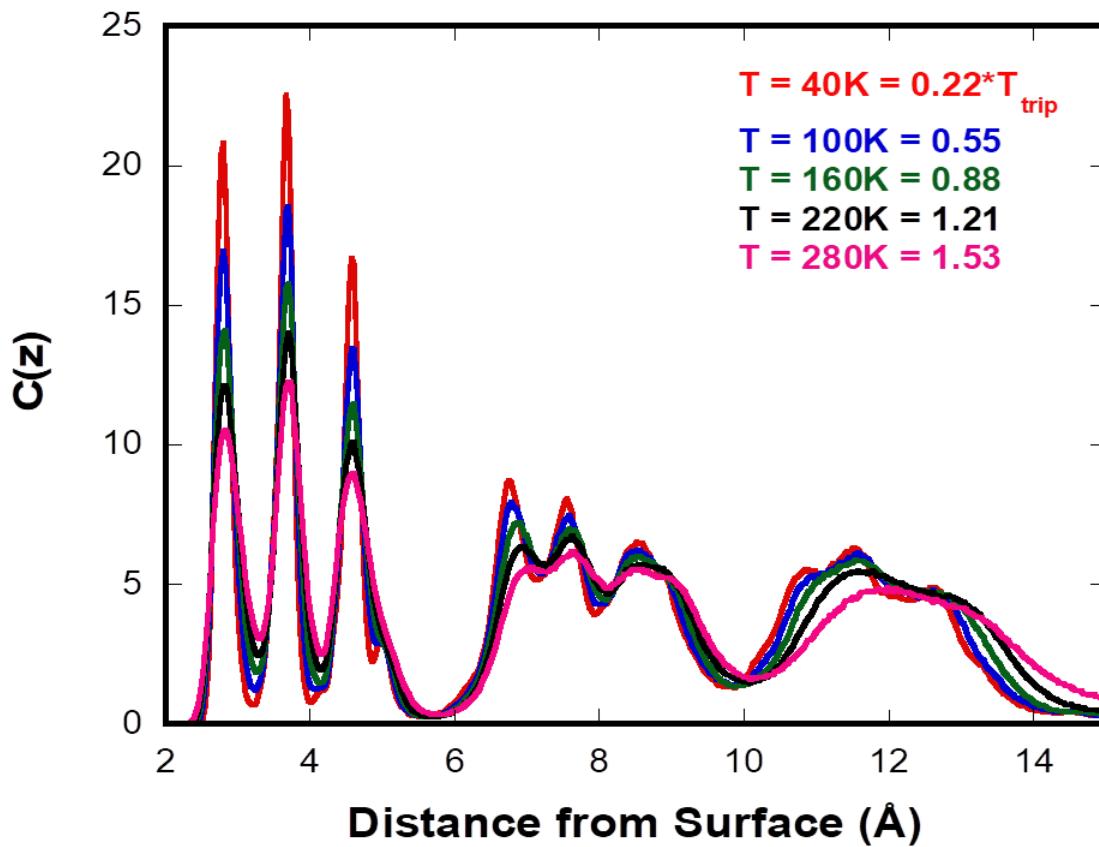Figure 104 – C(z) for trilayer coverage *n*-hexane adsorbed on hBN

Figure 105 – C(z) for trilayer coverage *n*-heptane adsorbed on hBN

## VITA

Nicholas A. Strange was born September 5, 1989 in Zeeland, Michigan. He spent his early life living in West Michigan, until relocating to Newburgh, Indiana in 1998. He attended Castle High School and graduated in 2007. Nicholas attended Indiana University- Purdue University at Indianapolis (IUPUI) where he pursued dual Bachelor's degrees in Chemistry and Forensic Chemistry. As a senior and post-undergraduate, he worked in the research group of Dr. John. V. Goodpaster. Upon graduation, Nicholas interned at the Bureau of Alcohol, Tobacco, Firearms, and Explosives National Laboratory in Laurel, Maryland working under Dr. Gui-hua (Lisa) Lang. Nicholas began his Ph.D. studies at the University of Tennessee and joined Prof. J.Z. Larese's research group in August 2012.